



HAL
open science

Beyond "clear wood": Appearance, structure, physical-mechanical properties and anisotropy of figured woods with different patterns of grain deviations

Hsien-Tsung Hu

► **To cite this version:**

Hsien-Tsung Hu. Beyond "clear wood": Appearance, structure, physical-mechanical properties and anisotropy of figured woods with different patterns of grain deviations. Structural mechanics [physics.class-ph]. Université de Montpellier, 2022. English. NNT : 2022UMONS038 . tel-04736048

HAL Id: tel-04736048

<https://theses.hal.science/tel-04736048v1>

Submitted on 14 Oct 2024

HAL is a multi-disciplinary open access archive for the deposit and dissemination of scientific research documents, whether they are published or not. The documents may come from teaching and research institutions in France or abroad, or from public or private research centers.

L'archive ouverte pluridisciplinaire **HAL**, est destinée au dépôt et à la diffusion de documents scientifiques de niveau recherche, publiés ou non, émanant des établissements d'enseignement et de recherche français ou étrangers, des laboratoires publics ou privés.

THÈSE POUR OBTENIR LE GRADE DE DOCTEUR DE L'UNIVERSITÉ DE MONTPELLIER

En Mécanique

École doctorale : Information, Structures, Systèmes
Unité de recherche Laboratoire de Mécanique et Génie Civil

Beyond «clear wood»: Appearance, structure, physical-mechanical properties and anisotropy of figured woods with different patterns of grain deviations

Présentée par Hsien-Tsung HU
Le 13 06 2022

Sous la direction de Iris BRÉMAUD
et Patrick LANGBOUR

Devant le jury composé de

M. Louis , DENAUD, Maître de conférences, Arts et Métiers, Cluny

M. Nicola MACCHIONI, Directeur de recherche, CNR, Firenze, Italy

Mme. Dominique LAFON-PHAM, Professeur, IMT Mines Alès

M. Jacques BEAUCHÊNE, Chercheur CIRAD, EcoFoG, Kourou

M. Joseph GRIL, Directeur de recherche CNRS, Institut Pascal, Clermont-Ferrand

M. Bernard THIBAUT, Directeur de recherche CNRS émérite, LMGC, Montpellier

Mme. Iris BRÉMAUD, Chargée de recherche CNRS, LMGC, Montpellier

M. Patrick LANGBOUR, Chercheur CIRAD, BioWooEB, Montpellier

M. Arnould OLIVIER, Maître de conférences, LMGC, Montpellier

Rapporteur

Rapporteur

Examinatrice

Examineur

Examineur

Examineur

Directrice de thèse

Co-encadrant de thèse

Invité



UNIVERSITÉ
DE MONTPELLIER

REMERCIEMENTS

The region Occitanie and the University of Montpellier financed the doctoral program. I am highly indebted to my supervisor Mme. Iris Brémaud and my co-supervisor M. Patrick Langbour, for their guidance, help, and dissertation writing.

I also want to send my gratitude to many people. Without their help and support, I cannot accomplish my study and dissertation.

Thanks to the people in LMGC, M. Gille Camp, M. Gilles Genevois, Mme Capucine Carlier, M. Olivier Arnould, and Stéphane Corn (IMT Mines Alès) for the fabrication, optimisation, and simulation suggestion for the new build-up vibrational torsion device.

Also, I want to acknowledge the BioWooEB team of CIRAD. M. Daniel Guibal and M. Alban Guyot taught me and helped me with the shrinkage and BING's experimental set-up. M. Sylvain Lotte helped with the sample preparation in the premier step.

I want to thank M Eric Rosenkrantz (from IES) for teaching and helping me with the ultrasonic measurement. M Tancrède Alméras (from LMGC) assisted me with the X-ray diffraction experiment—also, thanks to Arie van der Lee from IEM for setting up the X-ray diffraction instrument.

I am grateful for the suggestions, questions, and propositions from the jurys, M Bernard Thibaut, M Jacques Beauchêne, M Joseph Gril and Mme Dominique Lafon-Pham. Those opinions expanded my field of vision. Also, the rapporteurs, M Nicola Macchioni and M Louis Denaud, their gentle and constructive suggestions made my manuscript more completed.

For my family support, I want to express my gratitude to my mom, sister, brother, and cat in Taiwan for their encouragement, which helped me complete my dissertation. More, thanks to my girlfriend Yueh YIN for her cheer and accompanying.

To the friends I met in Montpellier, I am so lucky to meet you here and have your encouragement for Mme. Iria Gonzales, M. Dan Binyon, M. Frisco Nobilly, Mme. SueHan Lee, M. Ahmad Alkadri, Mme Tai-Yun Hsieh, M. Manuel Cárdenas, M. Issam Hrazmi; also, the hot-pot friends, Mme. Lee, Mme. Chen-Yi Yang, Mme. Roy Anne Wu, Mme. Elaine Lam, Mme Lily Cheng.

Lastly, I would love to acknowledge M. Joseph Gril (from the Institut Pascal), M. Eiichi Obataya (from the University of Tsukuba), M. Pierre Cabrolier, and M. Bernard Thibaut for my thesis concept development and idea generation for the method and the analysis. Lastly, again, M Paolo Pisani's Chatometry study proved the workability and functionality of the optical measurement I had proposed. I believe his work will bring the wood evaluation on the figured wood to a new area. Thanks to him for sharing his result in my Ph.D. defence presentation. It made me fully confident in my idea.

RÉSUMÉ

Le fil du bois n'est pas droit, et cette singularité existe couramment dans la nature. Certains arbres présentent fréquemment des motifs, ou schémas de fil, spécifiques, ce qui fait que le fil de leur bois dévie par rapport au sens de l'application. La conséquence est que ces bois ont un motif de fil et présentent une apparence attrayante sur les surfaces finies, et sont appelé bois figurés. La définition du bois figuré se situe entre les limites de "l'existence commune" et de "l'occurrence accidentelle". La définition est donc explorée en explorant leur existence et les termes lexicaux par des fournisseurs professionnels de bois.

L'information cachée de l'apparence attrayante est due à l'angle plongeant du fil par rapport à la surface. Ainsi, un essai optique en lumière visible avec des angles multiples a été tenté. Une équation analytique est également construite pour approcher leur structure. Par ailleurs, des essais de fendage dans la direction radiale démontrent la structure du fil du bois. De plus, certains motifs tels que « moucheté » présentent des changements soudains de direction de fil. Des schémas de fil comme pommelé et madré ne peuvent pas être simulés ou quantifiés. Outre les essais mésoscopique de la structure du fil, la méthode XRD (diffraction des rayons X) est utilisée pour des mesures locales de l'angle du fil (GA) et de l'angle des microfibrilles (MFA).

Deux méthodes mécaniques dynamiques (vibratoires) ont été utilisées pour mesurer les propriétés mécaniques longitudinales sur deux tailles de spécimens. De nouveaux développements ont permis de tester les propriétés dynamiques en cisaillement. Un test quasi-statique (ultrasons) a été utilisé pour étendre aux modules dans les autres directions. Les retraits et le point de saturation des fibres (FSP) ont été mesurés pour comprendre les propriétés hygromécaniques et leur relation avec les propriétés mécaniques. Ces valeurs de propriétés ont été comparées aux résultats de la littérature, en comparant la différence relative. L'anisotropie réduite a été confirmée comme une caractéristique des bois figurés.

Bien que les bois figurés soient caractérisés par des déviations de fil, leurs propriétés mécaniques longitudinales ne sont pas nécessairement dégradées, et entre des espèces très différentes, le MFA domine davantage. Cependant, en général, les déviations de fil diminuent le module d'élasticité longitudinal, et les modules de cisaillement sont relativement importants, ce qui entraîne une plus faible anisotropie axiale-cisaillement. De même, l'anisotropie des propriétés semble plus liée aux MFA car leurs valeurs dans l'espèce sont plus stables que celles de GA qui présente des variations très locales pour les structures de fil complexes. En fin de compte, le classement visuel des vendeurs de bois professionnels est indirectement prouvé car il est utile pour comparer les mêmes espèces avec différents degrés de figure pour le classement des propriétés mécaniques. Cependant, le MFA n'est pas détectable à l'échelle macroscopique.

Mots clés : bois d'artisanats, bois figurés, classement visuel, propriétés mécaniques, relations structure-propriétés, anisotropie.

ABSTRACT

The wood grain is not straight, and the singularity commonly exists in nature. Some trees frequently have specific grain patterns, causing their wood grain to deviate to the applying direction. The consequence is that those wood have the grain pattern and demonstrate an attractive appearance on the plane, called the figured wood. The definition of the figured wood is between the boundary of “common existence” and the “accidental occurrence”. The definition is thus defined by exploring their existence and lexical terms from the professional wood supply.

The hidden information about the attractive appearance is because of the diving angle. Thus, a trial with the visible light with multiple angles is made. Also, the analytical equation is built to approach their structure. Instead, the splitting along the radial direction demonstrates the grain structure in wood. Furthermore, some patterns, such as birdseye grain, have sudden grain changes against the radial direction. Pommele and swirling grain cannot be simulated or quantified. Besides the mesoscopic discovery for the grain structure, the XRD (X-ray diffraction) method is used for their grain angle (GA) and microfibril angle (MFA) local measurements.

Two dynamic mechanical (vibrational) methods were used for the longitudinal mechanical properties measurements in two sample sizes. Some new developments allowed testing dynamic properties in shear. A quasi-static test (ultrasonic) was used to expand to moduli in the other directions. The shrinkage properties and fibre saturation point (FSP) were measured to understand the hygro-mechanical properties and the relation to mechanical properties. Those properties values were compared with the literature results, comparing the relative difference. Reduced anisotropy was confirmed as a feature of figured woods.

Although figured woods are characterised by grain deviations, the longitudinal mechanical properties are not necessarily degraded, and between very different species, the MFA more dominates it. However, the grain deviations generally reduce the longitudinal modulus of elasticity, and the shear moduli are relatively large, causing smaller axial-to-shear anisotropy. Also, the anisotropy of properties appears more related to the MFA because it is more stable than the GA, which has very local variations for the complex grain structure. In the end, the visual grading from professional wood vendors is indirectly proving it because it helps compare the same species with different degrees of figure for the mechanical properties grading. However, the MFA is not detectable in macroscopic.

Keywords: woodcrafts, figured wood, visual grading, mechanical properties, structure-properties relationships, anisotropy.

TABLE OF CONTENTS

REMERCIEMENTS	i
RÉSUMÉ	ii
ABSTRACT	iii
TABLE OF CONTENTS	iv
General Introduction	1
I. Background, definitions, terminology and problematic of figured woods	3
Introduction of Chapter I	3
I.A. General elements on wood: Fibrous structure at different scales	3
I.B. Microscopic scale: fibres' cell wall and microfibril angle	3
I.B.1. Fibrous elements of wood at meso- and macroscopic scales	4
I.C. The supposed general case: “clear wood.”	5
I.D. Beyond “clear wood”: singularities, grain deviations and figured wood	6
I.D.1. Existence of variation in every tree/wood	7
I.D.2. Grain deviations with irregular variations within a trunk	7
I.D.3. Relatively constant patterns of grain deviation: the figured woods	9
I.E. Occurrence of figured wood: new statistical analysis from existing literature	11
I.F. A terminology for wood figures and figured woods	12
I.F.1. The figured wood and the wood figure	12
I.F.2. The Name of Wood Figure: wood structure or culture?	14
I.F.2.a) Selective discussion of linguistic aspects	14
I.F.2.b) An illustrated multilingual terminology of wood figures and figured woods	16
I.F.3. The problematic definition of “figured woods”: occurrence, structure and terminology	32
Summary of Chapter I and trends for further research	34

II.	Description of the structural organisation and some visual features of figured wood	36
	Introduction of Chapter II	36
II.A.	Modelling and simulation	38
II.A.1.	A tentative to describe the connection of possible grain patterns by an analytical model	38
II.B.	Optical and visual examinations	40
II.B.1.	Tentatives to characterise the wood surface of figured wood by optical methods	40
II.B.2.	Visual screening of CIRAD's xylarium to identify species with figured wood	45
II.C.	Experimental determination of the multi-scale orientation	48
II.C.1.	Materials in the current study	48
II.C.1.a)	Some of the known features of studied species	51
II.C.1.b)	General sampling and cutting plan	53
II.C.2.	Grain angle (GA) determination	55
II.C.2.a)	The splitting method and the figure evaluation	56
II.C.2.b)	Profiles of GA patterns	60
II.C.2.c)	GA measurement by X-Ray diffraction	62
II.C.3.	Microfibril angle (MFA) measurement	62
II.C.3.a)	Methodology for X-Ray diffraction	63
II.C.3.b)	Data analysis of X-ray diffraction	64
II.C.4.	Results of the multi-scale structural evaluation	66
II.C.4.a)	The visual appearance of the studied material of figured woods	66
II.C.4.b)	The diversity in GA patterns and the distribution of maximum and local GA values	69
II.C.4.c)	Distribution and categorisation of MFA values	72
II.C.4.d)	Comparing the variations in MFA and in GA	74

Summary of Chapter II	76
III. Characterisation of physical and mechanical properties and their anisotropy	79
Introduction of Chapter III	79
III.A. Overview of the sampling plan and types of measurements	81
III.A.1. The materials: basic information on the initial planks	81
III.A.2. The preparation of the specimens: processing and marking system	84
III.B. Shrinkage and Fibre Saturation Point (FSP)	86
III.B.1. Protocol	87
III.B.2. Calculations	87
III.B.2.a) Calculation of Shrinkage and FSP parameters	89
III.B.2.b) The calculation for taking into account ring angle in the R-T plane	90
III.C. Vibrational Measurements	92
III.C.1. Natural Bending Vibration in Free-Free Mode: BING®	92
III.C.1.a) Principle	92
III.C.1.b) The BING® device and software	92
III.C.1.c) The process for the test: multi-dimensions and multi-conditions	92
III.C.1.d) Samples preparation for the BING test: cutting dimension and conditioning	93
III.C.2. Non-contact Forced Bending Vibration in Free-Free Mode: Vybris	95
III.C.2.a) Principle	95
III.C.2.b) Preparation of specimens	96
III.C.2.c) The Vybris device	97
III.C.3. Forced Vibration in Shear: Developing Vybris-Torsion	100
III.C.3.a) Principle	100
III.C.3.b) Equations	101
III.C.3.c) Maximum rotation angle	105

III.C.3.d) Design of the device’s hardware	106
III.C.3.e) Theoretical validation: Preliminary methodological test and Finite elements modelling	108
III.D. Ultrasonic tests	110
III.D.1. Theory	110
III.D.2. Testing conditions and devices	114
III.D.3. Calculations for Post-processing of experimental data	117
III.D.4. Signal acquisition and phenomenon description in the case of shear waves	117
III.E. Generic Results: Methodological Effects and Range of Values in Physical-Mechanical Properties	119
III.E.1. Hygro-Mechanical aspects	119
III.E.1.a) The range of shrinkage values and of their anisotropy	119
III.E.1.b) FSP and Equilibrium Moisture Content at different conditions	125
III.E.1.c) Effects of hygrothermal conditioning on dynamic properties tested by BING	129
III.E.2. Dynamic mechanical properties comparison between different methods	132
III.E.2.a) Longitudinal modulus of elasticity by BING, Vybris and Ultrasound	133
III.E.2.b) Shear moduli by BING, Vybris and Ultrasound	134
III.E.2.c) Longitudinal damping by internal friction from BING and Vybris	138
III.E.2.d) Longitudinal and torsional damping by Vybris-bending and Vybris-torsion	142
III.E.3. The Range of Variability for the Mechanical Properties of Figured Woods	144
III.E.3.a) General comparison between species and between methods	144
III.E.3.b) The most variable properties and the most stable properties	150
III.E.3.c) Comparison of results on figured wood with literature data on “standard hardwoods”	151
Summary of Chapter III	153

IV.	Structure-properties relations and scale effects in figured woods	156
	Introduction of Chapter IV	156
IV.A.	Between-species diversity versus within-species variability in properties	158
IV.A.1.	Diversity and variability of the density	158
IV.A.2.	Diversity and variability of the axial modulus of elasticity and specific modulus	159
IV.A.3.	Diversity and variability of in-plane shear moduli	161
IV.A.4.	Diversity and variability of damping coefficients, longitudinal and in shear	162
IV.B.	Correlations between properties: Comparison of figured woods with standard relationships	165
IV.B.1.	Correlations describing anisotropic elastic moduli: comparison to the “Standard Hardwoods”	167
IV.B.1.a)	Correlations between density and anisotropic moduli	167
IV.B.1.b)	Correlations between the different ratios of elastic anisotropy	169
IV.B.2.	Correlations between shrinkage property and specific gravity: comparison with statistical trends on temperate and tropical hardwoods	171
IV.B.3.	Correlations describing the vibrational properties: comparison with standard trends between damping and dynamic moduli	172
IV.B.3.a)	The relation between longitudinal damping and specific modulus	172
IV.B.3.b)	The relation between axial-to-shear anisotropy in damping and moduli	175
IV.C.	Effects of Local Orientation on Physical-Mechanical Properties and their Anisotropy	177
IV.C.1.	Global analysis of the factors affecting the measured properties	177
IV.C.1.a)	All properties, at the scale of standard bar specimens (20× 20 mm ² transversal section)	178
IV.C.1.b)	Vibrational properties, at the scale of thin Vybris specimens (2×12 mm ² transversal section)	180

IV.C.2.	Effects of local orientation on anisotropic moduli measured by ultrasound	182
IV.C.2.a)	Grain angle and anisotropy (on ultrasound specimens)	184
IV.C.2.b)	MFA and anisotropy (from ultrasound tests)	184
IV.C.3.	Effects of local orientation on shrinkage properties	188
IV.C.4.	Effects of local orientation on vibrational properties	189
IV.C.4.a)	Effects of GA on the anisotropy of vibrational properties	191
IV.C.4.b)	Effects of MFA on the anisotropy of vibrational properties	192
IV.C.5.	Further Analysis for the selected Anisotropy Properties	193
IV.C.5.a)	The T-R Anisotropy of moduli of Elasticity and in Shear	193
IV.C.5.b)	The tangential specific elastic modulus and axial rigidity anisotropy	194
IV.C.5.c)	The T-R elastic-shear anisotropy and hygro-mechanical anisotropy	195
IV.D.	Superimposed effects: Cumulated effects of GA and MFA on the longitudinal specific modulus of elasticity	196
IV.E.	Grain deviations in figured wood: “quality” or “defect”?	202
IV.F.	Comparison of physical-mechanical properties with recorded appearance (Chapter II) and with appreciations (Chapter I)	203
	Summary of Chapter IV	205
	General Conclusion and Perspective	208
	Résumé étendu en français	211
	LIST OF FIGURES	223
	LIST OF TABLES	233
V.	References	235
VI.	Annexes	246

*“Wood quality is a statistical result, and it can be only evaluated by
appreciating the magnitude of variation.”*

- Larson PR 1969

General Introduction

As a natural material, wood has been adopted for thousands of years in many applications. According to the people's knowledge and experience, the wood utilisations and the selection criteria are different depending on the fields, e.g., artisan carpentry, instrument maker, engineering construction. Their preferences concern the wood's visual appearance and physical properties, and mechanical performance due to the wood biodiversity. Beyond the species biodiversity, if the wood variation further includes grain deviation, what would it be for their characteristics?

Straight or non-straight, the grain deviations from different aspects

From an engineering point of view, the grain angle and deviation negatively affect the mechanical performance and the rupture properties. Accordingly, having the grain deviation or non-straight grain is a disadvantage and a defect. Instead, the straight grain is relatively rare in nature. A piece of wood with an apparently-straight grain could be actually found of having grain deviation. Despite it, some specific grain patterns have been indicated and categorised. The wood with those grain patterns is thus named the figured wood.

For the artisanal carpenter or instrument maker, looking for a piece of straight grain wood is not always the priority but one of the options depending on the preference and purpose. For some utilisations, the figured wood for them would be a better option instead. Also, some applications are not replaceable with non-figured wood, in the opinion of the producer or woodworker, e.g., veneer or violin backplate. Moreover, the most featured characteristic of the figured wood is the alluring surface plane brought by the figured grain pattern, and some usages are because of it.

Objectives of the thesis

The objective is accordingly to explore the existence and the diversity of the figured wood. Then, the consequence of the grain pattern to the appearance, mechanical properties, hygro-mechanical properties. Further, the inter-relations from the above properties are also studied.

The organisation of the manuscript

The study is then organised as the following.

- Chapter I: the definition of the figured wood is made; the fraction of the figured wood is statistically studied; later, the terminology and figures are presented.

- Chapter II: the measurement and the analysis of the local orientation are made;
- Chapter III: the physical, mechanical, hygro-mechanical properties are characterised, and their generic results are presented;
- Chapter IV: the variability of figured woods' properties is presented, comparisons with standard trends from the literature are made; the anisotropic properties are studied; then the effects of local orientations on properties are studied.

I. Background, definitions, terminology and problematic of figured woods

Introduction of Chapter I

This introductory chapter attempts at describing what is meant by “clear wood” and “figured woods”. After some brief elements of general knowledge on wood structure and the supposed general case of “clear wood”, the different types of grain deviations will be presented on the basis of the literature. The difference between irregular and regular grain deviations, and their systematic or occasional occurrence, will be shortly discussed. The different elementary patterns of figured woods will be introduced. After these elements from the literature, the relation between the notions of “figured woods” and of the “figures of wood” will be discussed based on an original contribution of the present study, including an illustrated multilingual terminology built from the analysis of international woodworking resources.

I.A. General elements on wood: Fibrous structure at different scales

Wood as a natural fibrous material, the fibres’ direction and physical, chemical, and mechanical characteristics of fibres dominate the mechanical properties of a piece of wood. Among the different longitudinal cells, e.g., tracheid, fibre, vessel, parenchyma, in general (and in the present study), “fibre” will be referred to the cells in the axial direction that have a primarily-structural function, e.g., tracheids for softwoods and fibres for hardwoods.

I.B. Microscopic scale: fibres’ cell wall and microfibril angle

Wood fibre (or tracheid) cell wall is a multi-layered composite composed of cellulose, hemicelluloses, and lignins, with occasional extraneous components (organic extractives, inorganic ashes). The crystalline cellulose is organised into microfibrils. Structurally, the fibres’ cell wall consists of the primary cell wall (P), secondary cell wall (S), and middle lamella (ML) (Fig. 1). Commonly, the S2 layer in the secondary cell wall determines the fibre’s and wood’s mechanical and hygro-mechanical properties, because it is the thickest layer (without considering the particular organisations found in reaction woods). In the whole fibre, cellulose microfibril angle (MFA, μ) is the most influential factor for those above-mentioned wood properties. Herein, MFA is the included angle between the fibre’s direction (blue arrow in Fig. 1) and the microfibril’s orientation (in S2 layer only) (red arrow in Fig. 1).

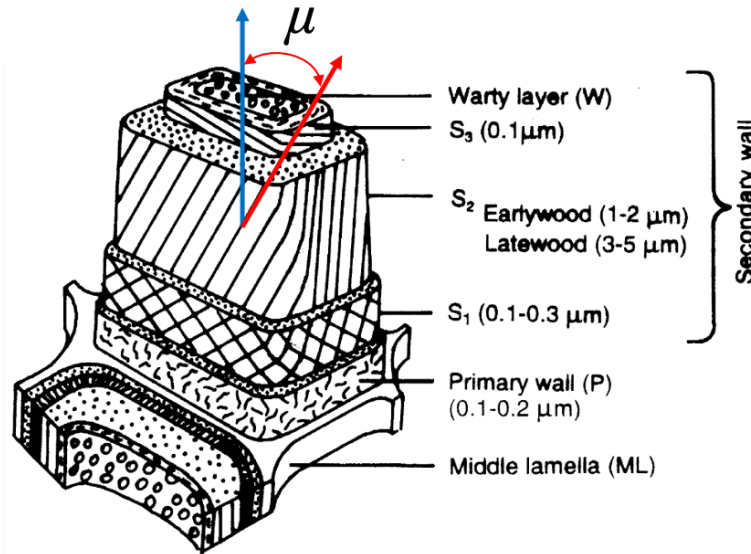


Fig. 1 The multi-layered microstructure of wood fibre cell wall (Edited from Huang et al. 2003). The blue arrow is the direction of the axial cell (fibre or tracheid), and the red arrow is the orientation of the cellulose microfibrils in the S2 layer. Thus, the included angle of two arrows is the microfibril angle (MFA, μ).

II.B.1. Fibrous elements of wood at meso- and macroscopic scales

In a macroscopic aspect, a tree grows and increases its height along the longitudinal / axial direction (L_{Tree}), i.e., the primary growth. Furthermore, a tree's growth includes the diameter expansion, i.e., the secondary growth. It has two corresponding directions of which are radial direction (R_{Tree}) and circumferential direction, i.e., the tangential direction of annual rings (T_{Tree}) (Fig. 2).

Accordingly, a piece of wood is usually considered from these three principal directions in the tree's stem. All the cellular anatomical elements in a wood piece align according to three principal directions. Thus, a mesoscopic-structure system, "grain", has been proposed to describe the "axial" fibres' alignment. Ogata et al. (2003) defined that grain is all the axially oriented elements, but not a single cell; while Kramer (2006) summed up from the other studies in a biological function aspect that grain is "the chief direction of water movement through intact xylem". In general, the grain is a concept of the continuous-longitudinal structure composed of the fibres (and other types of axial cells are often included in the definition) in the same secondary growth period (green dashed arrow in Fig. 2).

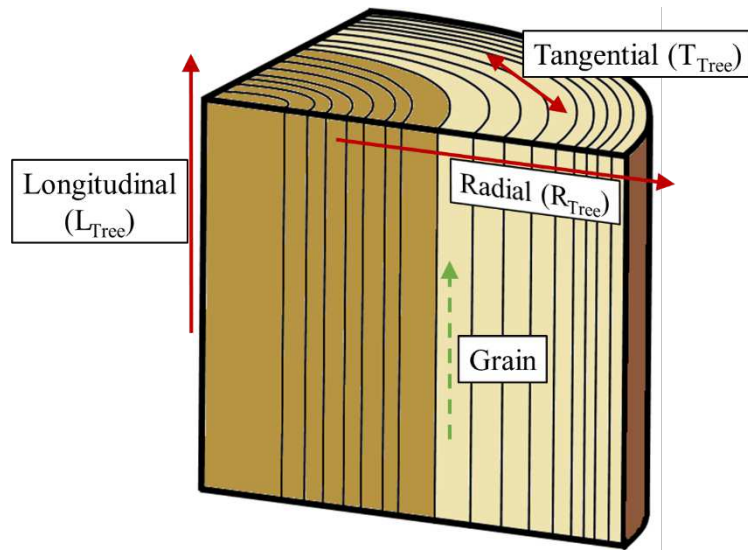


Fig. 2 Three principal directions (L_{Tree} , R_{Tree} , T_{Tree}) of tree, and the “grain” concept (green dashed arrow).

On the contrary, the term “grain” also has various meanings and definitions. For example, the grain can represent organisation of wood elements in a given geometric plane of a piece of wood, e.g., end grain (the cross-section plane of radial and tangential directions) and face grain (principal/wider plane of a piece of wood). Also, “diagonal grain” is the machining defect caused due to the misalignment of wood’s grain direction to the applied cutting tool direction (longitudinal) on a piece of wood. However, in the present study, “grain” means the longitudinal fibres’ alignment in the same secondary growth period to unify the word definition.

I.C. *The supposed general case: “clear wood.”*

Structurally, the cells, including fibres, are adjoint homogeneously in three principal directions, forming a tree/wood. The fibres (§II.A.1) direction is the same as the tree/wood’s longitudinal direction (§I.B.1). Also, there is no void between adjacent fibres, so the tree/wood disk is an almost-perfect cylindrical body in a relatively small longitudinal section. The wood is thus flawless

A flawless wood, or the so-called “clear wood”, could theoretically assume that wood’s structure and biological formation in any scale are homogeneous and without any “defect”. The fibre cross-section would be either perfectly round or rectangular (Gindl et al. 2001); the matrix between adjacent fibres would be homogeneous (middle lamella ML or compound middle lamella CML). Along the length of the fibre, the fibre would not be not twisted or bent.

Instead, in the experimental viewpoint, the “clear wood” represents a piece of wood without/with natural variation, but without the other defects, e.g., cracks (Xavier et al. 2009;

Kamala et al. 2014; Lukacevic et al. 2017). In general, the specimen dimension in those studies is relatively small (for example $2 \times 2 \times 36 \text{ cm}^3$ for bending test in European standard) The small specimen dimension effectively avoids including the defects in the experiments.

Therefore, in some studies, the variation of physical properties along the principal directions are included. For example, the microfibril angle (MFA) usually decreases along with radial and longitudinal directions. In contrast, the basic density (except the longitudinal direction), specific gravity, and fibre length increase (fibre length remaining almost the same after the juvenile part) (Donaldson 1992; Butterfield et al. 1993; Evans et al. 2000; Woodcock and Shier 2002; Hein and Brancheriau 2011; Kimberley et al. 2015).

As a result, some correlations were indicated under the definition of clear wood. MFA contributes highly to the wood's modulus of elasticity. At the same time, density (earlywood and latewood) could have no particular influence within a given species (Reiterer et al. 1999) (excluding in fast-grown species). Instead, the density correlates with the modulus of elasticity between different species (empirically, $r = 0.8$) (Missanjo and Matsumura 2016; Krajnc et al. 2019).

On the shrinkage behaviour, the tangential shrinkage increases and longitudinal shrinkage decrease when the MFA decreases (Harris and Meylan 1965; Meylan 1972; Barnett and Bonham 2004; Donaldson 2008). It is worth mentioning that the MFA in those studies was indicated as a dominating factor for the shrinkage properties (*However, MFA is not the only factor, and the applicable region is limited.*). Additionally, the shrinkage properties correlate to the cell wall layer fractions, and the anisotropy of shrinkage correlates to the density of fibre (Schulgasser and Witztum 2015).

In general, it is concluded that the clear wood has none non-straight fibre in the longitudinal direction, i.e., no misalignment of fibres in mesostructure, and no post-defect, e.g., micro-crack (Sakagami et al. 2009). At the same time, it is homogeneous and has a directional variation of physical properties.

I.D. *Beyond “clear wood”: singularities, grain deviations and figured wood*

Though the current topic is wood, it is still necessary to describe the reason for variation and deviation of grain from the main direction of tree, in the current section (I.D).

In the real-life circumstances, the tree according to its genetic heritage reacts to the environment and changes its structural formation and biological structure due to environmental

factors. Accordingly, the tree's reaction will cause the consequence seen as a "defect" (compared to the concept of "clear wood" in part I.C). In order to categorise the different kinds of variations in nature, the general scene (singularity) in nature is described. Then, the consequence of mesoscopic variation of grain is demonstrated. Lastly, consistent grain variations (grain pattern) and their categorisation for the figured wood is demonstrated.

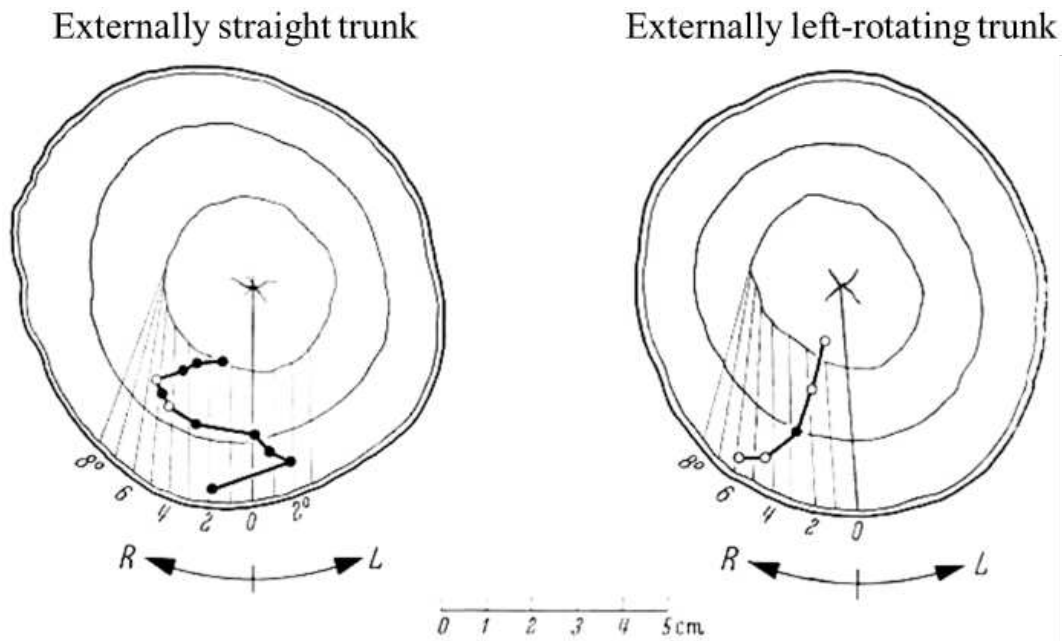
I.D.1. Existence of variation in every tree/wood

From a general scene, the tree has several types of microstructures. The tree uses them to have "anti-fragile" (*Nassim Nicholas Taleb proposed this vocabulary in his book in 2012*) behaviour to the environment. The tree trunk can be bent because of the slope of ground, of the wind, the tendency of sunlight, or all above (Mattheck and Kubler 1997; Gril et al. 2017). Those environmental factors cause the tree trunk not to be straight. Furthermore, tree adaptation causes the change of fibre microstructure inside a bent trunk (Yoshizawa 1986), also the reaction wood.

The phenomena mentioned above are tree adaptation reactions in macroscopy and microscopy. Those cause the tree to be not only non-straight but also heterogeneous (inner structure). Consequently, in a mesoscopic viewpoint, the straight and well-aligned grain pattern does not exist, and Harris (1989) indicated that grain deviation (non-straight grain) more or less happened in every tree/wood. Additionally, some environmental and external factors, e.g., branch growth (because of opened space or closed space), animal or insect injury, biological hazard, could cause more complicated results on the biological reaction of the tree, e.g., growing shape, traumatic resin ducts, burr (Richter 2015).

I.D.2. Grain deviations with irregular variations within a trunk

The grain deviation can be determined after the tree's reaction/behaviour/feedback to the environment. Some grain deviation has been detected, forming a spiral or interlocked grain, and it is not heritable (Knigge and Schulz 1959; Teissier du Cros et al. 1980) (Fig. 3). Furthermore, it was also recorded since a long time that the temperate species could have interlocked and wavy grain, based on the splitting observation in literature (Roth 1895) (Fig. 4). Those grain deviations are sometimes referred to as the function of optimising internal-mechanical resistance to gravity or environmental conditions, e.g., wind load (Page 48-59, Mattheck and Kubler 1997). Also, the grain deviations could be due to tree branch growth (causing cross-grain); moreover, the trunk deviates from the longitudinal growth, forming "fork(s)" (Lev-Yadun and Aloni 1990; Slater et al. 2014; Özden et al. 2017).



Change of rotating angle with tree age of two Beech trunks

Fig. 3 The internal grain development of Beech tree, detected from the bark. (Reprinted and translated from German to English from figure 12 in Knigge and Schulz 1959))

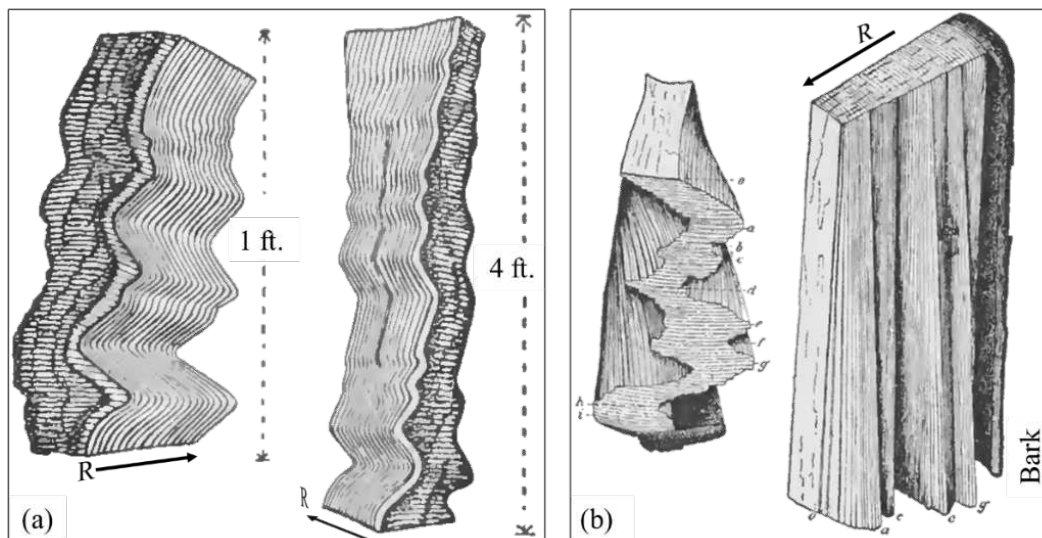


Fig. 4 (a) Wavy Beech and (b) interlocked Cypress. Reprinted record from "Timber: an elementary discussion of the characteristics and properties of wood" (Fig. 12 and 13 in p. 22, Roth 1895). (Figure edited for clarity, notation of direction added).

Generally, the question of grain deviation being common or unnormal in nature is brought up. Desch and Dinwoodie (1996) indicated that it is uncommon in temperate wood for having interlocked grain, but the interlocked grain would be in most tropical species. Instead, according to Northcott (1957) and Harris (1989), it is indicated that both temperate and tropical wood can have spiral/interlocked grain. However, the spiral grains in softwood and hardwood are fundamentally in different formations (Priestley 1945). Again, a specialized wood vendor for

woodworkers, Working the grain LLC, reports that some species generally have straight grain but occasionally have interlocked grain (for example, Marblewood, Chakte Viga, and Bloodwood/Cardinalwood), vice versa some species generally have interlocked grain but occasionally can have straight grain (like African Mahogany).

I.D.3. Relatively constant patterns of grain deviation: the figured woods

Despite discovering those uncertain, widely variable grain patterns that happened in tree/wood from nature, several “basic” grain patterns are categorised (Beals and Davis 1977): straight, spiral, interlocked, wavy/curly, circular growth ring depression (or “indented rings”), “blister” (Fig. 5). Beals and Davis (1977) used “wavy” and “curly” as synonyms, while, on the contrary, Richter (2015) defined the grain in two undulating directions into two different names, i.e., radial undulating for curly grain (Fig. 6a) and tangential undulating for wavy grain (Fig. 6b), but did not use the figure’s name “blister” (Fig. 5f) to describe this grain pattern. The following chapter and word usage for the curly and wavy grains will use the definitions from Richter (2015) (except the curly figure).

Suppose those grain patterns exist relatively consistently at the species level, i.e., a given grain pattern would have strong connection with certain species, the wood with the particular grain pattern is noted as “the figured wood”. Instead, the wood with grain deviation could be just “figured”, i.e., occasionally and partially figured, then belonging to the category of irregularly/variable grain deviation (§I.D.2), but not to the category of the figured wood. Last but not least, a piece of wood could have a combination of several grain patterns (Richter 2015), i.e., interlocked with wavy, curly with wavy.

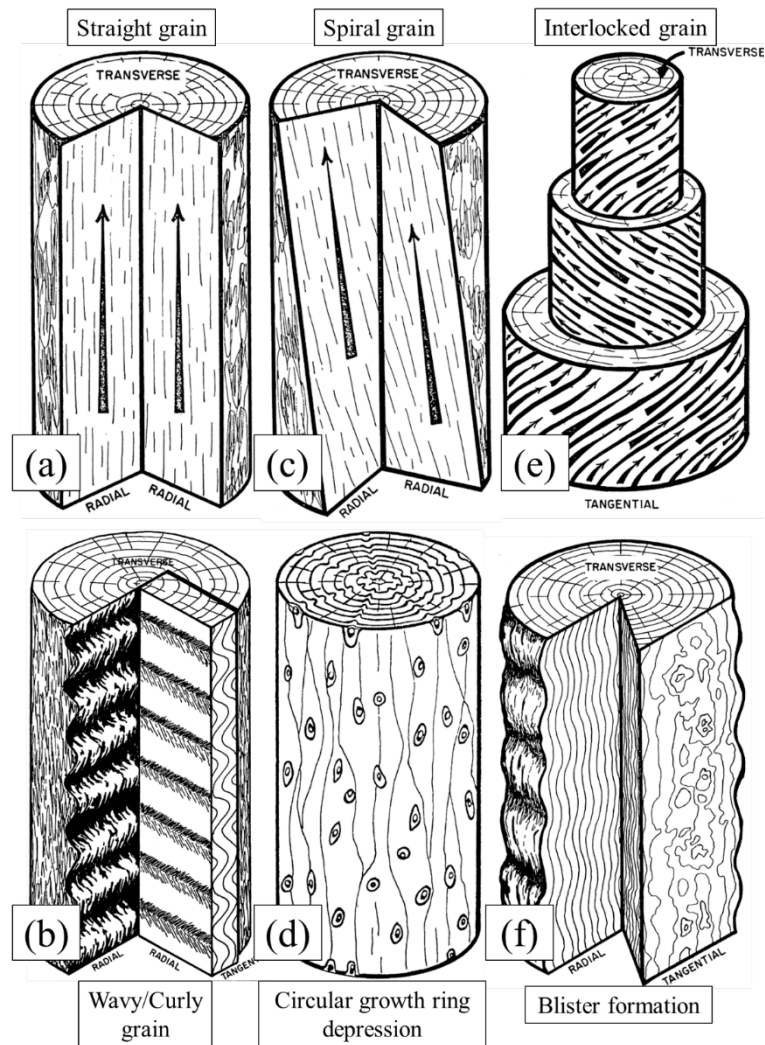


Fig. 5 The six types of grain patterns indicated by the literature (Beals and Davis 1977). (a) straight, (b) wavy/curly, (c) spiral, (d) ring depression, (e) interlocked, and (f) blister formation.

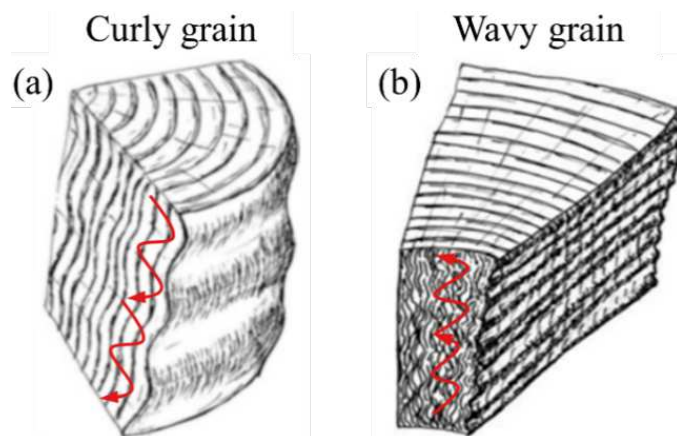


Fig. 6 The definition of (a) curly grain and (b) wavy grain by Richter (2015). (a) is from Fig. 5.112 and (b) is from Fig. 5.113 in the reference.

I.E. Occurrence of figured wood: new statistical analysis from existing literature

In nature, 60,065 tree species are currently identified in the world (Beech et al. 2017). However, the number of species having a certain grain pattern, i.e., the figured wood species, is less pointed out.

According to the book of Kribs (1950), “Commercial foreign woods on the American market”, cited by Hernández and Almeida (2003), 75% of species were prone to interlocked grain (total species: 258). On the contrary, in a current statistical survey conducted by Iris Brémaud, based on the data from “Atlas des Bois Tropicaux” (Gérard et al. 2016) (total species: 300), there are about 70% of species that could have more or less pronounced interlocked grain, i.e., the interlocked grain systematically (23%) or either straight or interlocked (47%), where 82% are mild interlocked grain, and 15% are very pronounced interlocked grain.

Furthermore, based on the USDA’s handbook “Tropical timbers of the World” (Chudnoff 1984) (total species: 371), there were 57% of species indicated as having (or could have) interlocked grain. Coincidentally, 23% of species only have the interlocked grain (Fig. 7) which is a similar proportion as identified above (Gérard et al. 2016). Moreover, 15% of species could have wavy and/or curly grain, and 68% would have straight grain. 18% of species indicated could have irregular grain. Although this literature reference separated the words “curly” and “wavy”, the author cannot distinguish the definition in the original meaning. Hence, the wavy and curly are categorised in the same grain pattern in the analysis (Fig. 7).

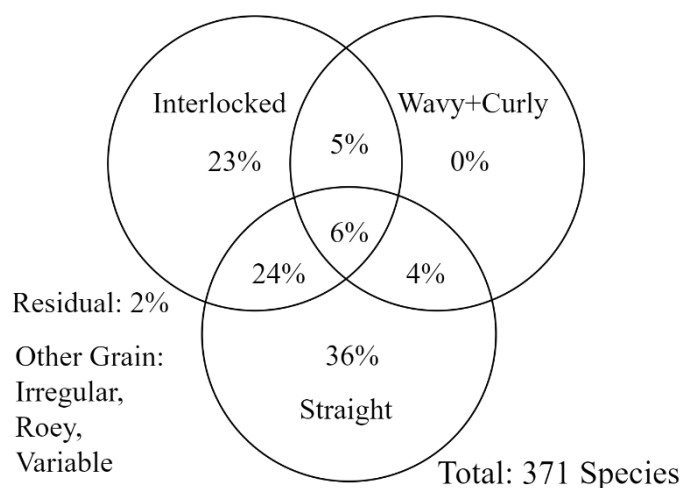


Fig. 7 The analysis of three selected grain patterns (straight, interlocked, and wavy+curly) from the literature data of Chudnoff (1984).

As a result, it could be concluded currently, that the tropical woods include more than 50% of species that have interlocked grain. On the contrary, the other grain patterns, i.e., wavy and curly grain, are less often indicated. The interlocked grain is indicated as a natural grain in the

tropical woods. The other grain patterns and combinations were less concerned; however, they are about 15% in general. The identification of these, and the combination of grain patterns, should be more reported.

I.F. *A terminology for wood figures and figured woods*

The most appreciated characteristic of the figured woods is their visual/aesthetic figures on the produced wood plane. The figure could be plain or plentiful depending on the grain alignment and on the fibres' optical properties, i.e., diffraction and reflection (Shen et al. 2000; Saarinen and Muinonen 2001; Simonaho and Silvennoinen 2004). Some species are indicated as having a specific grain pattern but having less preferred visual figures instead (Chudnoff 1984).

As a result, a piece of wood with grain deviation/pattern doesn't guarantee to have an appreciated visual figure. On the contrary, a piece of wood with a particular figure must have a particular grain pattern or other biological structure or tissue (depending on the definition of each given figured wood and wood figure).

Between species, certain species are more promised to have specific and preferred figures, e.g., Mahogany, Bubinga. It means those broadly recognised species connected to a certain figure (as indicated by the woodworking market or by the specialised wood vendors) could indirectly relate to the grain pattern and to the degree of strength of the grain variation, representing whether having those grain patterns is normal/common for these species in nature.

I.F.1. *The figured wood and the wood figure*

The term "figured wood" means the wood which has a specific (structural) grain pattern in it, while the term "figure" is the visual result on the wood plane aimed to be processed. Every piece of wood has a figure, but the figured wood doesn't guarantee a desirable figure. Eventually, the name of the grain pattern (structural) for a figured wood is seldom synonymous with the name given to its figure (visual/aesthetical). But the name of the figure sometimes can refer to the grain pattern, if the figure is a wanted one. Anyhow, it is certain that the grain patterns are always connected to a certain cutting plane to produce the preferred figure.

For example, the interlocked grain has (could have) the ribbon figure for the radial (or quarter-cut) board (L-R plane, the tree radius direction is equal to the board's width). The preferred board direction (cutting plane) for the wavy grain (Fig. 6b) is also radial, for obtaining a "wavy/curly/fiddleback" figure (Tab. 1), instead of having undulating grain. It is first noticed that the curly grain is the (structural) description of grain pattern (Fig. 6), and the curly figure is the glittering stripped figure on the board surface (or plane) due to the diving angle of fibres. On

the other hand, the preferred board direction (cutting plane) for the curly grain (Fig. 6a) would be tangential, providing a “waterfall” figure (Bubinga) or a “plum-pudding” figure (Mahogany) (Tab. 1).

The figures’ name could be interchangeable if the “figure patterns” (the visual effect on the board surface) are similar. For example, in Tab. 1, the “fiddleback figure” could be the same as the “curly figure”. Still, the fiddleback would be used when the shining stripes are homogeneously aligned, having no cross-figure effect. It is seen that the definition of the figure name caused by the wavy grain pattern could be different because of the misoriented grain structure. Also, different figure names can be referred to the same grain pattern.

Furthermore, one figure name could represent several grain patterns due to personal experience and definition. For example, the “pommel  ” (adj.) in French means “small round zone, having more or less space/distance”, according to the *Centre national de ressources textuelles et lexicales* (National centre for textual and lexical resources). However, the figure below (Fig. 8) shows the “pommele” (used as such in English) figure defined by two veneer vendors (Dooge Veneers and Eurogroup Belcaire, S.L.). The figure is not the same for the author in the present study, because different types of grain patterns cause figures listed under the same name. The definition of pommele could only work on the left sub-figure (for species Makore).

Again, for some specialized vendors/websites, dedicated to material with fine appearance for woodworking, the term pommele is defined as a “small-medium” blister (“Blister” means “a hollow rounded swelling that appears on a surface”, according to the online Cambridge Dictionary). The “small-medium” is confused, depending on personal experience and definition. Moreover, the minor blister could also be called “peanut shell” but not pommele. However, it is a more cultural aspect thought.



Fig. 8 The various figures could be indicated under a same figure name, here under “pommele”.

I.F.2. The Name of Wood Figure: wood structure or culture?

In every culture, each wood figure has its name. If the name is imported from abroad/from another language, the term is often literally translated. It is because the figure name describes the “figure shape”. However, the name sometimes cannot be exported: a specific figure/species could not be found in another country, or another country/culture has less association to the figure shape, e.g., “bamboo-leaves like” figure. As a result, the way and idea of naming figures represent both some cultural and biogeographical aspects.

I.F.2.a) Selective discussion of linguistic aspects

According to the author’s linguistic and woodworking background (Taiwanese Mandarin), the glitting effect caused by the diving fibres is “閃花”. In English, it is an alluring/shining effect brought by the diving angle. In English, it could be called the curly figure, curly stripe, and chatoyancy, and it is ondé (undulated) in French, and it is geflammtes (flamed) (needed to plus a name of the wood) in German.

Beyond 閃花, it could be the figure name or used as an adjective word. If it is used as the adjective, it often connects with “瘤” (burl) or “樹瘤” (tree’s abnormal growth, tree’s cancer) to describe the glitting effect on the burl surface (after surfacing). Anyhow, the figure names in this culture are few. Even if there is a figure name, it could be (mostly) from the personal naming or just the literal translation result from English or Japanese.

Understanding the linguistic perspective and including more data from different languages/countries could have more biogeographical and ethnographic aspects, species-culture-figure. Baumer (1952) connected the grain patterns and figures in four languages (French, English, German, and Flemish). Based on the same idea, the author of the present study tries to connect an Eastern language as the best effort, which is Japanese. The reason is that the woodworking culture in Japan is very well developed, and wood figures are important in all kinds of fine woodworking (Mertz M 2016).

The Japanese figure name could be from natural or artificial objects or even an artistic mood/concept. The element and structure of the figure name is a combination of “the objective or adjective” plus “柶 (figure)” or “柶目 (figured grain)”.

According to the grain complexity, the figure of the flat-sawn board (板目柶) (Fig. 9a) would become a premium (fine) flat-sawn board (上柶目) (Fig. 9b). Moreover, the finest among them, the rose-like figured grain (バラ玉柶) (Fig. 9c).

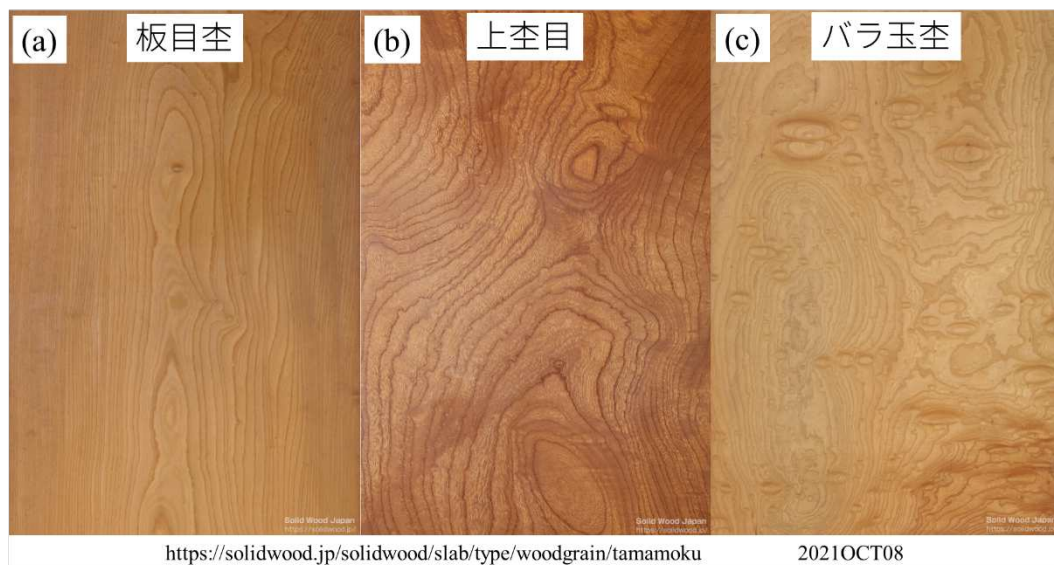


Fig. 9 Explaining the relationship between name and figure with three examples in Japanese for the grains and figures shown on the Keyaki (*Zelkova sp.*) flat-sawn board . (a): 板目柶 (flat-sawn board grain); (b): 上柶目 (premium/fine figured grain); (c): バラ玉柶 (rose (flower) figured grain).

I.F.2.b) *An illustrated multilingual terminology of wood figures and figured woods*

The table below (Tab. 1) is the organisation of names and pictures sourced from, primarily, the specialised veneer and wood vendors' websites. According to their descriptions of the figure, grain, and the photos listed on their websites, the categorisation of figure names in four selected languages, i.e., English, French, German, and Japanese, is made. Still, the figure names are interchangeable due to the definition and description in different languages. Two different photos could have the same figure name in one language but have different meanings in another language, and vice versa. The author in the present work only follows the acquired photo and the definition from the website. Nevertheless, it is not guaranteed that the categorisation can satisfy all the thoughts from people in different cultures, backgrounds, and preferences for naming the figure of the wood.

Tab. 1 The figure names in four languages and the meaning and reference photos.




Figure names in different languages				Meaning	Photo	Ref
English	French	German	Japanese			
Cathedral “grain”			中杓目 (なかもくめ) “The middle/inside” : 竹の子 (たけのこ) 筍杓 (たけのこもく) “Bamboo shoot” 山杓 “Mountain”	One stepped triangle shape in the middle with straighter grain along the edges. Bamboo-like (in Japanese) Bamboo-like grain (in Japanese) Mountain-like (in Japanese)		1
			笹杓 (ささもく) “Bamboo-leaves”	Bamboo-leaves-like figure: sharp, jagged grain on the plane, like folded bamboo leaves.		2
			絵巻杓 (えまきもく) “Handscroll” 波杓 (なみもく) “Waves”	A back-and-forth wavy grain (less sharp) shown on the plane.		2

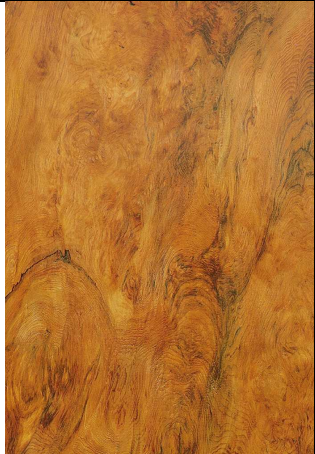


Figure names in different languages				Meaning	Photo	R e f
English	French	German	Japanese			
	Loupe		鶉杓目 (う ずらもく め) “Quail”	A quail-shape figure from the dense grain of Yaku Sugi (with abundant oil) of which is more than 1000-year-old.		1
			雉子杓目 (きじもく め) “Pheasant”	Feathers of Pheasant figure (from Yaku Sugi)		1
			蟹杓目 (か にもくめ) “Crab”	Figure from a crab- shell like grain		1




Figure names in different languages				Meaning	Photo	Ref
English	French	German	Japanese			
			玉杓 (たまもく) “Ball/Sphere”	Concentric circles grain on the plane. It can be with or without the glitting effect caused by the diving fibres. Interchangeable with the figures, 泡杓 and 珠杓 below.		2
	Loupe		泡杓 (あわもく) “Bubble” 珠杓 (たまもく) “Pearl”	Circular shape (by year ring) seemed like “bubbling” (with glitting effect) on the plane		2
			牡丹杓 (ぼたんもく) “Peony”	The grain pattern shows concentric circles and jagged edges on the plane. Peony-flower like (in Japanese)		2

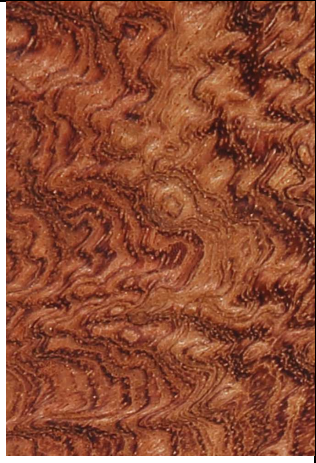

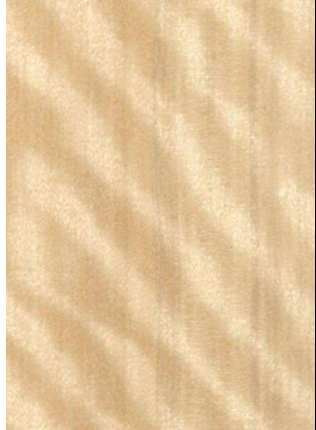
Figure names in different languages				Meaning	Photo	Ref
English	French	German	Japanese			
	Damassé		立涌杓目 (たてわき もくめ)	<p>“立涌 (Tachiwaki / Tatewaki)” is a traditional Japanese fabric figure, meaning the rising steam.</p> <p>The author (of the present study) assumes the figure is from the flat-sawn board due to the highly-developed curly grain (undulating grain in the radial direction).</p>		1
Waterfall Bubinga				<p>The figure is possibly caused by the curly grain. However, compared with the Tachiwaki figure, such a figure name, waterfall, is specifically assigned to Bubinga wood.</p>		3
Chatoyance, Cat's eye, Tiger's eye	Ondé, Moiré, Drappé	Geriegelt	縮杓 (チヂ ミモク) “Wrinkle fabric”	<p>The figure with glitting effect caused by any kind of wood element.</p> <p>It could be the general name for all the figures caused by curly/wavy grain.</p> <p>Or, strictly, the strong and large interval of glittering effect.</p>		4




Figure names in different languages				Meaning	Photo	Ref
English	French	German	Japanese			
Fiddleback	Ondé, Ondulé	Wellenformig, Wimmerig	バイオリン 杓 “Violin”	The name is under a specific form/type of violin, fiddle. It generally represents the wavy /curly figure—moreover, the figure in the tight, fairly uniform roll appearance. Violin figure (in Japanese)		4
Curly figure, Ripple, Flame	Ondé Moiré	Wellenformig, Wimmerig, Geriegelt, Riegel, Geflammt	縮杓 (チヂ ミモク) カーリー 杓 縮れ杓 絹糸杓 (け んしもく)	Almost the same as the fiddleback figure, the curly figure or ripple figure is the wavy/curly figure that is not so uniform/homogeneous. In Japanese, it is described as a “wrinkled” fabric/textile grain/figure.		4
Curly stripe, Tigerstripe	Moiré	Geflammt	虎杓 (とら もく)	Strong and wild curly/wavy figure It is noticed that the Tigerstripe is not identical to the tiger grain (caused by ray). However, in Japanese, the figure names could be the same to describe the tiger-stripe-like figure.		1




Figure names in different languages				Meaning	Photo	Ref
English	French	German	Japanese			
Crossfire	Ondé	Wellenformig, Wimmerig		The shining figure caused by the parenchymatic ray is equally strong with the figure brought by wavy grain.		5
Mottle	Moire, Ondé	Geschachtelt, Gepommelert		A wrinkled and blotch marking across the grain. The combination of interlocked grain and wavy grain		4
Bee's wing, Broken stripe	Moire, Ondé			As exactly the name of "Bee's wing". A smaller section/block of mottle figure Interlocked grain (mostly) with non-homogeneous growth.		3 4

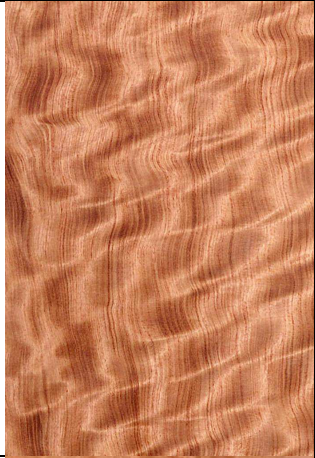

Figure names in different languages				Meaning	Photo	R e f
English	French	German	Japanese			
Block Mottle	Moire, Ondé			The mottle figure in a large block/section. Broad cross markings, causing blocks or checkerboard patterns.		4
Blister	Pomme, Pommelé, Matelassé	Gepommelert	如鱗杓 (じよりんもく) “Fish scale” ブリストー杓 “Blister”	Short, raised (glitting effect) sections in oval shapes.		4
Quilt / Quilted	Matelassé			The figure refers to the blister, which is elongated and crowded.		4




Figure names in different languages				Meaning	Photo	Ref
English	French	German	Japanese			
Pommele Dappled	Pommelé	Getraubt	如鱗杳 (じよりんもく) “Fish scale”	Small blister figure		4
Peanut shell				Quilted or blister figured wood by rotary cut produce a random wild grain pattern.		4
Blister			泡杳 (あわもく) “Bubble”	Bubble like figure: less connected and more individual section of a blister.		1

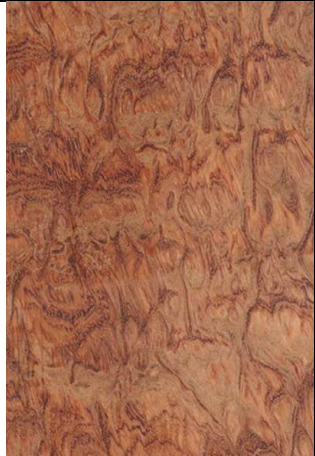
Figure names in different languages				Meaning	Photo	Ref
English	French	German	Japanese			
	Loupe		如鱗杳 (じよりんもく) “Fish scale”	Fish-scale like: sections of quilted / blister / pommele figure become more “individual” but align in serial.		1
Silver grain	Maille	der Spiegel	銀杳 (ぎんもく) “Silver grain” 虎斑 (とらふ) / シルバーグレイン) “Tiger stripe”	The figure because of the long parenchymatic ray of wood on the surface. (Quarter-sawn figure)		2
Flake, Fleck, Ray Fleck, Spotted figure, Lacewood grain	Maille	der Spiegel	斑紋杳 (はんもんもく) “Mottled”	Heavy parenchymatic rays cause the figure (tangentially wide and longitudinally height) and relatively short (rays) in the radial direction.		4



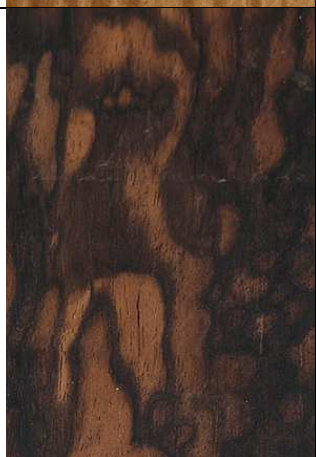
Figure names in different languages				Meaning	Photo	Ref
English	French	German	Japanese			
			朧杳目 (おぼろもくめ) 吟杳目 (ぎんもくめ)	An image refers to the Moon can be glanced through the clouds		1
Ribbon figure, Ribbon stripe, Stripe figure	Rubané	Gestreiftes	リボン杳 “Ribbon”	The ribbon figure caused by the (uniform and homogeneous) interlocked grain Mostly on the radial/quarter-sawn plane		4
Color Stripe <i>Due to the extractive's distribution, especially referred to Diospyros sp.</i>	Marbré	Gestreift	網杳 (あみもく) “Webbed” 網目杳 (あみめもく) “Webbed figure”	Webbed-like figure (caused by the extractive distribution)		1

Figure names in different languages				Meaning	Photo	Ref
English	French	German	Japanese			
	Veiné		縞杳 (しまもく) “White fabric stripe” 縞目杳 (しまめもく)	Black and white stripes (caused by the extractive distribution)		1
	Marbré		霞杳 (かすみもく) “Mist/fog”	Black stripe/webbed figure (caused by the extractive distribution) hazing on the surface.		1
	Veiné		縄目杳 (なわめもく) “Rod”	Stranded-ropelike (caused by the extractive distribution)		1
			孔雀杳目 (くじゃくもくめ) “Peacock” 小豆杳 (あずきもく) “Red bean/small bean” 孔雀小豆杳 (くじゃくあずきもく) “Peacock-red bean/small bean”	The figure caused by the extractive distribution looks like a Peacock tail feather (outer circle in green), “孔雀杳目.” While the circular/oval colour has no colour (black) inside, and the dimension is small, it is a preferred figure “小豆杳 (small bean)”. Moreover, the shape is small, and like the Peacock tail feather (right figure), it is the highest level.		1


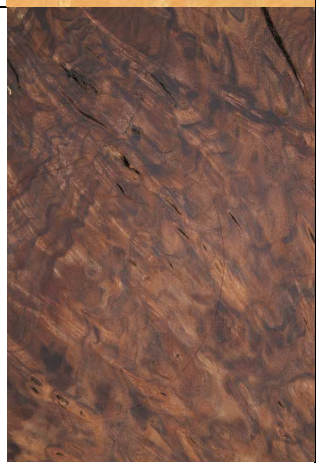
Figure names in different languages				Meaning	Photo	Ref
English	French	German	Japanese			
Curly Birch, Karelian Birch, Mazur/Masur Birch	Bouleau madré, Bouleau de Karelie, Loupe de Bouleau	Birke geflammt, Karelische Birke, Maserbirke Gefleckt		Sometimes called burlled growth. It has a swirl cell pattern caused by the abnormal activity of IAA-glucose synthase (Novitskaya et al. 2020).		4
Bear's claw, Bear scratch, Hazel figure	Chenille			Caused by the indented growth ring, it could be on the tangential or radial plane.		6
	Racine		放射杓 (ほうしゃもく) “Radiation” 後光杓 (ごこうもく) “Holy light of buddha/god” 火炎杓 (かえんもく) “Flame”	Generally, terms for describing the figure (by ray, grain, indented ring growth, extractive, etc.) are radiating appearance or flame.		1




Figure names in different languages				Meaning	Photo	Ref
English	French	German	Japanese			
Crotch figure, Swirl, Flame	Fourche, Ronce	Gabel, Zwiesel	沢目杓目 (さわめもくめ) 鯖杓 (さばもく) “Mackerel” サバ杓 “Mackerel” 二股杓 “Crotch”	The figure is acquired from the trunk near the crotch of tree. Though “鯖” in Japanese means Merkel fish, “鯖杓” does not mean Merkel-fish like grain, but more about the linguistic system of Japanese.		2
Birdseye, Bird's eye, Peacock's eye	Moucheté, Piqué, Œil d'oiseau, Œil de paon	Vogelauge n, Pfau Augen	鳥眼杓 (ちようがんもく) “Bird's eye”	As the name “birdseye” The figure looks like a bird's eye, and it has a shining and dark oval shape, which makes it different from “Cat's paw” or “cluster”.		4
Plum Pudding	Bois moucheté	Die Plumpudding-Zeichnung	浮玉杓 (うきたまもく) “Floating ball/sphere”	The figure name is very verbal: black/red plums mixed in a pudding. The formation is because of the distribution of extractives (causing dark colour) accompanying the bubbled-shaped grain. (On Mahogany or Rosewood) Floating-glass/ceramic-ball like figure (in Japanese)		1





Figure names in different languages				Meaning	Photo	Ref
English	French	German	Japanese			
Burl / Burly, Burred, Burlwood	Bois loupé, Bois de loupe, Ronce, Broussin	Maser, Marmorier -t	葡萄杓 (ぶ どうもく) “Grape” 舞葡萄 (ま いぶどう) 瘤杓 (こぶ もく) / 瘤 杓目 (こぶ もくめ) “Burl” パール杓	It is usually referred to as the grain, which is an abnormal tree growth. It could be found between the branches of a fork, near the root, in the middle of the trunk. The form and figure of the burl could be very different, depending on the growing position, species, developing/growing time.		1
Root figure	Racine		根杓 (ねも く) “Root” パール杓	The figure of inhomogeneous growth of the part near or at the root.		7
Spaghetti grain / pattern	Broussin	Maser		The burl of Oak species, specifically.		8

Figure names in different languages				Meaning	Photo	R e f
English	French	German	Japanese			
Cluster, Cluster burl, Cat's paw, Pippy	Loupe, Nouveux	Geapfelt, Geastet, Halbmaser		Scattered and partially distributed burl-like figure.		4

1. 杻目（もくめ）の種類, 一枚板の種類, 一枚板とは, 無垢材とは, 一枚板比較 (<https://solidwood.jp/solidwood/slab/type/woodgrain>) (in Japanese)
2. 杻の種類, 木材図鑑, 府中家具工業協同組合 - (<https://wp1.fuchu.jp/~kagu/siryo/moku.htm>) (in Japanese)
3. Cook Woods (<https://www.cookwoods.com/>) (in English)
4. Dooge Veneers (<https://doogeveneers.com/>) (in English)
5. Channel Veneers (<http://www.channelveneers.com/>) (in English)
6. McPherson Guitars (<https://mcpheersonguitars.com/custom-shop/wood-options/>) (in English)
7. Identification des bois: esthétique et singularités (Corbineau and Flandin 2009)
8. The post by Ashley Hampton Stump in the Facebook group “Wood Identification Group” on Jun 22, 2021.

I.F.3. The problematic definition of “figured woods”: occurrence, structure and terminology

Every tree or piece of wood is more or less “figured” during the growth. Whether the wood which is figured belongs to the figured wood (grain pattern) or only to the singularity in nature, knowing the constant occurrence, or the simple tendency to be formed, would be essential to distinguish their boundary.

The elementary grain patterns of figured wood have been indicated in the literature, i.e., straight, spiral, interlocked, wavy, curly, birdseye, and indented growth ring. On the contrary, the more complicated grain patterns, or the combinations of those elementary grain patterns, haven’t been widely introduced in the academic area. Their existences could be seen from the professional vendor’s resources and are broadly known from the industry (ex: veneer, instrument) and artisanal woodworkers.

The elementary grain patterns for the figured wood should be further expanded since the complicated grain patterns, or the combinations of patterns, exist commonly and uniquely.

Furthermore, another consideration for expanding the elementary grain pattern is that the figured woods exist worldwide. It gives to the figured wood some characteristics of geographical independence and culturally linguistic distinctiveness.

For further distinguishing and boundary determination of the figured woods, broadly and globally, linguistic study and cross-language categorisation are thus needed. The further and systematic organisation for the wood figure (from experienced craftsmen and professional vendors) seems more effective than broad field exploration of the whole diversity, as the observations have been empirically accumulated by woodworkers and suppliers.

Yet, the names of the figured wood in different languages are not a one-way street that the names given to the figured woods depend on the surface plane and the “magnitude” of the figure/grain pattern. Thus, the wood figure name (visual/aesthetical) could be both the figured grain pattern (structure) and the sawn pattern (cutting plane). The result could be therefore varied because of the sawn pattern.

Despite that, fundamentally, the names in different languages are in a sense related to culture. For example, the names for the wood figure are gradually less numerous in French, German, and Taiwanese Mandarin, than in Japanese and (lesser so) English. The different numbers of names do not mean a different number of existing, or used, figured woods. Instead,

most of the grain variations could be implicit in some languages; thus, the vocabularies for wood figures or the figured wood could be less numerous (or are not fully identified yet).

The names are not completely related between different languages except the co-using of species (imported woods and/or uses). Furthermore, the same vocabulary could represent different grain patterns. Presently, the solution is to connect the wood figure name to the species, limiting the possible combinations to the minimum or so. Herein, the visual/aesthetical appreciation and naming is the hidden message from the grain structure and species properties, which naturally represent the botanical (species) and structural (grain variation) aspects, representing the way and knowledge of how the artisanal woodworker choose and qualify wood material.

Summary of Chapter I and trends for further research

This first chapter aimed at reminding some basic elements of knowledge about the “general” structure of wood, as commonly studied in the case of “clear wood”. The main objective was to situate the notions of “grain”, “grain deviations”, “figured woods” and “wood figures” relatively to this context.

Based on the literature, the grain deviations could be categorised as those occurring on a rather variable and irregular basis within a tree stem; and those presenting a relatively constant or repeatable pattern, more or less periodic. Wood presenting such grain patterns are thereafter called “figured woods”. Six main patterns of grain are identified in the literature (i.e., straight, spiral, interlocked, wavy, circular/ring deformation, curly), although not all literature references give the same names to a structural pattern.

The term “wood figure” refers to the visual/aesthetical appearance of a wood surface. It results from the combination of wood structure, and of cutting plane. Every piece of wood has a “figure”, even the most straight-grained wood. Yet, the structural grain pattern of “figured woods” provide, under the appropriate cutting planes, very particular, sometimes visually striking “figures”, that can be highly sought after in some domains of woodworking.

Some new analyses have been started, based on existing resources, in this chapter:

- The statistical occurrence of some figured grain patterns has been evaluated from existing databases or handbooks.
- The relation (or not) between the grain patterns (structural) of “figured woods”, and the “wood figures” (visual) has been discussed.
- An illustrated multi-lingual (English, Japanese, French and German) terminology of wood figures has been proposed, based on the exploration of specialised woodworking websites.

Some preliminary conclusions arise from this chapter:

- Grain deviations are extremely frequent, either irregular, or organised in a grain pattern, either common, or uncommon, in a given species. The question could be posed whether the straight-grain “clear” wood can really be considered the general frame for wood description.
- Although 6 main types of grain patterns are identified in the literature, their actual degrees of variations are still lesser-studied. Also, different grain patterns can be combined in a

given wood. More descriptions of the structural organisation of figured woods seem to be needed.

-The different figured woods can be highly sought-after, and highly priced, for some woodworking utilisations, due to their visual/aesthetic appearance. Yet, the grain deviations that underly such appearance are expected to determine different physical-mechanical behaviour than for “clear wood”. However, the number of studies dedicated to the physical-mechanical behaviour of figured woods is still relatively scarce in the scientific literature.

From these considerations, some topics are decided for the present study:

-The relationship between the grain pattern of the figured wood and the wood figure will be examined by a comparison between the visual inspection and material structure.

-The present work will focus on the different grain patterns and different magnitudes of the grain deviations. Their structure will be evaluated at the mesoscopic scale (grain) but also microscopic (microfibril angle).

-In the literature, most studies that characterise the properties of different species consider the material as being “clear wood”, possibly assuming that their potential grain patterns are of relatively minor importance compared to between-species diversity. The present work will attempt at observing both species-effects and grain pattern-effects on physical-mechanical properties. A particular attention will be given to the anisotropy of these properties, that is likely to be affected by grain deviations.

II. Description of the structural organisation and some visual features of figured wood

Introduction of Chapter II

The most significant feature of the figured wood is that specific sawn patterns (cutting planes) could mainly produce the desired figure (visual) for each grain pattern (structural). Thus, the preference for the sawn pattern and the desired plane has been built for each figure (Fig. 10). For example, in the birdseye figure, the preferred cutting plane is its tangential plane; for the wavy grain, its preferred plane is on the radial plane. Generally, the preferred figure, ribbon stripe figure, would be shown on the radial plane for the interlocked grain. However, some exceptional species with the interlocked grain would show the more attractive figure on the tangential plane because of the combined curly growth, e.g., *Entandrophragma utile* (Dawe & Sprague) Sprague (Olorunnisola 2018) (EnU-B5-b1 in Fig. 10). In other words, the figure demonstrates the grain structure in the figured wood. Thus, the connection between the visual appearance and the grain structure is built.



Fig. 10 A demonstration of the figures and the preferred sawn planes. The codes correspond to specimens listed in §II.C.

Although the connection between the figure and the grain structure of the figured wood is decisive for the visual appearance, the grain structure is not the only factor that dominates the visual appearance of wood, e.g., MFA, diving grain, parenchymatic rays also play a role in appearance (Ban et al. 2018). Thus, this chapter is for describing figured wood's mesostructure including grain patterns and their grain angles (GA), but also microstructure with the microfibril angle (MFA). The chapter is organised into different approaches conducted during this thesis for the structural and visual/optical description of figured woods.

In the beginning of the present thesis, a tentative was made to build a model that could help to represent the possible variety of figured wood grain patterns. This proved to be unrealistic to continue given the time constraints of the other parts of the thesis, yet the basic idea is introduced below. Similarly, tentatives were made to use or develop optical methods for the characterisation of figured wood surfaces, the preliminary developments will be briefly explained. Then, in order to obtain a more general view of the occurrence of figured wood and wood figures, a visual screening of the archive specimens of the CIRAD's xylarium has been conducted, some illustrations will be shown.

The main part of this chapter consists on the selection, description and structural analysis of the main wood sampling that will be studied throughout the rest of this thesis. The known feature of the selected species, the origin of specimens and their preparation will be described. The macroscopic/mesoscopic evaluation of grain's structure for the figured wood is first studied by the commonly used method of blocks' splitting, and commonly used descriptors are derived. Also, the local GA and MFA are measured by the X-ray diffraction (XRD), providing the structural-physical information that will be used in the following chapters.

II.A. Modelling and simulation

II.A.1. A tentative to describe the connection of possible grain patterns by an analytical model

A trial of analytical modelling was made to achieve the surmise of the figured wood's structure. An analytical model based on the formation of the sinusoidal pattern was used to describe fibres' orientation in R and T planes. The model assumes the continuous fibre's alignment can be virtually seen as the combination of sinusoidal curves in the R or T plane, also R and T plane. In equation (1), argument (input variable), L , represents the position along the L direction and the "phase shift", P , corresponding to the magnitude shifting at the same L position.

$$g(P, L) = P + a(P) \sin\left(2\pi \frac{L}{S_L} + bP\right) \quad (1)$$

where $g(P, L)$ is the value of the function representing fibre's position in the tangential or radial plane; L is the longitudinal coordinate; P is the fibre's mean tangential/radial coordinate; of which $a(P)$ controls the amplitude of the radial or tangential axis' oscillation (2); in $a(P)$, S_L control the period of longitudinal oscillation; b is then the phase shifting factor.

$$a(P) = c + d \times \sin\left(2\pi \frac{P}{S_p}\right) \quad (2)$$

c is amplitude factor controlling; d controls the variety of tangential or radial's oscillation amplitude; S_p controls the period of tangential or radial amplitude.

For the possible outcome from the model, there are infinite possibilities that the crossing for grain in the same plane occurs. Thus, the limitation for the phase shifting is then found:

$$-\frac{1}{\max(|c-d|, |c+d|)} < b < \frac{1}{\max(|c-d|, |c+d|)} \quad (3)$$

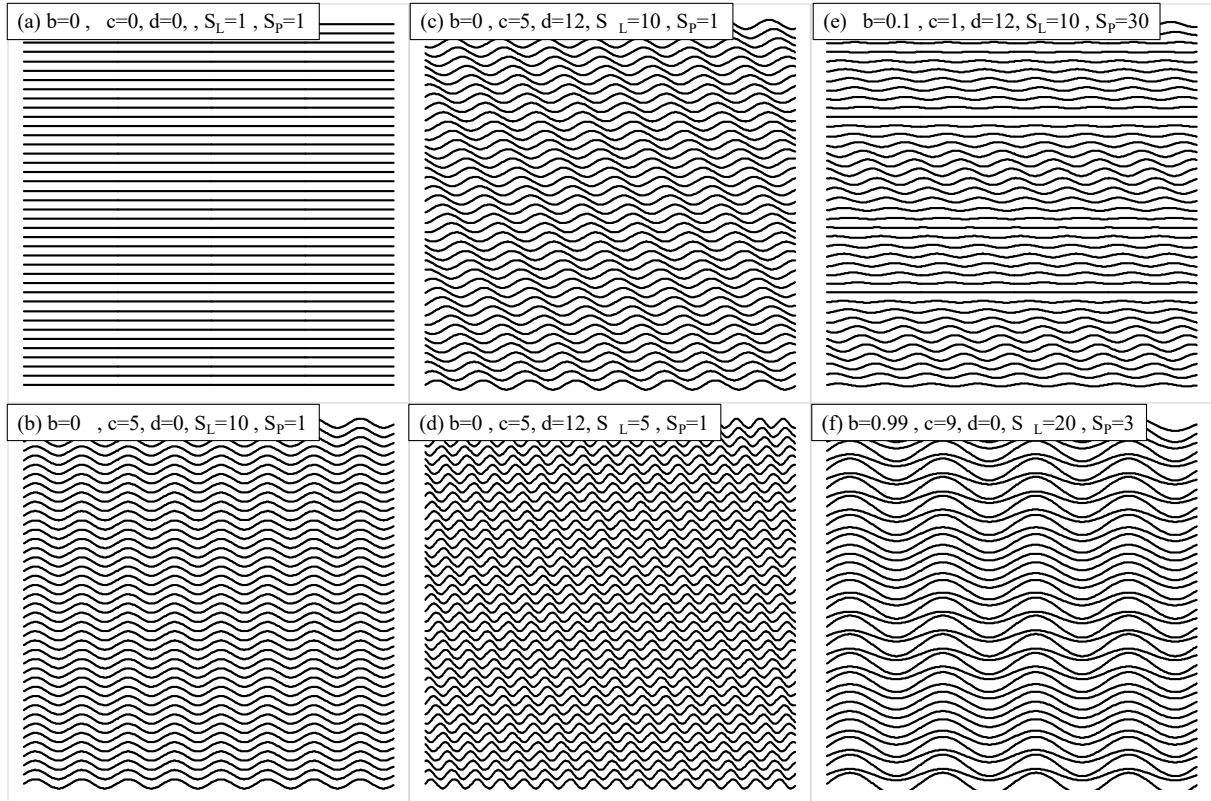


Fig. 11 A demonstration for the manipulation of parameters in equation (1). (a) is the straight grain; (b) is the wavy pattern; (c) and (d) is the phase-shifting in different amplitude, respectively; (e) is the phase-shifting including the amplitude shifting; (f) is the amplitude shifting without the phase shifting. In the program, L is set as 1 to 500 in step 1, and P is set as 5 to 395 in step 5. A smoothing aids for the visualisation. The parameters of L and P are for the intensity of the points on longitudinal coordinate and demonstrated density of curves.

The model demonstrates infinite possibilities to describe the grain pattern either in the R plane or T plane. However, compared with the actual circumstance seen and known, the structure and grain in a tree, the analytical model results still give excessive possibilities. Also, combining two planes, i.e., R and T , is another challenge. Because of the curly growth (radial variation) and the grain pattern on the T plane, the variation is not manipulatable from the 2D model. Besides, in particular cases, e.g., indented annual ring and birdseye or Karelian birch, another dimension issue arises from density changing. The entangling fibres cause phase transformation (indented annual ring) and grain crossing (spiral/swirl pattern in the local region). This description is from the point of view of the analytical model but not the biological explanation.

II.B. Optical and visual examinations

II.B.1. Tentatives to characterise the wood surface of figured wood by optical methods

The figured wood's grain/fibres are angled in one direction (tangential or radial to longitudinal). Thus, they will be off-plane directing to the other plane, and it causes the “diving angle” (elevation angle) in this plane (Shen et al. 2000; Liu and Lin 2016), which is also the preferred plane for the figured wood because of the alluring visual appearance. Furthermore, the diving angle of the fibres makes the figured wood's colour and light contrast shift due to the light's incident angle (Liu et al. 2016). Therefore, another attempt to connect the visual appearance and the grain structure for the figured wood is by using visible light to detect the “diving angle” of the fibres. Consequently, the measured plane for the structural analysis is also the preferred plane of how the figured wood is prepared and chosen in woodworking.

The preliminary test for the light-structure relationship was conducted with optical coherence tomography (OCT) (Thorlabs Ganymede Spectral domain-OCT). The type of OCT scan was B-scan (2D) with the 930 nm wavelength, scanning along the longitudinal direction of the specimen and the depth in the tangential direction, and the sample used was a piece of wavy Sycamore maple (*Acer pseudoplatanus* L.) (Fig. 12). The result indicated that the fibre's pattern on the surface would affect the contrast (brighter: more reflective; darker: less reflective) and the visual appearance because of the diving angle.

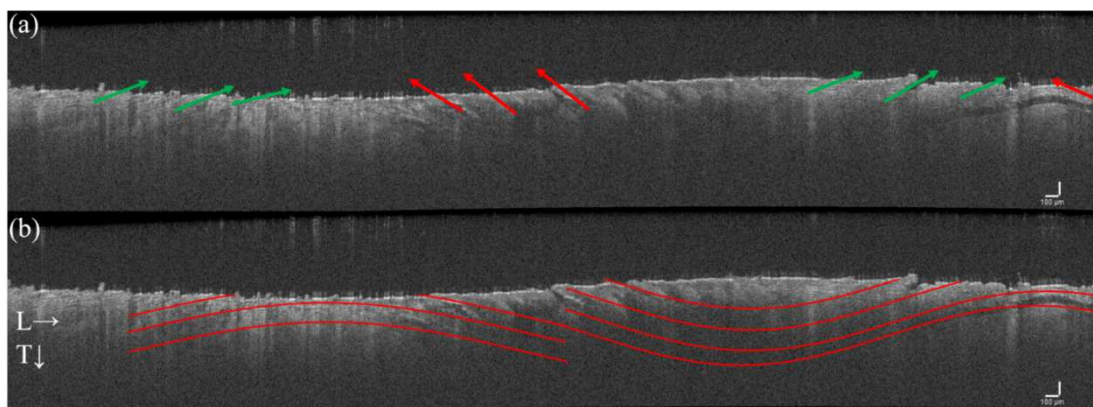


Fig. 12 The result of the OCT scan for the wavy Sycamore maple. (a) The fibres' directions are clear to be identified. (b) The schematic diagram of the known wavy grain pattern is drawn.

Therefore, a first trial with the visible light was based on an idea of the multi-directional approach (Carman et al. 2008; Huang et al. 2008; Sole et al. 2017), using a desk lamp with an angle between the light bulb and the sample's plane. The sample used here was a larger piece of wavy Sycamore maple. The light bulb's colour temperature (Sunvue[®] E27, BASF) was 4000 K,

and its general colour rendering index (CIE Ra) was higher than 95. The reason for choosing these specifications was that the 4000 K was close to the natural light. The higher Ra indicated the actual colour of the specimen (especially red and yellow colours). The image capture system was by the digital camera (Fujifilm X-E2 camera) in the focal length of 55 mm and the aperture f/5.6 (18-55 mm f/2.8-4R LM OIS, OIS off). The camera was set parallel between its focal plane and the sample's plane. The image format was transformed by Capture One Pro 10 (Phase One) from RAF to TIFF. Then, the image was read with the tiff package in the R environment. The three layers of red, green, and blue were separated and re-calculated into the greyscale (B/W) by equation (4).

$$\text{Greyscale value} = 0.2989\text{Red} + 0.5871\text{Green} + 0.1140\text{Blue} \quad (4)$$

The capture result and the setup were limited because the light was close to a type of spot emission, which caused the degradation from the light centre (Fig. 13a). Thus, the compensation was made with a blank test (an 80 gsm A4 sheet). The compensation was set according to the maximum value of the greyscale, which is 255 (for the 8-bits colour depth). Therefore, the maximum value of the greyscale result and the sample's result should not exceed 255. So, the blank test's result was calculated according to a linear correlation (5)(Fig. 13b).

$$\text{Compensate value} = \frac{\text{Max(Blanktest)} - \text{Min(Blanktest)}}{2} - ((\text{Max(Sample value)} + \text{Max(Blanktest)} - 255)) \quad (5)$$

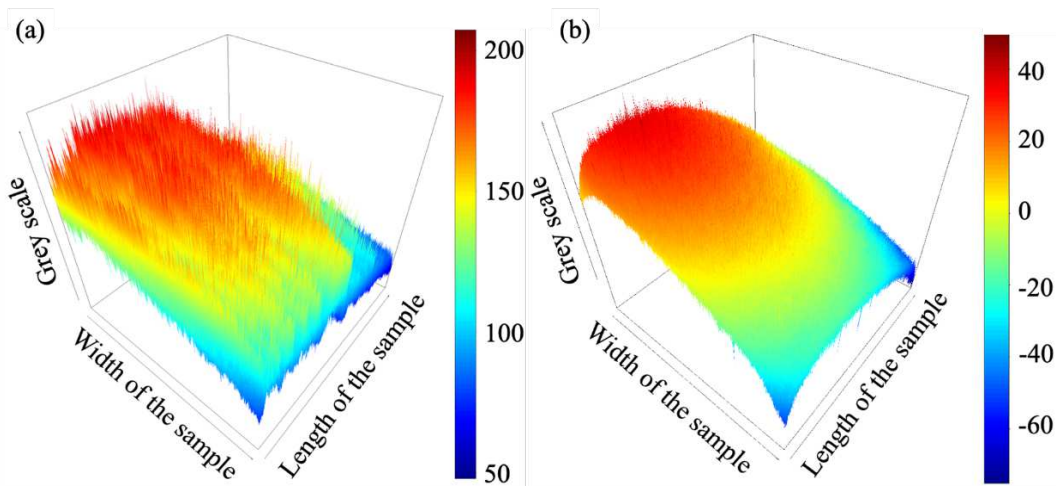


Fig. 13 The result drawn in 3D for the Sycamore maple from one diagonal angle of the incident light. (a) its original result (transformed into B/W) and (b) the result from the blank test. The result of the blank test was transformed to compensate for the degradation in the sample's result according to equation (5).

Thus, the compensated result (Sample's value minus corrected blank test values) was found in a 3D plot (Fig. 14a) compared with the original result (Fig. 13). Also, the 2D comparison along the sample's length to verify the light response was made (Fig. 14b).

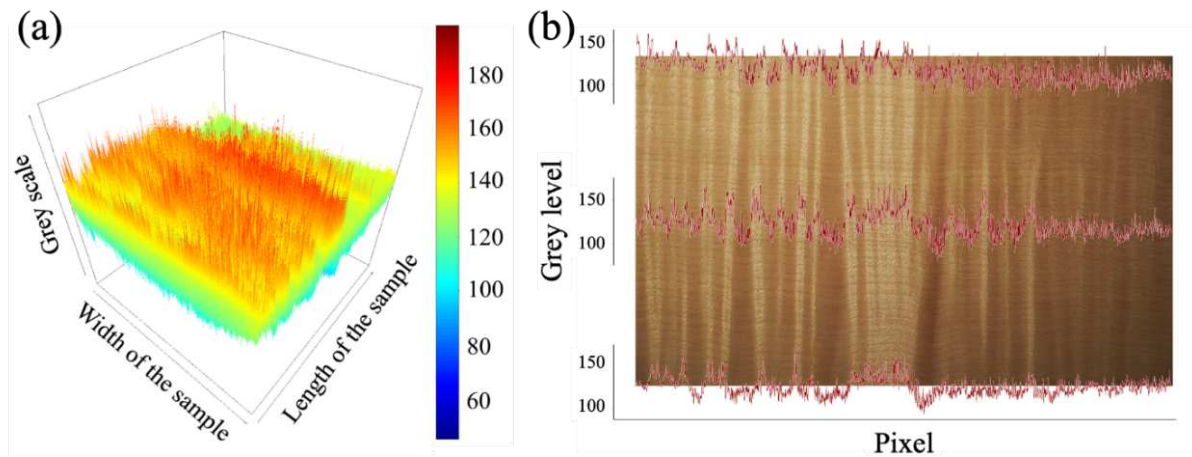


Fig. 14 The light response of the fiddleback figure on the Sycamore maple. (a) is the result after compensation made from the previous calculation, and (b) is the acquired response along the longitudinal direction.

According to the result, the compensation by the blank test could be used if the sample's area is close to the light source. However, if the area is too far from the light source, the “resolution” of the greyscale (for sample) would be too low, causing the result not compensatable, e.g., the right part of Fig. 14b.

On the ground of the trial in measuring the “diving angle” approach was workable. The next approach was then turned with the help of the digital image correlation (DIC). The analysis and the setting were helped by Jonathan Barés (LMGC).

The advanced trial's idea was extended that the measurement of fibres' angles was focused on all the fibre directions in azimuth angle. Still, the effect of different greyscales was due to the diving angle or the fibre's inclination according to the surface plane. The instrument adopted here was a flatbed optical scanner (CanoScan 9000F Mark II) connected to the Raspberry Pi 2. The scanner software was xsane (version 0.998), using 1,200 dpi resolution. Due to the angle between the incident light and the sensor (CCD) in the scanner (Fig. 15a), while the sample was rotated (azimuth angle from 0° to 360°) (Fig. 15b), the response of the same region should have only one maximum value and the only one minimum values according to the concept of the diving angle. Consequently, the scanned results' rotations were achieved with the DIC according to a piece of speckle pattern attached in the middle of the sample (a figured part of *Chamaecyparis formosensis* Matsum.).

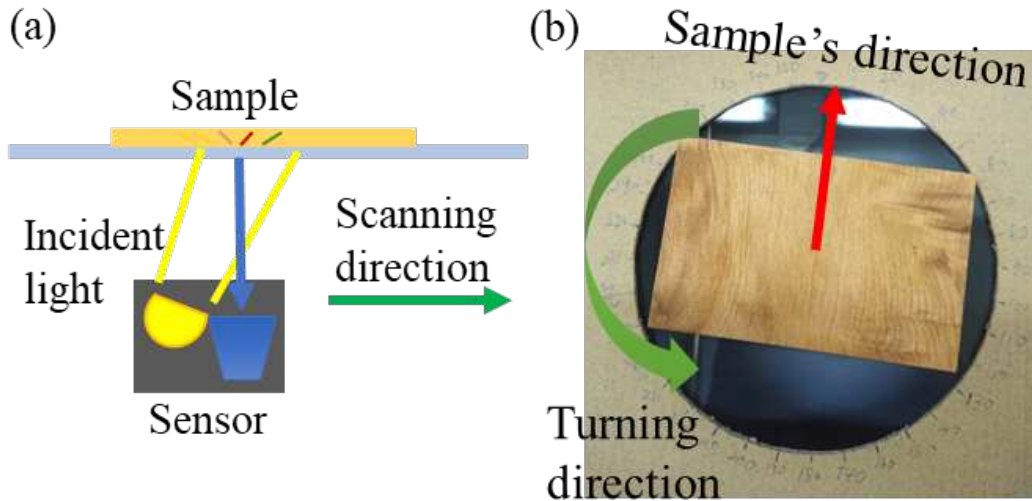


Fig. 15 The diagram of the experimental setup in the DIC analysis. (a) The included angle of scanner between the incident light and the optical sensor. (b) the rotation of the sample. The board was marked the rotated azimuth degree.

The DIC analysis showed two kinds of general and preliminary results: each pixel's maximum and minimum values from all the rotating results (Fig. 16a, c); the maximum and minimum grey values of each pixel corresponding to the rotating angle (Fig. 16b, d). The surface would demonstrate different greyscales during the rotation according to the fibres' reflection. While the light passes mostly in the L direction (Sugimoto et al. 2018), in other words, the less reflected direction would have occurred. Thus, theoretically, there would be only one lowest value. A result of one randomly selected pixel is then demonstrated (Fig. 17).

The two trials solved the measurement of the fibre's angle on the surface separately. One was the diving angle, and the other was the azimuth angle. Combining the two systems is much more complex and time-consuming, even budget consuming. The result could be species-dependent due to the relative response of each shape and length of the cells (Collings et al. 2021). Also, the equipment for distributing homogeneous light (by a parabolic reflector or the Fresnel lens) would be much more expensive (for the price and for the time). The further development of the method itself also leaves the main subject of the present study (the figured wood) too far. The achievement of this idea for the fibre angle measurement was stopped here, left for the dedicated and interested one.

Intensity from all the rotated results

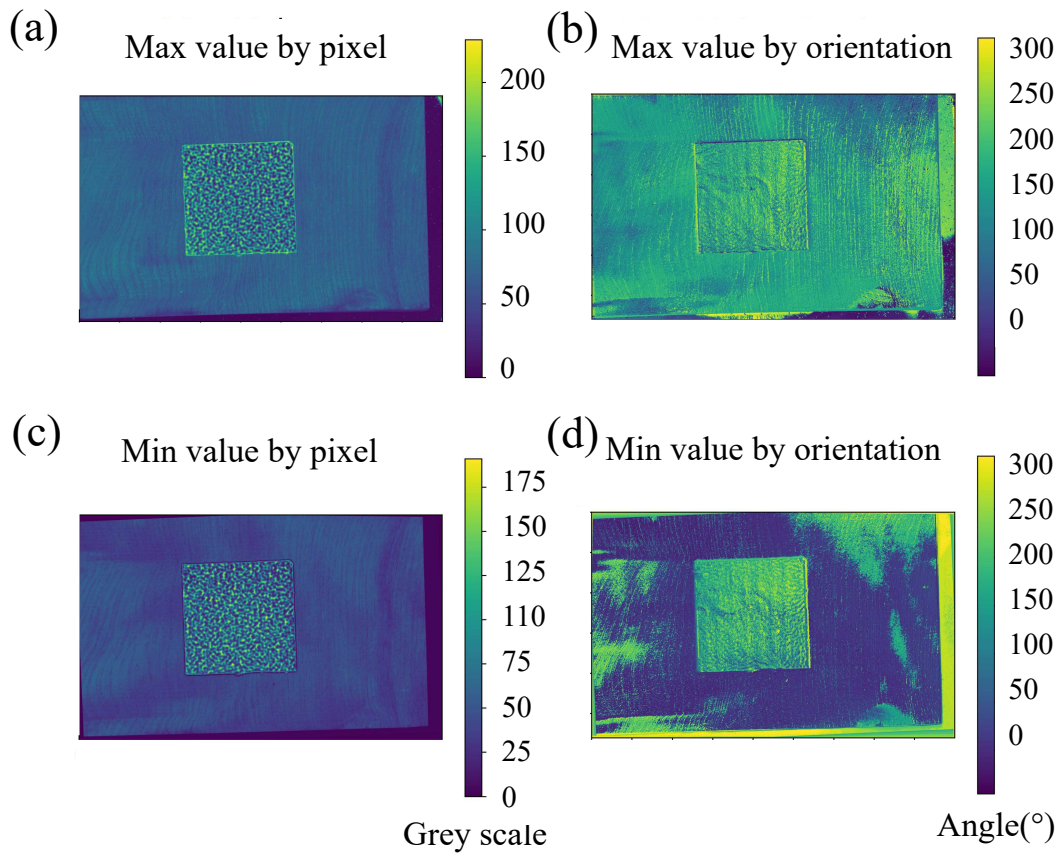


Fig. 16 The result of the DIC analysis in two kinds of demonstrations. (a) and (c) is the max and min values for each pixel. (b) and (d) is the max and min values of each pixel from the rotation.

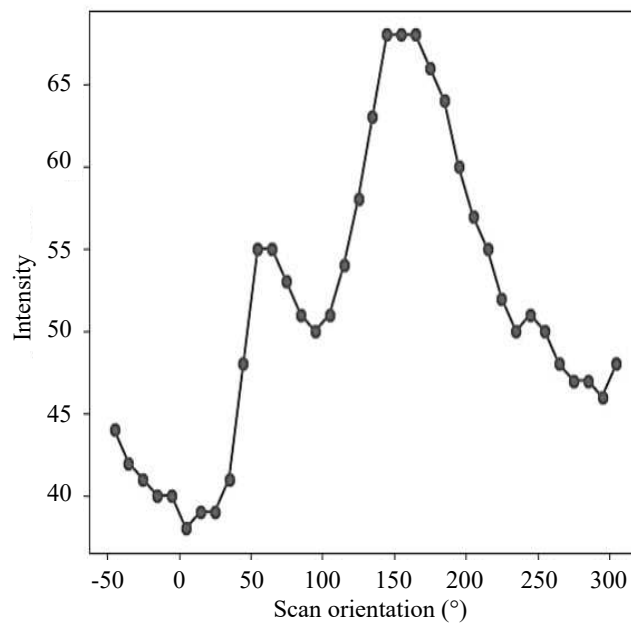


Fig. 17 A result of intensity and correlated rotation angle of a randomly selected pixel.

II.B.2. *Visual screening of CIRAD's xylarium to identify species with figured wood*

In order to identify relevant species for the study of figured wood, a wide-ranging screening was conducted. The main resource was the xylarium of BioWooEB laboratory, Centre de Cooperation International en Recherche Agronomique pour le Développement (CIRAD), Montpellier, France. This abundant collection of botanically identified wood specimens covers more than 8,400 species belonging to circa 2,200 genera from 235 families. Species come from all the continents, including softwood and hardwood from all the climate zones. It contains more than 34,000 specimens having dimensions of $13 \times 6 \times 1 \text{ cm}^3$ (Normand et al. 2017; Langbour et al. 2019). The screening was placed to verify all the specimens in CIRAD's xylarium by their visual appearances. Once a piece of wood was found with substantial grain variation, significant shifting of the figured pattern, or strong silver grain (i.e., the figure caused by parenchymatic ray's reflection), a photo was taken (Tab. 2). Afterwards, their scientific name was verified with CIRAD's xylarium database and the name indicated by the Plants of the World Online, Royal Botanic Gardens, Kew (POWO 2019).

The result under the author's criteria was 346 species (4% in 8,400) noted from the xylarium. It did not represent the total number of the figured wood in CIRAD's xylarium. Compared with the literature of which 75% of 258 tropical hardwood were prone to interlocked grain (Kribs 1950, as cited in Hernández 2007a), the author's visual inspection was much less. On the other resource, Atlas des Bois Tropicaux (Gérard et al. 2016), out of 300 commercial wood species about 70% were listed more or less with interlocked grain, systematically or occasionally, and 15% of them were described as having a very pronounced interlocked grain. Nevertheless, the author only concerned the most visually striking appearance during the record. Besides, the xylarium's wood collection is based on botanical sources but not intended for figured wood. The figure also concerns the individual tree, local position, and cutting plane. Consequently, the 4% didn't represent the figured wood in CIRAD's xylarium.

Tab. 2 A part of the photo record during screening CIRAD's Xylarium and the selecting reason for the figured wood.

<p><i>Aucoumea klaineana</i> Pierre</p>	<p><i>Cola cordifolia</i> (Cav.) R.Br.</p>	<p><i>Copaifera langsdorffii</i> Desf.</p>	<p><i>Cynometra alexandri</i> C.H.Wright</p>	<p><i>Lannea microcarpa</i> Engl. & K.Krause</p>
				
<p>Crossed ribbon figure High contrast reflection</p>	<p>High dense ray fleck</p>	<p>Non-regular wavy structure Curly grain</p>	<p>Fine and high dense wavy structure</p>	<p>Fine wavy figure with low density</p>
<p><i>Myroxylon balsamum</i> (L.) Harms</p>	<p><i>Myrsine sp. L.</i></p>	<p><i>Nauclea xanthoxylon</i> (A. Chev.) Aubrév</p>	<p><i>Pseudospondias microcarpa</i> (A. Rich.) Engl.</p>	<p><i>Pterygota macrocarpa</i> K. Schum</p>
				
<p>Interlocked grain with wavy grain several oscillating amplitudes and quick period shifting</p>	<p>Long and fine ray fleck</p>	<p>Slow oscillating change</p>	<p>Section wavy and interlocked grain</p>	<p>Strong ray fleck and distorted longitudinal cells</p>

The top 10 in the plurality of families were Fabaceae (70 species), Annonaceae (29 species), Dipterocarpaceae (24 species), Malvaceae (22 species), Anacardiaceae (16 species), Sapotaceae (16 species), Proteaceae (9 species), Apocynaceae (9 species), and Meliaceae (8 species), and Myrtaceae (7 species). However, several of these families have the most numerous species in the xylarium. Thus, a comparison of families between screened and recorded species with the database of CIRAD's xylarium was made, with 20 families and in intensities.

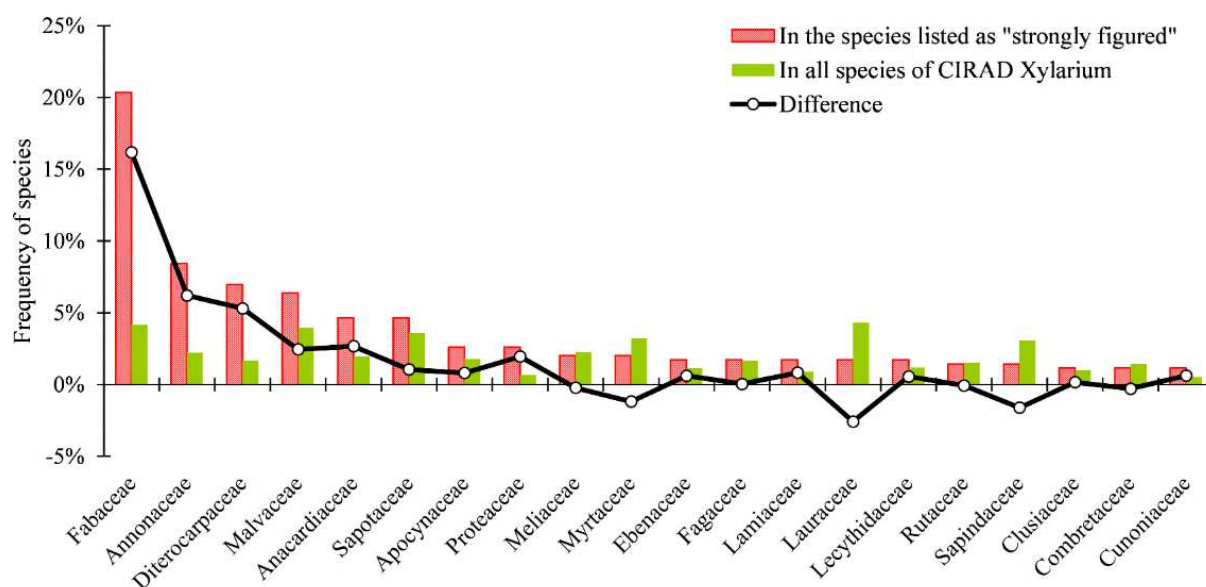


Fig. 18 The comparison between 20 families of the percentage of species recorded as “highly figured” under the author’s criteria, and of the global percentage of representation of species in the CIRAD’s xylarium.

II.C. Experimental determination of the multi-scale orientation

II.C.1. Materials in the current study

The present study aims to build structure-properties relations of figured woods, considering several properties, dimensions, and observation scales. The adopted methodology analyses the intra-pattern's deviation, i.e., different modalities of a given figure, and compares inter-species properties. Therefore, several grain patterns were concerned, including interlocked, wavy, pommele, and birdseye. There were 13 species selected from the CIRAD's wood stock for the interlocked grain. Moreover, materials were bought from commercial sources for the other types of figures. Primarily, the vendors were specialised in instrument-making wood's supply. As a result, there were 4 species bought from "Le Bois de lutherie", France, for the wavy, pommele, and birdseye patterns. Besides, two maple species expanded the modalities of pommele and birdseye figures. These were bought from "Madinter" for the birdseye pattern, and the other one was the pommele pattern from "Maderas Barber", two Spanish suppliers specializing in guitar-making wood's supply. Lastly, Karelian birch was from woodturning supplies from "FTFI", France.

Regarding the interlocked grain, the species' selection started from the visual screening conducted in the xylarium. Because the materials in wood stock are well-recorded with their botanical name, dimension, and serial numbers, in this stage, the work was done in excel files by examining the *species* and *genus*. After the preliminary selection was made, the recorded species were then organized by genus and compared with the list of CIRAD's sawmill wood storage to verify the material's availability that could be used for experiments.

The reason for examining *genus* and selecting *species* under the same *genus* was to compare species having some common anatomical features. Afterwards, the screened *genus*, *species*, and potential material availability were cross-examined, and a candidate list was made. At this step, most of the selected *genera* and *species* were divergent from those identified during the visual screening in the xylarium. Thus, the next step for the material selection was done on-site at CIRAD's wood sawmill stock while following the serial number recorded in the list. A small hand plane was used to check that the on-site materials fit the author's visual criteria and help identify the orientation of planks depending on the cutting plane. The dimensions were recorded to evaluate the possibility of further material preparation, i.e., due to the different sizes of specimens aimed for the other observations and tests of various properties. Consequently, there were 13 interlocked grain species selected.

The dimension and types of the materials from CIRAD were in several forms. In general, they were large dimension wood planks or blocks, which could provide further information of the interlocked grain along with the radius position (or radial position, from pith to bark on some of the planks). The advantage of the other commercial resources was that the description and appreciation for those grain patterns' usage were also acquired from the customer market. From "Le Bois de lutherie", the supplier categorized several "degrees" of the grain pattern within the same species. These were in small planks, but their dimensions still fit most of the experiments. The two guitar boards from "Madinter" and "Maderas Barber" were too thin to acquire several types of specimens for the general-purpose, so they were only included for the forced vibration test to compare with the mechanical property from the other specimens.

A summary of all the selected materials with their grain patterns, botanic names, families, and origins was listed below (Tab. 3). A shorter code and marking system was adopted to easily distinguish the species and specimens, based on the abbreviation of the first two letters from the genus and the first letter from the species. The first letter of the names was capitalized, e.g., PtS is *Pterocarpus soyauxii*.

Tab. 3 The involved grain patterns and the selected species.

Family	Botanical Name	Code	Origin	Grain Patterns	Qty	Test type
<i>Sapindaceae</i>	<i>Acer pseudoplatanus</i>	AcP-M	Europe	Birdseye	3	All
	L.	AcP-P		Pommele	4	All
	<i>Acer macrophyllum</i>	AcM-M	North	Birdseye	1	V, X
	Pursh	AcM-P	American	Pommele	1	V, X
<i>Oleaceae</i>	<i>Fraxinus sp.</i>	FrS	Europe	Straight, wavy	4	All
<i>Juglandaceae</i>	<i>Juglans regia</i> L.	JuR	Europe	Straight, wavy	3	All
<i>Betulaceae</i>	<i>Alnus glutinosa</i> (L.) Gaertn.	AlG	Europe	Straight, curly	3	All
	<i>Betula pendula</i> subsp. <i>pendula</i>	BePvar	Europe	Mazur Birch (Curly, Karelian)	3	US, V, X
<i>Fabaceae</i>	<i>Pseudopiptadenia suaveolens</i>	PsS	Guyane	Interlocked	1	All
	J.W. Grimes					
	<i>Daniellia oliveri</i>	DaO	Gabon	Interlocked	1	All
	Hutch. & Dalziel					
	<i>Pterocarpus tinctorius</i>	PtT	Burundi	Interlocked, wavy	1	All
	Welw.					
	<i>Pterocarpus soyauxii</i>	PtS	Cameron	Interlocked	1	All
Taub.						
<i>Hymenaea parvifolia</i>	HyP	Brazil	Crenulation(bark)		All	
Huber						
<i>Piptadeniastrum africanum</i>	PiA	Ivory Coast	Interlocked		All	
Brenan						
<i>Malvaceae</i>	<i>Nesogordonia papaverifera</i>	NeP	Ivory Coast	Interlocked	2	All
	Capuron ex N. Hallé					
	<i>Nesogordonia kabingaensis</i>	NeK	Congo	Interlocked	1	All
Capuron ex R. Germ.						
<i>Meliaceae</i>	<i>Entandrophragma cylindricum</i> Sprague	EnC	Ivory Coast	Interlocked, curly	2	All
	<i>Entandrophragma utile</i> Sprague	EnU	Ivory Coast	Interlocked		All
	<i>Khaya senegalensis</i> A.Juss.	KhS	Senegal	Interlocked		All
<i>Burseraceae</i>	<i>Canarium madagascariense</i>	CaM	Madagascar	Interlocked		All
	Engl.					
	<i>Pachylobus buettneri</i>	PaB	Gabon	Interlocked		All
Guillaumin						

V: Forced vibration measurement; US: Ultrasonic measurement; X: X-ray diffraction measurement for GA and MFA

II.C.1.a) *Some of the known features of studied species*

As a natural material, wood has a rich diversity in microscopic anatomical features depending on species. These anatomical and chemical features result from biological functions, but they can also influence the mechanical behaviour of wood. Thus, two references from the International Association of Wood Anatomists (IAWA) (Baas et al. 2004; Alfonso et al. 2007) provided the categorizing system of some anatomical features. While the present study does not concern the anatomical inspection on those aspects, the IAWA's standard and criteria (Tab. 4) of these selected features are adopted, i.e., the number of vessels per area and their diameter, type and width of parenchymatic rays. The IAWA's categorization provides beneficial information for a basic evaluation of their possible consequences, i.e., determining some surface appearance aspects such as coarseness of grain, "shininess", or "silver grain". Afterwards, the information of the features mentioned above for the selected species was acquired from the web database "Insidewood" (Wheeler 2011) for the later quantitative comparison (Tab. 5). The diversity of anatomical features and the extractives content (amount of secondary metabolites) were indicated below for the studied species. The global extractives content was retrieved from CIRAD's database on the chemical composition of wood (Gérard et al. 2019). However, the database does not concern the temperate species, so some studied species were not included.

Tab. 4 The indicated anatomical features in the present study and their marks used in IAWA.

Vessels diameter			Vessels quantity			Ray		
No.	$\Phi(\mu\text{m})$	Q.M.	No.	unit/mm ²	Q.M.	No.	Description	Q.M.
40	≤ 50	1	46	≤ 5	i	96	Rays exclusively uniseriate	a
41	50-100	2	47	5-20	ii	97	Ray width 1 to 3 cells	b
42	100-200	3	48	20-40	iii	98	Larger rays commonly 4- to 10- seriate	c
43	≥ 200	4	49	40-100	iv	99	Larger rays commonly > 10-seriate	d
			50	≥ 100	v	100	Rays with the multiseriate portion(s) as wide as uniseriate portions	e

Tab. 5 The relatively quantitative mark for the characteristics of the selected materials and the basic properties in the databases

Families	Species	Density (g/cm ³)	Rays width	Φ (μm)	Vessels (1/mm ²)	Extractives (%)	
						AB	W
Sapindaceae	<i>Acer macrophyllum</i> Pursh		bv, c	2	iii, iv		
	<i>Acer pseudoplatanus</i> L.	0.64	a	2	iii		
Oleaceae	<i>Fraxinus sp.</i> *	0.68	b	4	-		
Juglandaceae	<i>Juglans regia</i> L.	0.66	b	4	-		
Betulaceae	<i>Alnus glutinosa</i> (L.) Gaertn.		a	2	iv, v		
	<i>Betula pendula</i> subsp. <i>pendula</i>						
Fabaceae	<i>Pseudopiptadenia suaveolens</i> J.W. Grimes	0.80	a	3	ii		
	<i>Daniellia oliveri</i> Hutch. & Dalziel	0.55	b	4	i	6.0	3.7
	<i>Pterocarpus tinctorius</i> Welw.		a	4	ii		
	<i>Pterocarpus soyauxii</i> Taub.	0.79	a, b	4	i	12.0	1.5
	<i>Hymenaea parvifolia</i> Huber	0.94	b	3	i	8.7	1.9
	<i>Piptadeniastrum africanum</i> Brenan	0.70	c	3v, 4	iv,	7.9	2.7
Malvaceae	<i>Nesogordonia papaverifera</i> Capuron ex N. Hallé	0.76	b	2, 3v	ii	4.2	2.6
	<i>Nesogordonia kabingaensis</i> Capuron ex R. Germ.		b	2, 3v	ii, iiiv		
Meliaceae	<i>Entandrophragma cylindricum</i> Sprague	0.69	bv, cv	3	ii	2.1	3.3
	<i>Entandrophragma utile</i> Sprague		b	3, 4v	i, ii	4.7	1.9
	<i>Khaya senegalensis</i> A.Juss.	0.78	c	3	ii	8.3	4.6
Burseraceae	<i>Canarium madagascariense</i> Engl.	0.63	b	3, 4v	ii	1.1	4.5
	<i>Pachylobus buettneri</i> Guillaumin	0.59	b	3	i, ii		

The density data is from CIRAD's Tropix 7.

v: the suffix represents the feature sample by sample or the feature which is borderline with a tendency to show a feature according to the noting mark of InsideWood (Wheeler 2011).

*: the information of *Fraxinus sp.* was taken from *Fraxinus excelsior* in InsideWood.

AB: percentage of ethanol-benzene extractives, based on oven-dry weight

W: percentage of water extractives, based on oven-dry weight

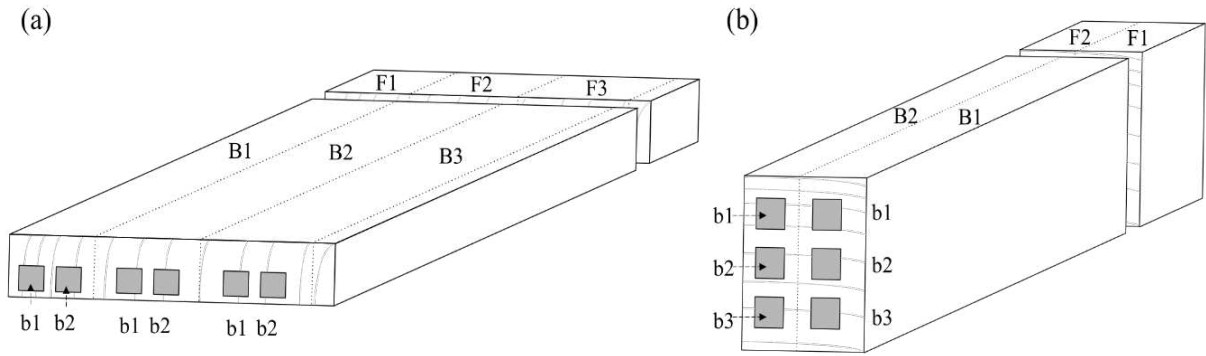
II.C.1.b) *General sampling and cutting plan*

The wood structure and mechanical properties depend on the position intra-tree, i.e., along the radial and longitudinal directions. Thus, a solution was proposed for the sampling to achieve the methodology in multi-dimensional and multi-disciplinary ways, i.e., different geometries and dimensions are needed for the different types of observations and testing properties. One larger dimension sample would be divided into several sub-dimension samples for several purposes, and the sub-dimension samples are in the same radial position.

Preparing material in several dimensions is to fit the requirements depending on the test types. For example, the microfibril angle (MFA) (and grain angle, GA) evaluation by X-ray diffraction (XRD) requires thin lath, and GA's measurement by splitting method requires radial blocks. The different test methods for physical-mechanical properties each require a standard geometry (the detail is in §III.A.2). The largest size of the specimen is in the form of a rectangular cross-section bar, in the nominal dimension of $360 \times 20 \times 20 \text{ mm}^3$ (L \times R \times T). The geometries for sub-dimension specimens can be prepared by re-cutting to fit each test's requirement.

According to the design mentioned above, the general scheme for the macroscopic sampling (Fig. 19) is to have bars in the same longitudinal position while in series for their radial positions. The bars were cut immediately adjacent (along L direction) to the blocks used for the GA measurement by the splitting method (Fig. 19). The record of the radial position of these bars relative to the splitting blocks was kept. Considering the original material was planks in several sawn-types, a re-orientation of the transverse section (R \times T) was also done when needed. If so, the dimensions will be initially kept in $360 \times 35 \times 35 \text{ mm}^3$ instead of $20 \times 20 \text{ mm}^2$ in the transverse section, then machined to the final dimensions when re-orienting the section.

Finally, after the concerned mechanical evaluations have been completely done (on rectangular bar), the bars were cut into thin strips. The measurement for the MFA and GA will be done after a non-destructive vibrational test for their dynamic mechanical characterisation.



Plank(Botanical name)
 Splitting block (F) | Sub-plank (B)
 BING bar (b)

Fig. 19 The general cutting plan for the macroscopic sampling. The geometries include the plank in original dimension, sub-dimension of the plank (B), and the final bar, BING bar (b1, b2...) within the sub-plank. The numbering detail is in the following section (§III.A.2). Also, the corresponding blocks for the splitting method are noted (F). All numbers are in series along with the radius/radial direction, from the smallest (bark) to the largest (pith). The subfigures of (a) and (b) represent the different types of the sawn pattern.

II.C.2. Grain angle (GA) determination

Wood is composed mainly of longitudinally axial anatomical elements: tracheid in softwood and fibre in hardwood. The global alignment of these axial cells in the same growth period is defined as grain in the present study. Consequently, the angle between this local orientation of fibres and the main longitudinal direction of the wood, or the applied direction, is the grain angle (GA).

The GA has been indicated as one of the factors influencing wood's mechanical (Hernández 2007b; Brémaud et al. 2011b) and hygroscopic-dimensional properties (Ormarsson and Cown 2005; Hernández 2007c, d; Straže et al. 2011). The occurrence and amplitude of GA vary depending on inter-species, intra-species, growth conditions, and within a tree. In order to evaluate the GA, image analysis and optical methods have been used in several pieces of research (Ogata et al. 2003; Ogata and Fujita 2005a, b; Thomas and Collings 2017). On the other hand, the radial splitting method has been used widely for evaluation because it is more efficient to acquire GA (Martley 1920; Hernández and Almeida 2003; França et al. 2020).

The advantage of splitting is that it can demonstrate grain variation in two-dimension and two directions instead of being limited for having in only one direction's characteristic. The method has been applied mainly to two grain patterns, i.e., interlocked grain and wavy/curly grain. For example, the diversity of interlocked grain has been shown in several articles, including some exploring the potential relation to biomechanical properties (Martley 1920; Détienne 1979; Cabroler et al. 2009). However, the splitting has to be done normal to the split plane (Miyaki et al. 1983, *in Japanese*); otherwise, an error could occur because of this deviation in the angle.

For the other more complicated grain patterns, including dual directions' variation, or only occurring in a tiny area, at the moment, there's no similar way to evaluate their GA, e.g., birdseye, pommele, crotch, bear claw. Their evaluation is replaced by the figure's intensity or by the criteria from their visual appearance.

Anyhow, due to the GA's significant variation along the circumferential direction (Martley 1920; Miyaki et al. 1983, *in Japanese*) and longitudinal position (França et al. 2020), the GA was considered of being able to be representative only in a local region of wood for the present study. Thus, the acquired blocks for the splitting experiment were located longitudinally nearest to the standard bars.

II.C.2.a) *The splitting method and the figure evaluation*

The height (L direction) of the blocks for splitting was set nominally in 5 cm width (R direction), while the widths of the blocks depended on the materials' original size (Tab. 9). Later, their angles in cross-section were measured at least five times consistently and were based on one of the R edges of the blocks. The drawn line, assigned as the R direction, to be split was drawn on the RT surface, and the projected line was also drawn on the other RT surface. After the R splitting line was drawn, a grafting knife (18 mm, Fujiwara Sangyo) was used for pre-cutting and pre-aligning the R splitting line less than 2 mm in depth.

The splitting method's quantitative analysis of the grain variation has been applied to two types of patterns, i.e., interlocked grain and wavy grain. For the interlocked grain, the maximum magnitudes of GA were aimed for its evaluation. The two most prominent peaks on the counter spiral directions, S and Z, on the block split were measured (maximum angular deviation, MAD) (Hernández and Almeida 2003) (6). For the other grain pattern, wavy grain, the method was based on the assumption that the wavy grain on a piece of wood fit the form of the sinusoidal curve. Therefore, the quantitative evaluation was made on the sinusoidal wavelength (λ) in the L direction and the period (T_w , which is T in the article) in the R direction according to the cambium movement (Hejnowicz and Romberger 1979). Moreover, a piece of research used the radial splitting method to acquire the tangential grain. Then, they calculated the representative angle of wavy grain in the L direction, that the result, in general, was the second derivative at the zero position (Alkadri et al. 2018).

$$MAD = \text{atan}\left(\frac{Z_i}{L_i}\right) + \text{atan}\left(\frac{S_i}{L_i}\right) \quad (6)$$

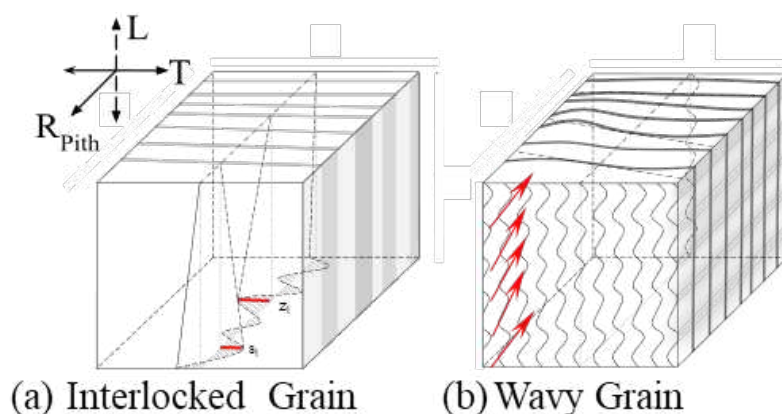


Fig. 20 The diagrams for the determination of GA for interlocked grain (a) and wavy grain (b) in literature. The MAD in (a) was calculated with the Z_i and S_i, the maximum angle in the split blocks.

In the present study, the measurement of GA for those grain patterns was not able to follow completely the same procedure due to the design of the sampling and the orientation of the cross-section. Because of the sawn type of materials, the sampling for the splitting blocks continued with the original cross-section direction in order to maintain the maximum radial splitting line. Consequently, the altered measuring methods were proposed to acquire the GA of the interlocked grain pattern and the wavy grain.

The used splitting tool was a 30 mm width chisel (with side bevel, MHG), which was hand sharpened into a convex-like shape bevel and 35° bevel angle. Furthermore, a rectangular block was used to assure the splitting angle to the plane, and the splitting was done section by section in length and gradually in-depth (L direction).

For the interlocked grain, all the possibly observable peaks were numbered according to the S and Z direction from the view of bark to pith direction. The Z-direction was marked with odd numbers, and the S direction was marked with even numbers. Two pieces of information were then acquired. The peaks' radial positions were recorded along the pre-drawn projection line from the splitting path. The other one was the GA of every recognizable peak measured with a plastic protractor (PASS, readout 1°). A piece of straight wood was clamped along the R split line (Fig. 21a), and another block was used for indicating the base plane (RT plane) of zero degrees. Therefore, the included angle indicated by the protractor was the GA, noted positive and negative for the Z and S direction, respectively (Fig. 21b).

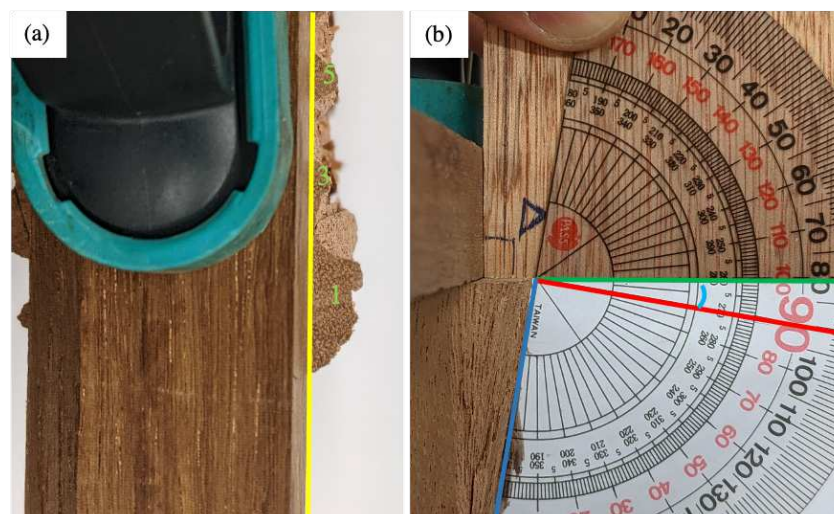


Fig. 21 The measurement of the GA for the interlocked grain pattern. In (a), the projected radial line (in yellow) was indicated by clamping a straight wood, also as the baseline for measuring the magnitude. The split peaks were therefore marked with a number. Later, in (b), another piece of wood was used to help the measurement of the GA (value of the included angle between the green line and the red line).

For wavy grain, an evaluator of their GA measurements was used as mentioned (Alkadri et al. 2018). Here, the measurement was not directly on the angle but was the distance between two peaks along the longitudinal direction and the tangential depth (Fig. 22). The peaks' space and the wave depth (2 times of the amplitude) decide the sinusoidal/cosinusoidal function. Therefore, the angle is determined with the slope (absolute value) at the point of 0.25 or 0.75 wave period (or frequency of a wavelength). The distance between two peaks was measured with a ruler (indicating 0.5 mm), and the depth was also measured by the vernier calliper's depth rod (end tail).

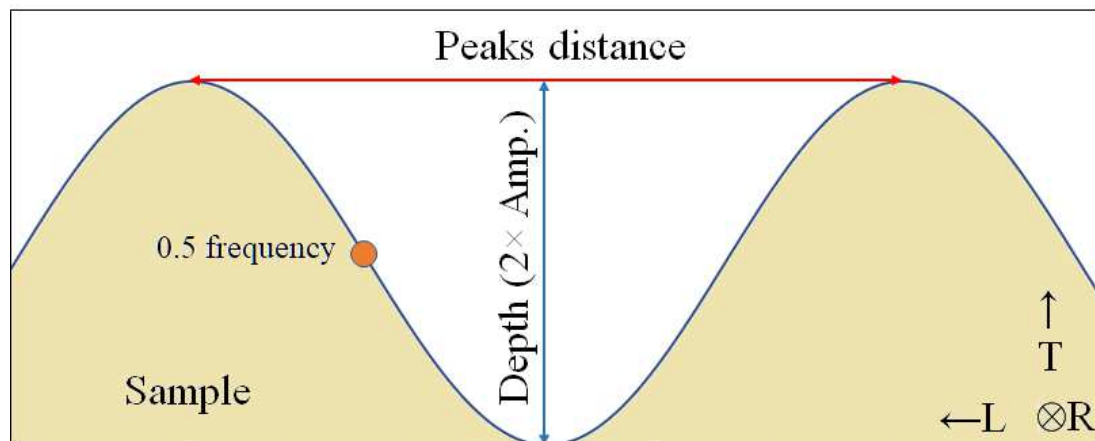


Fig. 22 The grain angle's measurement for the wavy grain pattern.

On the contrary, for several grain patterns it is not possible to evaluate their GAs (Fig. 23). However, they are still able to be visually quantified for the “degree of the figure” (thereafter called doF), e.g., birdseye (Fig. 23a) and pommele (with two directions' variation) (Fig. 23b) figures. For those grain patterns, the representative of their GAs is therefore adopted with the intensity of the figure on the surface.

Two cases are concerned with quantifying the degree if the figure is distinguishable from the surface. The one is that the figure includes a countable (calculatable) feature, then the unit is the figure quantity per area (Fig. 24), and the counting will be in half if the figure is on the border of the material. The other is the figure not countable nor calculatable, then the qualification and the evaluation of its figure would be by the visual appearance, e.g., pommele. Besides those two situations, another is that a piece of wood without any figured pattern shown on the surface has a non-straight grain structure (Fig. 23c, JuR). However, the detected region is limited. The undulating form is the low frequency that the measurement of its angle is not applicable because a whole periodic wave exceeds the specimen's dimension.

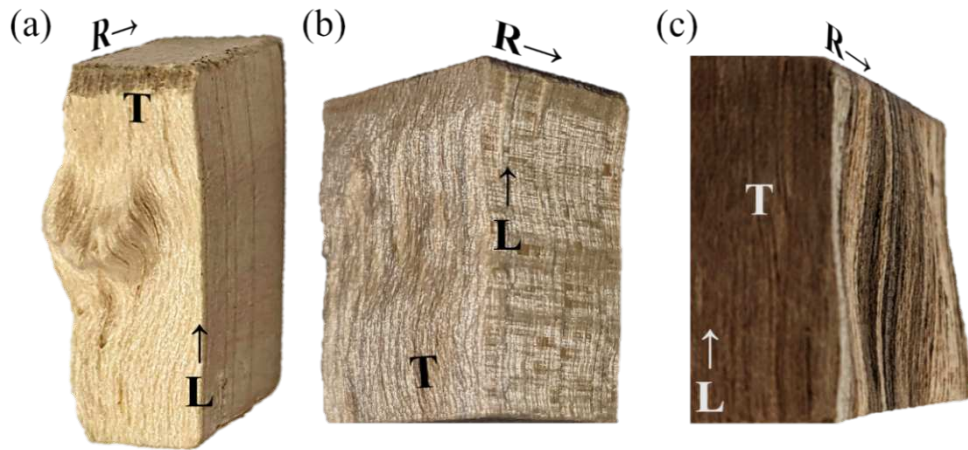


Fig. 23 Three figure types show the difficulty of evaluating their grain variations by the GA measurement due to the (a) non-parametricalized pattern, e.g., birdseye figure (AcP-M1), (b) pommele structure in the present study's material, and (c) the non-detectable (from the surface) (JuR1). (L length: 20 mm)

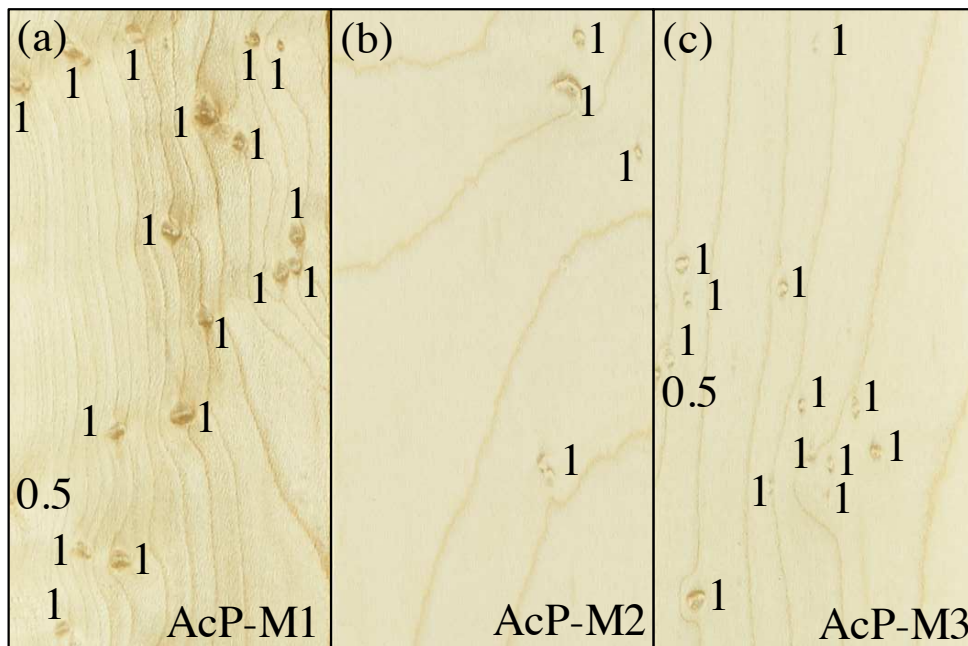


Fig. 24 The evaluation of the birdseye figure by the quantity of the figure per area. Three local captures of the birdseye maple (*Acer pseudoplatanus* L.). The doF (as graded by the wood vendor) is $a > b > c$. The scales of the three images are the same.

The intensity of the figure shown on the surface (Figure/area) represents the replaced way to quantify the GA and the diversity of the birdseye pattern (Fig. 24). The figure (Fig. 24) shows the level of the birdseye figure for three pieces from the “Le Bois de lutherie” (§II.C.1). In the order of figure intensity, the doF should be $AcP-M1 > AcP-M3 > AcP-M2$. However, each birdseye figure of the AcP-M2 is more prominent than AcP-M3, proving that the criteria from

the supplier are multi-factor. Thus, the level of the figure for the birdseye figure will continue with the supplier's grading in the following description.

II.C.2.b) Profiles of GA patterns

The result showed a great diversity of species and the figure. Thus, in the preliminary evaluation, the purpose is kept on the GA. For the interlocked grain, only the maximum values of peaks' position and their angles were recorded. The in-between information of the GA, i.e., the pattern of GA evolution along the radius, was not included. For this reason, an interpolation function developed for the in-between data points was developed by Tancrede Alm eras (LMGC, Montpellier) (7) to estimate the in-between values, the function also assured the interpolated data would pass through the measured data points.

$$y_i = y_n + \frac{(y_{n+1} - y_n)}{2} \left[1 - \cos\left(\frac{x_i - x_n}{x_{n+1} - x_n} \pi\right) \right] \quad (7)$$

y_i : the developed angle value (degree); y_n : the angle value (degree) on the first peak; y_{n+1} the angle value (degree) of neighboring peak to the first peak; x_i : the developed of the position value (cm); x_n : the position (cm) in radial direction of y_n ; x_{n+1} : the position (cm) in radial direction of y_{n+1} . The x_i decides the fineness of the section that we wanted to acquire, producing the corresponding y_i .

The sub-plank mark is not continuous because the number was according to the cutting steps. Consequently, the angle measuring method (Fig. 21) and the MAD method (6) are compared with each other (Tab. 6). Also, the results of the angle method and its simulated GA (7) on each splitting block for the interlocked grain and their representatives of the bars' approximated locations were recorded and compared (Annex Tab. 1).

The difference between the angle method (ANG) and MAD are small. The possible reasons causing the difference are mainly on two kinds of interlocked grain. The one is that the frequency of the grain amplitude's oscillation is high while the amplitude of GA is small, e.g., NeP. The other one is the amplitude of GA is large, e.g., PiA. These two caused the MAD method's measuring in error because of the possible damage on the projecting plane (opposite the splitting plane).

Tab. 6 The maximum IG angles' values are measured by the angle method (ANG) and the MAD method. All the values below, mean value and standard deviation are in degree.

Code-Subplank	MAD(Z)	MAD(S)	ANG(Z)	ANG(S)	MAD	ANG	Diff
CaM	5.10(0.03)	10.68(0.83)	6.50(0.71)	-12.00(1.41)	15.78(0.85)	18.50(0.71)	2.7
B3	5.10(0.03)	10.68(0.83)	6.50(0.71)	-12.00(1.41)	15.78(0.85)	18.50(0.71)	2.7
DaO	7.20(0.65)	6.26(0.57)	7.33(0.58)	-7.67(1.15)	13.45(1.18)	15.00(1.00)	1.5
B1	6.81(0.00)	5.69(0.00)	8.00(0.00)	-7.00	12.50	15.00	2.5
B2	7.95(0.00)	6.82(0.00)	7.00(0.00)	-7.00	14.77	14.00	0.8
B3	6.83(0.00)	6.26(0.00)	7.00(0.00)	-9.00	13.09	16.00	2.9
EnC	9.88(1.96)	5.97(0.40)	11.00(1.41)	-5.00	15.85(1.57)	16.00(1.41)	0.1
B2	11.27	5.69(0.00)	12.00	-5.00	16.96	17.00	0.0
B3	8.49(0.00)	6.25(0.00)	10.00	-5.00	14.74	15.00	0.3
EnU2	3.82(0.02)	3.83(0.00)	5.00(0.00)	-0.50(3.54)	7.67(0.00)	7.50(0.71)	0.3
B12	3.81(0.00)		5.00(0.00)	2.00(0.00)		7.00(0.00)	
B4	3.83(0.00)	3.83(0.00)	5.00(0.00)	-3.00	7.67(0.00)	8.00(0.00)	0.3
KhS	11.30(3.57)	8.28(2.46)	10.36(2.58)	-9.18(4.38)	18.21(1.61)	20.00(4.12)	0.8
B1	6.83(0.00)	10.34(0.82)	10.50(2.89)	-9.00(2.94)	16.46	19.75(0.50)	3.5
B2	12.57	6.99(1.15)	9.50(3.00)	-8.25(2.75)	18.56	18.75(4.92)	1.6
B3	14.5(0.00)	7.26(3.71)	11.33(2.08)	-10.67(8.14)	19.61	22.00(6.24)	0.4
NeK	6.61(5.28)	6.15(0.66)	7.33(2.52)	-6.33(0.58)	16.97	13.67(2.52)	1.0
B2	2.87(0.00)		5.00(0.00)	-6.00		11.00	
B3	10.34	6.62(0.00)	10.00	-6.00	16.97	16.00	1.0
B4		5.68(0.00)	7.00(0.00)	-7.00		14.00	
NeP1	9.51(0.00)	12.28	9.00(5.66)	-12.00(2.83)	21.79	20.00(9.90)	5.2
B1	9.51(0.00)	12.28	13.00	-14.00	21.79	27.00	5.2
B2			5.00(0.00)	-10.00		13.00	
NeP2	13.15	12.68(3.23)	13.33(2.89)	-12.67(5.13)	23.54	26.00(7.94)	5.5
B2		14.96	10.00	-7.00		17.00	
B3			15.00	-17.00		32.00	
B4	13.15	10.4(0.00)	15.00	-14.00	23.54	29.00	5.5
PaB			7.67(2.31)	-4.67(2.08)		12.33(3.51)	
B5			5.00(0.00)	-4.00		9.00(0.00)	
B6			9.00(0.00)	-7.00		16.00	
B8			9.00(0.00)	-3.00		12.00	
PiA	17.95(3.65)	18.74(7.38)	19.00(4.38)	-20.83(7.68)	36.69(7.22)	39.83(8.16)	3.1
B2	16.11(4.63)	17.78(6.28)	16.33(5.13)	-20.33(5.69)	33.89(2.71)	36.67(3.06)	2.8
B3	19.79(1.29)	19.7(9.69)	21.67(0.58)	-21.33(10.69)	39.49(9.98)	43.00(11.27)	3.5
PsS	5.40(1.20)	5.68(0.00)	4.50(0.71)	-11.00	10.24	10.00(7.07)	4.8
B11	6.25(0.00)		5.00(0.00)			5.00(0.00)	
B2	4.55(0.00)	5.68(0.00)	4.00(0.00)	-11.00	10.24	15.00	4.8
PtS	11.19(6.31)	10.36(2.11)	13.00(6.56)	-11.33(2.31)	21.55(6.52)	24.33(8.74)	2.8
B1	5.13(0.00)	11.83	7.00(0.00)	-10.00	16.96	17.00	0.0
B2	17.72	11.30	20.00	-14.00	29.02	34.00	5.0
B3	10.72	7.94(0.00)	12.00	-10.00	18.67	22.00	3.3
PtT	7.26(4.06)	10.39(3.69)	8.88(3.47)	-11.50(3.49)	17.65(6.10)	20.38(5.96)	2.2
B2	5.91(0.00)	15.07	12.00	-14.00	20.98	26.00	5.0
B3	2.14(0.00)	6.41(0.00)	4.00(0.00)	-10.50	8.55(0.00)	14.50	4.0
B7	10.01	11.23	10.50	-14.50	21.24	25.00	3.8
B8	10.99	8.83(0.00)	9.00(0.00)	-7.00	19.83	16.00	3.8

1: For PsS-B1, only one peak of maximum grain angle is recorded due to the limitation of the material's thickness (Annex Tab. 1).

2: For EnU2-B1, one of the MAD's calculations(negative side) is not considered (Annex Tab. 1, Page 246).

MAD: one direction of the MAD calculation by equation (6).

ANG: measurement of the angles by the procurator (Fig. 21).

Z: the Z spiral direction of the interlocked grain.

S: the S spiral direction of the interlocked grain.

II.C.2.c) GA measurement by X-Ray diffraction

Comparing the GA obtained by the splitting method, another evaluation by XRD was also done simultaneously with MFA's measurement. The GA's determination by XRD does not correspond to the same purpose as the splitting method. On the contrary, the purpose of measuring GA by XRD is to acquire the information at the same position on the same specimen used in the Vybris method (III.C.2). Therefore, measuring GA by XRD aims to correlate well for studying structure-properties relations for the local mechanical properties.

II.C.3. Microfibril angle (MFA) measurement

The microfibril angle (MFA) corresponds to cellulose microfibrils' spiral alignment respective to the cell axis. Generally, when referring to MFA concerning macroscopic properties, the considered MFA is only in the S2 layer of the secondary cell wall because it is the thickest in the cell wall, compared with S1 and S3. Here, the reaction wood was excluded from the discussion, however.

The MFA has been widely studied as a significant affecting factor on the wood's mechanical properties, swelling and shrinkage properties, and less frequently on the optical properties. There are several methods for measuring the MFA, including optical microscopic observation (with Iodine dyeing), near-infrared spectroscopy, and X-ray diffraction (XRD) (Donaldson 2008). Among these methods, X-ray diffraction (Cave 1966; Yamamoto et al. 1993) could provide a reliable and rapid measurement for the MFA. It can also measure the GA in the meantime (Evans et al. 2000; Buksnowitz et al. 2008).

In the present study, the setup of the XRD measurement for MFA was the (200) plane in the perpendicular transmission geometry (PTG) (Sarén and Serimaa 2006) for approaching the MFA's estimation. Assuming an angle (θ) is between the (200) plane and the incident X-ray beam, then the angle between the X-ray and the (200) plane will be 2θ . The scattered spots' distance from the centre of the circle would be noted $2\theta_{\text{dist}}$ forming the 2θ circle (Fig. 27b), and the radius of this circle depends on the distance from the sample to the sensor.

The conducted XRD measurement for the intensity peak of the (200) plane has two principal methods. One is by the $2\theta_{\text{dist}}$, which includes several crystalline planes' signals. The other one is by the intensity in the azimuth angle (Φ), of which there will be a mixture effect by 3 peaks in Gaussian distribution, including two signals of beam penetrating perpendicularly to the cell, i.e., front side and backside, and one parallel to the cell wall. The present study used the azimuth angle method for the estimation. Thus, the azimuth angle was transformed to the Cartesian

coordinate (Fig. 27a), where the horizontal axis was in the azimuth angle, and the vertical axis was the intensity of the data. Afterwards, the inflexion points were found automatically by defining the section for baseline. Then, the Cave’s parameter T was found for the MFA’s estimation (8).

$$\text{MFA} = 0.6T \tag{8}$$

II.C.3.a) Methodology for X-Ray diffraction

The X-ray diffractometer was Gemini-S. The sensor was graphite monochromator charge-coupled was Sapphire CCD (Fig. 26). All are from Agilent Technologies. The X-ray source was MoK α (Molybdenum) radiation tube ($\lambda=0.0709$ nm) and was operated in 50 kV and 30 mA for 10 seconds.

The sample was taken from the Vybris LT specimens (§III.C.2), i.e., the thin strip specimen in 2 mm nominal thickness, held by a sample base to the angle of 45° because of considering the X-ray stopper. The measurement included two kinds of values and four measuring positions. One was the GA, and the other one was the MFA. They were taken 2 cm from two longitudinal ends and 0.5 cm from two tangential sides (Fig. 25), i.e., 4 data points in total for each specimen. Three straight grained spruce specimens were used as the standard sample for GA’s calibration for the GA measurement. Their GAs’ values were measured and averaged, so the difference between the measured value (later) and the value from this averaged value was the GA of the sample. Also, due to the fixed rotation axis of the instrument, the specimen was flipped and turned for four positions’ measuring (Fig. 25). Therefore, the GA values on one of the flipped sides were then multiplied by negative ones.

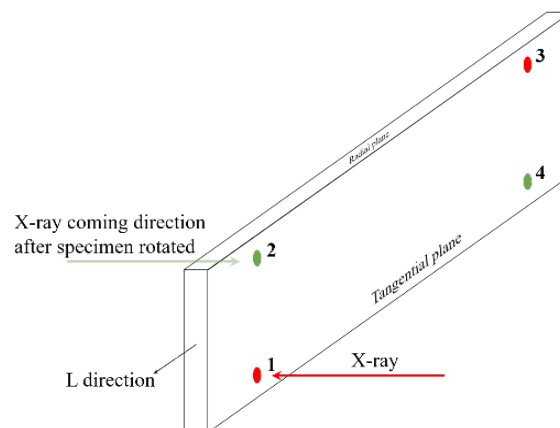


Fig. 25 The 4 measured positions by XRD on the Vybris specimen in the present study. The red and green colours represent the X-ray beam’s direction due to the flip of the specimen.

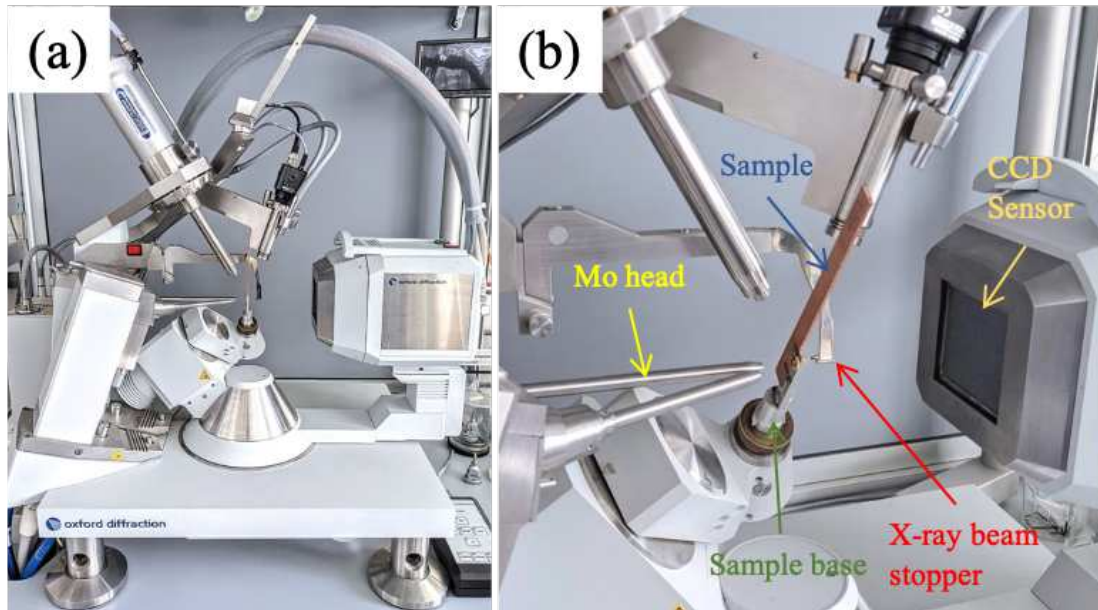


Fig. 26 The setup of the GA and MFA measurement. The general view of the instrument (a) and the detailed setup for the measurement (b). The holding base was rotated 45° vertically.

II.C.3.b) *Data analysis of X-ray diffraction*

After the data were acquired, the intensity around the (200) plane circle (caused by the diffracted beam) was transformed into a Cartesian coordinate where the x -axis was the azimuth degree from 0 to 360°, and the y -axis was the intensity (Fig. 27a). The form of the data was scattered points. So, the interpolating was done among all the points along the azimuth angle. Some specimens might have non-crystalline substances that caused the unwanted points on the plot, resulting in regional deformation of the smoothed curve. Hence, those spots were removed semi-automatically. Subsequently, the curve smoothing was completed, the process of MFA estimation was done automatically. That all-above-mentioned steps were done with the program written in Visual Basic for Application (VBA) by Tancrede Alméras (LMGC, Montpellier).

The automatic searching for the inflexion points was done for the MFA estimation, and the tangent lines were drawn (green in Fig. 27a). Two tangential lines cross the baseline (bottom line) of which is the blank signal of the sample in the 2θ circle, and the distance on the two crossing points was then the value T . For some specimens with wider intensity peaks, their inflexion points were found manually by a supporting plot indicating the second derivative value along the azimuth angle. Then, the tip of the peak was accordingly indicated by the median of the two angle values of the inflexion points, indicating the fibre's direction. Thus, the difference between the tip's value (in degree) and the standard specimens' averaged values was the GA value.

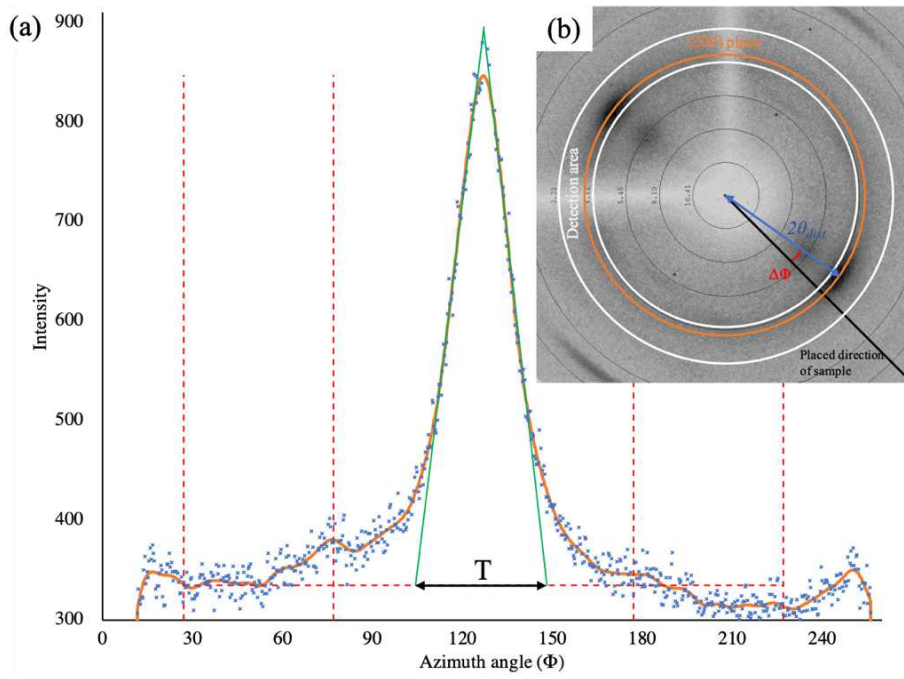


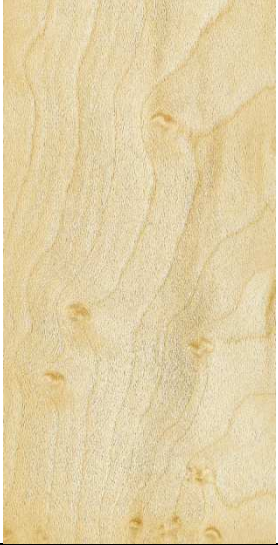
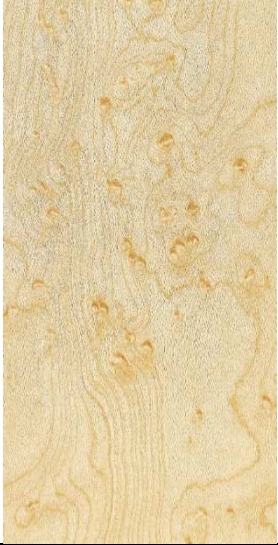
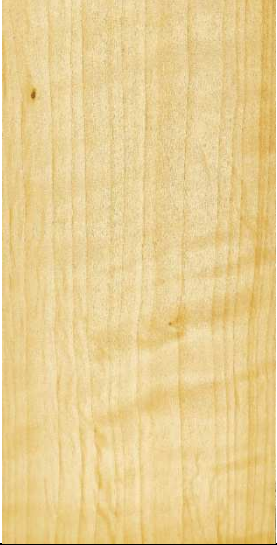



Fig. 27 The estimation for the MFA in the present study, exemplified with the measuring position 4, of HyP-B1-b2_2-T2 specimen (material preparation in topic III.C.2.b).

II.C.4. Results of the multi-scale structural evaluation




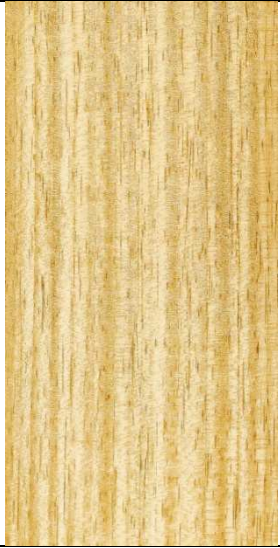


II.C.4.a) The visual appearance of the studied material of figured woods

The surface appearances and their figure's type are thus recorded to build the connection in the physical-mechanical aspect. The part of the figures is presented (Tab. 7). The aspect ratio below is not the same for all the photos. The demonstration is for indicating the figures in the selected materials and referred to the present study.


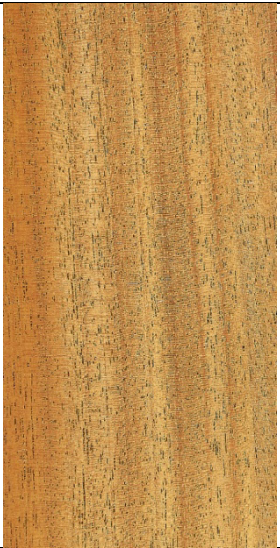




Tab. 7 The record of the figures of materials used in the present study.

Botanical name	<i>Acer pseudoplatanus</i>	<i>Acer macrophyllum</i>	<i>Alnus glutinosa</i>
Picture			
Grain	Birdseye	Birdseye	Curly + Wavy
Code	AcP-M1	AcM-M1G	AlG3
Botanical name	<i>Fraxinus sp.</i>	<i>Juglans regia</i>	<i>Betula pendula</i> subsp. <i>pendula</i>
Picture			
Grain	Wavy	Wavy	Mazur/Karelian/Curly Birch
Code	FrS4	JuR4	BePVar2

Tab. 7 (Continued)

Botanical name	<i>Acer pseudoplatanus</i>	<i>Acer macrophyllum</i>	<i>Canarium madagascariense</i>
Picture			
Grain	Pommele	Pommele/Quilted	Interlocked
Code	AcP-P4	AcM-P1G	CaM
Botanical name	<i>Daniellia oliveri</i>	<i>Entandrophragma cylindricum</i>	<i>Nesogordonia kabingaensis</i>
Picture			
Grain	Interlocked	Interlocked	Interlocked
Code	DaO	EnC	NeK

Tab. 7 (Continued)

Botanical name	<i>Nesogordonia papaverifera</i>	<i>Khaya senegalensis</i>	<i>Pachylobus buettneri</i>
Picture			
Grain	Interlocked + wavy	Interlocked	Interlocked
Code	NeP1	KhS	PaB
Botanical name	<i>Pseudopiptadenia suaveolens</i>	<i>Piptadeniastrum africanum</i>	<i>Pterocarpus soyauxii</i>
Picture			
Grain	Interlocked	Interlocked	Interlocked
Code	PsS	PiA	PtS

II.C.4.b) *The diversity in GA patterns and the distribution of maximum and local GA values*

The table compares the GA diversity and grain types (Tab. 8). Each species' visual appearance and grain pattern were shown, and their GAs was evaluated (if evaluable) in the previous methods (§II.C.2). Herein, the definition of “evaluable” means evaluating those grain patterns by the maximum magnitude of GA indicated in the literature. Thus, the diversity of the grain structures is then discussed in this section. However, as previously mentioned, some figures' GAs are not evaluated with the GA splitting method, e.g., birdseye and non-detectable ones (Fig. 23), but their figure's intensity was adopted in the evaluation (Fig. 24).

Tab. 8 The GA diversity of all the figures in studied materials.

<i>Botanical Name</i>	Code	Grain pattern	Sample Quantity	Frequency (Peak/cm)	Grain angle(°) Abs-Avg (stdev)	Max GA(°)
<i>Canarium madagascariens</i> Engl.	CaM	IG	2	1.73	5.58(0.60)	13.0
<i>Daniellia oliveri</i> Hutch. & Dalziel	DaO	IG	3	2.39	4.28(0.44)	9.0
<i>Entandrophragma cylindricum</i> Sprague	EnC	IG	2	1.35	4.64(0.51)	12.00
<i>Entandrophragma utile</i> Sprague	EnU	IG	2	1.37	2.39(0.15)	5.0
<i>Khaya senegalensis</i> A. Juss.	KhS	IG	11	1.49	5.99(1.17)	20.0
<i>Nesogordonia papaverifera</i> Capuron ex N. Hallé	NeK	IG	3	1.94	4.11(0.67)	10.0
<i>Nesogordonia kabingaensis</i> Capuron ex R. Germ.	NeP	IG	5	2.05	6.86(2.80)	17.0
<i>Pachylobus buettneri</i> Guillaumin	PaB	IG	3	2.17	6.17(1.76)	9.0
<i>Piptadeniastrum africanum</i> Brenan	PiA	IG	6	1.20	17.96(3.57)	28.0
<i>Pseudopiptadenia suaveolens</i> J.W. Grimes	PsS	IG	3	1.00	5.13(2.32)	11.0
<i>Pterocarpus soyauxii</i> Taub.	PtS	IG	3	0.81	5.50(1.64)	20.0
<i>Pterocarpus tinctorius</i> Welw.	PfT	IG	4	3.13	5.70(2.13)	14.5
	FrS2	W	3	0.70	31.90(22.19)	55.9
<i>Fraxinus</i> sp.	FrS3	W	3	1.04	36.77(16.34)	52.2
	FrS4	W	3	0.73	50.97(18.55)	68.4
<i>Juglans regia</i> L.	JuR3	W	1	0.70	13.08(00.00)	13.1
	JuR4	W	1	0.95	17.57(00.00)	17.6
				(Figure/cm ²)	Degree of figure	
	AcP-M1	B	1	0.20	2	
<i>Acer pseudoplatanus</i> L.	AcP-M2	B	1	0.11	3	
	AcP-M3	B	1	0.17	4	
<i>Acer macrophyllum</i> Pursh	AcM-M1G	B	1	0.19	1	

IG: Interlocked grain; W: Wavy grain; B: Birdseye

The table (Tab. 8) shows the developed interlocked grain's GA with the algorithm equation for each 0.01 mm radial length (7). The angles' values were compared between the generated profiles from split planes, and the XRD (§II.C.3.a) result (Fig. 29). In the x-axis, the samples' names are in the order of species' abbreviation names and the position (listed in §III.A.2). The quantity of the XRD result is 8 data from two Vybris specimens. In general, the distribution of the XRD and the splitting result fit each other, except that the splitting values are not enough numerous (due to the length of the splitting block). The XRD results show more extensive ranges (longer shapes) because the local fibre angle could be more deviated than the "grain-scale".

Therefore, the developed GA values were compared for all the interlocked grain species in the present study (Fig. 28). The intensity distribution is according to the species. Thus, the narrow and long shape indicate a quickly changing angle (or higher frequency) and large amplitude (large GA), e.g., PiA. On the opposite, the one with a broader and shorter shape means the lower frequency and smaller amplitude. Also, a baseline (0°) indicates the neutral axis of the amplitude. Suppose the values are biased to the positive (negative) side. In that case, generally, it means the interlocked grain is inclined more to the Z(S) direction due to the mixture grain pattern or the original material's direction. The latter reason is that it is almost impossible to know their real longitudinal direction without marking it at the beginning (trunk) of the tree with IG. Furthermore, the values were generated with the algorithm equation. If the splitting blocks were not long enough to acquire a whole period of the angle change, it also affected the result.

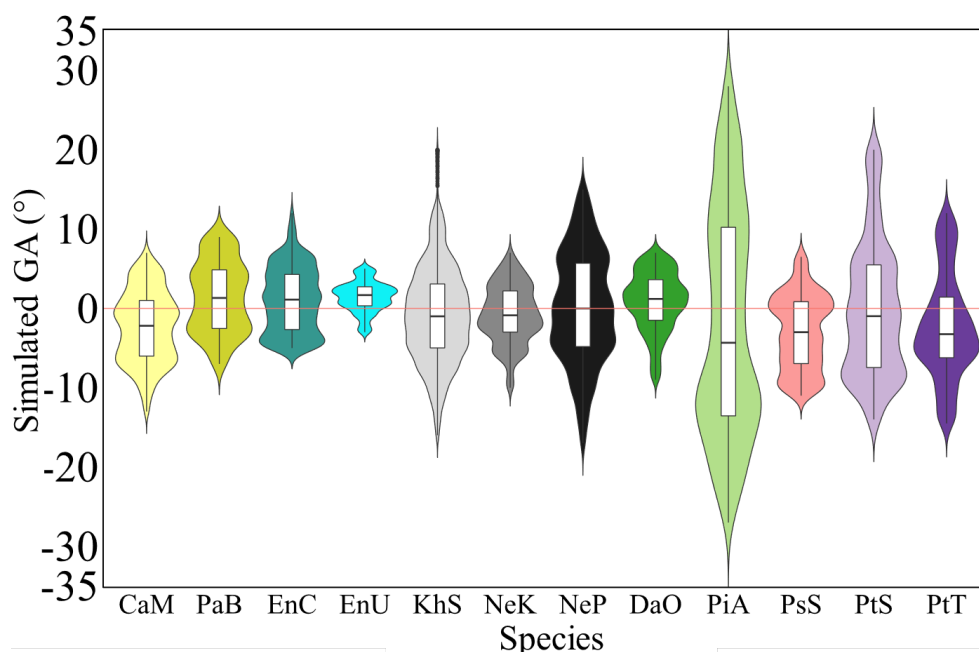


Fig. 28 The GA distributions of the interlocked grain species, from the interpolated profiles calculated from splitting blocks.

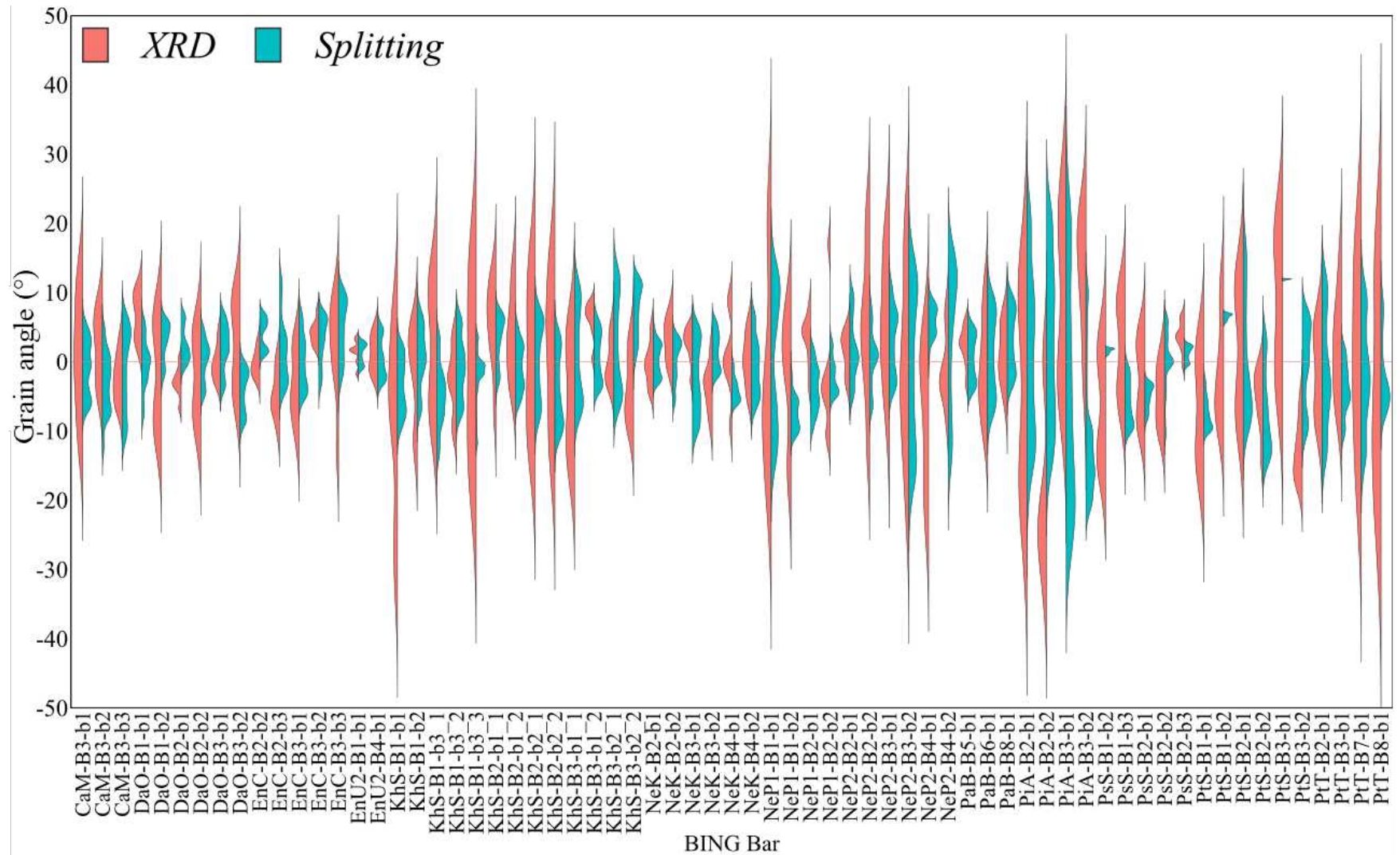


Fig. 29 The comparison of grain angle measurement by the splitting method (II.C.2.a) and XRD method (II.C.2.c).

II.C.4.c) *Distribution and categorisation of MFA values*

The descriptive statistics of MFA values were calculated and shown in the violin plot (Fig. 31) by species. In this representation, each width is based on the relative quantity of the data in total. From AlG1 to AcM-P1G, the temperate hardwood is on the left side, while the tropical hardwood (from CaM to PtT) is on the right side. In a statistical aspect, it can be seen (one-tailed *t-test*, $p < 0.05$) that the selected temperate hardwoods have larger MFA (from 10 to 30°), as a group, than the tropical species (7 to 20°) as a group. This tendency may reflect the growth rate and/or conditions of the different species and trees. The MFA is usually larger in fast-grown wood. Inside trees, MFA generally decreases abruptly during the juvenile wood zone, then stabilises in the adult wood, at least in temperate species. However, this radial trend can be reversed in tropical hardwoods, with MFA increasing from pith to bark in trees from natural forest (Zhang et al. 2011), or on the contrary decreasing in the same species from plantations (McLean et al. 2011). The temperate hardwood in the present study are from relatively smaller trees compared to the tropical ones, and their sampling position could be closer to the centre of a trunk, however, all the sampling positions are relatively far from the pith, i.e. they most likely exclude juvenile wood. Some of the studied temperate species (AlG, JuR, AcP and AcM) are generally categorized as relatively fast-growing species, however, for maple at least, wood selected for instrument making is usually slow-grown. The actual growth rate of the different species and trees studied here is not known, therefore the author can only indicate the observed difference in MFA between temperate and tropical hardwoods. The within-species distribution in MFA is wider for studied temperate species because they include several trees, with several degrees of figure. The distribution of MFA for the different individuals (planks) is shown in the next figure. No trend appears between the degree of figure and the values of MFA. For AcP, the birdseye (-M) figure appears to have smaller MFA than the pommele (-P), but the opposite is observed for the other maple species AcM.

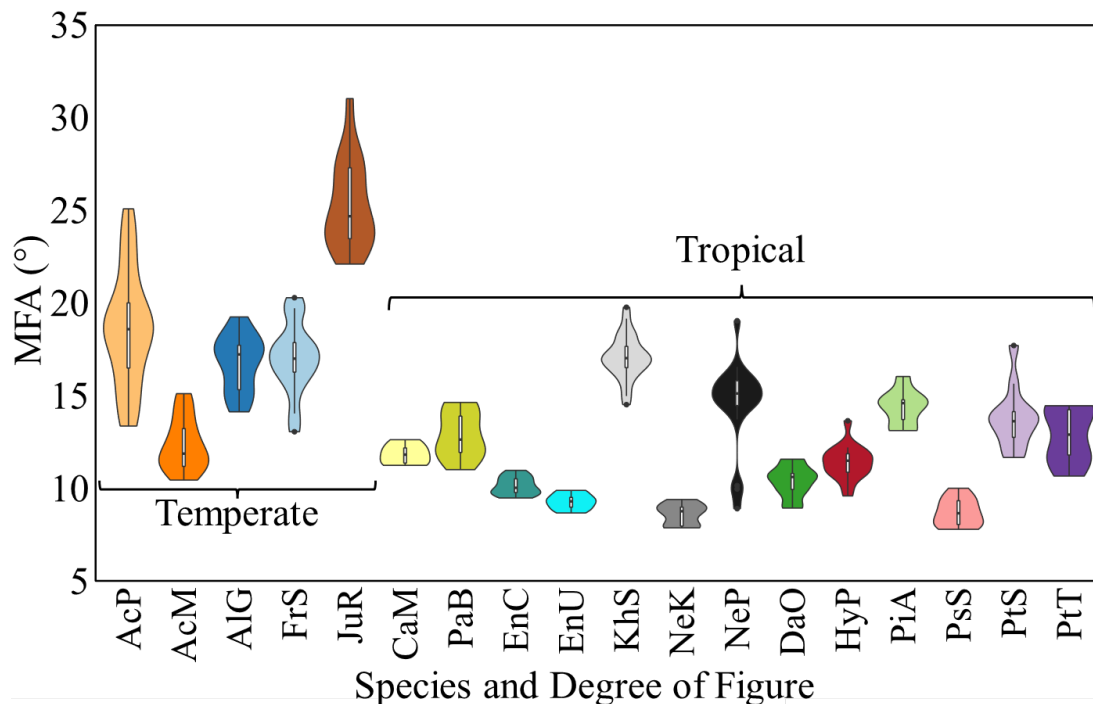


Fig. 30 The MFA values categorised by species. From AIG to AcM, left to right, are the temperate species.

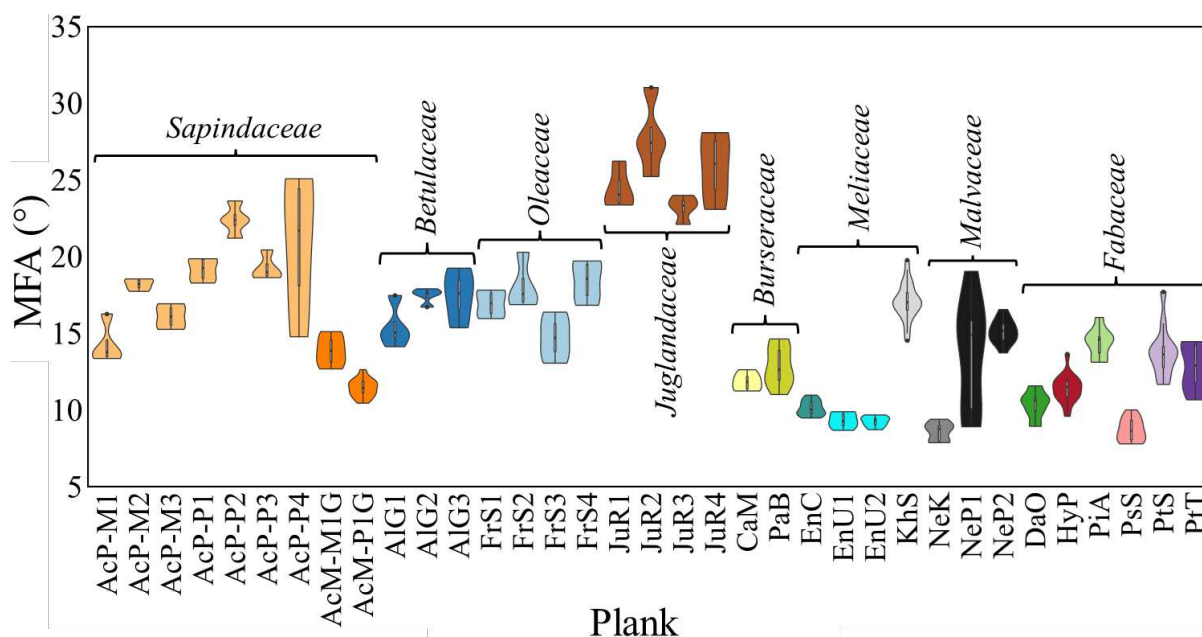


Fig. 31 The comparison of MFA values between different species and planks. The temperate species marked with a number means the doF categorized by the provider (the larger means the figure degree is higher, except the AcP-M. The order of AcP-M is reversed). In contrast, the marked number for the tropical ones means the different planks.

II.C.4.d) *Comparing the variations in MFA and in GA*

Previous studies showed the variation of GA in the radial direction having increasing trend (except the part of juvenile wood) in the tree for spiral grain (Priestley 1945; Cown et al. 2004, 2010; Ormarsson and Cown 2005; Gjerdrum and Bernabei 2009; Moore et al. 2015). Some studies, including MFA measurement and simulation, suggested that the MFA had the opposite trend against the (spiral) GA in the radial direction (Schulgasser and Witztum 2007). Though some of the studies didn't concern the MFA, lacking this information, the decreasing trend for MFA in a radial direction from pith to bark is a common observation, at least from temperate species, although, as seen above, this can be reversed in tropical species in natural forests (Mc Lean et al. 2011; Zhang et al. 2011). On the interlocked grain, in one tropical species, the amplitude of grain angle increased along the radial direction, from pith to bark, while the MFA decreased a common only in the few cm of the core and then remained stable over the radius (Bossu et al. 2018). Also, the standard deviation of the GA along the spiral grain patterns was shown to increase from the centre to the periphery (Gjerdrum et al. 2002). There's no definitive evidence for any relationship or correlation between GA and MFA, although, from pith to bark, they could follow opposite trends. The comparison in previous studies is either intra-tree or inter-tree in the same species. Since grain's orientation is an issue in the coordinates of the tree, i.e., L, R, and T for the whole tree and the applied direction, and the cellulose microfibril angle is the orientation in cell scale, it would not be not surprising that these two factors are independent, especially when a study does not include clear information on radial position. There's no necessity of having correlation between them. Anyhow, the general comparison of the two measured values, GA and MFA, was still explored (Fig. 32). In the figure, all the species have their distributions, while there are no clear correlations between GA and MFA in the present study. With the help of using the elliptical distribution (in 95% confidence interval), the distributions of GA to MFA by species were drawn. All the species have their range of MFA (same in Fig. 31), while the GA is widely distributed within species. The correlation coefficients, by species, are less than 0.01. The same was found when expressing the GA into absolute values, showing that there's no relationship between MFA and GA in the present study, where the two factors are measured at a very local scale. A previous study found, at a very local scale also, a possible correlation between MFA and GA in one interlocked grain wood (Brémaud et al. 2010), the present study does not confirm this. On the other hand, another study gave a very clear negative correlation between MFA and GA, between samples coming from 12 different individual trees with very different degrees of wavy grain (Alkadri et al. 2018). But in the present

study, the within-species sampling, i.e. number of trees and of degrees of figure, is too limited to compare to this last result.

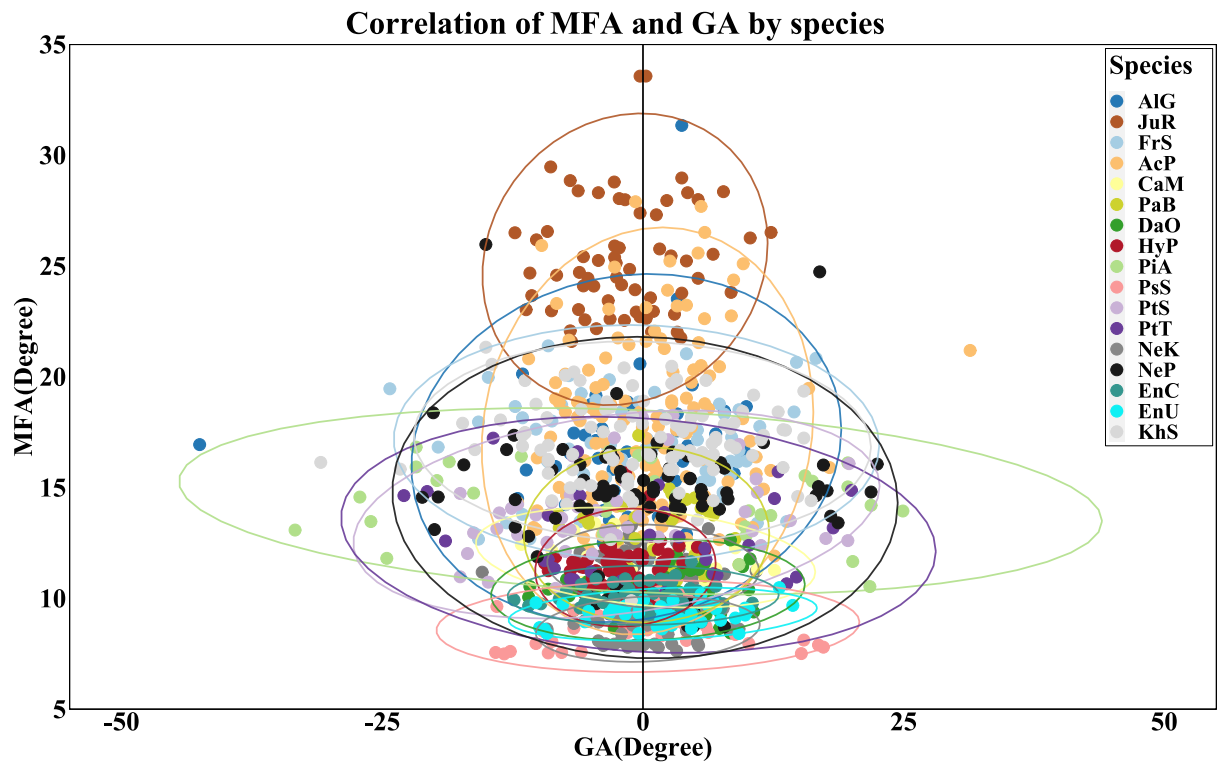


Fig. 32 The comparison of GA and MFA from the XRD measurement. The comparison shows that the GA and MFA have no relationship from the current study. The elliptical distribution (confidence level $\alpha = 0.95$) demonstrates that each species has its distribution.

Summary of Chapter II

The objective of this chapter was to describe the structural organisation of a variety of figured woods with different grain patterns.

Some tentatives were conducted for a modelling (analytical) that could describe most of the patterns and modalities of grain deviations; and also for optical measurements that could help to infer grain deviations non-destructively from wood surfaces. For time reasons, these tentatives could not be continued in the frame of the present thesis, but may be interesting to further by others that would be interested in the topic. Then a visual inspection of all the archive specimens of the CIRAD Xylarium was conducted, allowing the author to better grasp the diversity and occurrence of figured woods.

The main part of Chapter II presented the selection and structural description of the wood sampling that will then be studied throughout the rest of this thesis. The present materials include seven types of grain patterns, i.e., straight, interlocked, wavy, birdseye, pommele, Karelian birch, curly plus wavy. Several grain patterns have different degrees of figure (doF). The materials come from seventeen species, from the tropical and temperate climatic zones. Their structural organisation (including grain angle GA, then microfibril angle MFA) has been studied by two main methods: splitting of wooden blocks, and X-Ray diffraction. The conducted work can be summarised into the following elements, regarding the advantages and limitations of these methods, and regarding the obtained results:

-Generally, the visual grading from the sawn plane could roughly evaluate the wood grain by its wood figure. According to the figure intensity or frequency, the professional vendors' visual grading is proved from the splitting result. Nevertheless, visual grading is not the only parameter involved. The AcP-M group grading reveals that the birdseye figure frequency is not the only parameter in the vendor's grading, but the figure's size is also involved. Yet, the sample number is relatively small, and the samples are from one vendor only. A further examination is needed for the relationships between the degree of figure (doF), the figure intensity or frequency and the figure size. Those parameters could be beneficial for the figured wood selection and grading, but only for the same figure pattern and species.

-The splitting method keeps the information in 2 wood principal planes/directions (R and T), saving more 3D grain patterns and structural information for the grain structure analysis. Accordingly, some grain patterns which haven't been revealed in the literature are thus recorded. The birdseye grain has an abrupt bi-directional structure, revealing the partial variation grain

change against the T plane. Also, the grain near the birdseye is thus distorted around the birdseye variation. Another abrupt changing pattern, Karelian Birch (BePVar), has a swirl grain structure. However, it has no regularity for the grain pattern seen from the splitting result. The same observation is done for the pommele grain. The splitting result cannot describe in a simple way the pommele grain pattern. Herein, the pommele refers to the maple with pommele figure/grain (AcP-P) in the present study. The splitting blocks could partially observe its periodically curly longitudinal and the wavy grain pattern for the pommele grain. However, there's no describable value of grain angle (GA) from the splitting sample. One of the possible reasons is that their undulating frequency is too small (i.e., their period too large) for the splitting blocks. Equally, the curly and/or wavy grain pattern for the AIG species had the same issue. Thus, further examination and exploration in future are needed for those grain patterns. The wavy grain samples studied here generally have relatively wide undulating periods. Moreover, the wavy grain could be non-visible/subdued from the sawn plane (for JuR1). In general, the sizes of studied wavy grain planks was small, so variations along the radial and tangential directions or shown on the split planes could not always be observed. Therefore, the recommended dimension for the wavy grain splitting would be 5 cm (R) by 5 cm (T) for the general exploration (for all species). Based on the above considerations, using the splitting method for the grain angle measurement is thus not applicable for all the grain patterns. One reason is that the complicated grain patterns (ex. birdseye, swirl) are not measurable (or not efficiently) by using the traditional angle measuring. Another is due to the dimension that the complete grain undulating period is not revealed.

-The specificities of figured wood also implied some limitations and/or precautions regarding XRD measurements. Some of the studied materials were very difficult, or sometimes impossible, to measure by XRD. The extreme case is on the BePVar (Karelian birch) specimens, with no GA nor MFA value measured/estimated by XRD. Their XRD scan results have no peaks (or that's to say, the signal intensity is too homogeneous). Also, the XRD estimations for the GA and MFA have limitations due to the fibres diving directions.

-In the future, it would be recommended to test other non-destructive GA measurement for the figured wood, while considering more complicated grain patterns in nature, and relatively large areas or volumes, more representative of the figured wood grain structure. Some technologies that could be tested would maybe include terahertz or microwave imaging, or (micro-) tomography.

Notwithstanding the above experimental difficulties or limitations related to the most complex grain patterns and/or to the limited initial dimensions of material, the distribution of GA and MFA have been quantitatively assessed for the majority of the studied figured wood grain patterns:

-For interlocked grain, the average period of alternating GA ranged from 0.3 cm to 1.2 cm, that is, relatively tight interlocked grain. In the studied wavy grain species and samples, the (measurable) period of undulation was at least of 1 cm, i.e., relatively wide (at least when compared to the best-known “fiddleback” wavy figure).

-The amplitude of grain deviation, as expressed by maximum GA, depended on the more or less “local” types of measurements, with direct measurement of maximum angles on splitted blocks > interpolated values, and values by XRD (point-measurement) > values from splitting profiles.

-In all cases, the range of GA amplitude varied clearly between the different studied materials, with maximum GA being from 7.5° to nearly 40° for the different species with interlocked grain. The maximum GA of the two measurable species with wavy grain were relatively wide (close to 15° for wavy walnut JuR, more than 30° for wavy ash FrS).

-The MFA values assessed by XRD are mostly located between 5 to 20 degrees (up to 25-30° for some of the temperate hardwoods). As a group, the temperate hardwoods tend to have higher values of MFA than the tropical ones. The distribution of MFA within species is much more focused than observed for GA, except for species with different individuals and degrees of figure.

-No trend between the degree of figure and the MFA could be observed, at least with the present number of samples. The point measurements of GA and of MFA shows no correlations within-species (and all the less between-species). Instead, the distribution of MFA appears rather linked to a species (or tree), independently of the range of GA that can be encountered. Regarding literature, this observation might be mitigated if many different individuals of a same species, or if a fine survey of radial variations within and individual, were studied. But in the present results, there is no correlation between GA and MFA.

III. Characterisation of physical and mechanical properties and their anisotropy

Introduction of Chapter III

Wood is a cellular, fibrous, and composite material. Its structural, mechanical, hygro-mechanical properties are anisotropic. These properties are influenced by the macrostructure, i.e., grain orientation and the heterogeneity of the xylem components, and the microstructure, i.e., the contribution due to the cell wall ultrastructure (cell wall layering, properties and microfibril angle (MFA) of the S2 layer mainly). The previous chapter (Chapter II) selected various figured wood based on their specific grain patterns and visual appearance. Two scales of their structural orientation were measured: grain angle (GA) and microfibril angle (MFA). Chapter III describes selected physical and mechanical properties and their anisotropy for this variety of figured wood. Several methods were used to combine their aptitude to address different scales of wood samples and different properties, i.e., hygro-mechanical (shrinkage and fibre saturation point), mechanical properties (elastic moduli and damping by internal friction), and different directions and planes of anisotropy.

This chapter first presents the sampled material, its characteristics and its modalities of sample preparation to attain the goal of multiple characterisations. Then, the used (or developed) methods are presented. A method based on natural vibrations (BING) provided longitudinal modulus of elasticity (MOE) and damping, and transverse shear moduli estimates. BING was used for its versatility in testing different dimensions of relatively large specimens (from planks to normalised beams). Another method based on forced vibrations (Vybris) allowed testing specimens of small dimensions, thus revealing the local heterogeneity at a scale that can be easily related to the structural evaluations made in the previous chapter. Vybris provided precise characterisations of longitudinal elastic modulus and damping. A new development made during the present thesis allowed to extend it to two shear planes, both for elastic moduli and damping. Also, the ultrasonic test assessed the anisotropic properties for the engineering stiffness tensors. Lastly, the shrinkage and fibre saturation point (FSP) were characterised in the radial and tangential directions.

The second part of this chapter will then present the generic results obtained for these selected physical-mechanical properties. It will examine some methodological factors, such as the effects of specimens' preparation and conditioning and comparing values obtained by the

different testing methods. It also presents the range of variation of the different measured properties for the different wood species studied.

III.A. Overview of the sampling plan and types of measurements

III.A.1. The materials: basic information on the initial planks

The basic information for the initial condition is revealed here to indicate the situation and more detailed information for all the materials. Here, the abbreviation mark for indicating/coding all the species follows the same rule as in the previous chapter (Tab. 9, as in Tab. 3 in §II.C.1). Furthermore, a number was added after the abbreviation mark for distinguishing the different planks for certain species. Again, for *Acer pseudoplatanus* L. (AcP), two other figures are involved, which are Birdseye (AcP-M) and pommele (or “quilted” depending on vendors’ naming) (AcP-P) (Tab. 9).

Additionally, for the pommele (quilted) and Birdseye, their figures were indicated depending on the tree's geographical location and an individual variation (genetic) (Bragg et al. 1997; Fan et al. 2013; Krajnc et al. 2015). Thus, within one species several degrees of figure (doF) were selected. Herein, the supplier made the doF’s categorisation (II.C.2.a). On the contrary, the selection for the interlocked grain was made by the tangential sectioning since the doF of interlocked grain is due to the relative location, i.e., longitudinal and radial, in individuals.

The consideration of material selection was made without the concern of the structural function in the tree, i.e., sapwood (SapW), heartwood (HeartW), and juvenile wood (JW). However, due to the material that could be acquired, the volumes of those parts were therefore noted (by visual inspection). Indeed, this is not an accurate anatomical and biological definition for the JW and SapW. The colour is convincing to distinguish SapW from HeartW because of the extractive deposition. However, JW is based on a microstructural difference. Though the anatomical validation part is not deemed, the calculation of JW’s volume was still conducted just in case the distinction was necessary for the following comparisons, e.g., for PtT (Fig. 33b).

The volume calculation is done by the computer-aided design (CAD) software (Autodesk Fusion 360). Firstly, the dimensions of the specimens were measured (Matsui M-15; 5 m KDS tape ruler, Tab. 9) and, then, the same dimension bodies were built in CAD. Secondly, rectangular nets were drawn by pencil on material surfaces in the dimension of $10 \times 5 \text{ cm}^2$ to verify the distortion in post-processing (12.1.3, Capture One, Phase One). Thirdly, photos of the specimen surfaces were taken (at 55 mm - f/5.6, 18-55 mm f/2.8-4R LM OIS, by Fujifilm X-E2), except when the surfaces were not clean or without any effect on the further calculation. Fourthly, the photos were inserted in the CAD models according to the built body. Fifthly, the boundary

of the SapW and HeartW were drawn and then separated from the built body. Lastly, the software computed the volumes information (Tab. 10). Herein, the irregular part was thus calculated.

Tab. 9 Species and dimensions in the initial condition of the specimens

Family	Botanic Name	Code	Density (g/cm ³)	L (cm)	W (cm)	T (cm)	Test not involved	Note
Sapindaceae	<i>Acer pseudoplatanus</i>	AcP-M1	0.65	59.05	5.95	2.59		
		AcP-M2	0.57	60.00	6.05	2.50		
		AcP-M3	0.55	60.10	6.10	2.47		
		AcP-P1	0.53	60.30	6.55	2.58		
	<i>Acer macrophyllum</i>	AcP-P2	0.52	60.20	6.15	2.60		
		AcP-P3	0.52	60.30	6.15	2.60		
		AcP-P4	0.62	60.30	6.10	2.61		w
		AcM-M1G	0.47	50.00	25	3.5	B, US, S	
AcM-P1G	0.73	50.00	18	3.5				
Oleaceae	<i>Fraxinus sp.</i>	FrS1	0.81	60.30	6.15	2.59		
		FrS2	0.78	60.28	6.25	2.58		
		FrS3	0.79	60.05	6.15	2.50		
		FrS4	0.76	60.30	6.15	2.60		
Juglandaceae	<i>Juglans regia</i>	JuR1	0.54	60.00	6.00	2.50		sw
		JuR2	0.55	60.05	6.12	2.53		sw
		JuR3	0.64	60.25	6.02	2.60		
		JuR4	0.64	60.20	6.30	2.59		
Betulaceae	<i>Alnus glutinosa</i>	AlG1	0.51	60.05	6.05	2.52		
		AlG2	0.47	60.05	6.10	2.48		
		AlG3	0.48	60.30	6.26	2.59		
	<i>Betula pendula subsp. pendula</i>	BePVar1	0.73	20.00	5	5	B, S	
		BePVar2	0.75	20.00	5	5		
Fabaceae	<i>Pseudopiptadenia suaveolens</i>	PoS	0.89	68.79	16.82	2.38		wh
	<i>Daniellia oliveri</i>	DaO	0.36	49.30	21.75	4.88		c, cf, dk, jw
	<i>Pterocarpus tinctorius</i>	PtT	0.88	52.70	23.05	3.88		c, dk, lk, jw, sw
	<i>Pterocarpus soyauxii</i>	PtS	0.74	70.60	35.95	3.63		sk
	<i>Hymenaea parvifolia Huber</i>	HyP	0.99	69.90	14.43	6.84		b, c, s, sw
	<i>Piptadeniastrum africanum</i>	PiA	0.84	73.40	23.70/18.30	5.29		hs, s, sw
	Malvaceae	<i>Nesogordonia papaverifera</i>	NeP1	0.76	54.09	12.04	3.64	
<i>Nesogordonia kabingaensis</i>		NeP2	0.73	48.43	19.19	6.52		c, dk, lk, s, sw
		NeK	0.81	49.90	23.09/21.66	6.12		c, dk, sw
Meliaceae	<i>Entandrophragma cylindricum</i>	EnC	0.67	68.75	18.65	7.93		sk
	<i>Entandrophragma utile</i>	EnU1	0.68	69.10	13.75	4.96		lk
		EnU2	0.65	48.45	13.45	5.08		sw
	<i>Khaya senegalensis</i>	KhS	0.75	70.60	25.25	10.7/3		c, dk, s, sw

<i>Burseraceae</i>	<i>Canarium</i> <i>madagascariense</i>	CaM	0.60	49.50	21.81	9.82	c, jw, s, sk
	<i>Pachylobus</i> <i>buettneri</i>	PaB	0.51	68.30	20.59	3.66	dk

The density here indicates the values measured at room temperature without conditioning.

Type of test: B (BING, §III.C.1), US (ultrasound, part III.D), S (FSP and shrinkage, part III.B)

* Abbreviated mark on the note: bark (b), check (c), honeycomb splits (hs), compressed fractures (cf), knot (live knot: lk; dead knot: dk), shake (sk), splits (s), wane (w), wormhole (wh), watermark (wm), sapwood (sp), and possible juvenile wood (jw).

Tab. 10 The record of the composition and the type of sawn pattern for specimens with heartwood (HeartW) and the sapwood (SapW), calculated with the CAD software

Code	Volume(cm ³)			Error (%)	Composition (%)			Sawn type
	CAD	Measured	Non-regular		SapW	HeartW	JW	
HyP	6858.00	6899.21		1	38.92	61.08		Quarter-sawn
PtT	4707.10	4713.17	6.50	0	4.42	95.58	29.81	Flat-sawn
NeP2	6063.10	6059.50		0	15.64	84.36		Flat-sawn
NeK	6833.00	6833.06		0	19.65	80.35		Flat-sawn
EnU2	3308.90	3310.39		0	20.25	79.75		Flat-sawn
KhS	19133.00	19127.83		0	6.50	93.50		Quarter-sawn
NeP1	2370.90	2370.53		0	13.66	86.34		Quarter-sawn

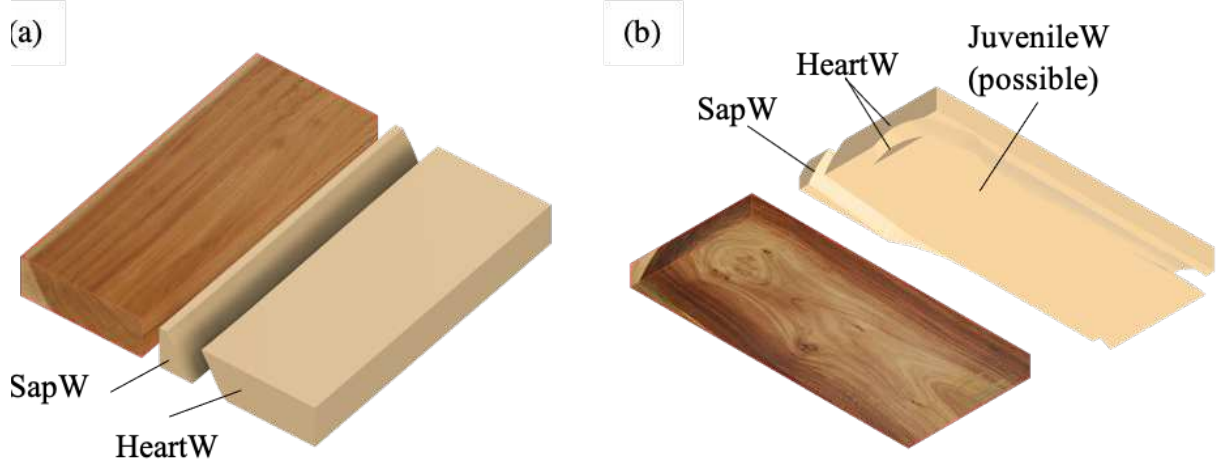


Fig. 33 The demonstration of the separation of HeartW from SapW by using CAD software (Fusion 360). For example, (a) a flat-sawn specimen, NeP2, was separated according to its SapW and HeartW; (b) a flat-sawn specimen, PtT, was noted as having characteristics of SapW, HeartW, and possibly a part of JW.

III.A.2. *The preparation of the specimens: processing and marking system*

The acquired materials were in various dimensions and several sawing patterns (cutting planes). The main objective is to obtain a rectangular beam (cross-section) in the nominal size of $360 \times 20 \times 20$ (mm³), and also the splitting blocks for the grain angle (GA) are at the same radial position (Fig. 19 in §II.C.1.b) and Fig. 34).

The first treatment for preparing the specimens in CIRAD was to plane their surface to inspect material conditions. Thus, the defects were visually found and marked. Furthermore, two species, i.e., PiA and PtT, whose cross-section was not a rectangular prism or not identical to the other side, were also noted (Tab. 9).

The marking system is adopted as follows, in sequence by their cutting order and the relative position according to the radial direction:

$$\text{SpeciesCode} - [\text{F}, \text{B}]_{\#_1} - [\text{b}]_{\#_2} - [\text{V}_{(\text{L-R}, \text{L-T})}, \text{US}, \text{TR}]_{\#_3}$$

F: specimen for splitting.

B: block cut from the large & original material (sub-plank).

B: 360 cm long rectangular (cross-section) bar.

V: Vybris specimen, longitudinal (plane L-R = quarter-sawn, or L-T = flat-sawn), in the nominal dimension $150 \times 12 \times 2$ mm³ (L × R × T or L × T × R, respectively).

US: cube for the ultrasonic measurement, in the nominal dimension $19 \times 19 \times 19$ mm³.

TR: sample for the fibre saturation point (FSP) and shrinkage test, in the nominal dimension $10(\text{L}) \times 20 \times 20$ mm³.

#₁: numbers based on radial position in the trunk, from the bark to the pith, mostly denoted from a small to a large number; or following the acquisition order.

#₂: numbers following the order of R direction, from the bark to the pith, small to large numbers. If the neighbouring specimen is merely at the same distance as the current one, then an underline will be used to distinguish them.

#₃: numbers to indicate different specimens.

For example:

AcP-P1-F1: a specimen for splitting method from AcP-P1.

AcP-P1-B1-b1: a sample from the specimen AcP-P1 obtained from the first cutting procedure (sub-plank, B1), and the specimen is closer to the bark side (b1) than the other one (b2).

AlG1-B1-b1_1: a 360 mm beam from AlG1. Since it is a tangentially-matched specimen, there's no difference in the radial position with the neighbouring specimen, so it is marked 1_1 and the neighbour 1_2.

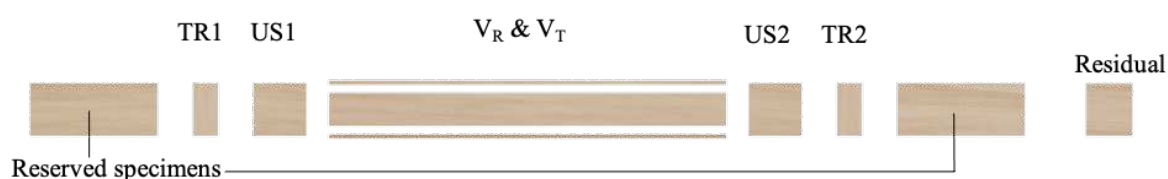


Fig. 34 Exploded view of a 360 mm length beam cut into several specimens for conducting the multi-disciplinary experiments. US2 was also reserved.

Consequently, all the specimens were traceable from the original “standard bar” specimen and their relative radial position in the original plank. The data could be traced back to the same B specimen with its relative position in the original plank in different experiments.

In the present study, due to some limitation of initial wood supply and machining, the acquired materials were not always in exact scientific definition of the radial (R) and tangential (T) directions. There are two reasons. The original plank dimensions (thickness) were not always large enough to allow for an axial rotation (re-orientation in transverse plane). The other is that the acquired materials were flat-sawn or quarter-sawn planks, lacking directional information from the tree. For example, in the case of interlocked grain, one cannot distinguish its actual longitudinal direction from the quarter-sawn or the flat-sawn board. So, the unavoidable defect due to the material machining and processing, i.e., diagonal grain, was more or less important for the acquired wood sample, inducing disorientation of the annual ring. Therefore, to simplify the noting expression, the R and T used in this chapter refer to the quarter-sawn and flat-sawn direction, respectively, closer to the visible R and T directions.

III.B. *Shrinkage and Fibre Saturation Point (FSP)*

As a hygroscopic material, wood reacts to the temperature (here noted Temp) and moisture change in the environment, i.e., Relative Humidity (RH), causing the internal wood moisture content (MC) to change. The MC state has relations to the wood physical and mechanical behaviours due to hydrogen bond force weakened/strengthened because of the distance between microfibril chains, and also of the softening of the amorphous matrix, which are changed by moisture content. When the MC reaches a balanced state, having a dynamic equilibrium state with the environment, the wood weight and volume no longer change due to water's adsorbing or releasing. It is the equilibrium moisture content (EMC).

The degree of wood dimensional reaction to the different Temp and RH is anisotropic, i.e., the length change in a given direction from higher to lower is $T > R \gg L$. Also, change in length in the L direction is sometimes negligible because it is remarkably smaller than T and R (Cave 1972). Several factors were indicated to influence wood hygroscopic behaviour, e.g., MFA, grain angle, density, extractives. Large MFA, high density, and large grain angle cause big volumetric change due to wood shrinkage and swelling properties. From the anisotropic point of view, large MFA causes lower R and T shrinkage and larger L shrinkage. Dense wood would less deform in its T direction than light wood (Yamamoto et al. 2001; Hernández and Almeida 2003; Ormarsson and Cown 2004; Hernández 2007d; Schulgasser and Witztum 2015).

Furthermore, the dimension change positively correlates with the fibre saturation point (FSP) (Sekhar and Rajput 1967). Thus, the experiment focused on shrinkage properties in the R and T directions and the FSP. Two assumptions were made before conducting the measurement and the calculation. Firstly, the volume change from the FSP to the fully saturated state (free water in the lumen) is negligible (Siau 1984; Almeida and Hernández 2006). Secondly, the change in length in the L direction is considered negligible.

III.B.1. Protocol

The dimensions in two directions, T and R, and the weight were recorded for 5 experimental states of specimens, and the notation of those states was marked afterwards with a suffix (h) according to the mentioned condition or state, where h is sa (for saturated state), FSP , 18 , 12 , 6 , and 0 . The environmental conditions (Temp and RH) corresponding to these notations are described below. The starting point of MC was saturation point (MC_{sa}), and the endpoint was MC_0 , obtained using the 103°C drying method (oven-drying). Sequentially, three MC states were set in the succession of MC_{18} , MC_{12} , and MC_6 .

Two sections, of nominal dimensions 10×20 (T-dir.) \times 20 (R-dir.) (mm^3), were taken from the standard bars (TR1 and TR2, Fig. 34). They were marked with a black circle in the centre of the R and T faces. The inner diameter fitted exactly to the diameter of the comparator probe. The samples were bottled by species. Distilled water was then poured into the bottles. Webbed plastic caps were used onto the bottlenecks, forcing the samples to be fully submerged during the saturating process. Then, the bottles were placed in an autoclave, and saturation was achieved by placing the container under vacuum at regular intervals: 4 h (-1 Bar), 5 h (0 Bar), 15 h (-1 Bar), 4 h (0 Bar), 5 h (-1 Bar), and 15 h (0 Bar). Here, the pressure is the gauge reading number.

Once saturation was reached, the specimens were taken out of the container. Also, their state was checked by the fact that all specimens were sinking even after removing the plastic cap. During the measurement, their surfaces were kept moist with the water from their bottles until being weighted (MC_1 , Laboratory LC620S, Sartorius). Subsequently, the length (l_h , $h = s$, 18 , 12 , 16 , 0) in the T and R directions were recorded by a digital comparator (ID-H0560, 543-563-2, Mitutoyo). Then, the specimens were placed in a climate chamber (HPP 108, Memmert) for different points of MC, as previously mentioned. The setup of the points followed the empirical EMC of wood (ASTM D4933-99 2014) for the temperatures and humidity, which were 30°C -85 % RH (supposed to reach an average EMC of 17.4%, code 18), 20°C -65 % RH (12.0% supposed average EMC, code 12), and 20°C -30 % RH (6.2% supposed average EMC, code 6). Finally, the specimens were placed at 103°C in an oven for 3 days (anhydrous state, noted 0).

III.B.2. Calculations

In order to make sure the specimen is fully saturated or in the same saturation state, the correlation between the oven-dry density and density in the saturated state is made. In the assumption, the cell size change is isotropic in the R-T plane and linear with the MC. The size of the lumen doesn't change or is small enough to be neglected compared to its original shape in

the MC₀ state. The wood's density is linearly proportional to the thickness of the cell wall (p.31 in Siau 1984 and 4.4.1 in Skaar 1988). The bonded water in the cell wall is roughly assumed of having the same density as the free water in lumen (the bonded water density doesn't change). Then, the saturated state of density and the fully oven-dry density would be a proportional relationship. In the following equation, the left part is the density in MC₀, and the right part is in MC_{sa}:

$$\frac{m_0}{V_0 + V_{Lu}} \approx \frac{m_0 + V_{CW}^w D_w + V_{Lu}^w D_w}{V_0 + V_{Lu}^w + \Delta V} \quad (9)$$

m is the mass; V is volume; D is density; 0 is the state at MC₀; w is water; Lu is lumen; CW is the cell wall. While D_w is equal to 1, and the lumen volume doesn't change. The equation is then listed as follows, and the frames are for the non-changed parameters in the following:

$$\frac{\boxed{m_0}}{\boxed{V_0 + V_{Lu}}} \approx \frac{\boxed{m_0} + \boxed{\Delta V} + V_{Lu}^w}{\boxed{V_0 + V_{Lu}} + \boxed{\Delta V}} \quad (10)$$

Accordingly, the $(m_0 + \Delta V)/(V_0 + V_{Lu} + \Delta V)$ is the fibre saturation density, and the $(V_{Lu}^w)/(V_0 + V_{Lu} + \Delta V)$ is the free water in lumen. The density is proportional to the thickness of the cell wall. Thus, the equation is linear and can be listed as follows:

$$D_{sa} = aD_0 + b \quad (11)$$

The linear relationship between density in saturated state and oven-dry state could examine the saturated situation for the experiment.

The MC values were calculated by their mass (g) (introduced in the next topic, (12)). Therefore, the FSP was calculated by the least-squared linear regression (Microsoft Excel 2019) with four testing points, from MC₀ to MC₁₈, by the length difference (l_{diff}) in R-dir., T-dir., and area ($R \times T \text{ mm}^2$) from the saturated state. The length or area change values were taken as the independent variables (x -axis), and the MC values (12) were their dependent variables (y -axis). Then, the intersection on the y -axis corresponds to an estimate of FSP (Fig. 35). Thus, FSP_R , FSP_T and FSP_{area} values were obtained.

Furthermore, the shrinkage coefficients and the total shrinkage were then calculated (III.B.2.a).

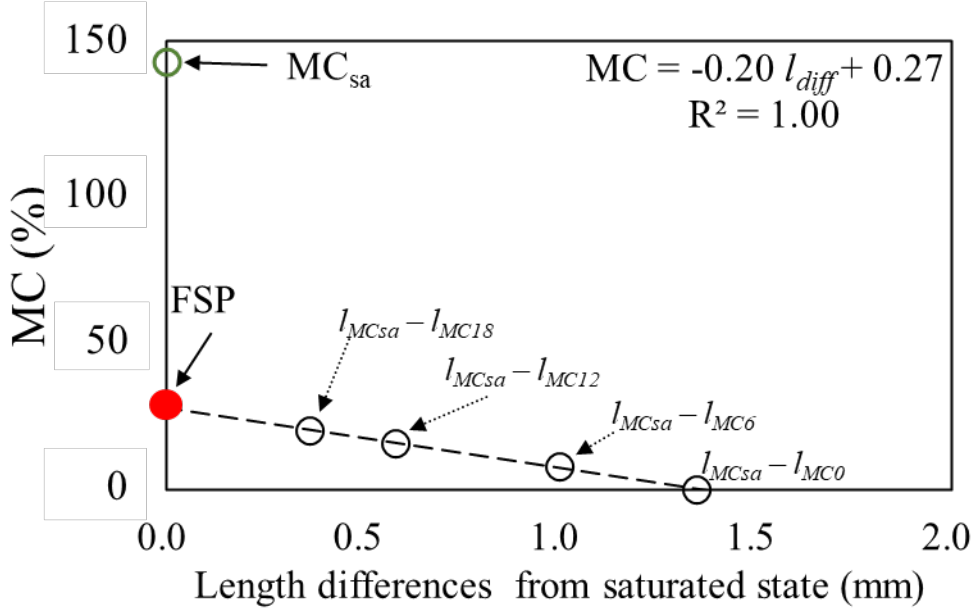


Fig. 35 The calculation of FSP by the intersection on the y-axis (solid red circle), taking the JuR-B1-b2_TR2 specimen's result (FSP = 27%) as an example.

III.B.2.a) Calculation of Shrinkage and FSP parameters

The MC at h measurement point is calculated as the difference of mass between step h and mass in oven-dry conditions m_0 divided by m_0 , where m_h represents the mass for the h measurement point:

$$MC_h (\%) = \frac{m_h - m_0}{m_0} \times 100 \quad (12)$$

Thus, according to the FSP estimated by the R and T dimensions and area changes as stated above, the estimated MC value (%) can then be used to estimate the mass of the whole wood sample at the FSP:

$$m_{FSP} = (MC_{FSP} + 1) \times m_0 \quad (13)$$

Furthermore, the density at FSP state is calculated, the l is the length in different directions:

$$D_{FSP} = \frac{m_{FSP}}{l_{sa}^T \times l_{sa}^R \times l_{12}^L} \quad (14)$$

The dimensional change in per cent is also studied for the hygro-mechanical behaviour. Let l_{MC1} and l_{MC2} be the lengths in MC condition 1 and 2, respectively, with $MC1 > MC2$. Since the experiment is carried out following a drying (shrinkage) schedule, l_{MC1} is larger than l_{MC2} .

$$\Delta_h^{(T,R)} (\%) = \frac{l_{MC1}^{(T,R)} - l_{MC2}^{(T,R)}}{l_0^{(T,R)}} \times 100 \quad (15)$$

According to the change in length for different MC states, the shrinkage/swelling coefficient α can be found:

$$\alpha_{\Delta h}^{(T,R)} = \frac{\Delta h^{(T,R)}}{\Delta MC} \quad (16)$$

In the present study, these shrinkage coefficients α are defined as positive for further calculations.

Lastly, the total shrinkage in the R direction (total radial shrinkage, TRS or Rs) and the T direction (total tangential shrinkage, TTS or Ts) are also calculated as follows:

$$\text{TTS or TRS (\%)} = \frac{l_{MC_{sa}}^{(T,R)} - l_{MC_0}^{(T,R)}}{l_{MC_0}^{(T,R)}} \times 100 \quad (17)$$

III.B.2.b) *The calculation for taking into account ring angle in the R-T plane*

The calculations above are for the R and T directions; however, several specimens are misoriented with the direction of their faces between the R and T directions (result is listed in Tab. 13). Thus, a re-orientation process was performed based on calculation.

The strain (ε) of 1 and 2 directions (measured) is listed as a matrix form:

$$[\varepsilon] = \begin{bmatrix} \varepsilon_1 & \gamma_{12}/2 \\ \gamma_{12}/2 & \varepsilon_2 \end{bmatrix}_{(1,2)} \quad (18)$$

A rotation matrix (R_θ) is thus:

$$R_\theta = \begin{bmatrix} \cos \theta & -\sin \theta \\ \sin \theta & \cos \theta \end{bmatrix} \quad (19)$$

As a result, the oriented (or wanted) values ε_R and ε_T can be acquired by the rotation according to equations (18) and (19):

$$[\varepsilon]_{(R,T)} = R_\theta^t [\varepsilon]_{(1,2)} R_\theta \quad (20)$$

In which, the R_θ^t is the transpose matrix of R_θ . According to the above process, the more detailed expression is:

$$[\varepsilon]_{(R,T)} = \begin{bmatrix} \cos^2 \theta \varepsilon_1 + \sin^2 \theta \varepsilon_2 + \cos \theta \sin \theta \gamma_{12} & -\cos \theta \sin \theta \varepsilon_1 + \sin \theta \cos \theta \varepsilon_2 + \frac{\gamma_{12}}{2} (\cos^2 \theta - \sin^2 \theta) \\ -\cos \theta \sin \theta \varepsilon_1 + \sin \theta \cos \theta \varepsilon_2 + \frac{\gamma_{12}}{2} (\cos^2 \theta - \sin^2 \theta) & -\sin^2 \theta \varepsilon_1 + \cos^2 \theta \varepsilon_2 - \cos \theta \sin \theta \gamma_{12} \end{bmatrix} \quad (21)$$

Then, the elastic and shear strain terms are:

$$\begin{cases} \varepsilon_R = \cos^2 \theta \varepsilon_1 + \sin^2 \theta \varepsilon_2 + \cos \theta \sin \theta \gamma_{12} \\ \varepsilon_T = -\varepsilon_2 \cos^2 \theta + \varepsilon_1 \sin^2 \theta - \cos \theta \sin \theta \gamma_{12} \\ 0 = \cos \theta \sin \theta (\varepsilon_2 - \varepsilon_1) + \frac{\gamma_{12}}{2} (\cos^2 \theta - \sin^2 \theta) \end{cases} \quad (22)$$

If the rotation angle is small, which fits the conditions:

$$\begin{cases} \cos \theta = 1 - \frac{\theta^2}{2} + 0(\theta^2) \\ \sin \theta = \theta + 0(\theta^2) \end{cases} \text{ and } \begin{cases} \cos^2 \theta = 1 - \theta^2 + 0(\theta^2) \\ \sin^2 \theta = \theta^2 + 0(\theta^2) \end{cases} \quad (23)$$

Then, ε_R and ε_T strains are now expressed as below, according to equations 22 and 23, where $\theta \ll 1$ and $\gamma_{12} \ll 1$:

$$\begin{cases} \varepsilon_R \sim (1 - \theta^2)\varepsilon_1 + \theta^2\varepsilon_2 \\ \varepsilon_T \sim -\theta^2\varepsilon_1 + (1 - \theta^2)\varepsilon_2 \end{cases} \quad (24)$$

Where the shear strain (below equation) is negligible under the condition that $\varepsilon_R - \varepsilon_T \ll 1$:

$$\gamma_{12} = \cos \theta \sin \theta (\varepsilon_R - \varepsilon_T) \quad (25)$$

Thus, the calculation of ε_R and ε_T from the measured strains (ε_1 and ε_2) can be now written as, in which $[I_2]$ is a 2×2 identity matrix:

$$\begin{bmatrix} \varepsilon_R \\ \varepsilon_T \end{bmatrix} \approx \left[[I_2] - \theta^2 \begin{bmatrix} 1 & -1 \\ 1 & 1 \end{bmatrix} \right] \begin{bmatrix} \varepsilon_1 \\ \varepsilon_2 \end{bmatrix} \quad (26)$$

III.C. *Vibrational Measurements*

III.C.1. *Natural Bending Vibration in Free-Free Mode: BING®*

III.C.1.a) *Principle*

The BING® system uses the spectral analysis of natural vibrations under the transversal bending mode or in longitudinal compression mode (Brancheriau and Bailleres 2002). The basic assumption of the measurement is that the specific modulus (E/γ) of material is proportional to the square of the wave velocity, constant, during the propagation in the material. The material is assumed homogeneous along the longitudinal axis.

III.C.1.b) *The BING® device and software*

The system includes the BING® software (version 9.6), a microphone and an acquisition data logger (PicoScope 4224). The specimens were placed on two rubber bands to approximate the free-free vibration condition. The position of the rubber bands corresponds to that of the vibration nodes of the first bending mode, i.e., 0.224 the length of the sample from its edge. The setup of the signal processing for the original beam specimens in bending is 40,000 Hz for the sampling frequency and 32,768 points for the spectral acquisition.

Furthermore, the link between the elastic behaviour and the vibration frequencies can be made using two different theories, i.e., Bernoulli (without shear) and Timoshenko (taking shear into account), so that the shear modulus along the cross-section can also be estimated during the test. Therefore, it is required to test the samples in two directions, by rotating them on the rubber bands, to obtain G_{RL} and G_{TL} values, by hitting in the direction of R (hitting on LT plane) and in the direction of T (LR plane), respectively.

III.C.1.c) *The process for the test: multi-dimensions and multi-conditions*

The experiment was conducted with the original size (board) of the specimen and (smaller) rectangular beams too, from the non-regulated room temperature (MC is supposed to be about 10 to 12%, III.C.1.d)) to controlled and stable 20 ± 2 °C and 65 ± 5 % RH (later expressed as 20-65, or, “standard air-dry” condition), the detailed diagram of the experiments is listed in Fig. 36. The main type of test was in bending mode. The hitting direction was R and T except for the material in the original dimensions (planks). Because the original materials were mostly in flat-sawn, the notation would still be used as R and T. The hitting position on the specimens was in the middle (width) at the end of one side, longitudinally; on the other side, longitudinally, the probe (microphone) was also in the middle (width) to receive the sounds emitted after hitting (Fig. 37b). The weight of each beam was measured before the measurement on the same day.

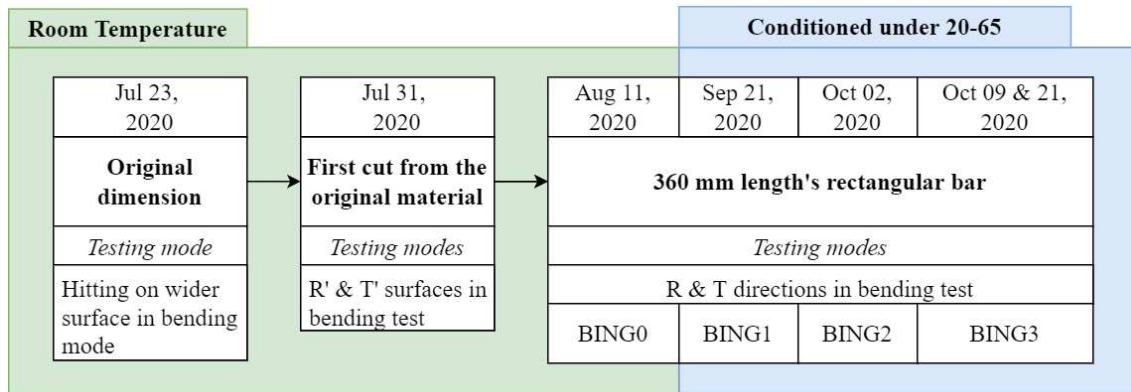


Fig. 36 The diagram of BING experiments under different dimensions and conditions, with the date of the tests.

Two wooden sawhorses and two 8 mm rubber bands were adopted for simulating a free-free boundary condition (Fig. 37a) for oversized materials. The setup was as follows: two wooden bars were placed on two sawhorses, and the elastic wires were hung from the bars to support the beams under test so that the position of these flexible wires could be changed freely.

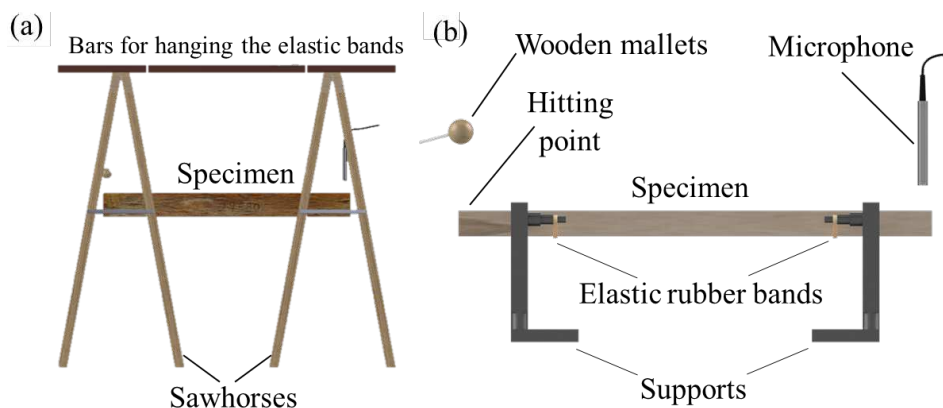


Fig. 37 The schematic of the BING experiment in bending mode. The hit is on one end, and the receiver (microphone) is on the other end. The supports made of elastic wires were chosen depending on the specimen's dimension and weight. For (a), the test for the original specimen dimension, two sawhorses were used to support two wooden bars to hang the specimen on with elastic wires; for (b), the standard test for the smaller dimension bars.

III.C.1.d) *Samples preparation for the BING test: cutting dimension and conditioning*

The boards have been well seasoned at room temperature for a very long period (many years) in the storage room of CIRAD carpentry, Montpellier, which is shaded, cool, and well ventilated. Therefore, the word used hereafter to describe the room temperature corresponds to the condition in which the samples were tested without conditioning, contrary to 20°C – 65 %HR, but in equilibrium with the ambient environment. The actual MC in the materials was unknown since stabilising such a large dimension would be impossible in just a few months. Also, local humidity and temperature records on the testing day were not reliable for estimating the moisture

content of materials in such large samples. For this reason, broader range values of nominal EMC for wood (ASTM D4933-99 2014) were thus referenced according to the meteorology records in Montpellier. From January to August 2020, the EMC was calculated between 10.3 % and 16% using the standard chart from the ASTM standard. From May to August (28th) 2020, it was around 10.29 % and 12.66 %. These reference values were calculated from the average value of the different months considered (data acquired on August 29th, 2020, <https://www.historique-meteo.net>)

The weight of the specimens in their original dimensions was measured with Sartorius IC34000P, which has a maximum capacity of 8 kg and a readout of 0.1 g. After the test in the original dimension at room temperature, all the specimens from CIRAD with interlocked grain were cut with a table saw. The cuts were made in widths of 3.5 or 7 cm depending on the materials state to avoid defects or allow for reorientation. The cutting procedure for the specimens obtained from the commercial suppliers doesn't consider reorientation or defects. It followed the preference from the high-end market, based on customer satisfaction, i.e., by emphasising the figure. As a result, the specimens were cut into the same length in this process. Compared with the original board, these specimens in smaller dimensions were also tested by the BING method at room temperature.

Therefore, the processing of reorientation and cutting into the final dimension was done after the first BING measurement. The specimens were cut and planed into the "standard beam shape". Their dimensions and noting method have been described in the previous section (§III.A.2). Thus, the mark of R and T will describe the directions relatively close to the theoretical definition of radial and tangential directions, respectively. The total produced was 119 beams ("standard bars").

All the standard beams/bars were first tested at room temperature (BING0). Then, they were stabilized in the 20-65 climatic room. Whether the samples MC are stabilised is defined that the ratio of the weight change (in g) to the averaged weight (115.08 g) must be less than 0.008% (read-out and repeatability of the scale). Their weight was monitored in the form of a measurement every 3 or 4 days, with a Precisa LS3200C scale, whose maximum capacity is 3200 g, the readout is 0.01 g, and reproducibility is 0.01 g. If the average variation of all standard beams is less than 0.008% twice, then they are all considered completely stabilised. Consequently, the standard beams were thus assumed to be stabilized, as far as MC is concerned, on 2020 Sep 04th (starting from 2020 Aug 11th, 25 days in total).

III.C.2. *Non-contact Forced Bending Vibration in Free-Free Mode: Vybris*

The resonant response, based on forced vibrations, is another method for measurement of the mechanical properties. It has the advantage of working on a given mode of vibration, i.e., there is little effect of signal processing (that would be needed when observing multiple modes simultaneously), therefore the measurement is more a “mechanical” one than an “acoustical” one. When used in the “non-contact free-free” mode, the uncertainties due to boundary conditions are also much limited. This type of measurement provides more reliable characterisation of the viscoelastic part, here the damping coefficient. Practically, the employed devices are designed to work on small-scale specimens, therefore also allowing a more direct comparison between measured properties, and the local structural variations (GA and MFA) that were measured in the previous chapter (Chapter II).

In this work, two different set-ups, providing two sets of mechanical properties, were used.

The first one is the Vybris device intended for testing bending vibrations, an experimental set-up developed in LMGC, Montpellier, based on a long-established principle, but optimised regarding the speed and reproducibility of experiments. The “classical” Vybris in bending provides measurements of the dynamic specific modulus of elasticity (E/γ), and of the damping coefficient $\tan\delta$, usually in L direction (also in R direction with different specimens, but that was not usable with the present material)

The other device is a new development, made during this thesis on the basis on earlier literature, called Vybris-Torsion. It allows the measurement of the material shear moduli G_{TL} or G_{RL} with the associated damping $\tan\delta_G$.

III.C.2.a) *Principle*

The specimen is set into vibration following a frequency sweep, and its response (here, displacement) is measured over the ramp in frequency. In the “non-contact forced vibrations of a free-free beam” principle (Fukada 1950; Obataya et al. 2000), the specimen is simply supported by thin threads at the non-vibrating points (nodes of vibration of the considered mode), and the frequency sweep is imposed by an electro-magnet facing a thin iron plate glued on one-end of the specimen.

The frequency of a vibration mode is used to calculate the mechanical properties corresponding to that mode. The system can measure two parameters: one is the resonant frequency, and the other is the damping properties. In the Vybris device, damping can be

measured, successively, through two methods, i.e., quality factor (Q^{-1}) by the bandwidth at half-power of the curve (-3 dB) of the resonant peak (in the frequency-domain); and (in the time-domain) by analysing the envelope of the decreasing displacement amplitude, also called “logarithmic decrement” (λ). The damping coefficient ($\tan\delta$) obtained by both methods (frequency- and time- domains) are theoretically equal in the range of values expectable for wood-material ($\tan\delta \approx Q^{-1} \approx \lambda/\pi$). The longitudinal specific dynamic modulus of elasticity (E'/γ) is calculated from Euler-Bernoulli’s bending equation (27), which implies that the effect of the in-plane shear modulus can be neglected. For the first bending mode, this condition (negligible effect of shear) is respected for a slenderness ratio (length/thickness of the specimen) > 50 (effect of shear $< 1\%$ over all wood types), and is therefore indeed negligible for the slenderness ratio of 75 of the studied specimens (Brémaud et al. 2012; Brémaud 2016).

$$\frac{E'}{\gamma_{12}} = \frac{48\pi^2 l^4 f_b^2}{m_1^4 t^2} \quad (27)$$

E' : storage longitudinal Young’s modulus (kPa); γ : specific gravity (here in 20-65 condition) (unitless); l : the length of the specimen (m); f_b : resonant frequency of first bending mode (Hz); m_1 : Euler-Bernoulli’s constant of the first bending mode (unitless); t : the thickness of the specimen (m).

III.C.2.b) *Preparation of specimens*

The specimens were taken along the section of the standard beam-bar specimens (V_{L-LR} and V_{L-LT} in Fig. 38), and two pairs were prepared, one pair in the LT (flat-cut) plane and one pair in the LR (quarter-cut) plane (Fig. 38). The cutting was done using a table saw (Proxxon No. 27070) with a width of 12.5 mm, a thickness of 2 mm, and the length was homogenized between all specimens. Additionally, the edges were sanded with a sanding sponge (P2000-P1800) to remove the splinters (or fibre fuzzies). After the above preparation, the specimens were conditioned in the 20-65 condition (HP260, Memmert climate chamber) for 21 days to stabilize the damping, which takes longer time to be stabilised than EMC does (Brémaud and Gril 2021a). Then, their dimensions were measured after two weeks. The width (CD-15AX, Mitutoyo) and thickness (547-401, Mitutoyo) were measured in three positions along the specimen, corresponding to the two vibration nodes at the first bending mode (0.224L from the edge), and the centre of the specimens. The length was measured in the middle of the width. Their weights were measured two times with a digital scale (ME204, Mettler Toledo) to verify the stabilisation condition: one was two weeks after stabilisation, and the other was after three weeks.

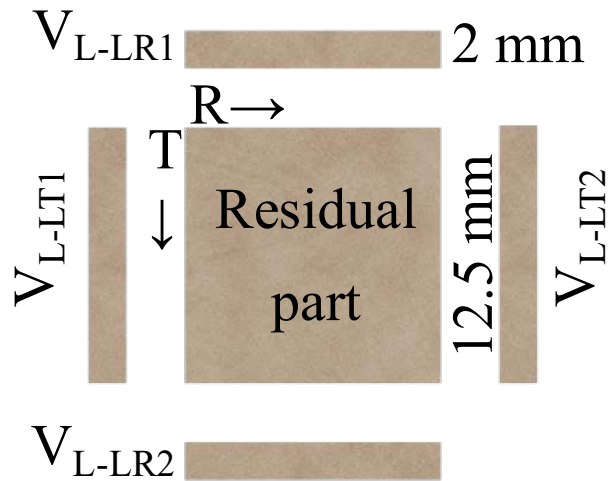


Fig. 38 The cross-section of the “standard beams/bars” showing the subsequent cutting for four Vybris specimens, two in each of the two planes L-R (quarter-sawn) and L-T (flat-sawn).

III.C.2.c) *The Vybris device*

Based on the well-documented general principle introduced above, the present study used the experimental device/system, Vybris, developed in LMGC-CNRS, Montpellier, described in Brémaud (2006) and Brémaud et al. (2012). Compared to the general principle of measurement, the main features of the Vybris device is to include a home-built hardware (electronics) and software (user-interface) that allow very rapid (< 1 minute per test) yet precise (error < 2%) measurements.

The testing condition was close to a free-free boundary one with the device set-up in Fig. 39. Two thin sewing threads hang the samples on their vibration nodes of the first bending mode. The magnetic actuator/exciter was then gently placed to put the sample in vibration. For this purpose, a steel plate of dimensions $12.7 (l) \times 0.05 (t) \times 1\sim 1.5 (w) \text{ mm}^3$ (h+s Präzisions-Folien GmbH) is glued to one of the longitudinal edges of the sample using adhesive (Super Glue Mini Trio, Loctite). The weight of this plate is measured for each specimen, it is about 0.5 % of that of the sample (on average), and its influence is taken into account when calculating the specific dynamic modulus (Brémaud et al. 2012).

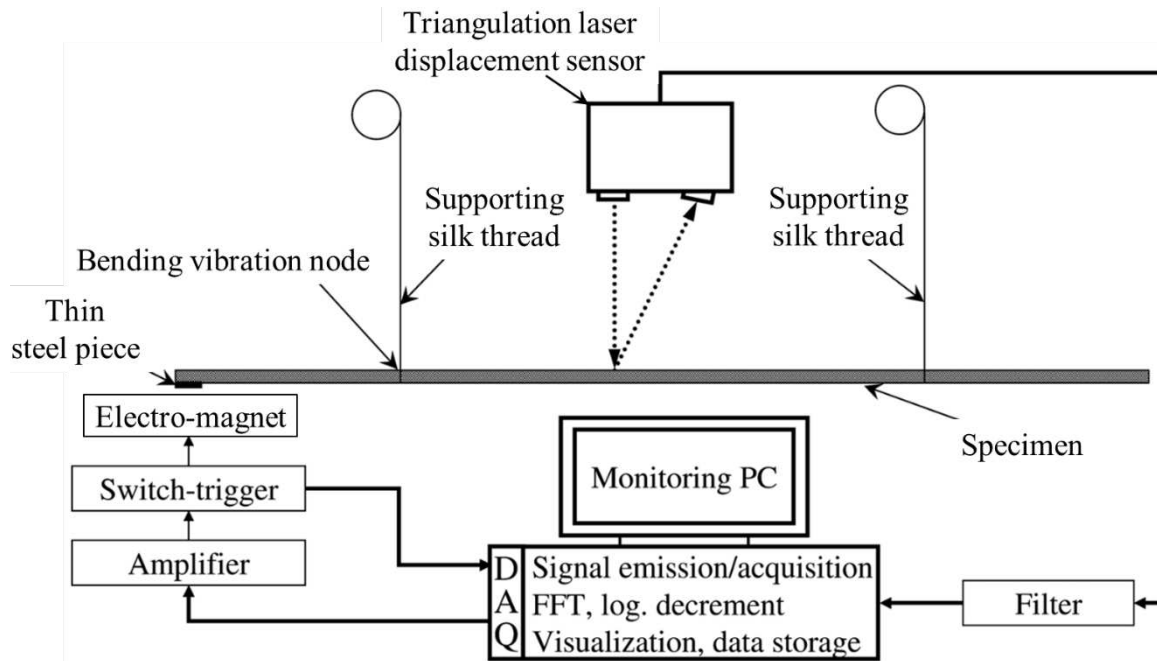


Fig. 39 Diagram of Vybris device for the resonant bending frequency measurement. Figure adapted from Fig 1 in Brémaud (2012).

The main potential sources of error for this principle of experiment have been evaluated, notably in the Japanese scientific literature, over the past decades. The main factors to take into account, and identification of some additional factors, have been shortly reviewed (Brémaud 2006; Brémaud et al. 2012; Brémaud and Gril 2021a). Altogether, the method is very robust, and can accept some minor variations in the specimen positioning without losing its accuracy.

However, in the present study, additional precaution was taken. In order to minimize the effect of gravity or unbalanced tension force caused by the threads, the platform was adjusted with an electronic spirit level (Version 1.0.1, MobileTools, Makita). Furthermore, a circular steel wire was placed on the threads, with three marks: two at the position of the nodes and one at the position of the laser point (Fig. 40). Once the horizontal positions have been set, the length of the wires is adjusted by placing a wood dummy sample to check that the laser is focused on the sample surface. Then, the steel wire is used again to check the different horizontal distances. Thus, after the spirit level and tilt level of threads (with sample) were set, the magnetic block was then placed carefully in regard of the sample. This procedure was also used to check whether the relative positioning of the specimens would cause any “parasite” oscillating.

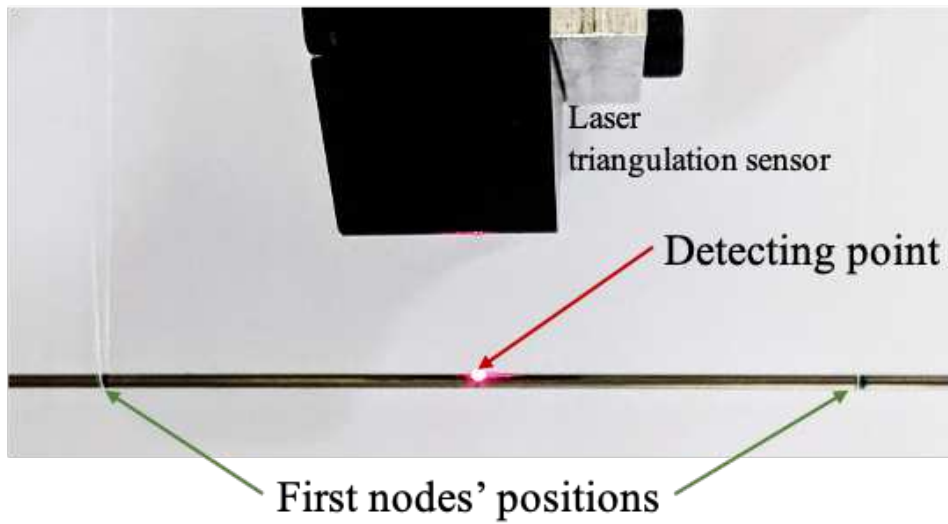


Fig. 40 A circular steel wire in place of the wood sample was placed on the threads to verify the vertical adjustment of the system and the detecting position of the laser and its focus.

III.C.3. *Forced Vibration in Shear: Developing Vybris-Torsion*

III.C.3.a) *Principle*

Regarding orthotropic material, wood, its mechanical properties have been discussed majorly on its longitudinal direction. Herein, the longitudinal Young's modulus and associated damping property are mainly concerned, and the in-plane shear properties are comparatively less highlighted, especially so for shear damping. However, the shear properties are an essential mechanical factor for several domains of wood behaviour and application. Regarding the "sound quality" of wood, it was proved that the G_{LT} modulus plays a critical role in the soundboard of string instruments (Viala et al. 2018). Also, E_L/G_{LT} and $\tan\delta_G/\tan\delta_L$ high ratio are considered to generate a low-pass filter to suppress high-frequency noises, making the sound of wood distinguishable from other materials (Nozaki et al. 1988).

It is known that the mechanical properties of a material can be deduced from the natural or resonance frequencies of an object of known dimensions made from that material. Well-known beam theories, e.g., Euler-Bernoulli or Timoshenko, were adopted widely for static or dynamic bending. Timoshenko's approach can calculate more complex situations, including rotational inertia or transverse shear (Huang 1961). Compared with it, Euler-Bernoulli's beam theory could still give a reasonable result for low vibration modes and samples having a relatively high slenderness ratio (Dudek 1970; Chui and Smith 1990; Brancheriau and Bailleres 2002).

The torsion measurement was widely adopted, and it included several aspects of the properties measurement, including shear moduli, torsional damping, or failure (Hearmon and Barkas 1941; Morihiro and Mori 1973; Ono 1980; Obataya et al. 2000; Yang et al. 2013; Yoshihara and Maruta 2018). The torsional vibration is a semi free-clamped mode within the different torsion tests. The axis is assumed to remain the same during the rotation from the original (initial) position to the maximum torsion angle if the twist angle is small enough. Also, the unit rotation angle amplitude along the longitudinal direction is homogeneous (Fig. 41). These assumptions are applied in the present study since they are easily achieved with the current forced vibration system (III.C.2) with most existing components.

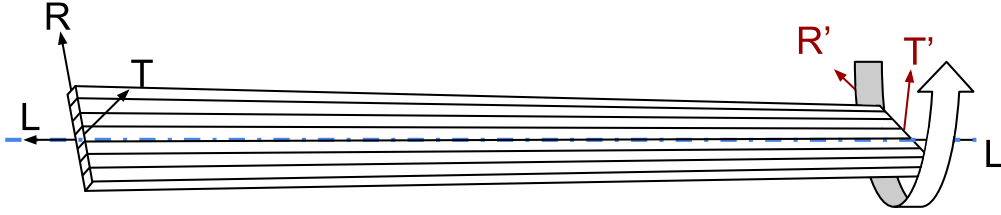


Fig. 41 The diagram of the dynamic torsional rotation in the present study for measuring, for example, G_{RL} . The two ends are clamped.

III.C.3.b) Equations

Under the cantilever beam with an end mass boundary condition, the relationship between the resonant frequencies with bending (28) and torsion (29) movements could be analytically written (isotropic and homogeneous material) (equation 3c for bending and 8c for torsion in Table 16.1 in Young and Budynas (2002)):

$$f_b = \frac{1.732}{2\pi} \sqrt{\frac{EI^B g}{Ml^3 + 0.236ml^4}} \quad (28)$$

$$f_t \approx \frac{1}{2\pi} \sqrt{\frac{Cwt^3 G}{3(I_m + I_s/3)S}} \quad (29)$$

or if we want to have the longitudinal elastic and shear moduli from the above equations (28) and (29), the equation is modified as below (30) (31):

$$E = \frac{4\pi^2 f_b^2 l^3}{3I^B} (M + 0.236ml) \quad (30)$$

where f_b is the resonant frequency (Hz) of the first bending mode; I^B is the second moment of area (m^4); l is the beam length (m); M is the end mass (kg); m is the sample mass (kg).

$$G \approx \frac{12\pi^2 S f_t^2 (I_m + I_s/3)}{Cwt^3} \quad (31)$$

where f_t is the resonant frequency (Hz) of the first torsional mode; C is a shape factor (dimensionless) for rectangular prismatic beam (including the correction for warping); w is the sample width (m); t is the sample thickness (m) (while $w > t$); S is the span (m) corresponding to the length of the non-clamped part of the sample; I_m is the mass moment of inertia (rotational inertia, $kg \cdot m^2$) for the end mass, including the bottom clamp and sample part clamped in it; I_s : the mass moment of inertia ($kg \cdot m^2$) of the free part of the sample between the clamps. Herein,

in some researches, $J \approx Cwt^3/3$ is the moment of inertia of the cross-section of the sample, or C would be noted as $\beta/3$ or $k_2/3$, e.g., III.2.3 in Vincent (2006).

Anyhow, the discussion will proceed to the relationship of torsion movement at this moment.

According to the shear modulus and resonant frequency, equation (31) can be written more precisely, including the small section of the clamped sample and the detail part's notation:

$$G'_{wL} \approx \frac{S\pi^2 f_t^2}{Cwt^3} [12I_m(t) + \rho_s tw(w^2 + t^2)(s + S/3)] \quad (32)$$

With G' the storage shear modulus (MPa); S the span between the clamps (m); $I_m(t)$ the mass moment of inertia of the bottom clamp ($\text{kg}\cdot\text{m}^2$) (33); s is sample section clamped in the bottom clamp (m) (Fig. 42):

$$I_m(t) = 0.5m_c \left[\frac{(w_c^2 + t_c^2)}{12} + \left(\frac{t_c^2}{2} + \frac{t_s^2}{2} \right) \right] \quad (33)$$

The subscripts for w and t are added with c and s temporarily in equation (33) to distinguish clearly the thickness and width of the bottom clamp (t_c and w_c , respectively) and sample's (t_s and w_s , respectively).

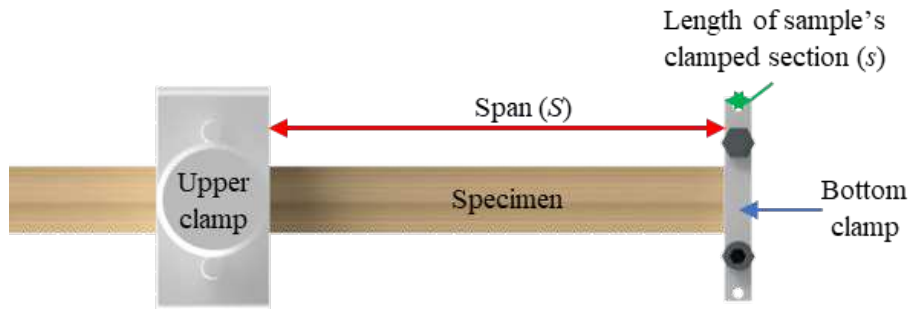


Fig. 42 The diagram for the span S between the bottom and upper clamp and s the length of the sample in the bottom clamp.

The constant C has several forms depending on different approximations. The full equation is the summation of a hyperbolic-tangent function, see equation (34) (Equation 2 in Nederveen and van der Wal 1967). In different references, simplified approaches were made to reduce the calculation, e.g., with a constant number as in equation (35) (Semenov 1966; Ono 1980), or a hyperbolic function (page 401, Young and Budynas 2002), or a simplified hyperbolic-tangent function as in equation (36) (1.99, p.152, Kohlrausch 1996). In the listed equations, u equals w/t , and the comparison between the different approximated C values and the full values is listed in Tab. 11.

$$C_{\tanh} = 1 - \frac{192}{\pi^5} \frac{1}{u} \sum_{n=0}^{\infty} \frac{\tanh\left[(2n+1)\frac{\pi}{2} \cdot u\right]}{(2n+1)^5} \quad (34)$$

$$C_{\text{Semenov}} = 1 - 0.63/u \text{ and } C_{\text{Ono}} = 1 - 0.6302/u \quad (35)$$

$$C_{\text{Physik}} = 1 - \frac{192}{\pi^5} \frac{1}{u} \tanh\left(\frac{\pi}{2} u\right) \quad (36)$$

Compared with the results given by the original full equation (34), the single coefficient estimations (35) show a larger error when u ratio is small, while C_{Physik} (36) gives a better result.

Tab. 11 The comparison of different approximated C values with C_{\tanh} of equation (34) for different u ratios and the error (%).

t	w	u (w/t)	C_{\tanh}	C_{Semenov} (%)	C_{Ono} (%)	C_{Physik} (%)
1.00	10	10.00	0.937	0.937 (0.03)	0.937 (0.03)	0.937 (0.00)
1.25	10	8.00	0.922	0.921 (0.04)	0.921 (0.04)	0.922 (0.00)
2.00	10	5.00	0.875	0.874 (0.06)	0.874 (0.06)	0.875 (0.00)
2.50	10	4.00	0.843	0.843 (0.08)	0.842 (0.08)	0.843 (0.00)
3.00	10	3.33	0.812	0.811 (0.10)	0.811 (0.10)	0.812 (0.00)
3.50	10	2.86	0.780	0.780 (0.12)	0.779 (0.13)	0.780 (0.00)
4.00	10	2.50	0.749	0.748 (0.16)	0.748 (0.17)	0.749 (0.00)
5.00	10	2.00	0.687	0.685 (0.36)	0.685 (0.37)	0.687 (0.00)
7.00	10	1.43	0.571	0.559 (2.03)	0.559 (2.05)	0.571 (0.00)
8.00	10	1.25	0.517	0.496 (4.15)	0.496 (4.18)	0.517 (0.00)
9.00	10	1.11	0.469	0.433 (7.62)	0.433 (7.66)	0.469 (0.00)
9.90	10	1.01	0.429	0.376 (12.24)	0.376 (12.29)	0.429 (0.00)

As wood is taken as an orthotropic material, two axial shear moduli in the width plane and thickness plane are anticipated to play in the torsion response. It should be noted that the shear moduli for the wider face (w) are G_{wL} , and G_{tL} for the narrow face (t). The ratio of G_{tL} and G_{wL} is noted G_a , $G_a = G_{tL}/G_{wL}$. Therefore, equation (36) could be rewritten as follows:

$$C'_{\text{Physik}} = 1 - \frac{192}{\pi^5} \frac{1}{u\sqrt{G_a}} \tanh\left(\frac{\pi}{2} u\sqrt{G_a}\right) \quad (37)$$

The torsion test cannot measure one shear moduli. Two shear moduli are then involved during the test. However, it is also clear that for a large u ratio, the effect of anisotropic shear moduli is less concerned, i.e., one of the shear moduli has a predominant effect. The shear moduli ratio can be estimated with the already known values to know the relative contributions. The databases from 3 resources (Nakai 1985; Guitard and El Amri 1987; Ross 2010) were then used

to acquire the shear moduli ratio (G_{LR}/G_{LT}) range. It is from 0.75 (*Picea sp.*) to 2.62 (*Picea sp.*) for softwood. For hardwood, it is from 1.06 (*Humbertia madagascariensis* Lam.) to 2.00 (*Cavanillesia platanifolia* (Bonpl.) Kunth). All the extreme values are from data collected by Guitard (1987). Referencing Nakai's data (1985), the smaller ratio for tropical wood is around 0.65 (*Anthocephalus cadamba* (Roxb.) Miq. and *Pterocymbium beccarii* K.Schum.), and the larger ratio is approximately 1.31 (*Ailanthus sp.* and *Aquilaria malaccensis* Lam.).

If u ratio is taken from 1.01 to 10 and the range of G_a from 1 to 3, then we can compare the effect of taking them into account through the ratio $((C_{\text{Physik}}/C'_{\text{Physik}} - 1) \times 100\%)$ (Fig. 43).

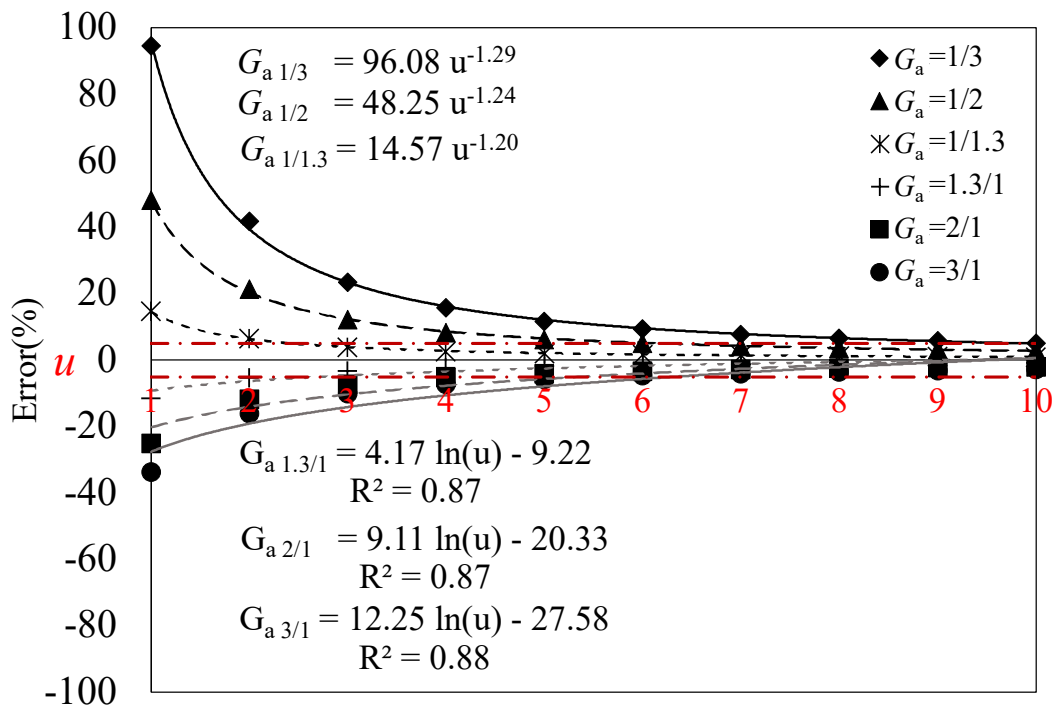


Fig. 43 The comparison between considering anisotropic shear moduli involved in the calculation and without considering it with $G_a = G_{tL}/G_{wL}$. The red dashed lines are the $\pm 5\%$ indicator lines. The x -axis is u ratio from 1.001, 2, 3, ...8, 9, 10 (from left to right). The black regression lines are for $G_a < 1$ ($R^2 = 1.00$), and the grey regression lines are for $G_a > 1$ (R^2 is on the plot).

It shows that if the criteria for the error is less than $\pm 5\%$, for G_a between 1/1.3 and 2, u must be greater than around 5 and, for G_a between 1/1.3 and 3, u must be greater than around 6. It is also clear that neglecting the shear moduli anisotropic effect could be achieved for large u . However, according to the experiment design (III.C.2.b) and Fig. 38), u is always greater than 6, and the error effect could probably be neglected.

III.C.3.c) *Maximum rotation angle*

Also, the rotation angle is restricted to control the material deformation because the torsion will cause the material warping, and warping will cause several stresses, e.g., normal stress, in-plane bending, shear. Thus, the larger angle rotation would combine more unwanted stress, causing the shear modulus measurement to be over-estimated (larger than actual).

According to the ISO 6721-2 (2019) for the torsional vibration test (at low frequency) of plastic samples, that the dimension is $50 \times 10 \times 1 \text{ mm}^3$, for the rigid (vitreous) plastic, the maximum rotation angle is 1.5° , and for the soft (rubber) plastic is 3° . While the calculation of γ_{max} from equation III.18 in Vincent (2006) is:

$$\gamma_{max} = \left(\frac{t}{w}\right) C_{Physik} (3w + 1.8t) \frac{\theta_{max}}{l} \quad (38)$$

Thus, according to the suggested angle and dimension from ISO 6721-2 (2019), the γ_{max} is then around 0.052% (1.5°). According to the dimension in the present study, and the consideration of shear anisotropy, the equation based on θ_{max} is listed as:

$$\theta_{max} = \frac{\gamma_{max} l}{(3a + 1.8b) C_{Physik}} u \quad (39)$$

Consequently, we can have the maximum rotation angle to limit unwanted warping effects. The consideration of shear anisotropy (Fig. 43) is also considered. The same G_a values are used to calculate the maximum rotation angle ($w = 12 \text{ mm}$ and $t = 2 \text{ mm}$). The maximum angle according to the span is then acquired (in degree):

$$\theta_{max} = 0.0288S, u = 6 \quad (40)$$

Then, the maximum amplitude of the bottom clamp rotation (μm) can be seen as the following equation (41) and the figure for the amplitude's diagram (Fig. 44):

$$Amp_{max} = \tan \left[\tan^{-1} \left(\frac{t_c + t_s/2}{l_c/2 - d} \right) + \left(\frac{\theta_{max}}{2} \right) \right] (l_c/2 - d) - (t_c + t_s/2) \times 10^{-3} \quad (41)$$

Lastly, the maximum amplitude according to the bottom clamp used in the study ($l_c = 36 \text{ mm}$, $d = 1 \text{ mm}$, $t_c = 3 \text{ mm}$, in III.C.3.d), Amp_{max} is acquired according to the span while $w_s = 12 \text{ mm}$ and $t_s = 2 \text{ mm}$:

$$Amp_{max} = (4.315S - 1.532) \times 10^{-3} \quad (42)$$

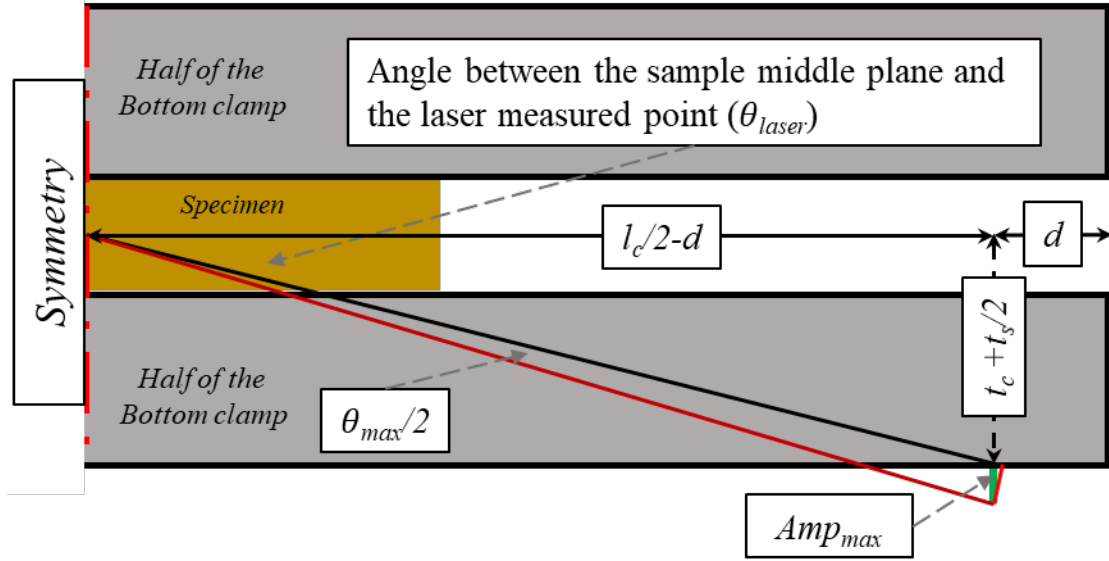


Fig. 44 The detection of the maximum amplitude (green line). The diagram is the half of the cross-section for the bottom clamp (grey) and the specimen (brown).

III.C.3.d) *Design of the device's hardware*

The ratio between E and G moduli is also essential for the study. Moreover, the dynamic properties of wood depend on the loading frequency (Caracciolo and Giovagnoni 1996; Ouis 2002). Thus, the frequency in torsion should be comparable with the bending condition (30) (III.C.3.b). As the equation (43) shows, parameters that could control the frequency are s (width of the clamp) and $I_m(t)$ while assuming the span and sample dimensions are fixed (the framed parameters mean non-considered nor changed in the current consideration):

$$\boxed{G'_{wL}} \approx \frac{\boxed{S} \boxed{f_t^2} \boxed{\pi^2}}{\boxed{Cwt^3}} \left[12I_m(t) - \boxed{wt\rho_s(w^2 + t^2)}(s + \boxed{4S}) \right] \quad (43)$$

While $s \propto f_t^2$ and $I_m(t) \propto 1/f_t^2$ mean the small cross-section of the sample, less mass, and larger s lead to a higher f_t^2 . However, diminishing $I_m(t)$ is the most effective considering the two parameters: s and $I_m(t)$. Several limitations need to be considered here: a) the thickness of the metal part forming the bottom clamp must resist during screwing, b) the minimum length of the metal part must allow the widest specimens (up to 15 mm width) to be clamped, and c) the minimum diameter of the screw allowing a good tightening and without breaking.

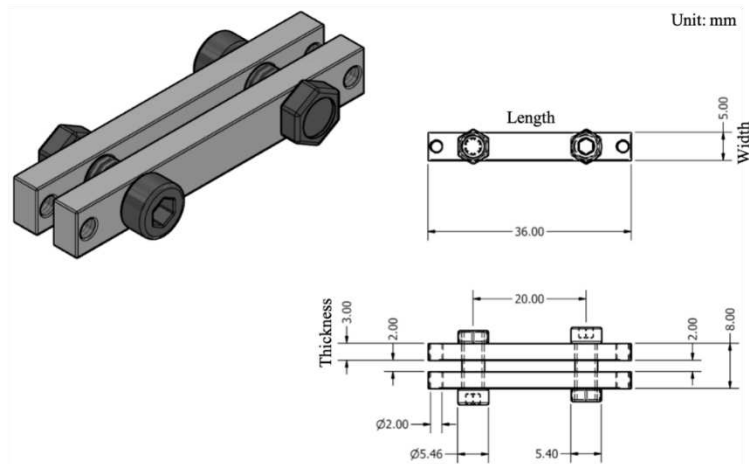


Fig. 45 The drafting for the bottom clamp geometry and size for forced torsion device. It was made by the Autodesk Fusion 360 and Autodesk Inventor.

Theoretically, the torsion test is a cantilever beam system with an end mass. In the real circumstance, the two ends of specimens are clamped (fixed condition). The consequence is that the variation along the width of the longitudinal deformation is restricted regionally (two ends). The “clamping effect”, or gripping effect, has been mentioned for the torsion test (Nederveen and van der Wal 1967; Nederveen and Tilstra 1971; Janowiak and Pellerin 1992). The in-plane (cross-section) shear and normal axial deformations are restricted, causing the measured shear modulus could be higher than the actual. The solution is a limited rotation angle (III.C.3.c) and a longer span (demonstrated later in III.C.3.e).

Furthermore, several unwanted instrumental factors are also indicated as enhancing the clamping effect. It concerns the width of the clamp to specimen thickness, of which $w_c > 2t$ would make that the correlation due to the length was independent to w_t (Nederveen and Tilstra 1971). Accordingly, s was set to 5 mm, while 5 mm is two times more than 1.96 mm (specimen’s thickness).

The bottom’s mass moment of inertia was simulated in Autodesk Inventor with different materials for the different parts of the clamp. The chosen material for the clamp must be relatively long-lasting considering the risk of oxidization, low density of clamp (to diminish $I_m(t)$), and stiff enough to maintain the geometry during screwing. Thus, an aluminium alloy was chosen. The screws and nuts are steel for their magnetic property (due to the magnetic triggering method). Eventually, there were seven sets of bottom clamps made by technician Genevois Gille, LMGC. The mass of a set is 5.0125 g (stdev= 0.0014 g). The measured value was then set to adjust the mass of the CAD file in Inventor by changing the density value till the difference is 0%. Then, because the thickness of the different samples is not the same, this changes the

distance between the pieces of the bottom clamp and thus $I_m(t)$. Using CAD and linear regression, the mass moment of inertia depending on the sample thickness ($\text{kg}\cdot\text{m}^2$) (44) was built:

$$I_m(t) = (1.2531 \times 10^{-9})t^2 + (6.5196 \times 10^{-9})t + (5.55486 \times 10^{-7}) \quad (44)$$

III.C.3.e) *Theoretical validation: Preliminary methodological test and Finite elements modelling*

A preliminary test was conducted with an isotropic material to verify the compatibility between the measurement and analytical result without shear anisotropy. A piece of PS polymer material was adopted for the purpose. Its density is 1.04 g/cm^3 , and the Poisson's ratio (ν) is 0.35 source: <https://www.polymerdatabase.com> and Mott et al. 2008). The dimension was trimmed to $15 \times 1.27 \times 150 \text{ mm}^3$.

Thus, a cross-verification was made. The first approach was from E and ν to acquire G ($G = E/2(1+\nu)$), and the other was with the current developed torsion device. The free-free bending vibration test (III.C.2.c) was used from the first one, and E is 3.25 GPa; thus, G is 1.20 GPa. After that, the shear modulus was then measured with the current developed device, which is 1.2 GPa. The two results were the same, which proved that the device was workable.

The other verification was done using finite element modelling (FEM) (ANSYS 2021 R1) to compare the above-mentioned experimental result. The model boundary conditions were: a) sample in the upper clamp was modelled as a rigid body, b) the bottom clamp was simplified without involving screws and nuts, c) all the contact surfaces were perfectly bonded, d) the position of the upper clamps was fixed. The discretization was done using the quadratic 3D element with 0.4 mm minimum side length, and the simulation environment was the modal mode for acquiring the resonant frequency. In the first bending mode (cantilever beam with an end mass (30) and torsion mode, the first resonant frequencies (bending and torsion) were compared for several span distances (Fig. 46). The maximum differences in bending and torsion frequencies between the experimental and FE simulation were less than 5 %. The FEM model was then used for further examination.

Another demonstration was done by using the wood elastic properties from Guitard and El Amri (1987) (§III.D.1) to see the span effect on the shear moduli (G_{RL} and G_{TL}) measurement (Fig. 47). The simulation results in Fig. 47 shows that the higher density wood is more sensitive to the span change, and the lower density wood is less affected due to the span change. The y -

axis is the square resonant frequency because it can represent the affected result (shear modulus) directly according to equation (32).

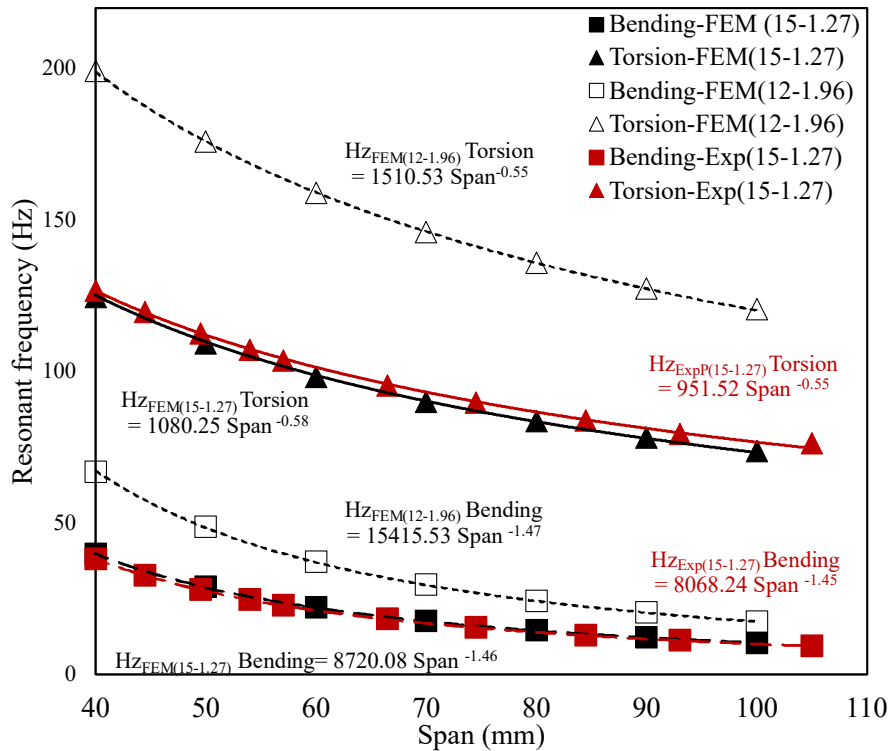


Fig. 46 The comparison between experimental results and simulation by FEM for different span settings. Two types of section are tested, $w/t = 15/1.27$ and $w/t = 12/1.96$. The filled red symbols are the experimental result, and the black filled symbols are the FEM results for the same w/t ratio, and the hollow symbols are for another w/t ratio.

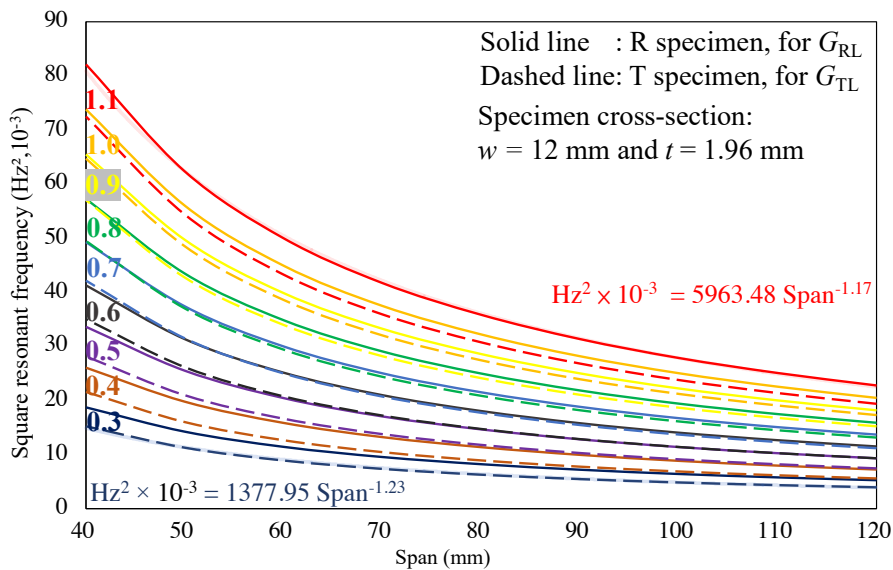


Fig. 47 The demonstration of the influence of span for different simulated wood in different densities (Guitard's hardwood) to the torsion test result (f_t^2 , y-axis). Different densities are in different colours.

III.D. Ultrasonic tests

III.D.1. Theory

One part of the experiment plan is to acquire the anisotropic elastic properties for figured wood. The ultrasonic (US) measurement fulfils this purpose with small specimen size. Thus, one small piece of the standard bar was enough. For this purpose, the later analysis adopted the basic assumption that the present material was linear-elastic orthotropic. Its constitutive equation can be listed as in the following equation (45) with v_{ii} the phase velocity (m/s) of the wave propagating along the measuring direction (Anderhub and O'Brien Jr 1987) and ρ the sample basic density (kg/m^3). Note that the ultrasound wavelength used here was small enough to measure the velocities of a semi-infinite medium (Tu et al. 1955; Ashman et al. 1984), thus giving the stiffness matrix components and not directly the moduli of elasticity. According to the measurement made in different directions and with two kinds of probes (longitudinal and shear waves), the three longitudinal stiffness (C_{11} , C_{22} , C_{33}) and the three shear stiffness (C_{44} , C_{55} , C_{66}) of the 2D matrix representation in the orthotropy frame of the fourth-order stiffness tensor $[C]$, equation (46), can be measured using a cubic sample.

Generally, the indices 1, 2, and 3 are taken as R, T, and L, respectively, in the stiffness matrix, equation (46). C_{44} , C_{55} , and C_{66} are thus respectively C_{TLTL} , C_{RLRL} , and C_{RTRT} . Experimentally, we can potentially measure 6 shear waves velocities by switching the propagation and polarization directions, thus giving 6 apparent shear moduli, i.e., G_{LR} , G_{LT} , G_{RL} , G_{RT} , G_{TL} , and G_{TR} , that should be equal in pairs due to the symmetry of the strain and stress tensors, equation (47), assuming wood is a homogeneous and orthotropic material. This apparent non-symmetry in wood could come from non-straight growth rings and heterogeneity due to the alternation of early- and late-wood together with the grain structure and grain orientation that is a common phenomenon in the tree (wood) (Harris 1989; Soma et al. 2002; Brémaud et al. 2010; Krauss and Kúdela 2011). To simplify this mechanical aspect, which is out of the scope of this thesis, each pair of the shear stiffness moduli is averaged as it is usually done, e.g., $(G_{RL} + G_{LR})/2$.

$$C_{ii} = \rho v_{ii}^2 \quad (45)$$

$$[\sigma_{ij}] = \begin{bmatrix} C_{11} & C_{12} & C_{13} & & & \\ C_{21} & C_{22} & C_{23} & & & \\ C_{31} & C_{32} & C_{33} & & & \\ & & & G_{44} & & \\ & & & & G_{55} & \\ & & & & & G_{66} \end{bmatrix} [\varepsilon_{ij}] \quad (46)$$

$$G_{LR} = G_{RL}, \quad G_{LT} = G_{TL}, \quad G_{RT} = G_{TR} \quad (47)$$

As said above, the measurement conditions here lead to obtaining the stiffness tensor components. Therefore, estimating the samples' Young's moduli E_i ($i = L, R, T$) requires knowing the *Poisson's ratios* (ν_{ij}). However, due to the lack of information on ν_{ij} , an estimating approach is adopted using Guitard's empirical laws for "standard wood" (Guitard and El Amri 1987).

The compliance tensor S for hardwood (at 12% MC) from Guitard's equations (1987) are listed in equations (48) (all the sub-equations are in MPa) where ρ is the density.

$$\begin{aligned} S_{11}^{-1} &= E_R = 1810 \times \left(\frac{\rho}{0.65}\right)^{1.30} \\ S_{22}^{-1} &= E_T = 1030 \times \left(\frac{\rho}{0.65}\right)^{1.74} \\ S_{33}^{-1} &= E_L = 14400 \times \left(\frac{\rho}{0.65}\right)^{1.03} \\ S_{44}^{-1} &= G_{TL} = 971 \times \left(\frac{\rho}{0.65}\right)^{1.26} \\ S_{55}^{-1} &= G_{LR} = 1260 \times \left(\frac{\rho}{0.65}\right)^{1.14} \\ S_{66}^{-1} &= G_{RT} = 366 \times \left(\frac{\rho}{0.65}\right)^{1.74} \\ -S_{12}^{-1} &= -S_{21}^{-1} = \frac{E_T}{\nu_{TR}} = \frac{E_R}{\nu_{RT}} = 2680 \times \left(\frac{\rho}{0.65}\right)^{1.41} \\ -S_{23}^{-1} &= -S_{32}^{-1} = \frac{E_L}{\nu_{LT}} = \frac{E_T}{\nu_{TL}} = 31200 \times \left(\frac{\rho}{0.65}\right)^{1.09} \\ -S_{13}^{-1} &= -S_{31}^{-1} = \frac{E_R}{\nu_{RL}} = \frac{E_L}{\nu_{LR}} = 37300 \times \left(\frac{\rho}{0.65}\right)^{0.913} \end{aligned} \quad (48)$$

According to the above equations (48) and the orthotropic form of the matrix, the compliance matrix $[S]_{Gui}$, equation (49), and the determinant of the upper right quarter of the matrix Δ_S are listed for helping the conversion from $[S]$ to stiffness matrix $[C]$, equation (50).

$$[S]_{Gui} = \begin{bmatrix} S_{11} & S_{12} & S_{13} & & & \\ S_{21} & S_{22} & S_{23} & & 0 & \\ S_{31} & S_{32} & S_{33} & & & \\ & & & S_{44} & & \\ & 0 & & & S_{55} & \\ & & & & & S_{66} \end{bmatrix}_{Gui} \quad (49)$$

$$\Delta_S = S_{11}S_{22}S_{33} - S_{11}S_{23}^2 - S_{22}S_{13}^2 - S_{33}S_{12}^2 + 2S_{12}S_{23}S_{13} \quad (50)$$

Therefore, the relationship between the compliance matrix components [S] and the stiffness matrix ones [C] are listed in equations (51). Note that the form of the [C] matrix is the same as [S] in that the symbol C and S is interchangeable (changing C to S, vice versa) in equation (51).

$$\begin{aligned} C_{11} &= \frac{S_{22}S_{33} - S_{23}^2}{\Delta_S} & C_{22} &= \frac{S_{33}S_{11} - S_{13}^2}{\Delta_S} & C_{33} &= \frac{S_{11}S_{22} - S_{12}^2}{\Delta_S} \\ C_{12} &= \frac{S_{13}S_{23} - S_{12}S_{33}}{\Delta_S} & C_{13} &= \frac{S_{12}S_{23} - S_{13}S_{22}}{\Delta_S} & C_{23} &= \frac{S_{12}S_{13} - S_{23}S_{11}}{\Delta_S} \\ C_{44} &= \frac{1}{S_{44}} & C_{55} &= \frac{1}{S_{55}} & C_{66} &= \frac{1}{S_{66}} \end{aligned} \quad (51)$$

In order to allow for the estimation of Young's moduli, for comparison with the literature data, an empirical procedure is set up based on the estimation from Guitard's regression laws. This procedure is based on the use of correction factors α_i in each direction of orthotropy $i = L, R$ or T such that the diagonal terms of the stiffness matrix from Guitard are equal to those measured by ultrasound. Moreover, as a correction is applied in each direction, the diagonal terms are corrected by α_i^2 while the off-diagonal ones are corrected by $\alpha_i\alpha_j$:

$$[\alpha_i C]_{Gui}^\varphi = \begin{bmatrix} \alpha_1^2 C_{RR}^{Gui} & \alpha_1 \alpha_2 C_{TR}^{Gui} & \alpha_1 \alpha_3 C_{LR}^{Gui} & & & \\ \alpha_2 \alpha_1 C_{RT}^{Gui} & \alpha_2^2 C_{TT}^{Gui} & \alpha_2 \alpha_3 C_{LT}^{Gui} & & \approx 0 & \\ \alpha_3 \alpha_1 C_{RL}^{Gui} & \alpha_3 \alpha_2 C_{TL}^{Gui} & \alpha_3^2 C_{LL}^{Gui} & & & \\ & & & G_{TL}^{Exp} & & \\ & & & & G_{RL}^{Exp} & \\ & & & & & G_{RT}^{Exp} \end{bmatrix} \quad (52)$$

III.D.2. *Testing conditions and devices*

The setting for the temperature and humidity during the measurement was the same as the previous test, which was 20-65 (samples conditioned at 20°C and 65% RH). The setup of the instruments (Fig. 48) included several parts: two Sonaxis probes, longitudinal transducer (CMP123) and transverse shear polarized transducer (CMP124), with a central frequency of 500 kHz and 15mm active diameter; a signal generator (Keysight 33210A) to excite the transmitting probe with a sinusoidal wave train (tone burst) of 3 to 5 cycles at 500 kHz and 10 V peak-to-peak amplitude; a preamplifier (Panametrics Model 5800) magnifying the signal from the transmitted wave received by the second probe; a digital oscilloscope (Tektronix TDS 3032B) for the acquisition of the excitation and received signals with several acquisitions of 10,000 points at 500 MHz and 9 bits; computer with LabView software for the management of the data acquisition and Matlab software with signal processing toolbox to measure the time of flight of the ultrasonic wave, i.e., the maximum of the envelope of the inter-correlation between a reference echo (obtained by placing both probes directly in contact) and the ones that passed through the sample (by placing both probes on the surfaces of the sample facing each other). The bandwidth of the burst was narrow enough to obtain an almost monochromatic transmitted signal. Under these conditions, the group velocity differed very little from the phase velocity (Brillouin 2013; Orfanidis 2016). The acoustic coupling was achieved using honey as it is effective for shear waves and has been widely used in previous studies (Kohlhauser et al. 2009; Camara et al. 2010; Cegla et al. 2011). In addition, it is very easy to remove with a minimum of water and penetrates very little into samples, so it does not induce significant variation in mass or moisture.

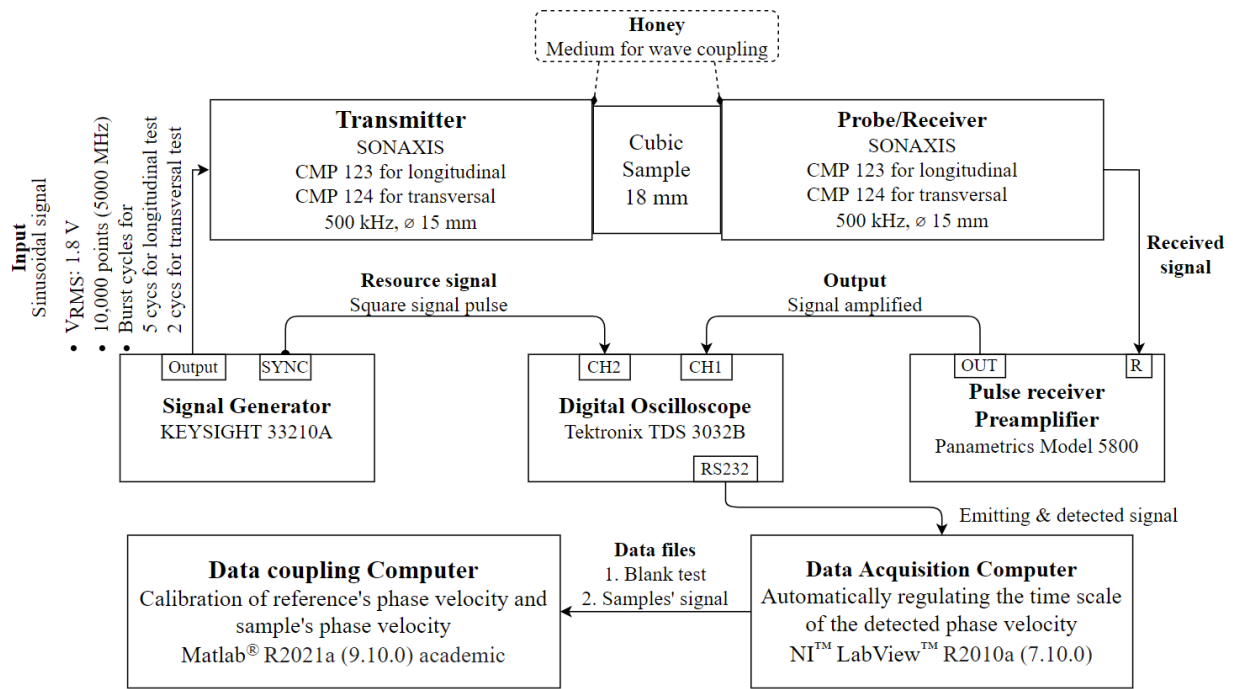


Fig. 48 Diagram of the devices used in the US measurement. Two sub-types of measurements were involved, i.e., longitudinal and transverse measurements. The previous one measures C_{ii} by CMP 123, and the latter measures transversal elastic properties (G_{ij}) by CMP 124.

The cubes were acquired from the standard beams (cutting plane from Fig. 36), and they were stabilized in a climatic chamber (HPP 110, Memmert) for 30 days in the beam form and 18 days after being machined to 19^3 mm^3 cubes (nominal dimension). Their weights were measured by the electronic scale (ME204, Mettler Toledo), and the dimensions were measured by thickness gauge (293-234-30 with 156-101-10, Mitutoyo) in the middle of the opposite faces, i.e., L, R, and T faces.

In order to have a reference for the determination of the phase velocities, a referential signal (or blank test) was measured by placing both probes directly in contact and coupling with liquid honey (Keunecke et al. 2007). A drop of liquid honey was placed on the centre of the effective area of the US probes and extended gradually until the whole circular area was covered.

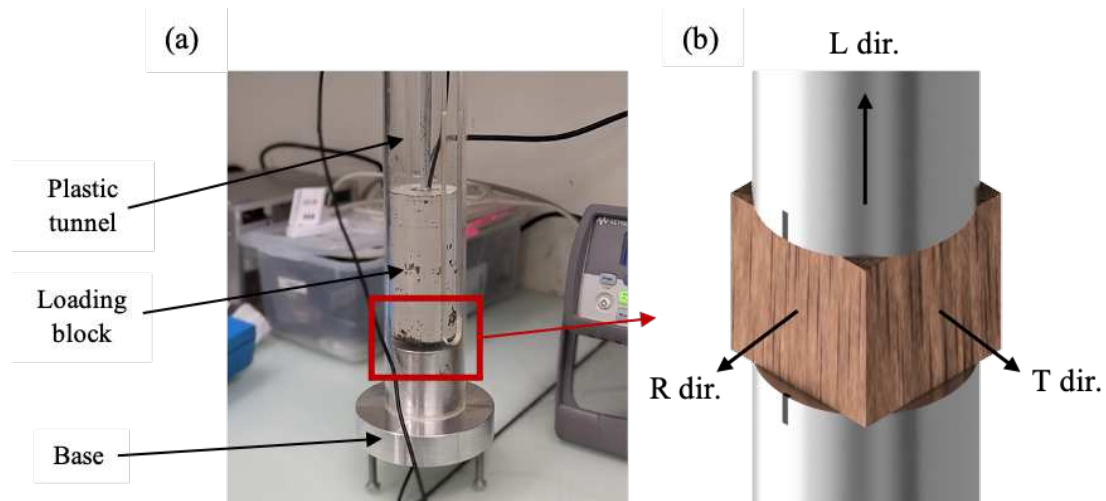


Fig. 49 (a) without the sample for the reference signal, the self-aligning and self-centring equipment. A loading block with a certain weight allows a slight and repeatable pressure to be applied between the sample and the US probes. (b) a zoom showing the positioning of the sample during the test with the two transverse probes whose polarization direction is marked by the black line, e.g., G_{LR} is measured in this case.

III.D.3. *Calculations for Post-processing of experimental data*

Each reference and sample signal (Fig. 50a) had their envelopes computed by the code developed in Matlab. The two signal envelopes were then super-positioned using Matlab Signal Processing Toolbox to obtain the time-of-flight (Fig. 50b).

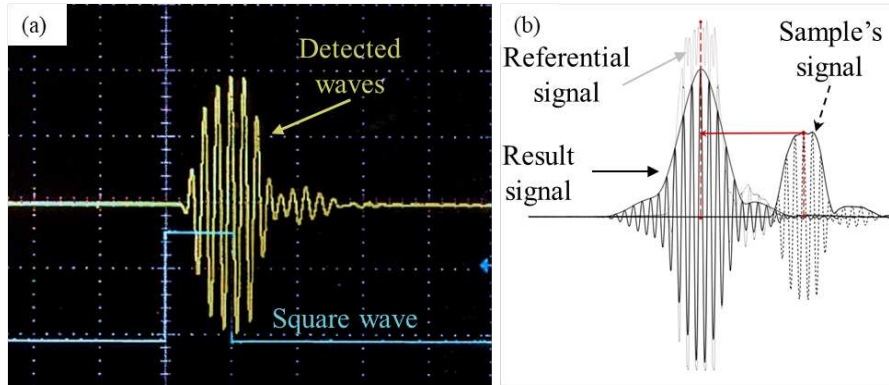


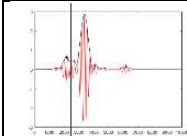
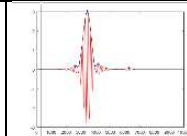
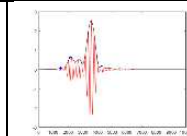
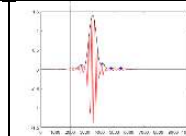
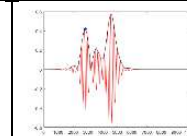
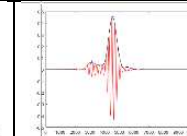
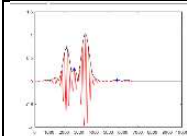
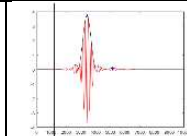
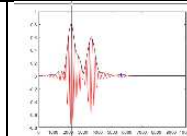
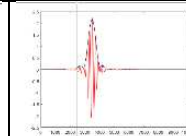
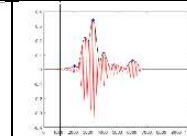
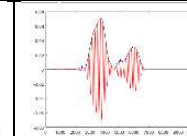
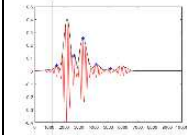
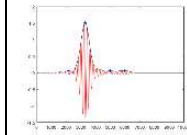
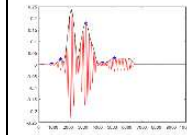
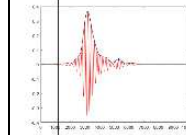
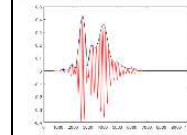
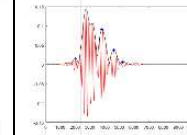
Fig. 50 An example of a detected longitudinal wave. (a), signals on the oscilloscope: the yellow waves are the received signal measured on an AcP sample, while the square wave (blue) is the generator synchronisation signal of the input wave. (b) the calibration of the reference signal and sample signal and their result.

III.D.4. *Signal acquisition and phenomenon description in the case of shear waves*

Most of the signals during shear measurements had multiple correlation peaks due to the shear wave splitting. This phenomenon makes the measurement of the time of flight complex because it is necessary to determine which peak of correlation it corresponds to. The correlation signal peaks acquired from different directions and with three different samples correlated responses were listed on Tab. 12.

The signal from the RL and TL directions gives a single peak contrary to the LR and LT directions, where the results from RL and TL are used to find which peak should be used. Compared with the longitudinal signal, the transverse shear signals were more complicated. The signal correlation and selection could only rely on the orthotropy characteristic (G_{RL} is close or equal to G_{LR} , theoretically) to find the most approached value during the selection (example, CaM-B3-b2 in Tab. 12). However, for the example in Tab. 12, PtS-B1-b1 shows a larger variance of C_{RT}/C_{TR} . Thus, the selection was based on the second peak in the RT direction, and the most approached value in the TR direction was selected.

Tab. 12 The transverse shear wave response of three samples: CaM-B3-b2, DaO-B3-b1, and PtS-B1-b1. The correlated peaks are in different forms for the LR, LT, RT, and TR measurements. On the contrary, the RL and TL direction's signals are single peaks.

CaM-B3-b2		$C_{LR}/C_{RL} = 1.09$	$C_{LT}/C_{TL} = 0.97$	$C_{RT}/C_{TR} = 0.97$	
LR	RL	LT	TL	RT	TR
					
1.17	1.07	0.91	0.94	0.33	0.34
DaO-B3-b1		$C_{LR}/C_{RL} = 0.98$	$C_{LT}/C_{TL} = 0.90$	$C_{RT}/C_{TR} = 1.00$	
LR	RL	LT	TL	RT	TR
					
0.65	0.66	0.54	0.60	0.08	0.08
PtS-B1-b1		$C_{LR}/C_{RL} = 1.03$	$C_{LT}/C_{TL} = 0.98$	$C_{RT}/C_{TR} = 0.78$	
LR	RL	LT	TL	RT	TR
					
1.59	1.54	1.84	1.87	0.61	0.78

III.E. *Generic Results: Methodological Effects and Range of Values in Physical-Mechanical Properties*

The obtained data on all tested physical-mechanical properties will be examined under two complementary viewpoints in the following sections. One aspect of these analyses concerns how the obtained data are affected by methodological aspects, i.e., the cutting plan of the specimens, the conditioning protocols, or the different employed testing methods. The other aspect will describe the range in measured values of the different properties. In Chapter III, the value ranges will be mostly presented at the between-species level of diversity compared to general knowledge on these properties. However, when needed, some elements of variability at the within-species level will also be shown to introduce the more detailed analyses of structure-properties relationships that will constitute the next Chapter IV.

III.E.1. *Hygro-Mechanical aspects*

The studied hygro-mechanical aspects concern three main topics, described in the three sections below: the shrinkage and its anisotropy, the fibre saturation point (FSP), and how the duration of conditioning of specimens in a climatic room affects the measured vibrational properties.

Herein, the first one is the amplitude of dimensional change in each tested direction, and the total shrinkage is used for its evaluation (17). The second is the corresponding length change due to the moisture change (15) and the shrinkage coefficient (α) (16). The last part is the total shrinkage in R (TRS) and T (TTS) directions because the ratio of T and R's dimensional change is also related to the anisotropic mechanical properties. It will have more discussion in the next chapter.

III.E.1.a) *The range of shrinkage values and of their anisotropy*

The shrinkage assessment was based on measured dimensions in R and T directions at five MC states (§III.B). The present study's comparisons are on shrinkage properties' magnitude and its anisotropy between R and T directions. For the magnitude, two parameters are considered: one is the total shrinkage, and the other is the shrinkage coefficient. Meanwhile, the anisotropic ratios between R and T are also compared.

The first part of the comparison results is the total shrinkage and its T/R ratio. In Tab. 13, the comparing unit is the values in an average of each plank, and the number of specimens depends on the produced standard bars from the plank. Two groups of values are presented: the original value ("Exp" in Tab. 13), and the re-oriented value due to the ring angle in TR plane

within some specimens (“ExpD” in Tab. 13), calculated according to equation (26). Also, a CIRAD’s database (Tropix 7) was used to provide the general information of the total shrinkage properties of the studied species, compared to the present results. However, the AIG values were acquired from another reference (Peck 1960), where the species was *Alnus rubra* (instead of *A. glutinosa* here).

The purpose of presenting the comparison by plank first, rather than directly by species, is because the actual degree of Ring Angle (RA in Tab. 13) depends mostly on cutting plan limitations imposed by the initially sampled material (i.e., planks). Depending on the initial planks, some specimens could be cut with nearly no RA in the R-T plane, while for some other planks, it could not be avoided, the maximum value of RA being 35° (for plank AcP-P2).

The second purpose of presenting the comparison by planks in Tab. 13 is to explain some differences in a range of values per species, depending on the number and types of initially sampled planks. Typically, the studied temperate hardwoods cover a sampling of 3 to 4 initial planks each, coming from different trees, and covering different “degrees of figure” (doF) for the wavy, Birdseye, and pommele (quilted) figures.

The different ranges in total shrinkage are presented between species in Fig. 51 and Fig. 52. The temperate species' much broader range, which consists of samplings of more numerous individual trees with different doF each, is seen. Also, Fig. 51, Fig. 52, and Fig. 53 compare their values and ratios, as previously discussed, i.e., original values (dashed line shape) and re-oriented values due to the annual ring angle (solid line shapes). The corrected/calculated values are 6% higher on average, but this varies widely depending on the RA in different initial planks and samples.

Tab. 13 The comparison of total shrinkage in T and R directions (TTS and TRS) and T/R shrinkage anisotropic ratio (TTS/TRS). Mean values and (standard deviation in brackets). Raw experimental values (Exp) and the rotated values (ExpD) were obtained by calculation according to R-T Ring angle (RA, °). Ref. = Literature values (-.- means no standard deviation in the literature reference).

Specimens			TTS (%)			TRS (%)			TTS/TRS		
Plank	n	RA(°)	Exp	ExpD	Ref.	Exp	ExpD	Ref.	Exp	ExpD	Ref.
AcP-M1	4	25	9.97(1.2)	9.09(2.2)		6.18(0.6)	6.31(0.7)		1.61	1.47	
AcP-M2	4	5	8.29(0.3)	8.17(0.3)		3.84(0.1)	3.88(0.1)		2.16	2.11	
AcP-M3	4	11	8.31(0.5)	7.77(0.7)		4.01(0.3)	4.20(0.2)		2.08	1.85	
AcP-P1	4	7	7.68(0.4)	7.50(0.4)	7.8(-.-)	4.10(0.1)	4.16(0.1)	4.5(-.-)	1.87	1.80	1.7
AcP-P2	4	35	5.41(0.8)			5.28(0.9)			1.02		
AcP-P3	4	15	7.27(0.3)	6.43(0.6)		4.03(0.2)	4.27(0.2)		1.80	1.51	
AcP-P4	4	5	9.27(0.7)	9.56(0.7)		3.77(0.3)	3.84(0.4)		2.58	2.51	
AlG1	4	20	7.78(0.8)	7.95(0.1)		4.21(0.4)	4.14(0.5)		1.85	1.93	
AlG2	4	33	5.94(0.8)		7.3(-.-)	5.04(0.2)		4.4(-.-)	1.18		1.7
AlG3	4	29	4.32(1.1)	3.43(-.-)		3.71(1.2)	3.69(-.-)		1.16	0.93	
CaM	6	6	8.16(0.2)	7.93(0.2)	6.5(-.-)	5.50(0.1)	5.55(0.1)	4.2(-.-)	1.48	1.43	1.5
DaO	11	4	7.32(0.3)	7.23(0.3)	6.8(1.0)	3.08(0.3)	3.12(0.3)	3.5(0.7)	2.38	2.34	1.9
EnC	12	17	7.33(0.2)	6.45(0.6)	7.2(0.9)	5.33(0.1)	5.45(0.2)	5.0(0.6)	1.37	1.19	1.4
EnU1	6	4	6.47(0.3)	6.39(0.3)		5.51(0.4)	5.52(0.4)		1.17	1.16	
EnU2	6	6	6.29(0.6)	6.14(0.6)	6.4(0.7)	4.99(0.2)	5.00(0.2)	4.6(0.7)	1.26	1.23	1.4
FrS1	4	17	13.35(0.6)	11.43(1.0)		7.23(0.4)	7.80(0.4)		1.85	1.47	
FrS2	4	14	12.02(0.4)	10.65(1.4)		6.08(0.4)	6.52(0.6)		1.98	1.66	
FrS3	4	25	10.68(0.1)	8.22(0.7)	9.6(-.-)	7.00(0.5)	7.12(0.3)	5.7(-.-)	1.53	1.16	1.7
FrS4	4	11	10.69(0.6)	9.98(0.5)		5.71(0.3)	5.92(0.5)		1.87	1.70	
HyP	16	7	7.91(1.1)	7.66(1.1)	7.5(1.2)	5.17(0.6)	5.22(0.6)	3.9(1.4)	1.53	1.47	1.9
JuR1	4	27	6.03(0.3)			4.60(0.1)			1.31		
JuR2	4	23	5.17(0.7)	4.92(-.-)		3.97(0.5)	4.39(-.-)		1.30	1.12	
JuR3	4	29	8.68(0.5)	6.16(-.-)	7.5(-.-)	6.33(0.1)	6.61(0.1)	5.5(-.-)	1.37	0.93	1.4
JuR4	4	30	8.19(0.4)	7.01(-.-)		6.64(0.5)	6.38(-.-)		1.23	1.10	
KhS	26	2	6.35(0.6)	6.32(0.7)	5.6(0.8)	5.59(1.3)	5.49(1.2)	4.9(0.6)	1.14	1.18	1.1
NeK	12	20	9.93(0.7)	9.15(1.2)		7.71(0.3)	7.78(0.3)		1.29	1.18	
NeP1	8	6	9.54(2.6)	9.31(2.6)	7.5(0.8)	6.35(0.8)	6.40(0.8)	5.1(0.4)	1.50	1.43	1.5
NeP2	12	20	7.16(0.6)	7.09(0.5)		5.94(0.4)	5.82(0.2)		1.20	1.22	
PaB	10	2	6.90(0.3)	6.86(0.3)	7.3(0.9)	4.37(0.3)	4.37(0.3)	5.2(0.5)	1.58	1.57	1.4
PiA	7	3	8.32(1.0)	8.21(1.0)	8.5(1.2)	4.97(0.3)	4.99(0.3)	3.8(0.6)	1.67	1.666	2.2
PsS	12	13	8.69(0.7)	8.24(0.7)	6.9(0.7)	5.78(0.4)	5.87(0.4)	4.6(0.6)	1.50	1.41	1.5
PtS	11	10	3.85(0.3)	3.53(0.4)	5.0(0.5)	2.35(0.4)	2.42(0.4)	3.2(0.3)	1.64	1.51	1.6
PtT	8	10	4.44(0.2)	4.09(0.4)		2.62(0.3)	2.70(0.3)		1.69	1.55	

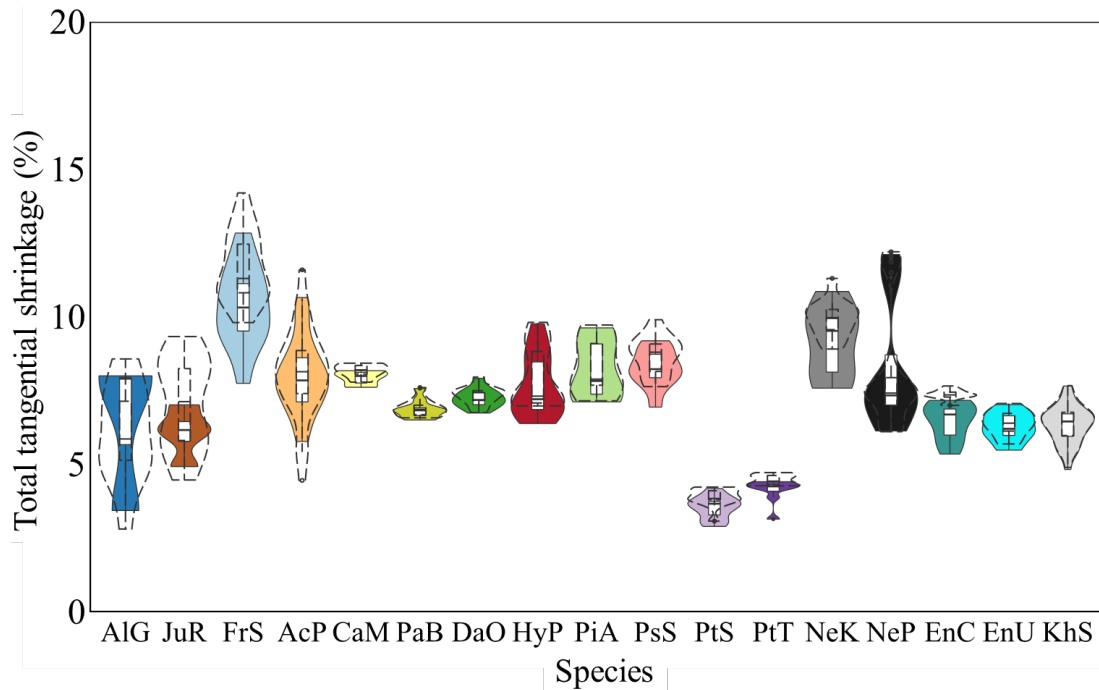


Fig. 51 The total tangential shrinkage categorised by species. The shapes in the dashed line are the result without the correction of the ring angle rotation, and the solid line filled with colours are the rotated result. The order follows the temperate-tropical species and the species' families.

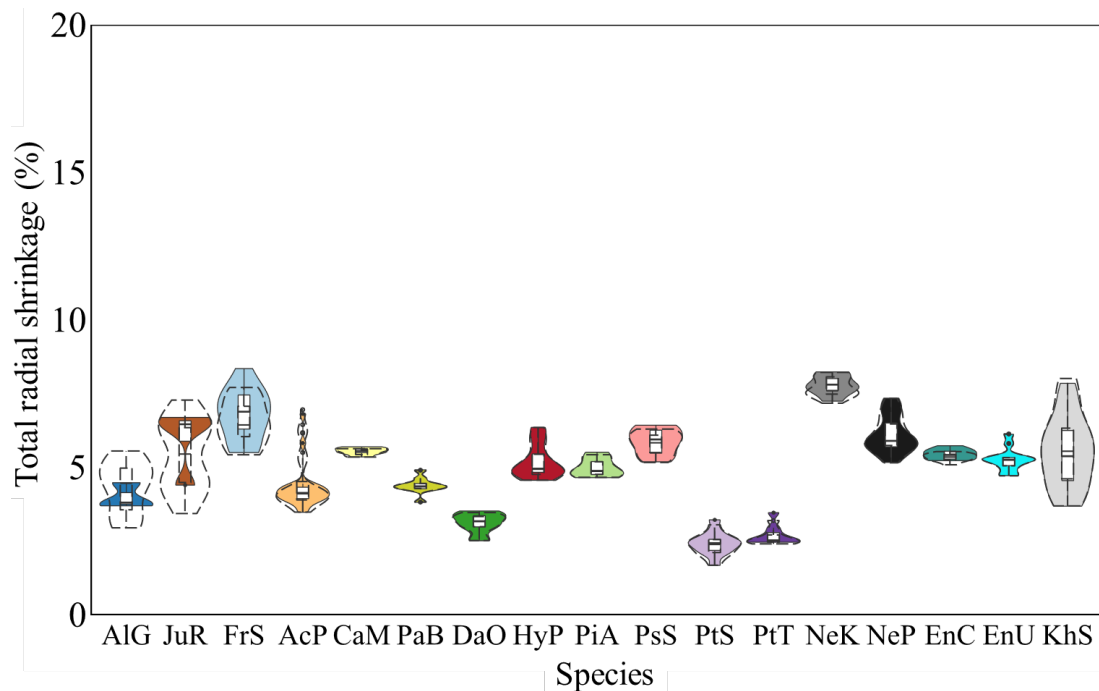


Fig. 52 The total radial shrinkage categorised by species. The shapes in the dashed line are the result without the correction of the ring angle rotation, and the solid line filled with colours are the rotated result. The order follows the temperate-tropical species and the species' families.

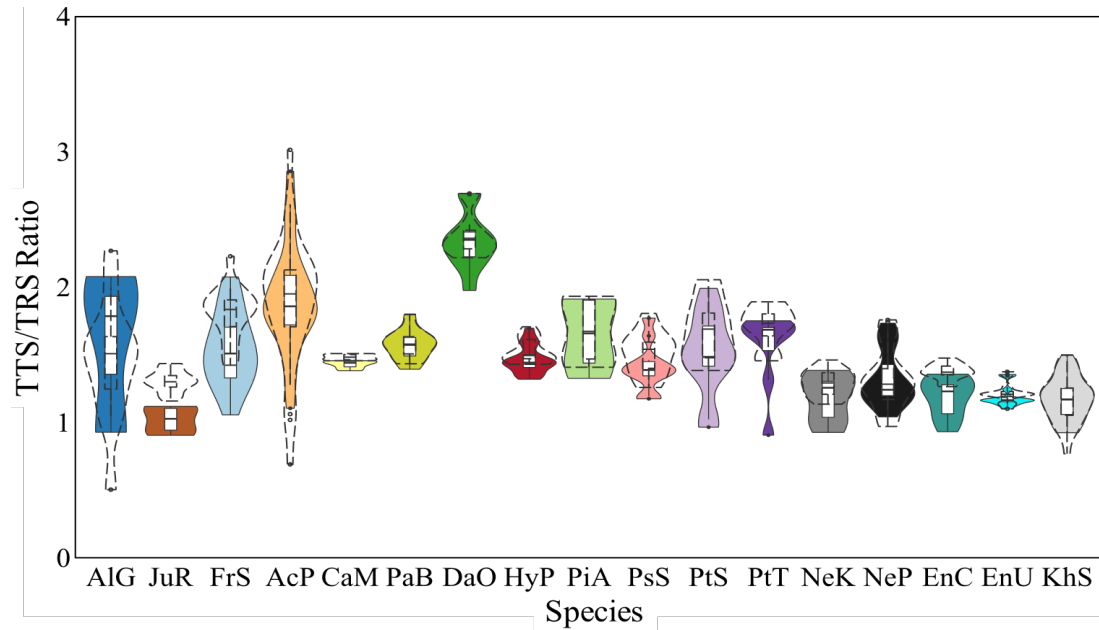


Fig. 53 The anisotropic ratio of total shrinkage (TTS/TRS) categorized by species. The shapes in the dashed line are the result without the correction of the ring angle rotation, and the solid line filled with colours are the rotated result. The order follows the temperate-tropical species and the species' families.

Globally, the values of total shrinkage as measured in the present study are consistent with the ranges known from the literature. On average, the TTS (ExpD) is 7.2 %, and the TRS is 5.0%, versus 7.6 % and 4.7% from literature, respectively. The averaged measured ratio of anisotropic shrinkage TTS/TRS was 1.49 (reoriented values), which is smaller, but still comparable, to a literature value of 1.61 for the same species, since the sampling is comparatively small for the present materials. However, interestingly, these studied species tend to have a lower ratio of shrinkage anisotropy than observed over the whole CIRAD database (1.82, on average).

Some species (material) have larger ring angles, which causes the rotation not to be applicable. Thus, the values were abandoned, causing the violin-plot distribution is much smaller than the original measurement one, e.g., AlG, JuR.

Furthermore, the shrinkage properties based on MC change, i.e. the shrinkage coefficients (α_R and α_T), are presented in Fig. 54 and Fig. 55. The values of the MC and dimensions used in the calculation are between two RH and MC states, which are MC₁₈ (30°C and 85% RH) and MC₆ (20°C and 30% RH). One reason is that the values in this range are more approaching the common environmental condition (as in the application). The other is that the α value is not of linear change near the very high MC (below FSP) and low MC (just above M₀). The last one is that the FSP is estimated but not from the direct measurement, so the range between MC₀ to FSP is not actually measured but calculated.

The behaviour of these relative values (shrinkage coefficients α) between species (Fig. 51 and Fig. 52) is very comparable with the distributions observed for total shrinkage, except for PiA, PtS, and PtT. PiA has a more extensive distribution in the T direction, while it has the most significant GA and GA variation. The PtS and PtT have larger than expected shrinkage coefficients. Their MC₁₈ values are much lower (13.3% on average) than the other species. In contrast, their EMCs at MC₆ are 6.1% on average.

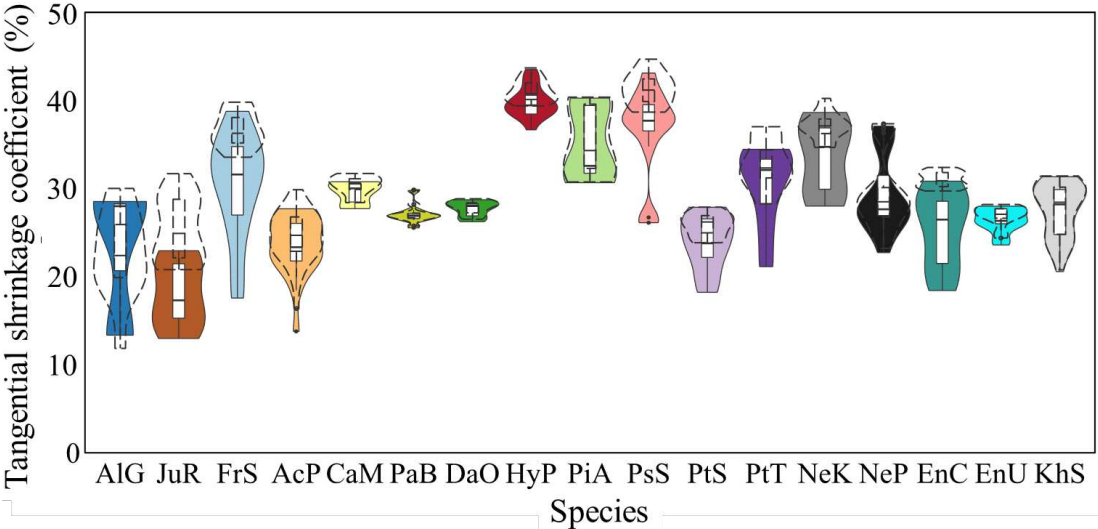


Fig. 54 The tangential shrinkage coefficient compared by species. The shapes in the dashed line are the result without the correction of the angle rotation, and the solid line filled with colours are the rotated result. The order follows the temperate-tropical species and the species' families.

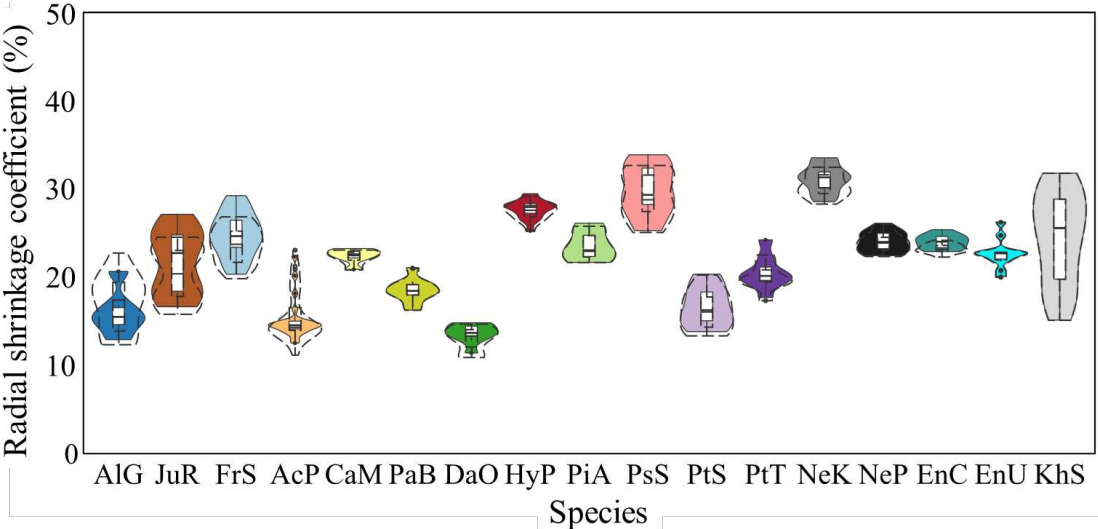


Fig. 55 The radial shrinkage coefficient compared by species. The shapes in the dashed line are the result without the correction of the angle rotation, and the solid line filled with colours are the rotated result. The order follows the temperate-tropical species and the species' families.

III.E.1.b) FSP and Equilibrium Moisture Content at different conditions

The Fibre Saturation Point (FSP) represents the moisture content (MC) when the cell walls are fully saturated (by bound water), but there is no free water in the cell lumina. In the adopted protocol (following the standard procedure in CIRAD-BioWooEB), this is studied by starting from the water-saturated state of wood.

The degree of water saturation of wood specimens was examined in the experiment. A first examination was made by comparing the density in the water-saturated state and the density in the oven-dried state. The scatter plot (Fig. 56) is categorized by species, and the elliptical distributions in 95% interval are also drawn. Then, a linear fitting line was drawn without considering the outlier species. The coefficients (a and b) in equation (11) are acquired by the least-squared method, about 0.26 and 1, respectively.

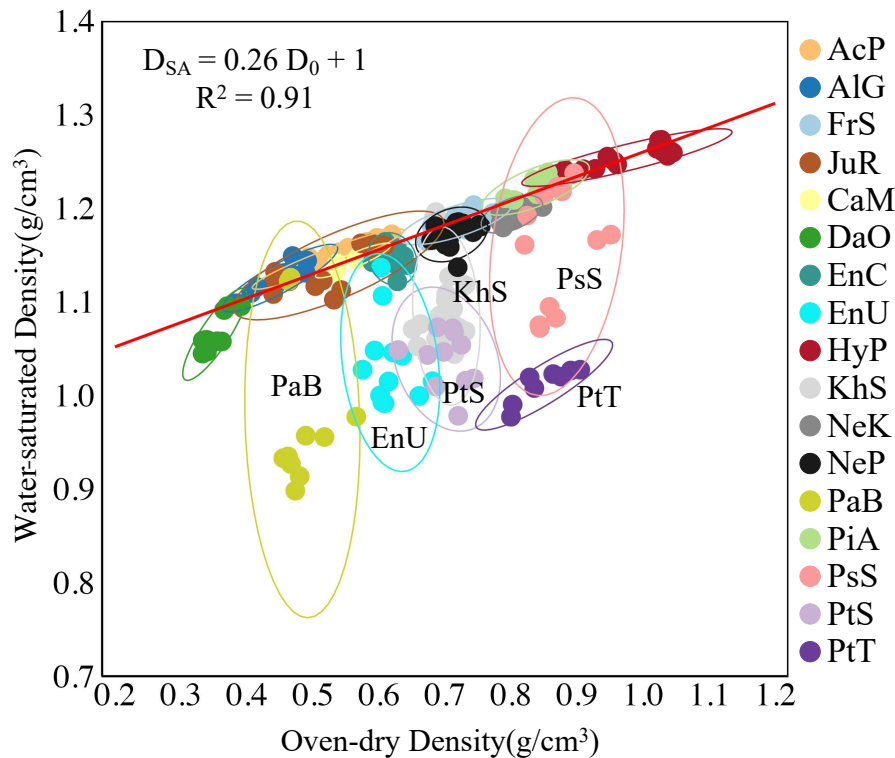


Fig. 56 The criteria for the saturation state. The outlier groups are the specimens of EnU, KhS, PaB, PsS, PtS, and PtT.

The above deduction does not consider the ratio of extractives in wood nor the effect of extractives. Also, the debate for saturating priority of the bonding water or free water saturation is not considered. However, the result shows that most of the species and specimens were saturated to the same state. The outlier data belong to 6 species (Tab. 14) and could be due to the extractives or the priority of free water to the bound water. However, practically, to ascertain the

validity of the specimen's FSP calculation, it is considered only necessary to verify that the value of MC_{sa} is higher than 40 %.

Consequently, according to the experimental results in Tab. 14, PtT (*Pterocarpus tinctorius*) is probably not fully saturated, with an MC_{sa} of only 28%. Nevertheless, its FSP value fits the previous data (17% in the CIRAD database versus 15% in present results). PsS and PtS also have relatively low values of MC_{sa} (53% and 58%) and low values of FSP. This could have been expected for PtS (*Pterocarpus soyauxii*, same genus as PtT). This species is well-documented for having extractives that strongly affect its physical-mechanical behaviour (Brémaud et al. 2011a; Jankowska and Kozakiewicz 2016). Although FSP values obtained here (15%) are lower than average in the CIRAD database, they are still consistent for this species. PsS shows a relatively lower value of FSP (22%) than its mean value in CIRAD database, but is still compatible with its previously recorded variability in FSP ($27 \pm 11\%$).

Tab. 14 The MC_{sa} and related FSP (in %) of the outlier species

Specimens	MC_{sa} (Av.)	MC_{sa} (sd.)	FSP _R	FSP _T	FSP' _R	FSP' _T	FSP _{area}	FSP' _{area}
EnU	88	13	23.5	24.9	23.5	24.9	24.4	24.4
KhS	73	9	23.2	24.4	23.2	24.5	24.0	24.0
PaB	126	25	23.8	26.6	23.8	26.6	25.6	25.6
PsS	53	10	20.6	22.3	20.8	22.4	21.8	21.8
PtS	58	10	15.8	15.2	15.8	15.1	15.4	15.4
PtT	28	4	15.1	15.0	15.1	15.0	15.1	15.1

In a further step, MC_{sa} and the D_0 (oven-dry density) are compared as a mean to evaluate the lumen fraction (=available for free-water uptake) as expressed by D_0 (Fig. 57). The outlier species are essentially the same as in the previous analysis (Fig. 56). Yet, PsS is now in the examination's fitting curve range, which possibly suggests the water was not fully bound to cell walls while the free water had already filled in the lumen.

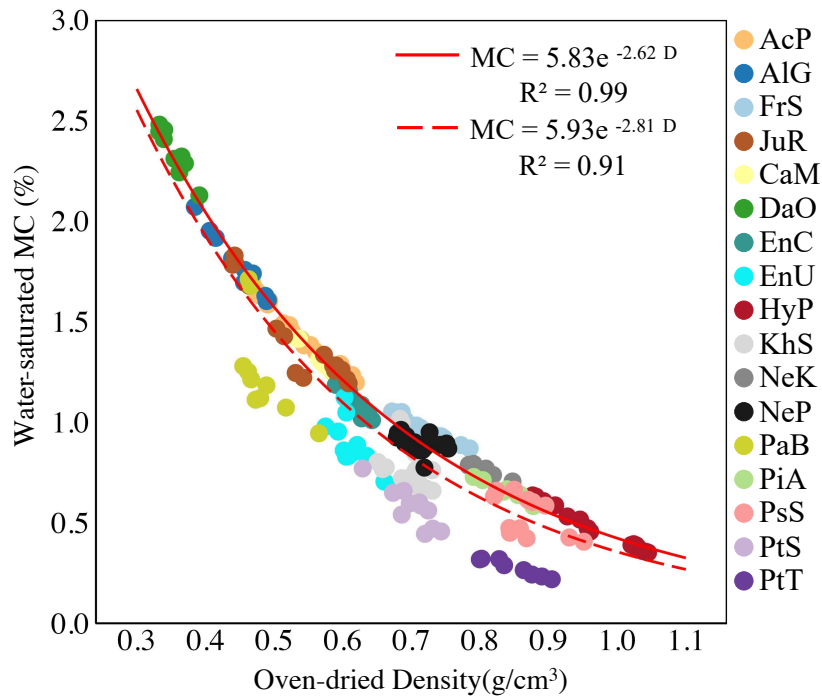


Fig. 57 The oven-dry density and MCsa comparison. The solid regression line represents the result with removing the outliers: EnU, KhS, PaB, PtS, PtT. In contrast, the dashed line is the regression line for all the species.

According to the calculation of FSP_R , FSP_T , and equations, the FSP and the relative dimensional change are then re-calculated (FSP'_R , FSP'_T) (Fig. 58).

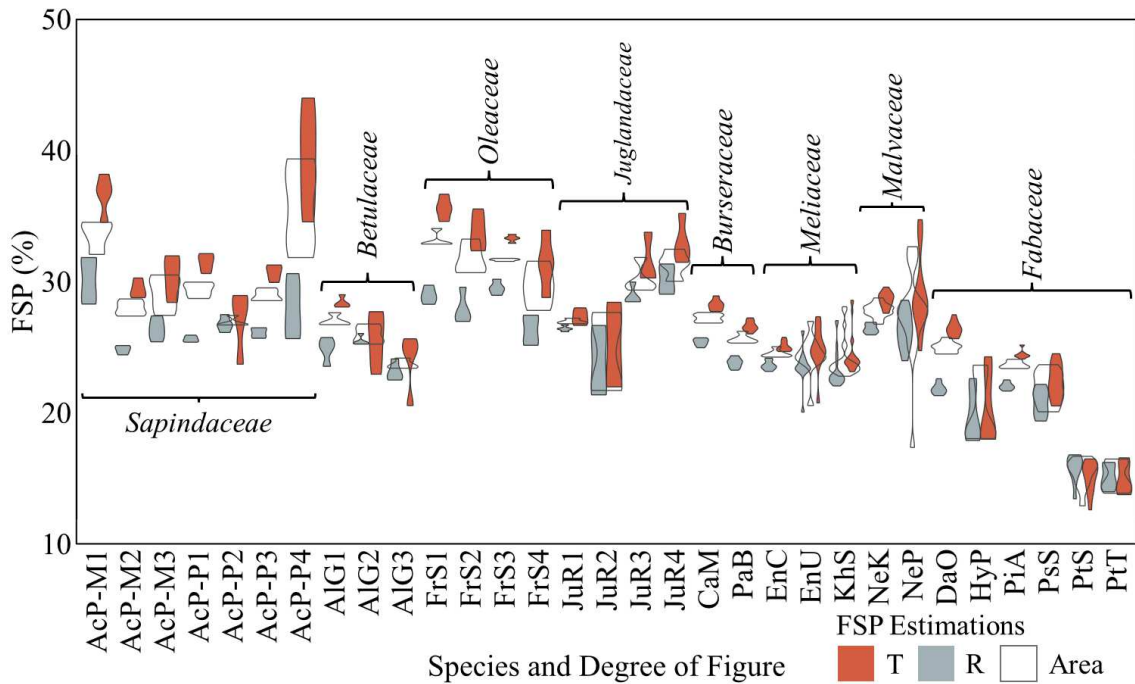


Fig. 58 The comparison between FSP's estimations (re-calculated values) in R-direction (grey colour), T-direction (red colour), and by area (light grey colour frame).

The FSP'_{area} value is between FSP'_T and FSP'_R . Previous researches showed the same trend that $FSP_T > FSP_{volumetric} > FSP_R$ (Passarini and Hernández 2016). In consequence, the FSP'_{area} is closer to the FSP'_T . Still, the larger ring angle to be reoriented (by calculation) could induce a larger error because of the assumption from non-shear deformation.

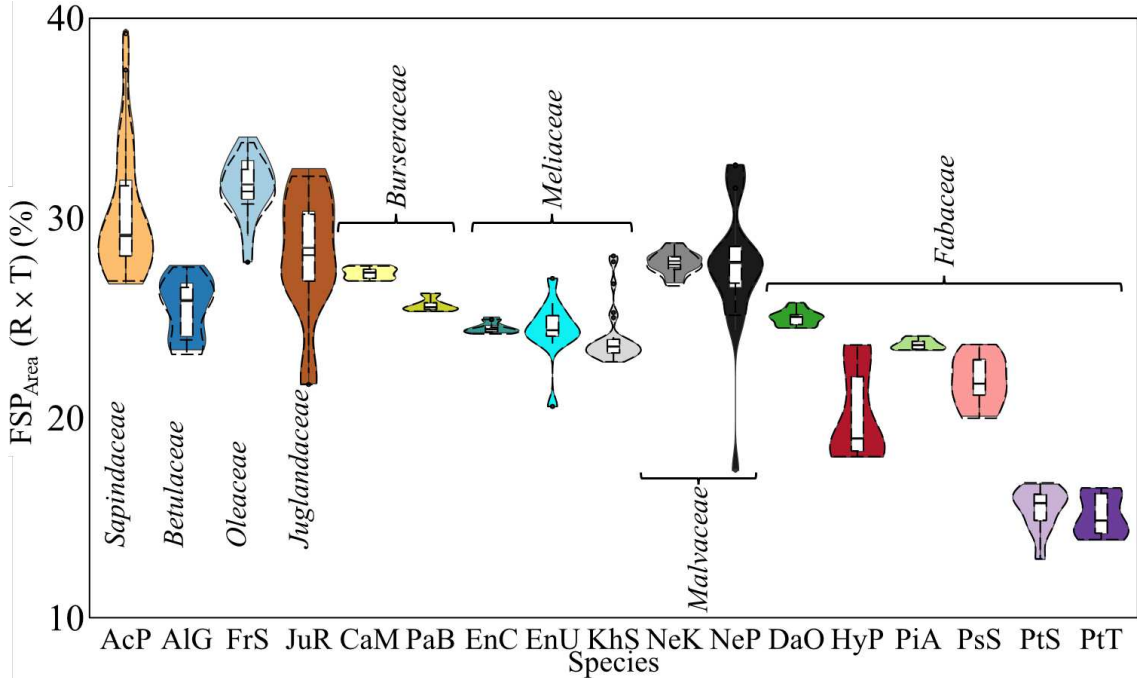


Fig. 59 The comparison of FSP calculated by area ($R \times T$), categorised by species and family. The shapes in the dashed line are the result without the correction of the angle rotation, and the solid line filled with colours are the rotated result.

III.E.1.c) *Effects of hygrothermal conditioning on dynamic properties tested by BING*

Another aspect of hygro-mechanical behaviour is that of changes in mechanical properties according to specimens' hygro-thermal conditions and of the duration of conditioning.

According to the plan of the BING experiment, the measurement was in several subsequent steps of conditioning (Fig. 36). The rationale for this protocol was that the material/specimens dimensions were trimmed from the sizes of original planks (tested in uncontrolled ambient conditions) to the standard BING-bar size (nominal cross-section: $20 \times 20 \text{ mm}^2$), and during this process, the environmental conditions also changed from uncontrolled ambient conditions to progressively conditioned in a climatic room set at nominal conditions of 20°C and 65% RH (detail in §III.C.1).

The comparison between several conditioning states is shown, which are BING0, BING1, BING2, and BING3 (codes in Fig. 36). Due to the sample's quantity, which is 119 standard BING-bars specimens, the comparison is based on the "standardised" values, i.e., the relative difference between values at a given step, from values at the initial uncontrolled ambient conditions (BING0) (Fig. 60). Also, the BING values considered here are an average of two experimental configurations (hitting the standard BING-bars on their quarter-sawn L-R surface and on their flat-sawn L-T surface).

The general trend of MOE_L values is slightly decreasing with a longer time of stabilisation in controlled conditions. Compared with mean values tested at BING0, BING1 was +0.47%, BING2 was +0.73%, and BING3 was -1.31% (the BING measure error is less than 1%). Meanwhile, during these subsequent steps of BING measurements, the mass of specimens (indicating changes in moisture content MC) was always increased, compared to mass measured in the initial uncontrolled conditions. This is quite logical if one considers that the initial, uncontrolled ambient condition was that of a dry summer in Montpellier and that the controlled climatic room is set at nominal values of 20°C and 65% RH. The specimens' mass evolution, based on BING0, is BING1 (+0.89% after 39 days) > BING2 (+0.77%, after 50 days) > BING3 (+0.76%, after 69 days). The fact that mechanical properties still evolve between 50 and 69 days, despite comparable values of mass, means that samples were still not fully stabilized (from a physical point of view) according to the nominal hygro-thermal environmental conditions. Yet, the MOE_L values appears to be slightly decreased at BING3 (from BING0 is -1.2 %; from BING1 is -1.7 %), which is consistent with the general trend that elastic modulus decreases with an increase in moisture content generally by circa -1.1% decrease in MOE per % on MC (Brémaud

and Gril 2021a). However, the very slight increases in MOE during BING1 and BING2 steps are counter-intuitive, but may just reflect that the conditioning of thicker wood would take a longer time.

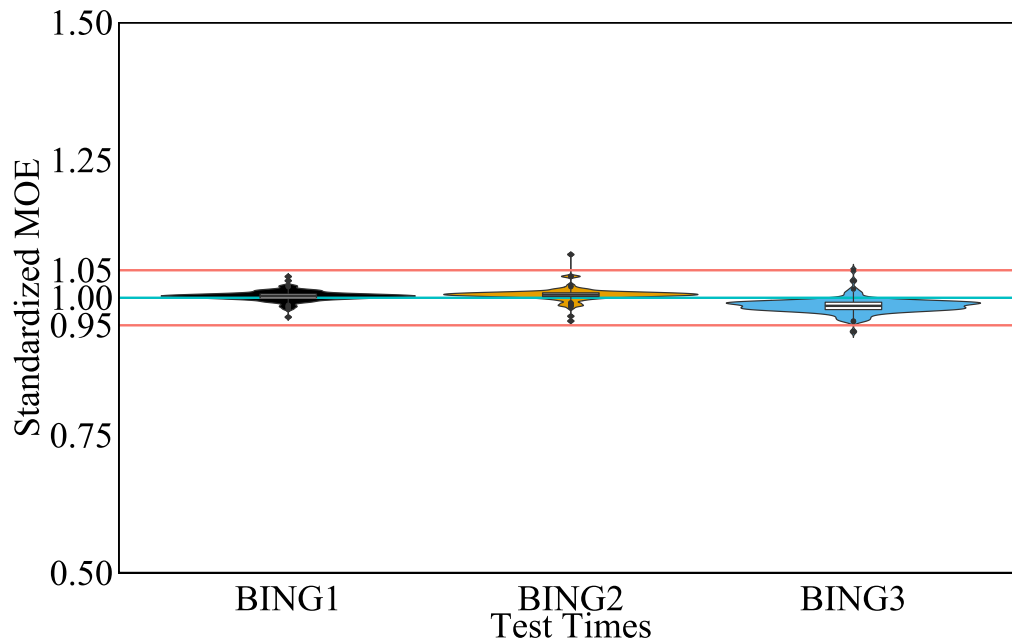


Fig. 60 The comparison of MOEL values of standard bars tested at different times (see Fig. 36). The standardized MOEL values show a general decreasing trend. The cyan line indicates the 0 difference (standardized value = 1), and the two red lines indicate the $\pm 5\%$.

For the shear moduli G_{TL} and G_{RL} the trend between the tests are not clearly distinguished at first, because the experimental error on evaluation of G is higher than that for MOE. Yet, the differences between values tested at different times are generally more significant than the MOEs' differences. Comparing the mean values at BING0, for G_{RL} , the values at BING1 is -1.39%, BING2 is -0.79%, and BING3 is -2.34%. In contrast, BING0's mean value of G_{TL} , BING1 is +0.07%, BING2 is -0.30%, and BING3 is -0.93%.

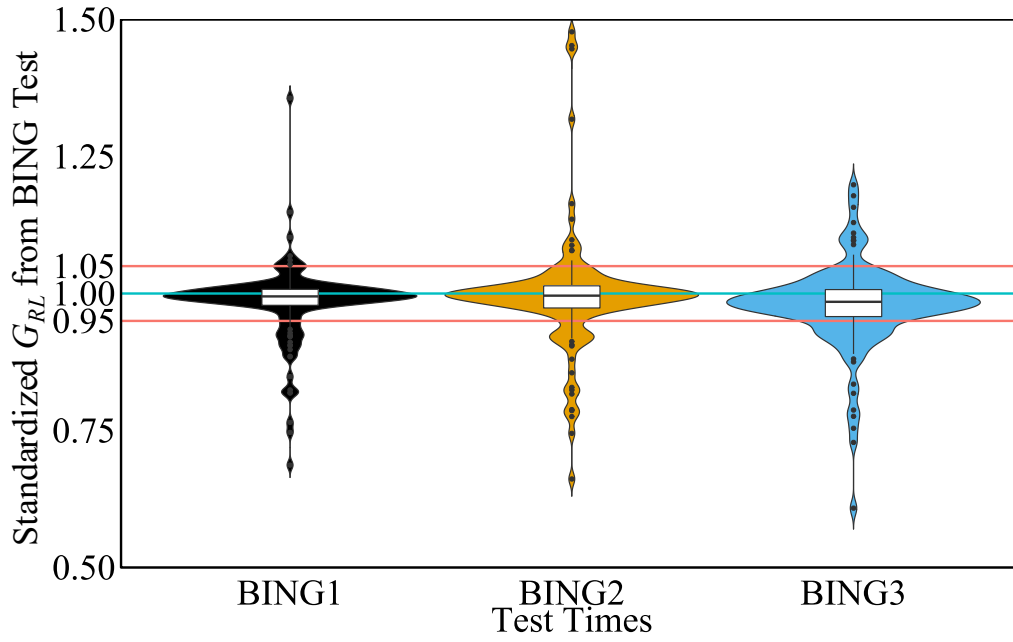


Fig. 61 The comparison of shear modulus G_{RL} estimated by Timoshenko theory. The values are standardized, and the comparisons are made from different testing times (Fig. 36). The cyan line indicates the 0 difference (standardized value = 1), and two red lines indicate the $\pm 5\%$.

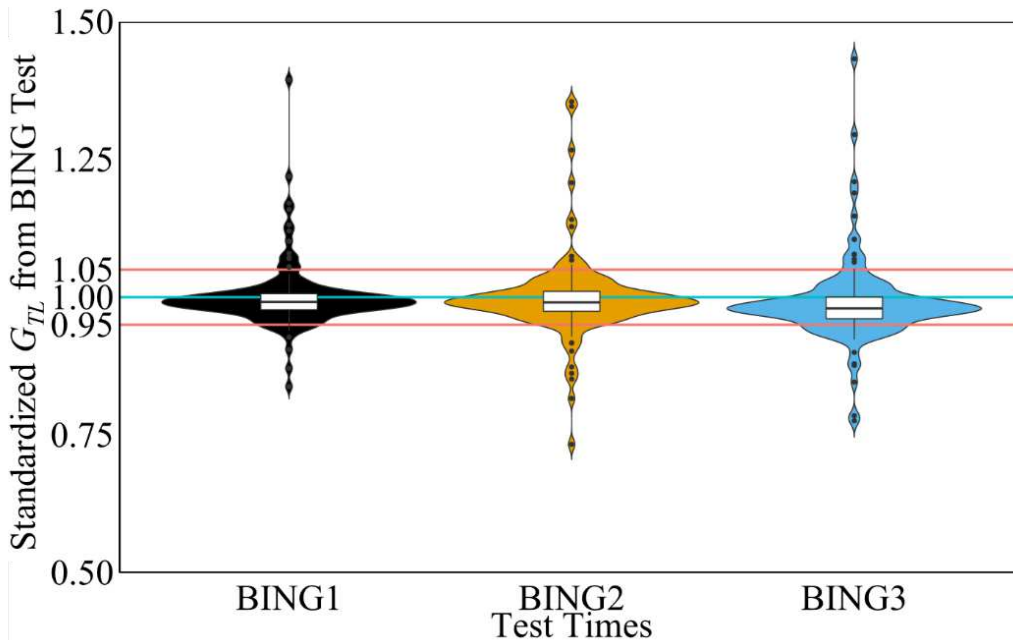


Fig. 62 The comparison of shear modulus G_{TL} estimated by Timoshenko theory. The values are standardized, and the comparisons are made from different testing times (Fig. 36). The cyan line indicates the 0 difference (standardized value = 1), and two red lines indicate the $\pm 5\%$.

III.E.2. *Dynamic mechanical properties comparison between different methods*

The dynamic mechanical tests are then compared, which are BING (B, §III.C.1), Ultrasonic (US, III.D), and Vybris (V, §III.C.2). The BING method calculates the MOE and estimates the shear modulus by frequencies from different vibration modes. On the contrary, the US is a quasi-static measurement, which measures the speed between probes (emitter and receiver) with a high-frequency compressive wave. At the same time, it is known that the dynamic modulus' measurement is frequency-dependent, at least when wide-bands of frequencies are considered. The higher frequency gives a higher modulus (Haines et al. 1996; Ouis 2002; De Borst and Bader 2014; Chauhan and Sethy 2016).

On the other hand, the frequency dependence is very small, or even negligible, in the frequency range of approx. 100 to 3,000 Hz (Ono and Kataoka 1979), as considered in the conducted vibrational measurements. The US measurement's interest is that it provides information of six moduli (E_L , E_R , E_T , G_{LR} , G_{LT} , and G_{RT}) (considering wood as orthotropic material) from one sample. The other dynamic properties' measurement in the present study is the Vybris test. The Vybris measurements' frequency is in the comparable range to the 1st, fundamental frequency from the BING measurements. However, Vybris measurement could be seen differently with three aspects from BING. Firstly, the very thin specimen would reflect a more local effect of variations in mechanical properties. Secondly, the anisotropic properties could be more prominent if the material is very heterogeneous in its orientation. Lastly, the shear modulus (storage G modulus) measurement is a direct measurement and is also accompanied by measurements of torsional damping properties.

The acquired values of the same properties but obtained by different methods are then compared with each other for the longitudinal elastic modulus (E_L) and in-plane shear moduli G_{RL} (or G_{LR}) and G_{TL} (or G_{LT}). The BING and Vybris methods tests have two testing configurations (BING) and two types of specimens (Vybris) for the longitudinal elastic modulus E_L . For this reason, the E_L or MOE_L only refers to the quarter-cut (L-R) specimens for the Vybris test, or to the measurement by hitting the bars on their quarter-cut (L-R) surface (bending along the T direction) for the BING method, respectively, to avoid confusing the noting expression. Also, as mentioned at the beginning of the current Chapter III, due to the material's sawing pattern could not always fit in the theoretical definition of radial and tangential direction, the "R" notation in the following represents the material's direction which is closer to the theoretical radial direction, and "T" is the direction closer to the tangential direction. Since the material's

preparation did not include the reorientation from the standard bar to the ultrasonic specimen or the Vybris specimen, the directional mechanical properties keep the same global behaviour.

III.E.2.a) Longitudinal modulus of elasticity by BING, Vybris and Ultrasound

The longitudinal modulus (E_L) comparison is based on the result of the Vybris test (E_{L-V}) on the x -axis (Fig. 63). The E_V values are averaged between two paired specimens (§III.C.2.b). For BING, the MOE (MOE_B) values are from the measurement by hitting the bars on their quarter-cut (L-R) surfaces. From the US test is the E_{US} . Herein, there's no BING measurement for the BePVar species. Therefore, the sample quantity of B-V is 119 and for US-V is 122.

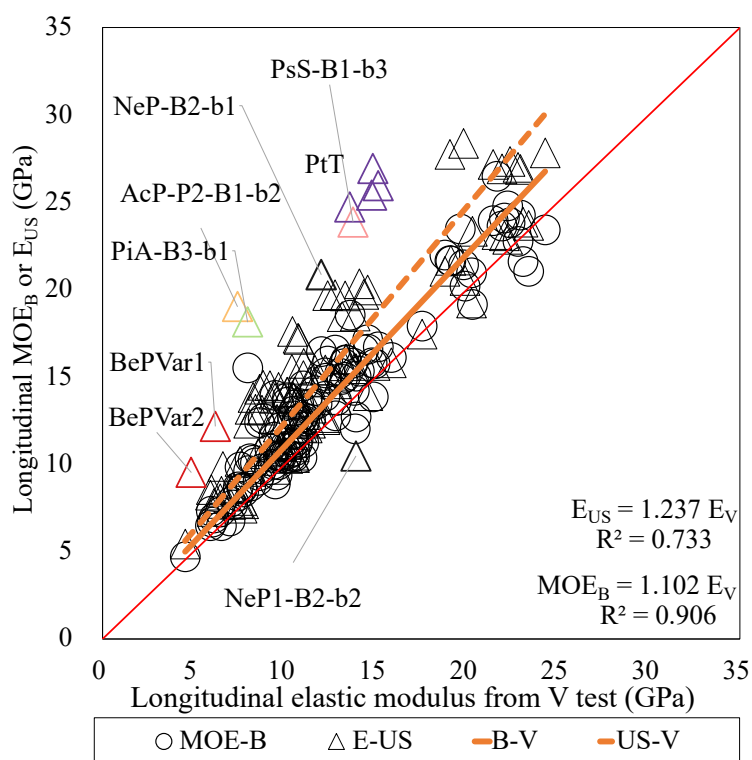


Fig. 63 The comparison of longitudinal elastic modulus (E_L) as measured by three methods BING, Vybris and ultrasounds.

The difference between E_L values obtained by BING and Vybris is about 1.10 times higher for BING than for Vybris. As both methods had already been compared (Brémaud et al. 2012) and gave very similar values of E_L (only +1% for BING than Vybris, or a factor 1.01), the larger discrepancy observed here probably reflects structural effects, local heterogeneities in grain angles for the studied figured wood. The ultrasonic result is around 1.24 times higher than the E_V values. In general, the values' comparison between the ultrasonic and vibrational V tests fit the range from the literature. In Rakotovolononimanana et al., (2015), the difference of MOE values (in MPa) between the US (US10) and acoustic method (A, in the literature) is [MOE

US10] = 1.18 [MOE A]-2354. In Haines et al.(1996) research, the values of E_L obtained by ultrasound was, on two softwoods, between 1.17 and 1.22 times higher than for natural bending vibrations (as BING). While in the present study, the E_L values obtained by the US are 1.14 times higher than those by BING.

The extreme values of differences (if $\text{Value}_{\text{US}}/\text{Value}_{\text{Vybris}} - 1.237$ fits the conditions: > 0.5 or < -0.5) between the US and V tests are noted in the figure (Fig. 63). When observing the proportion of those extreme values inside the corresponding species, AcP-P2-B1-b2 (1 specimen out of 8), PiA-B3-b1 (1 of 4), and PsS-B3-b1 (1 of 6), it can be seen that extreme values are a minority in these species. Yet when comparing the US and V tests results, the species PtT (4 specimens out of 4) and BePVar (2 of 3) contains mostly “extreme values” compared with the others, which means the extreme values could be not extreme, but the common result for these species. The only common physical characteristics of these two species are the small and fine grain variation. Unlike PtT, BePVar is the Mazur Birch (Karelian Birch), which has no certain grain direction of its figure. No determinable smoothing curve was found during estimating MFA and GA (§II.C.2 and §II.C.3), which means the structure through XRD is more isotropic in the measuring setting at the measured points. For PtT, its interlocked grain is very fine (medium amplitude and small period), and also mixed with wavy grain. Still, those descriptions do not explain the difference between US and V for the BePVar and PtT. The author assumes the phenomenon is not about the grain structure but more about the dimensional effect caused by the grain structure.

III.E.2.b) *Shear moduli by BING, Vybris and Ultrasound*

After the comparisons between three methods for the longitudinal elastic moduli, the other comparisons are made on the shear moduli of G_{RL} and G_{TL} . For the B method, its shear moduli were acquired by the in-plane rigidity of Timoshenko theory from different bending modes. According to the experimental vibration triggering (hitting) direction (§III.C.1), two shear moduli were acquired: G_{RL} (GRLB) and G_{TL} (GTLB). On the contrary, the shear moduli’s measurement from the US method (§III.D) depends on the polarizing probes’ positions to the sample’s direction, i.e., G_{LR} and G_{RL} . However, in the present study, the material is treated as orthotropic material (angle-ply orthotropy), and an assumption is made about the symmetry of shear moduli. The paired values of shear moduli are thus averaged, e.g., G_{LR} & G_{RL} , G_{LT} & G_{TL} , and G_{RT} & G_{TR} . The notation for the US will be then stated as G_{RL} (GRLUS) and G_{TL} (GTLUS) in the following, for the average of G_{LR} and G_{RL} (G_{LT} and G_{TL}), respectively. On the contrary,

the V method uses the torsional vibrational test for measuring the shear moduli (§III.C.3). The shear moduli acquirement depends on the specimens' wider plane, G_{RL} (GRLV) for the quarter-sawn (L-R) specimen and G_{TL} (GTLV) for the flat-sawn (L-T) specimen.

The comparisons were made separately for these two moduli, G_{RL} (Fig. 64) and G_{TL} (Fig. 65). For the G_{RL} , the sampling of the V specimens is two times more numerous than the B and US. Because the grain pattern is the same in this plane of specimens, the G_{RL} values are averaged. Also, the BePVar specimens have no measurement from the B method, so the comparing quantity between US-V is 122 and for B-V is 119. On the contrary, the comparison of G_{TL} modulus is different. The quantity of the V specimens is also two times higher than the US and the B measurements. However, because the flat-sawn (L-T) specimens of V could be seen as a single layer (i.e., relatively homogeneous grain angle, for most grain patterns), the meaning of the in-plane shear modulus G_{TL} for V is different from the US and B methods (for which specimens are still layered structures including different grain angles). So, the comparison is made based on two V flat-sawn (L-T) specimens. The quantity is 244 for US-V and 238 for B-V, where values from two V specimens are each time compared to values from one B or US specimen. As a result, the correlation coefficients R^2 are also lower than the G_{RL} one.

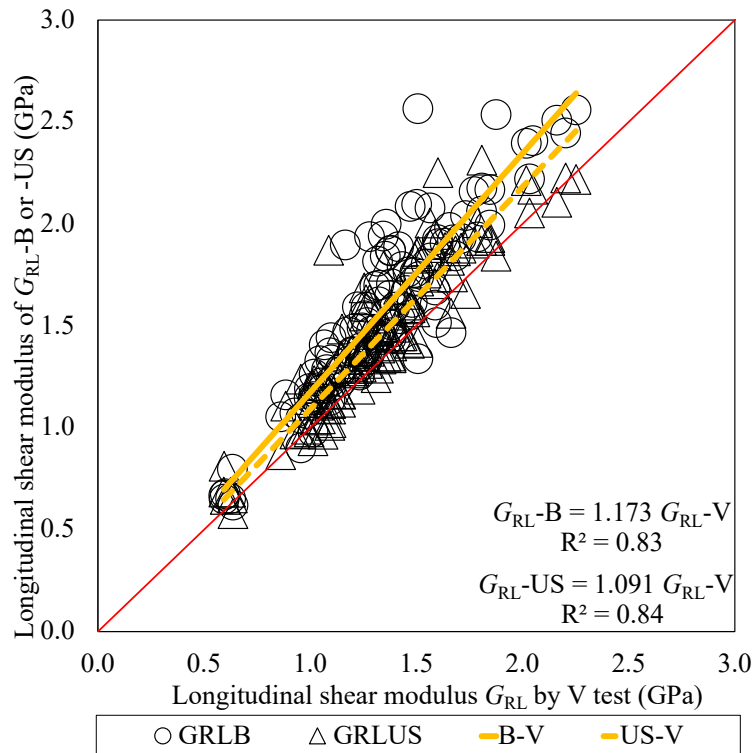


Fig. 64 The comparison of longitudinal shear modulus, G_{RL} between BING, Vybris and ultrasounds test.

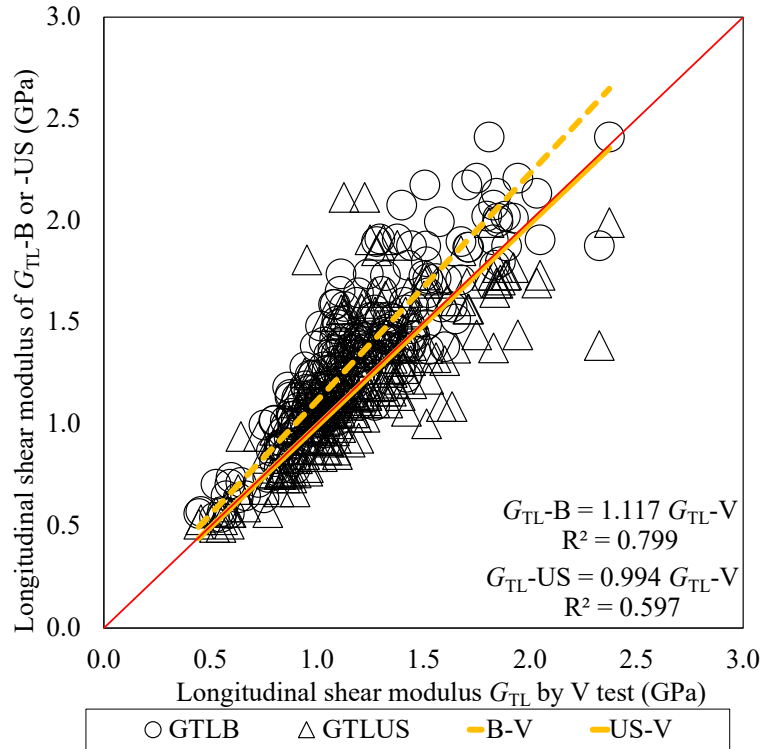


Fig. 65 The comparison of longitudinal shear modulus, G_{TL} between BING, Vybris and US test.

While comparing two analyses of G_{RL} and G_{TL} , the phenomenon in common but different from the comparison of longitudinal elastic modulus (E_L) is that the US values are now much closer to the V values. The difference between US and V is less than 10% for the G moduli. However, between the B and V values, the difference is more than 10% larger for BING values. This result disobeys the theoretical trend for dynamic properties, in which the moduli values should be frequency-dependent. Also, the differences between B and V in the comparisons of longitudinal elastic modulus and in-plane shear moduli are more consistent, both about 10%. On the contrary, the difference is more significantly distinctive when comparing the longitudinal elastic modulus and the shear modulus. The correlation between US and V is 1.23 times for E_L , but G_{RL} is 1.09 times, and G_{TL} is 0.99 times.

The anisotropic ratio between two in-plane shear moduli (G_{RL} and G_{TL}) are also compared between these three different methods. Due to the quantity of the flat-sawn (L-T) and quarter-sawn (L-R) specimens of the V test, with paired specimens, each time, the shear moduli values are averaged, respectively (L-T1 with L-T2, and L-R1 with L-R2). The result on this anisotropy ratio ranges from 0.5 to 2, with a majority being close to 1.2, which is consistent with previous values from the literature on many species, where this ratio is on average of 1.15 to 1.3 (Guitard and El Amri 1987; Brémaud et al. 2011b). Yet their values show no correlations (of their G_{RL}/G_{TL}

ratio) between different methods (Fig. 66). This anisotropic ratio appears individual- and test-dependent, although the values of each shear moduli are highly correlated between different methods (Fig. 64 and Fig. 65).

One reason for having no correlation of the anisotropic ratio G_{RL}/G_{TL} between different methods could be that, as previously stated, the specimens for G_{LT} measurement by Vybris include much more local variations in grain angle. This means a scale effect due to local heterogeneities that are measured by V but not by B or US. Another reason could be that the BING method's shear moduli calculation is based on frequencies of successive vibration modes. While in the present study, the triggering method for the vibrational movement is with a wooden mallet, the bar's cross-section is square. The square cross-section's advantage is to measure the shear moduli equally in two planes (G_{RL} and G_{TL}). However, the disadvantage is that the triggering could induce three possible dynamic movements corresponding to 3 frequencies: vertical bending, horizontal bending, and torsional bending. Because of the square cross-section, multiple peaks can appear in different frequency modes and could be approached but not distinguishable for their corresponding movement. This could bias the observed G_{RL}/G_{TL} ratio.

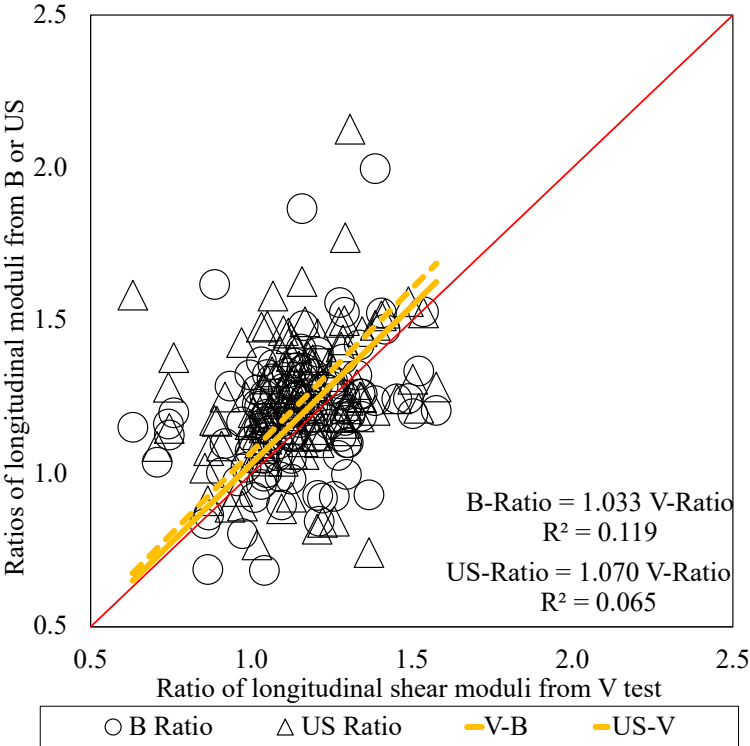


Fig. 66 The comparisons of the anisotropic ratio between shear moduli G_{RL}/G_{TL} were measured using three methods and on three specimens' dimensions: BING, Vybris and ultrasounds.

III.E.2.c) *Longitudinal damping by internal friction from BING and Vybris*

While comparing the properties from three testing methods for elastic moduli, only two of them can measure the material's internal friction (damping, $\tan\delta$, or Q^{-1}), i.e., BING (B) and Vybris (V). The B measurement included damping values obtained from tests in two experimental configurations (i.e., hitting the standard bars either on their flat-sawn L-T surface or on their quarter-sawn L-R surface). However, only values obtained from hitting the standard bars on their quarter-sawn (L-R) surfaces are used in comparisons in the general perspective of this section. Also, according to the experimental plan (§III.C.1.c), there were four conditioning steps for the BING measurements (Fig. 36). They are BING0 (0 days, after cutting standard bars) at uncontrolled ambient conditions; then BING1 (42 days), BING2 (52 days), and BING3 (60 & 72 days) during the stabilization in a climatic room nominally set at 20°C and 65% RH.

The first part of this section compares the damping ($\tan\delta_L$) and conditioning time, i.e., BING0, BING1, BING2, and BING3 (Fig. 36). The subsequent damping values are standardized based on each specimens' value as measured in BING0 (Fig. 67). The values' ranges are varied, and the extreme values/outliers were removed. The removing reason is believed to be due to the triggering method for setting the specimen in vibration in the B test (i.e., hitting the specimens with a wooden-head standard mallet). However, the damping values' general decreasing trend is still detectable from BING1 to BING3. The mass of specimens increased by +0.76% between BING0 and BING3. However, it was stable between BING2 and BING3, meaning the specimens' MC was probably stabilized from BING2 at 50 days. However, the damping $\tan\delta_L$ was still decreasing between BING2 and BING3. It probably reflects the phenomenon that damping takes a much longer time to be stabilised than the time indicated from MC evolutions (Brémaud and Gril 2021a). More surprisingly, values at BING3 were, on average, -17% lower than at BING0, while the MC had slightly increased. Normally, damping increases with increasing MC, by approx. +3.7% per % MC (Brémaud and Gril 2021a). Therefore, this decrease in damping for BING3 is not explainable by moisture content itself. However, damping always increases due to destabilisation after changing humidity conditions. It then slowly decreases again, and this destabilisation can be more important than the MC effects in the case of small-MC steps, furthermore the destabilisation lasts longer for small MC-steps (Brémaud and Gril 2021b). This probably indicates that, on relatively massive specimens such as the standard BING-bars, the destabilisation of $\tan\delta$ lasts longer than on the small-scale specimens used for Vybris. We cannot be sure that $\tan\delta$ had been stabilized till the last measurement after 72 days (see also III.E.1.c).

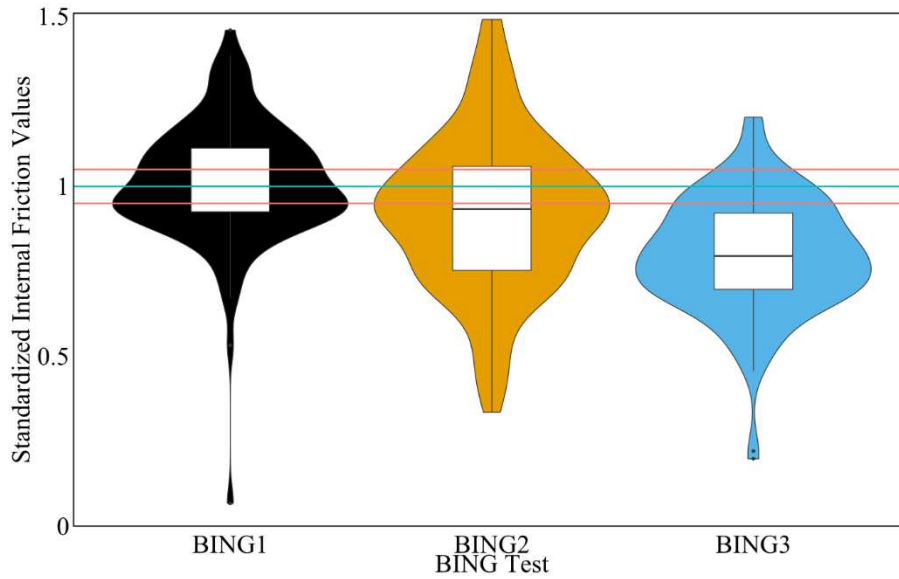


Fig. 67 The standardized $\tan\delta_L$ values of BING1, BING2, and BING3 tests (in the order of the testing time, 42 days, 52 days, and 60-72 days after starting the conditioning in a climatic room set at 20°C and 65% RH). The cyan line indicates the non-changed values, and the red lines indicate $\pm 5\%$ differences from the values in uncontrolled ambient conditions.

Still, the BING3 values are assumed to be the most stabilized ones compared with the other testing times. Therefore, its values are used to represent the damping values of the B test, and the values are grouped by species (Fig. 68).

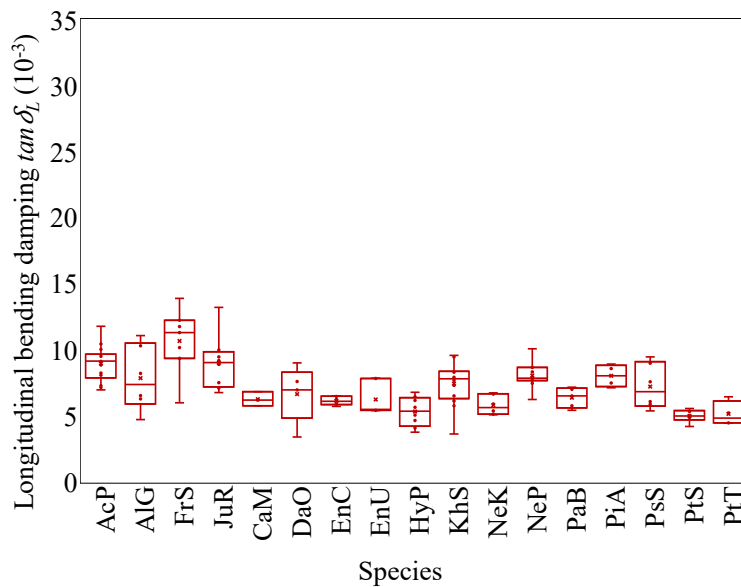


Fig. 68 The longitudinal bending $\tan\delta_L$ values grouped by the species from the last BING test (BING3). The values are from the BING test made by hitting on the L-R plane.

On the contrary, for the V test, the measurement is only in one environmental condition, which is 20°C and 65 % RH (as for BING), and the conditioning lasting at least four weeks, as usually considered enough for stabilisation on these small-scale specimens. The values are presented here by the species.

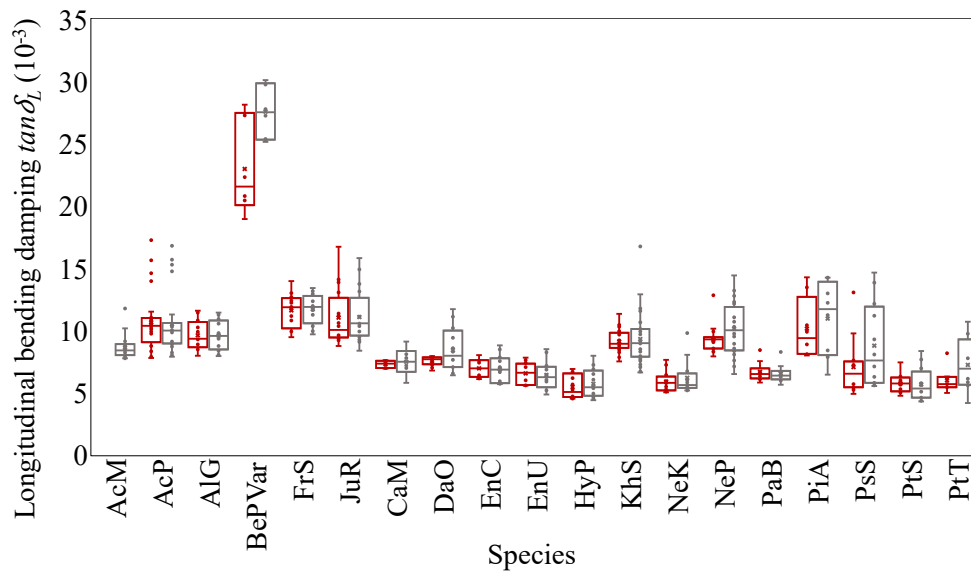


Fig. 69 The longitudinal bending damping $\tan\delta_L$ values are grouped by the species. The red colour is for the quarter-sawn specimens (wider side on the L-R plane), and the grey colour is for the flat-sawn specimens (wider side on the L-T plane).

Globally, the differences between species in damping $\tan\delta_L$ values are comparable between B and V data (although the scale of the *y-axis* is large because of the very high values of BePVar, tested only by V). Yet, differences between species are more finely discriminated by the Vybris values of $\tan\delta_L$. For Vybris tests, the measured $\tan\delta_L$ on the flat-sawn specimens tend to show either larger values, or a wider range of values inside a species, than those measured on the quarter-sawn specimens (except for the wavy grain species). It indicates that the flat-sawn specimens include wider local variations in grain angle.

As previously mentioned, only the quarter-sawn (L-R) specimens' values from the V test and the values tested by hitting the bars on their quarter-cut surfaces (L-R) from the B test are used for the comparison (Fig. 70). The B values are according to the damping values of BING3, and the V values are average from the pair of two quarter-sawn specimens. The values of $\tan\delta_L$ by BING appear here 0.86 times smaller than those by Vybris. However, in a previous study, a relation close to unity had been found between these two methods (Brancheriau et al. 2010). Some possibilities, which cause the correlation to be weaker, could be due to the vibration triggering method of the BING test. Also, as mentioned before, when testing wood with strong

grain deviations in the form of a square-section bar, modes of vibration could include indissociable double-peaks that would reduce the viability of signal-processing for calculation of internal friction by BING. While in Vybris, the geometry of the specimens, and the fact that it is a direct measurement of one given mode by frequency sweep in forced vibrations, makes this method more robust for the types of wood under study.

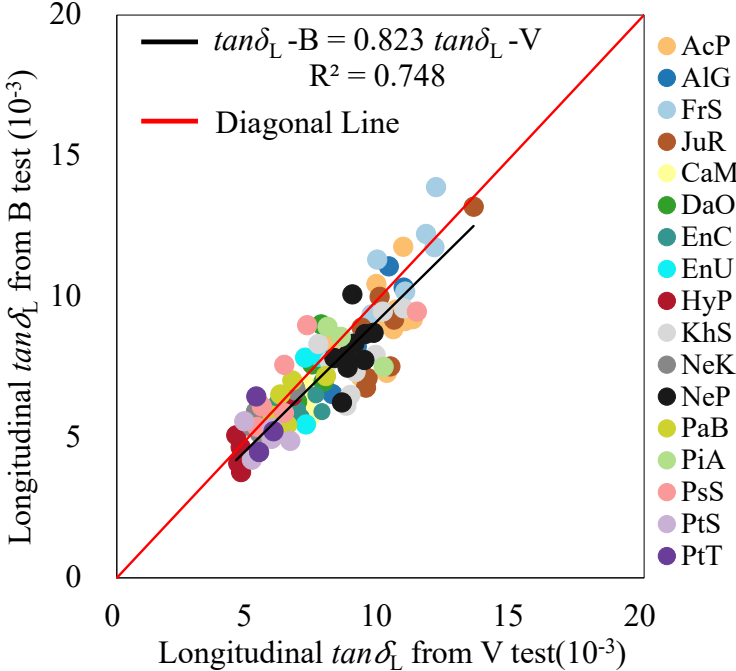


Fig. 70 The comparison of $\tan\delta_L$ values acquired from the BING (BING3) and Vybris test (average of two quarter-sawn specimens).

III.E.2.d) Longitudinal and torsional damping by Vybris-bending and Vybris-torsion

Furthermore, the V test includes two types of damping values: longitudinal ($\tan\delta_L$) (Fig. 69), but also in-plane torsional dampings ($\tan\delta_G$) thanks to the new setup in torsion presented in this work (§III.C.3). The notation is then written as $\tan\delta_{GTL}$ and $\tan\delta_{GRL}$ for flat-sawn specimens (wide side in L-T plane) and quarter-sawn specimens (wide side in L-R plane), respectively.

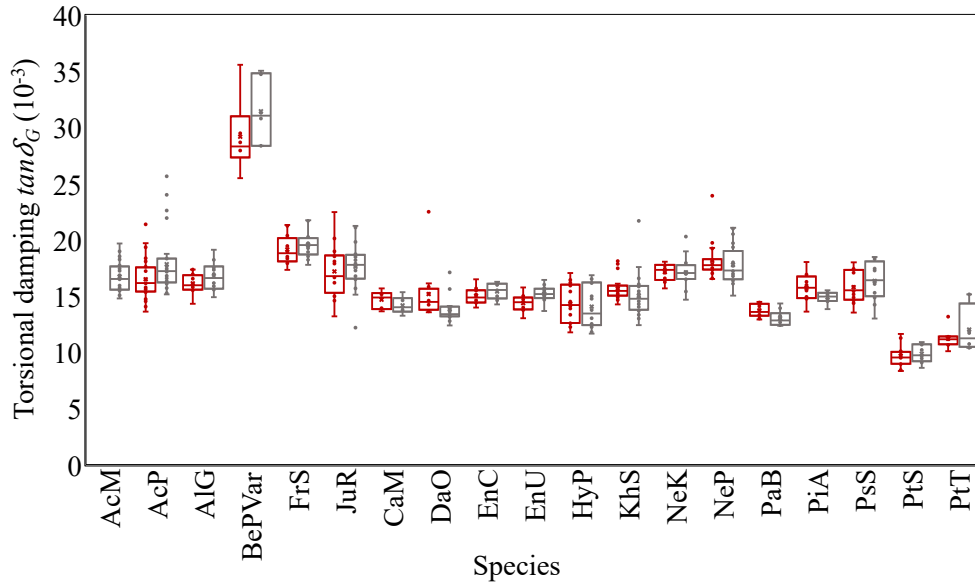


Fig. 71 The in-plane shear damping values are grouped by the species. The red colour is for the quarter-sawn (L-R) specimens ($\tan\delta_{GRL}$), and the grey colour is for the flat-sawn (L-T) specimens ($\tan\delta_{GTL}$).

After comparing the $\tan\delta_G$ and $\tan\delta_L$ by all the species, another comparison on the aspect of anisotropic damping between $\tan\delta_G$ and $\tan\delta_L$ was made separately for the Vybris L-R and L-T specimens, i.e., $\tan\delta_{GRL}$ versus $\tan\delta_{L-LR}$ and $\tan\delta_{GTL}$ versus $\tan\delta_{L-LT}$ (Fig. 72). The coefficient of correlations (for all the materials) is moderate for both L-R and L-T specimens, i.e., $r = 0.79$ for both. Also, the $\tan\delta_G$ is about 1.65 times higher than $\tan\delta_L$. This anisotropic ratio obtained here on a wide range of wood with grain deviations is smaller than the average ratio on hardwoods, i.e., 2.14 for $\tan\delta_{GRL}/\tan\delta_L$ and 2.27 for $\tan\delta_{GTL}/\tan\delta_L$, from a previous literature review (Brémaud et al. 2011b). On the extreme, BePVar species has exceptionally high longitudinal and shear $\tan\delta$, and their anisotropic ratios are lower than the others.

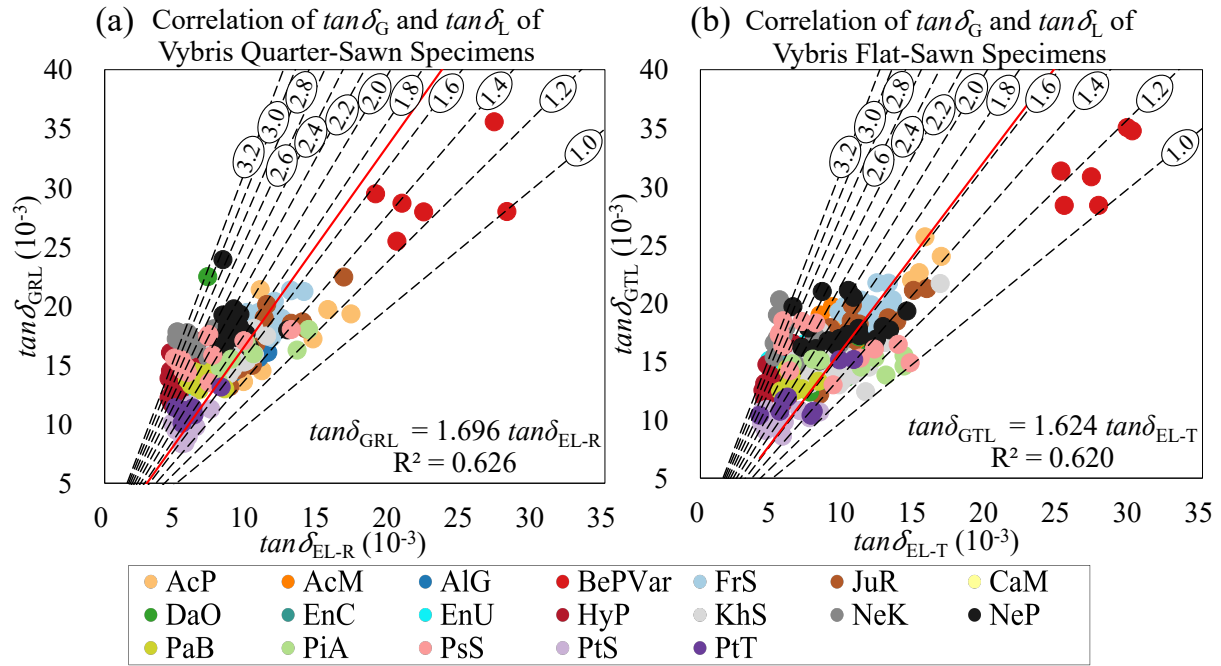


Fig. 72 The correlation of anisotropic damping of the Vybris R and T specimens. The solid lines in (a) and in (b) are the regression lines of all the data points. The dashed lines represent the anisotropic ratio of longitudinal shear and bending damping from 1.0 to 3.2.

While comparing this ratio of anisotropy, the proportions $\tan\delta_G/\tan\delta_L$ is physical- and chemical-factors dependent. The factors include the MC, fibre's shape, fibre's orientations (in-plane and off-axis), a volumetric ratio (fibre and matrix), chemical composition, MFA, and S1 layer (Sun et al. 1985; Suarez et al. 1986; Obataya et al. 2000; Chandra et al. 2002; Yamamoto and Kojima 2002; Brémaud et al. 2010, 2011b; Khashaba 2015). In the present study, there's no involvement for studying all these aspects, but rather to summarize the range of this anisotropy. Thus, the ratios from 1 to 3.2 (dashed line, 0.2 intervals) are drawn in the figures (Fig. 72a and Fig. 72b). Generally, in the view of among species or within species, the L-R specimens are more aggregated, and the L-T specimens are more dispersed, except that the BePVar and AcP are opposite to them. Understandably, the off-axis and mixture GA (grain angle) would be more the factors while comparing the results between L-R (Fig. 72a) and L-T (Fig. 72b).

III.E.3. *The Range of Variability for the Mechanical Properties of Figured Woods*

III.E.3.a) *General comparison between species and between methods*

The dynamic mechanical properties of all the concerned materials are summarized in this section. The comparison is between the species scale to demonstrate the mechanical properties' diversity and the range of the mechanical properties by species. Therefore, the presentations in this part are the mean value (μ) of species and the sample's coefficient of variation (COV, in % = σ/μ , where σ is the standard deviation) within the species. In the end, the total range of all the specimens' physical and mechanical properties are listed (noted *All* in following Tables).

The arrangement of the below tables (Tab. 16, Tab. 17, Tab. 18) follows the alphabetical order of the species while also grouping the temperate species (from AcM to JuR) and tropical species (from CaM to PtT). The abbreviation code to the corresponding species was listed in Tab. 3 in §II.C.1. The specimens' quantities of each species are firstly listed for each method (Tab. 15). The specimens' quantity is the same for the BING and US methods because of following the multi-dimensional experimental plan, except that the US has three additional BePVar specimens. The thin specimens' sampling results in the Vybris test are two times that of BING and US (Fig. 28 in part III.C) and one additional species: AcM. Also, because of the two planes of cutting/sampling, there are the quarter-sawn L-R specimens (V-LR) and the flat-sawn L-T specimens (V-LT) for the Vybris specimens.

In Tab. 16 and Tab. 18, there is no difference between the densities measured on different specimens' sizes in the same species. When comparing it with the density of ultrasonic specimens (Tab. 18), most of them are the same, while BePVar's US specimens' density is lower (but still in the range). This could be because the Karelian birch has a more heterogeneous figure with some void structure. Thus, the density would vary when comparing a long specimen (V-LR and V-LT) with the small cube (US).

The comparisons between methods B, V, and US for the dynamic elastic modulus in axial direction were described in section III.E.2.a), for the in-plane shear moduli in the III.E.2.b) and for the damping in the III.E.2.c) and III.E.2.d). Instead, the comparison here is for the diversity of the mechanical properties and also the density. In the below figure (Fig. 73), the COV (in %) are listed for the mechanical properties (Fig. 73b to f) and the density (Fig. 73a) of specimens from different tests (B, US, and V). Herein, the B values are as in the previous sections that the values are from the ones hitting the bar-specimens on its quarter-sawn (L-R plane) surface. And the V results are from the quarter-sawn (wider side in L-R plane) specimens, except that the G_{TL}

is from the flat-sawn L-T specimen (V-LT). Thus, the first comparison is the COV between species, including different methods.

In general, the mechanical properties' COVs are in a similar range between three methods (B, V, and the US), except for the E_L (Fig. 73c) and E_L/γ , for which the COVs among PiA, PsS, and PtS species have a more significant difference when comparing between three methods. The author assumes the possible reason for the V specimen is the local sampling. The wood has more considerable grain variation regarding either the period or the amplitude of the grain pattern. The V specimen is much thinner (thickness: 2 mm) than the one for B (thickness: 20 mm) and US (thickness: 20 mm) specimens so that the local variation is much more demonstrated in V. On the contrary, the B test involves the selection of frequencies for successive modes of natural vibrations, and the higher vibration modes are involved in the calculation. So, during the test, the PiA, PsS, and PtS which have larger GA, tend to produce higher-mode frequencies that were not the exact theoretical ones but affected the MOE values, consequently causing the higher COV (test-dependent). Instead, the US's COV is much smaller than the other two. After all, the specimen's quantities for those three species are relatively lower than the others (while they also have larger GA variation).

The unstable values produced with the B measurement due to the manner of doing the test (specimen hit with a wooden mallet) are also shown in the result of the two longitudinal shear moduli (Fig. 73b, d). Although PiA has the largest GA, it is not enough to explain that its COV of G_{RL} is so much above the other variations (coming from material and/or from experimental uncertainties).

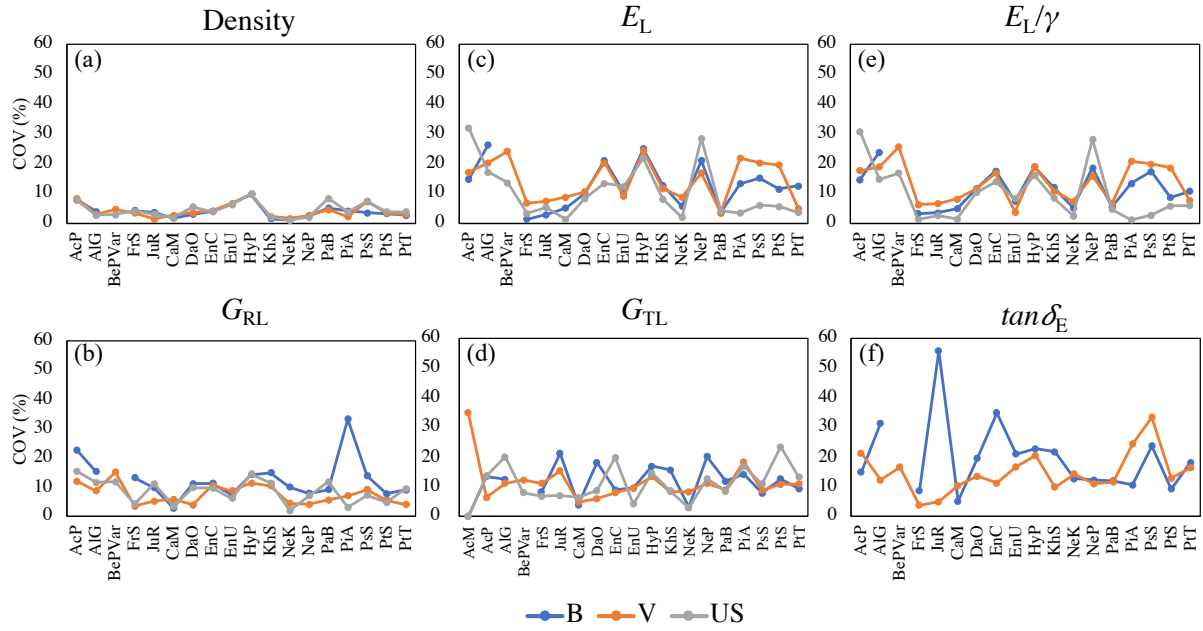


Fig. 73 The comparison of different properties' COV among the species and methods. The line between the species doesn't mean the data are continuous.

Tab. 15 Specimen quantity of each testing method

Species	BING	US	V-LR	V-LT
AcM				21
AcP	14	14	28	28
AlG	6	6	12	12
BePVar		3	6	6
FrS	8	8	16	16
JuR	8	8	16	16
CaM	3	3	6	6
DaO	6	6	12	12
EnC	6	6	12	12
EnU	6	6	12	12
HyP	8	8	16	16
KhS	13	13	26	26
NeK	6	6	12	12
NeP	10	10	20	20
PaB	5	5	10	10
PiA	4	4	8	8
PsS	6	6	12	12
PtS	6	6	12	12
PtT	4	4	8	8
All	119	122	244	265

Tab. 16 The mean values and the coefficient of variation (COV, %) of species' density, longitudinal elastic modulus and in-plane shear moduli for the different species and from different methods. Specimen quantity: Tab. 15

Species	Density(g/cm ³)*			E _L (GPa)			G (GPa)			
	B	V-LR	V-LT	B	V-LR	V-LT	B-RL	B-TL	V-RL	V-TL
AcM			0.57 23%			11.4 31%				0.92 35%
AcP	0.57 8%	0.57 8%	0.57 8%	9.0 15%	8.3 17%	8.3 20%	1.51 23%	1.17 13%	1.27 12%	1.02 6%
AlG	0.50 4%	0.50 3%	0.50 5%	9.27 26%	8.73 20%	8.48 24%	1.07 15%	0.81 13%	0.97 9%	0.79 11%
BePVar		0.74 5%	0.75 4%		5.89 24%	4.62 19%			1.19 15%	1.09 12%
FrS	0.79 4%	0.79 4%	0.78 5%	12.96 21%	12.69 20%	12.07 22%	1.87 11%	1.38 9%	1.56 11%	1.26 8%
JuR	0.60 10%	0.59 10%	0.60 9%	7.53 25%	7.08 24%	7.02 25%	1.72 14%	1.30 17%	1.26 11%	1.12 14%
CaM	0.60 4%	0.60 3%	0.61 6%	15.61 1%	13.24 7%	13.68 11%	1.21 13%	1.07 8%	1.07 4%	0.95 11%
DaO	0.37 4%	0.37 1%	0.38 8%	9.83 3%	8.53 7%	8.59 11%	0.67 10%	0.65 21%	0.61 5%	0.57 15%
EnC	0.66 2%	0.65 3%	0.67 4%	15.79 5%	13.57 9%	14.68 13%	1.25 3%	1.04 4%	1.14 6%	1.02 5%
EnU	0.67 3%	0.66 4%	0.67 3%	14.48 10%	13.04 11%	13.74 12%	1.21 11%	0.97 18%	1.05 4%	0.87 6%
HyP	1.03 6%	1.01 7%	1.01 7%	22.52 10%	21.18 9%	20.92 15%	2.31 7%	1.85 10%	2.04 9%	1.78 10%
KhS	0.76 2%	0.75 2%	0.75 3%	12.54 13%	10.79 12%	11.05 18%	1.74 15%	1.38 16%	1.42 11%	1.16 8%
NeK	0.85 1%	0.84 2%	0.84 2%	22.34 6%	21.24 9%	20.92 9%	1.38 10%	1.19 3%	1.32 5%	1.22 8%
NeP	0.76 2%	0.75 3%	0.76 5%	11.39 21%	10.33 17%	10.36 31%	1.43 8%	1.41 20%	1.27 4%	1.23 11%
PaB	0.52 5%	0.51 5%	0.52 7%	12.89 4%	11.11 4%	11.99 13%	1.11 9%	0.98 12%	0.98 6%	0.90 9%
PiA	0.90 4%	0.89 2%	0.90 8%	13.58 13%	11.44 22%	11.78 34%	1.97 33%	2.15 14%	1.71 7%	1.86 18%
PsS	0.91 4%	0.89 7%	0.88 10%	20.76 15%	20.33 20%	18.91 34%	1.64 14%	1.48 8%	1.56 9%	1.48 9%
PtS	0.75 3%	0.74 3%	0.72 4%	12.82 11%	10.88 20%	11.95 16%	1.71 8%	1.71 13%	1.44 6%	1.36 11%
PtT	0.90 3%	0.88 3%	0.87 (4%)	16.07 13%	14.59 5%	13.53 32%	2.02 9%	1.91 9%	1.79 4%	1.64 11%
All	0.71 23%	0.71 23%	0.69 23%	13.52 35%	12.15 39%	12.09 40%	1.55 28%	1.31 29%	1.33 25%	1.16 29%

*The density's calculation is based on the last weight measurement of the BING test (BING3), which is in the condition of 20°C and 65 % RH.

B: Values of BING specimen; V-LR: Values of Vybris quarter-sawn (L-R) specimen; V-LT: Values of Vybris flat-sawn (L-T specimen); V-RL: G_{RL} values from the Vybris L-R specimen; V-TL: G_{TL} values from the Vybris L-T specimen

Tab. 17 The mean values and the coefficient of variation (COV, %) of species' longitudinal specific modulus of elasticity (E_L/γ), longitudinal bending damping ($\tan\delta_L$) and shear (torsional) damping ($\tan\delta_G$) from different methods.

Species	E_L/γ (GPa)*			$\tan\delta_L$ (10^{-3})			$\tan\delta_G$ (10^{-3})	
	B	V-LR	V-LT	B-LR	V-LR	V-LT	V-RL	V-TL
AcM			19.86 10.76%			8.58 10.71%		16.74 8.17%
AcP	15.8 15%	14.5 18%	14.5 20%	9.0 15%	10.6 21%	10.5 22%	16.5 11%	17.9 15%
AlG	18.45 24%	17.43 19%	16.98 22%	7.85 31%	9.58 12%	9.55 13%	16.13 5%	16.78 7%
BePVar		8.00 26%	6.18 18%		22.97 17%	27.57 8%	29.21 12%	31.47 9%
FrS	16.23 18%	15.90 17%	15.34 19%	9.79 35%	11.58 11%	11.68 10%	19.16 7%	19.59 6%
JuR	12.50 19%	11.85 19%	11.67 19%	9.01 23%	10.99 21%	11.05 19%	17.19 14%	17.63 13%
CaM	25.83 3%	22.07 6%	22.46 11%	6.26 9%	7.25 4%	7.45 15%	14.69 5%	14.18 5%
DaO	26.28 4%	23.26 7%	22.65 11%	5.61 56%	7.52 5%	8.39 22%	15.20 16%	13.84 9%
EnC	23.76 5%	20.77 8%	21.90 11%	6.13 5%	6.92 10%	6.82 16%	15.02 5%	15.42 4%
EnU	21.67 12%	19.68 12%	20.66 12%	6.25 20%	6.52 14%	6.39 18%	14.39 5%	15.22 5%
HyP	21.88 7%	20.93 4%	20.75 11%	5.32 21%	5.41 17%	5.67 20%	14.32 12%	14.07 13%
KhS	16.52 12%	14.38 11%	14.77 17%	7.44 22%	9.07 10%	9.28 24%	15.67 6%	15.01 13%
NeK	26.29 5%	25.37 7%	24.85 9%	5.81 13%	5.85 14%	6.15 23%	17.16 4%	17.12 9%
NeP	14.89 19%	13.71 16%	13.55 28%	8.06 12%	9.21 11%	10.09 21%	18.17 9%	17.78 10%
PaB	24.77 6%	21.67 7%	23.02 11%	6.37 12%	6.63 12%	6.48 11%	13.72 4%	13.03 5%
PiA	15.11 13%	12.85 21%	13.21 36%	8.03 11%	10.11 24%	10.91 28%	15.76 9%	14.88 4%
PsS	22.86 17%	22.87 20%	21.08 28%	7.22 24%	7.02 33%	8.73 39%	15.80 9%	16.36 11%
PtS	17.10 9%	14.72 19%	16.62 15%	4.98 9%	5.70 13%	5.61 24%	9.67 10%	9.88 8%
PtT	17.92 11%	16.66 8%	15.57 34%	5.14 18%	5.94 16%	7.18 31%	11.23 8%	12.03 17%
All	19.00 25%	17.19 28%	17.40 29%	7.24 30%	8.73 38%	9.10 42%	15.99 21%	16.20 22%

*The longitudinal specific modulus of elasticity's calculation is based on the last weight measurement of the BING test (BING3), after long stabilisation at 20°C and 65 % RH.

B: Values of BING specimen (BING3); V-LR: Values of Vybris quarter-sawn (L-R) specimen; V-LT: Values of Vybris flat-sawn (L-T) specimen; V-TL: $\tan\delta_G$ values from the Vybris L-T specimen; V-RL: $\tan\delta_G$ values from the Vybris L-R specimen

Tab. 18 The mean values and the coefficient of variation (COV, %) of the ultrasonic test results. Specimen quantity: Tab. 15

Species	Density (g/cm ³)*	E_L (GPa)	E_R (GPa)	E_T (GPa)	G_{RL} (GPa)	G_{TL} (GPa)	G_{RT} (GPa)	E_L/γ^* (GPa)
AcP	0.57	10.35	1.85	1.07	1.43	1.14	0.32	18.06
	8%	32%	25%	23%	15%	14%	21%	31%
AlG	0.49	10.47	0.97	0.55	1.11	0.88	0.23	21.19
	3%	17%	36%	14%	12%	20%	18%	15%
BePVar	0.70	10.53	2.20	1.66	1.72	1.66	0.41	15.02
	3%	14%	29%	35%	12%	8%	11%	17%
FrS	0.79	15.01	2.60	1.80	1.89	1.50	0.60	18.96
	4%	13%	9%	13%	10%	20%	14%	14%
JuR	0.60	8.66	1.67	1.21	1.43	1.27	0.46	14.46
	10%	22%	19%	29%	15%	15%	24%	16%
CaM	0.61	15.72	1.72	0.93	1.09	0.95	0.32	25.95
	4%	3%	3%	6%	4%	7%	4%	1%
DaO	0.37	13.33	1.04	0.45	0.68	0.55	0.08	36.03
	3%	5%	3%	11%	11%	7%	14%	3%
EnC	0.66	19.85	1.97	1.35	1.14	0.91	0.51	30.17
	2%	1%	6%	5%	4%	7%	4%	1%
EnU	0.66	14.25	1.83	0.95	1.05	0.76	0.48	21.50
	6%	8%	7%	9%	10%	9%	52%	10%
HyP	1.02	23.30	3.51	3.04	2.10	1.69	1.14	22.75
	6%	12%	10%	12%	6%	4%	15%	8%
KhS	0.76	14.59	2.29	1.48	1.59	1.08	0.58	19.30
	2%	8%	5%	27%	11%	9%	9%	8%
NeK	0.85	27.44	2.21	1.72	1.35	1.12	0.68	32.17
	1%	2%	6%	3%	2%	3%	10%	3%
NeP	0.76	11.59	2.24	1.81	1.38	1.24	0.62	15.33
	2%	28%	9%	23%	7%	13%	17%	28%
PaB	0.51	12.63	1.54	0.84	1.02	0.86	0.21	24.75
	8%	4%	12%	21	12%	9%	27%	5%
PiA	0.90	18.06	3.23	2.21	1.82	1.63	0.82	20.15
	4%	3%	8%	24%	3%	17%	10%	1%
PsS	0.90	22.76	2.47	1.83	1.57	1.31	0.67	25.28
	7%	6%	16%	20%	7%	11%	19%	3%
PtS	0.73	14.56	2.57	2.54	1.50	1.59	0.66	19.92
	4%	6%	10%	29%	5%	23%	7%	6%
PtT	0.89	25.76	3.04	1.71	2.03	1.53	0.83	29.06
	4%	4%	7%	23%	10%	13%	8%	6%
All	0.71	15.41	2.16	1.51	1.45	1.19	0.54	21.87
	23%	37%	32%	48%	26%	29%	49%	29%

*The densities were measured at 20°C and 65 % RH condition. The longitudinal specific modulus of elasticity is also based on this condition.

G_{RL} , G_{TL} , and G_{RT} values are mean pair values by each specimen's result.

III.E.3.b) *The most variable properties and the most stable properties*

A comparative analysis of the ranges of variation of the different measured properties was conducted to examine which properties are the most variable and which properties are the most stable. This also included a preliminary observation of the between-species versus within-species variability, which will be further detailed in Chapter IV. Two levels of synthetic COV were calculated. A “within-species” COV was calculated as the average of the individual COVs calculated for each species. A “between-species” COV was calculated from the average values of properties per species, i.e., by dividing the standard deviation between species by the average overall species. This analysis is shown in Fig. 74.

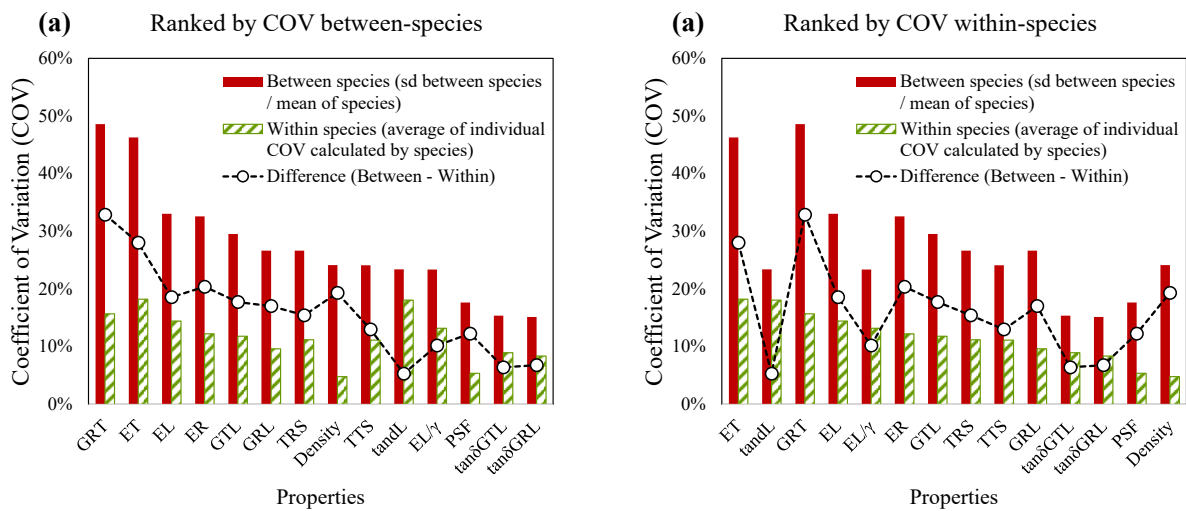


Fig. 74 Comparison of the coefficients of variations (COV) for the different measured properties, (a) ranked by order of higher variability between species; (b) ranked by order of higher variability within-species.

Between species, the most variable properties are the moduli (especially transverse ones, followed by longitudinal and in-plane shear). On the contrary, the density, shrinkage, longitudinal vibrational properties, FSP, and lastly, the torsional dampings are the least variable properties between species. While considering within species, the axial vibrational properties are now in the group of the most variable properties, together with the moduli (especially transverse ones), followed by shrinkage and in-plane shear (shear moduli being more variable than torsional dampings). FSP and density are the least variables, i.e., they are relatively stable within-species. From a last point of view, that of the respective parts of within- and between-species variability, the properties for which the variability is most strongly expressed within species (compared to differences between species) are the vibrational properties: longitudinal and shear dampings, and longitudinal specific modulus of elasticity.

III.E.3.c) Comparison of results on figured wood with literature data on “standard hardwoods”

The measured values comparison is made to compare the present results and selected literature data (Tab. 19). Incidentally, Tab. 19 also illustrates that the present dataset is rather complete as it includes data on the anisotropy both of elastic moduli, of damping coefficients, and of hygromechanical properties. In the present results, the E_L is in the range of the literature data. On the contrary, E_R , E_T and three shear moduli are larger than the literature values, especially the two transverse moduli. There might be a slight effect of density/specific gravity, that is usually considered as positively correlated to the moduli, since the specific gravity of the present study is slightly higher than the literature ones. However, when eliminating the influence of density by observing the specific modulus E_L/γ , it proves that the grain structure/orientation does affect much the longitudinal stiffness. Therefore, the $\tan\delta_L$ is also slightly higher than in references, according to the above idea (grain structure/orientation), but with a less pronounced difference. For the hygroscopic properties, the TTS is smaller, while the TRS is close to the literature values, showing the possibility of grain direction influence (most is tangential direction). Due to the PtS, PtT, and some species with lower MC_{sa} , the FSP is generally lower than the references.

Tab. 19 Comparing data from the present study with data from three wide-scale references. The data is hardwood only, and the average is made between the mean values of each species.

Ref	γ	E_L	E_R	E_T	G_{RL}	G_{TL}	G_{RT}	E_L/γ	$\tan\delta_L$	$\tan\delta_{GRL}$	$\tan\delta_{GTL}$	TTS	TRS	FSP
		GPa							$\times 10^{-3}$			%		
Guitard ¹	0.58	12.7	1.7	1	1.1	0.8	0.4	21.9						
Brémaud ²	0.66	13.5	1.7	0.9	1.2	1.0		20.5	8.1	17.3	18.4			
CIRAD ³	0.74	16.0						21.6				8.3	4.7	28.6
Present ⁴	0.71	13.3	2.2	1.5	1.4	1.2	0.5	17.9	8.9	16.0	16	7.2	5.0	24.6

1: Guitard and El Amri, 1987; 2: Brémaud et al., 2011; 3 : CIRAD Database

4: for present results, that γ , E_L , G_{RL} , G_{TL} , E_L/γ , $\tan\delta_L$, $\tan\delta_{GRL}$, $\tan\delta_{GTL}$ are from Vybris tests, and E_R , E_T are from the US test.

Further comparisons are also made specifically on the ratios of anisotropy (Tab. 20), based on the table of the moduli, damping, and shrinkage properties above. All the selected comparisons of the anisotropic values are lower than the references values. Undoubtedly, the less E_L over the other higher elastic moduli (E_R , E_T) would cause smaller anisotropy ratios. Furthermore, E_R/E_T is smaller because E_T is about 58% larger, while E_R is only 29% higher than the literature. In contrast, the anisotropy of shear moduli (G_{RL}/G_{TL}) has no difference. However, it is based on that G_{RL} is 22% higher and G_{TL} is 33% higher than the references, which could imply the influence of the figured grain patterns.

Tab. 20 Anisotropic ratios for all studied properties. Data from wide-scale literature references are compared to average anisotropic ratios obtained in the present study.

Ref	E_L/E_R	E_L/E_T	E_R/E_T	E_L/G_{RL}	E_L/G_{TL}	G_{RL}/G_{TL}	$\frac{\tan\delta_{GRL}}{\tan\delta_L}$	$\frac{\tan\delta_{GTL}}{\tan\delta_L}$	$\frac{\tan\delta_{GTL}}{\tan\delta_{GRL}}$	TTS /TRS
Guitard ¹	7.5	12.7	1.7	11.5	15.9	1.4				
Brémaud ²	7.8	15.4	2.0	11.7	13.7	1.2	2.1	2.3	1.1	
CIRAD ³										1.8
Present ⁴	6.2	8.8	1.4	9.2	10.9	1.2	1.8	1.8	1.0	1.6

1, 2, 3, 4 are the same as in the previous table (Tab. 19).

Summary of Chapter III

The objective of this chapter was to characterize physical and mechanical properties and their anisotropy, over a variety of figured woods with different patterns of grain deviation. Based on the species selected in the previous chapter (II), this chapter III first presented the detailed sampling, material preparation, and the methods used for physical-mechanical characterisations. Then, some generic results were explored, regarding some methodological effects, and regarding the range of variability in properties obtained for the various selected species with different grain patterns.

As previously described (Chapter II), the sampling under study covers seventeen species, and seven types/patterns of figured wood. The initial materials were in several forms and dimensions of planks. The sampling methodology that was developed implied to keep the traceability of each specimen from its original position, and this, while considering the multiple dimensions associated to the different types of measurements to be done. An original tool was also designed with CAD in order to represent the volume fraction of different types of wood (for example sapwood) in the initial planks. The CAD technique for the volume fraction estimation is worth further development. The CAD software allowed to obtain the shape of the irregular cross-sections and then estimate their volume fractions along the sample length.

The measurement methods that were used aimed at obtaining a wide panel of physical-mechanical properties and their anisotropy. Some of the methods are well-established, rather classical tools, while some new developments (in terms of protocols, of devices, or of analysis) were also built during the present thesis. Some elements of the methodology are summarized below:

- The total sampling included nearly one thousand specimens, intended at the different tests.
- Measurements of longitudinal modulus of elasticity, and estimates of two in-plane shear moduli, were conducted on semi-bulk specimens using the natural vibration method BING. The BING method was tested from the original planks' dimensions to the standard beam dimension, representing the macroscopic elastic behaviours. The effect of moisture conditioning on such dimensions was also tested.
- After the BING measurement, the “standard beams” were cut into several dimensions to fit the other requirements of tests, including an ultrasonic cube, two shrinkage samples, two quarter-sawn Vybris slices, and two flat-sawn Vybris slices from each beam. The advantage of

the series sampling (from the standard beam to those sub-dimension specimens) is to keep the wood properties information in the same radial position (the principal directions of wood), minimising the wood variation due to the different growth periods.

-Ultrasonic measurements were used to expand the knowledge of six moduli (three moduli of elasticity and three shear moduli). The test was without measuring the diagonal terms (elastic-elastic) in the orthotropic stiffness matrix, so the elastic moduli were calculated according to Guitard's hardwood result and the parameter estimation. Also, six shear moduli were measured. The peak selections for the G_{LR} , G_{LT} and G_{TR} were according to the G_{RL} , G_{TL} , and G_{RT} , respectively. The previous set has only one (or least) peak that can be selected. Then, the pair value can be found according to this. The pair values were averaged, e.g., G_{LR} with G_{RL} .

-The forced-vibration method called Vybris (in LMGC, Montpellier) was used to characterize viscoelastic vibrational properties, i.e., including dynamic modulus and damping by internal friction. The rather small section of specimens means that measured properties are more close to the mesoscopic scale of wood, therefore can be more directly related to the structural assessments made in previous Chapter II.

-A new experimental development was made during the present thesis, in the form of a Vybris-Torsion device, that allows to measure dynamic mechanical properties in shear. The validity of this new device has been tested experimentally and theoretically.

-Hygroscopic/hygro-mechanical measurements (fiber saturation point and shrinkage), were conducted following the standard protocol in BioWooEB CIRAD. Some verifications about the saturation states were done. Further, a calculation for taking into account the potential ring angle in the transverse section is described.

The generic results from this chapter III concern both some methodological points, and the observation of variability in properties for figured woods. Some points can be summarized as follows:

-The FSP values are generally above 26%, which fits the literature and general experience. However, several species had exceptionally low values of FSP, that can indicate a probable influence of extractives.

-The shrinkage values are also consistent with the literature data, but revealed a higher variability within the species that had more variations in figure/grain patterns. The studied tropical species, with interlocked grain, had a lower ratio of anisotropy in shrinkage (TTS/TRS).

-The comparison between different dynamic mechanical methods confirmed known trends, like Young's modulus being higher values in ultrasound. The sources of uncertainties for the different methods were discussed. This comparison also highlighted the effects of local heterogeneities in grain angle when testing specimens of different sizes and geometries. For example, the most recognised one is the interlocked grain. Its flat-sawn specimen could be taken as a single angle grain, but the quarter-sawn specimen is the combined one. Furthermore, the different thicknesses and sampling locations would have different values/properties due to the grain variation. Thus, the grain structure variation is unavoidably included in the multi-dimensional test for the figured wood, and the sampling plane and directions have more meaning than in the case of the straight grain wood.

-The wide amount of obtained data on shear dynamic mechanical properties (i.e., including damping) constitute a rather new insight on these lesser-documented properties.

-The range of variability was different depending on considered properties, and also between the different species.

-The properties most variable between species are moduli, especially transverse ones. The density and fiber saturation point are rather stable within a given species. The properties for which the variability is most strongly expressed inside a given species are vibrational properties.

-Compared to existent references or databases, the present study covers a rather more complete panel of the different domains of anisotropy, i.e., elastic, viscoelastic (with damping by internal friction) and hygro-mechanical (with shrinkage).

-The studied material had, in average, clearly lower ratios of anisotropy for almost all properties, than average data from the literature. This reduced anisotropy could be considered a "signature" feature of figured woods.

IV. Structure-properties relations and scale effects in figured woods

Introduction of Chapter IV

Many factors determine wood mechanical properties, e.g., microfibril angle (MFA), grain angle (GA), density, and chemical composition (structural or polymeric, non-structural such as extractives). These factors vary depending on several aspects, including environmental parameters (i.e., provenance, growth conditions), differences between individual trees (genetics), and within an individual tree. For instance, the density is often said to increase along the radial direction, while MFA generally decreases with the passage from juvenile to mature wood, but this radial pattern can be reversed in tropical species, or between natural forests and plantations.

Also, the figured woods exhibit variations of grain patterns (and of GA). In addition, the grain pattern may not be uniform within a tree; for example, there might be some trend along the radius, in which the grain pattern's GA may increase from pith to bark. Therefore, material behaviour depends both on the between-species diversity in wood structure and composition and the within-species variations of the above factors.

When taking the grain pattern as cells' organisation in a specific scheme (figured wood), it is expected to cause the figured wood to have degrees of anisotropy, e.g., in mechanical and hygro-mechanical properties, differing from the straight-grain wood. Also, it depends on the type and intensity of the grain pattern. Understandably, both the axial (considered respective to the trunk axis) properties and the degree of anisotropy would decrease if the general orientation of cells makes a higher angle (GA) with respect to the axis of the trunk (and of a piece of wood). Thus, the type of figure and its degree (GA) are decisive for the behaviour. However, all the factors conjointly determine the material's properties.

The measured mechanical and hygro-mechanical behaviours depend on density, MFA, and grain pattern (GA), their superimposed effects, and chemical composition. The composition may be fundamentally different between species (notably regarding extractives). Thus, the comparison between species with the same grain pattern and within the same species with different grain patterns is therefore not in the same "material".

In Chapter IV, figured wood's variability and diversity are analysed at several levels. The analyses are based on the structural characteristics evaluated in Chapter II, i.e., appearance, MFA, and GA, and on the mechanical and hygro-mechanical properties measured in Chapter III.

This chapter (IV) will first present the global properties observed in both between-species diversity and within species variability, covering several species for a given type of grain pattern (for instance, interlocked grain) or several degrees of figure within a species (for example, for wavy grain). This presentation of variability will consider some possible scale effects, that may be rather moderate in straight-grain, “clear wood”, but may be rather important in figured woods due to the local variations in GA.

Then, the correlations between different physical and mechanical properties will be analysed. The results here obtained on figured woods will be compared to general knowledge based on “standard trends” obtained from the literature, for instance, the generally obtained correlations between density, elastic moduli (and shrinkage), and their anisotropy, or the relationships between viscoelastic damping and specific dynamic modulus. These analyses will search for possible shifts from these standard trends that may represent the figured woods.

The third section will examine the structure-properties relations based on the locally recorded orientations at two scales: the grain angle GA (meso-macro scale) and the microfibril angle MFA (micro-scale). After observing the individual effects of each of these two scales, their superimposed effects on axial mechanical properties will be analysed.

Finally, the respective results obtained on the different physical-mechanical properties, as well as recorded appearance, will be shortly discussed under the question to evaluate if figured wood can be considered as a “defect” or as a “quality”.

IV.A. *Between-species diversity versus within-species variability in properties*

In the part III.E, the properties’ comparisons mainly focused on the between-species level and the different testing methods. Instead, species’ variations of material properties (e.g., physical and dynamic mechanical) have not been detailed yet.

Several figure patterns were selected according to the material’s sampling of figured wood. One species could have more than one figure pattern, or a given figure pattern could have several degrees of figure (doFs). In the previous chapter, the variation due to the grain pattern and the doF was not stated. Therefore, at the beginning of this chapter IV, the variation in properties is examined within species. It focuses on the properties that have been measured on the largest number of specimens per species, i.e., the properties measured on Vybris specimens (density, dynamic moduli and damping coefficients in the longitudinal direction and in-plane shear).

IV.A.1. *Diversity and variability of the density*

The first comparison within species is made on density (Fig. 75) since it is an important parameter. From the preliminary overview analysis at the end of Chapter III, the density appeared rather stable within species while being most variable between species.

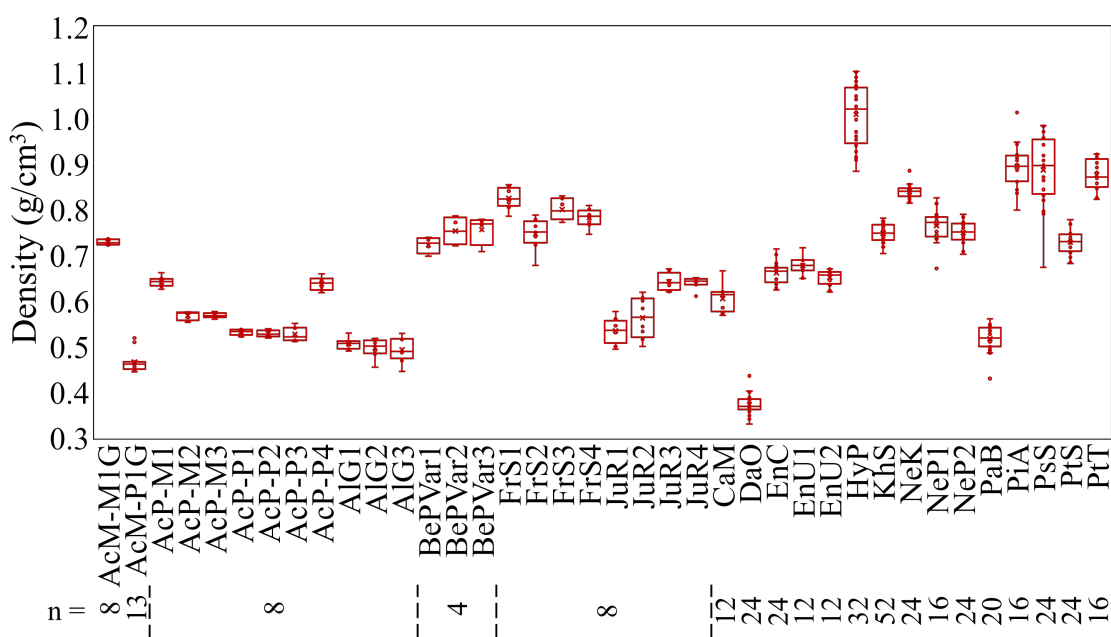


Fig. 75 Variability of the density, categorised by species and initial plank. Data from the Vybris’ quarter-sawn and flat-sawn specimens, n: specimen number from each plank.

From the point of view of the figure patterns’ comparison, there is no relation between the doF and the density for the pommele maple (AcP-P), curly plus wavy grain alder (AlG), wavy ash (FrS), nor the Karelian birch (BePVar). On the contrary, there are trends between density

and doF for the birdseye maple (AcP-M) and wavy walnut (JuR). Nevertheless, the doF is not a measurement but a vendors' evaluation/grading, and the sample number is too limited to conclude here. For the interlocked grain, only two species had two planks (EnU and NeP), which does not allow to analyse differences between individuals. Globally, the differences in density are pronounced between species, while the range between different specimens cut from an individual (plank) is rather narrow.

IV.A.2. *Diversity and variability of the axial modulus of elasticity and specific modulus*

The comparison is then on the dynamic mechanical properties, the first on the longitudinal modulus of elasticity and specific modulus.

According to the same idea as above, comparing the doF within species, the longitudinal elasticity of quarter-sawn and flat-sawn (Fig. 76) specimens shows a more interesting behaviour than for density. For the AcP, the doF has a slightly negative relation for the AcP-M (birdseye) quarter-sawn specimen (doF: AcP-M1 > AcP-M2 > AcP-M3), but no difference between the flat-sawn specimens. Instead, the AcP-P (pommele) relation of elastic modulus to doF is not so determined for the quarter-sawn specimen but more related to the flat-sawn specimen. For BePVar (Karelian birch), there is no relation to doF.

Besides those grain patterns, the wavy grain patterns, AlG, FrS and JuR, give an opposite result of the E values while comparing their doF. While FrS and AlG show a negative relation between doF and E (for the quarter-sawn and flat-sawn specimens), it is reasonable that the doF represents the GA. Instead, the JuR has a positive relationship between the doF and the E values. The author assumes the difference is due to the density since the density is highly correlated to wood's stiffness. The FrS specimens do not have much difference in density, so the GA dominates more on its longitudinal elastic modulus. On the contrary, the difference in density among JuR specimens is more significant (Fig. 75), and the density could affect the longitudinal elastic modulus more than the GA (or doF).

Compared with the other grain patterns, the interlocked grain species have no particular relationship with the density nor the doF (compared between the species). Instead, the EnU1 has a larger density than EnU2, but it has smaller E values than the EnU2. However, the range in E is usually larger for the flat-sawn specimens, than for the quarter-sawn ones.

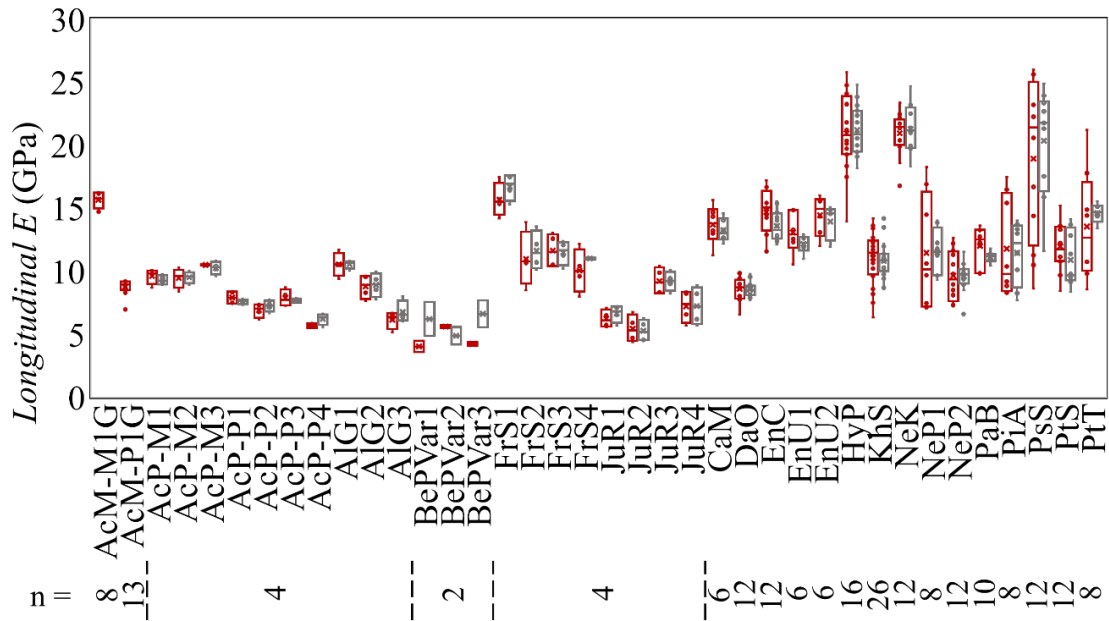


Fig. 76 Variability of the longitudinal elastic modulus, categorised by species and by initial plank. Data from the Vybris' quarter-sawn (in grey) and flat-sawn (in red) specimens, n: number of specimens from each plank.

However, examining the variability of the longitudinal elastic modulus is not very informative when comparing between and within-species because it depends on the between-species differences in density. The comparison based on the longitudinal specific modulus of elasticity (E_L/γ) is much more relevant as it is more directly affected by the orientation of wood elements (Fig. 77). The relation between the doF and the E_L/γ within species is obvious for the AcP-M, AlG, and FrS. On the contrary, the doF and E_L/γ are no longer related to the JuR and AcP-P.

Generally, the values for flat-sawn specimens show broader distributions than quarter-sawn specimens coming from the same plank. The exceptions are for AlG and BePVar that quarter-sawn specimens' values are more broadly distributed than for flat-sawn ones. Their wood grain patterns mainly vary in the R direction for these two species. In contrast, the other grain patterns' variations are mainly in the T direction in the present study. Thus, the difference because of the grain variation's direction is detectable in the result. However, the specimen amounts for the temperate species are relatively low (Fig. 76), so the accurate distribution and the distinction of the quarter-sawn and flat-sawn values, depending on the grain pattern, should be further examined.

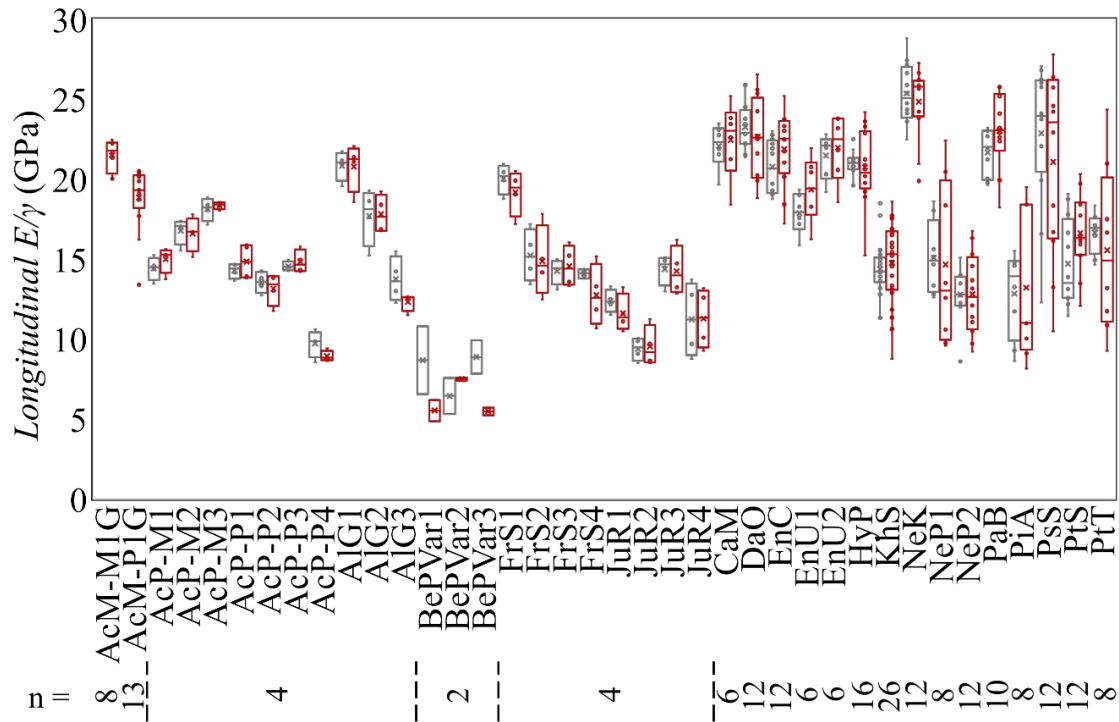


Fig. 77 Variability of the longitudinal specific modulus, categorised by species and initial plank. Data from the Vybris' quarter-sawn (in grey) and flat-sawn (in red) specimens, n: number of specimens from each plank.

IV.A.3. Diversity and variability of in-plane shear moduli

The in-plane shear moduli's comparisons continue the same idea as above. The variability within AcP-M (birdseye maple) shows no particular relation between G_{RL} and the doF, but there is a positive relation with the G_{TL} values. Instead, the AcP-P (pommele maple) tends towards a positive relation of G_{RL} with doF and a possible negative relation for G_{TL} . The strong relation between doF and values in one shear plane, while having a weak or merely no relation on the other shear plane, also occurs for FrS. However, the situation of FrS (wavy ash) is opposite to that of AcP-P. The FrS has a strong relation between G_{RL} and the doF but no relation with G_{TL} . Besides different degrees of variability between two planes of shear moduli of those species, the JuR (wavy walnut) has the same relations between doF and G_{RL} and G_{TL} .

For the interlocked grain pattern, the shear moduli are generally in a small range/distribution within each species, except for PiA which has the largest GA and undulation in a short period, which result in the widest distribution in G_{TL} . Differently, HyP (nearly no interlocked grain) and KhS are the thicker planks, and they have the sampling made radially and tangentially. Herein, "tangentially" means the neighbouring specimens at the same radial and at the same longitudinal position. Also, these two species have a broader sampling along the radius (wider board). The

author assumes these are the reasons for having relatively broader value distributions for these two species.

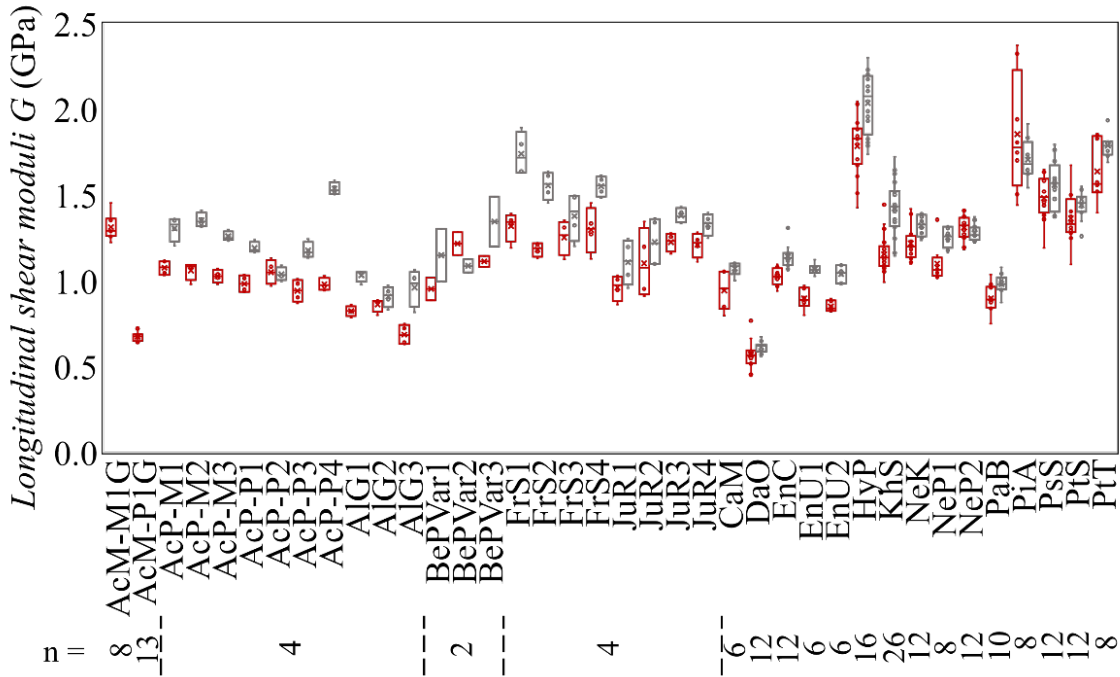


Fig. 78 Variability of the in-plane shear moduli (G_{RL} in grey, G_{TL} in red), categorised by species and by initial plank. Data from the Vybris' quarter-sawn (in grey) and flat-sawn (in red) specimens, n: number of specimens from each plank.

IV.A.4. Diversity and variability of damping coefficients, longitudinal and in shear

The comparison is then conducted on the damping coefficients. The results include the damping in longitudinal direction $\tan\delta_L$ (measured by bending vibrations) (Fig. 79) and in two planes of shear (torsional vibrations), obtained from quarter-sawn and flat-sawn specimens (Fig. 38), expressed as $\tan\delta_{GRL}$ and $\tan\delta_{GTL}$, respectively (Fig. 80).

The same negative relations exist within species when comparing the doF and the damping values for the AcP-M and FrS. Again, the larger number after the abbreviation of the species means having higher doF, except for the AcP-M (II.C.2.a) and II.C.2.b). The doF for AcP-M is $AcP-M1 > M2 > M3$, while for the others, for example FrS, the doF is $FrS4 > FrS3 > FrS2 > FrS1$. The higher doF generally show larger $\tan\delta_L$ and $\tan\delta_G$ values (Fig. 79 and Fig. 80). The $\tan\delta_L$ measured on Karelian birch (BePVar) is remarkably high, reaching values as high as 30×10^{-3} : it exceeds all values collected in previous research on 450 species (Brémaud et al. 2009), where the maximum values of $\tan\delta_L$ were of 20×10^{-3} . For the species with the interlocked grain (CaM to PtT), the range of variation in $\tan\delta_L$ is broader between the flat-sawn specimens than between the quarter-sawn specimens. In contrast, for all the other grain patterns (AcM to JuR),

the range is either similar or slightly higher for quarter-sawn specimens. This tendency is much less visible for the shear damping $\tan\delta_{GRL}$ and $\tan\delta_{GTL}$.

Generally, the tropical species' (grouped on the right side, CaM to PtT) $\tan\delta_L$ values tend to be relatively lower than those of the temperate species (grouped on the left side, AcM to JuR), even when excluding the very atypical Karelian birch (BePVar). This trend is also observed for the $\tan\delta_G$ values, however with a smaller amplitude of difference between temperate and tropical species.

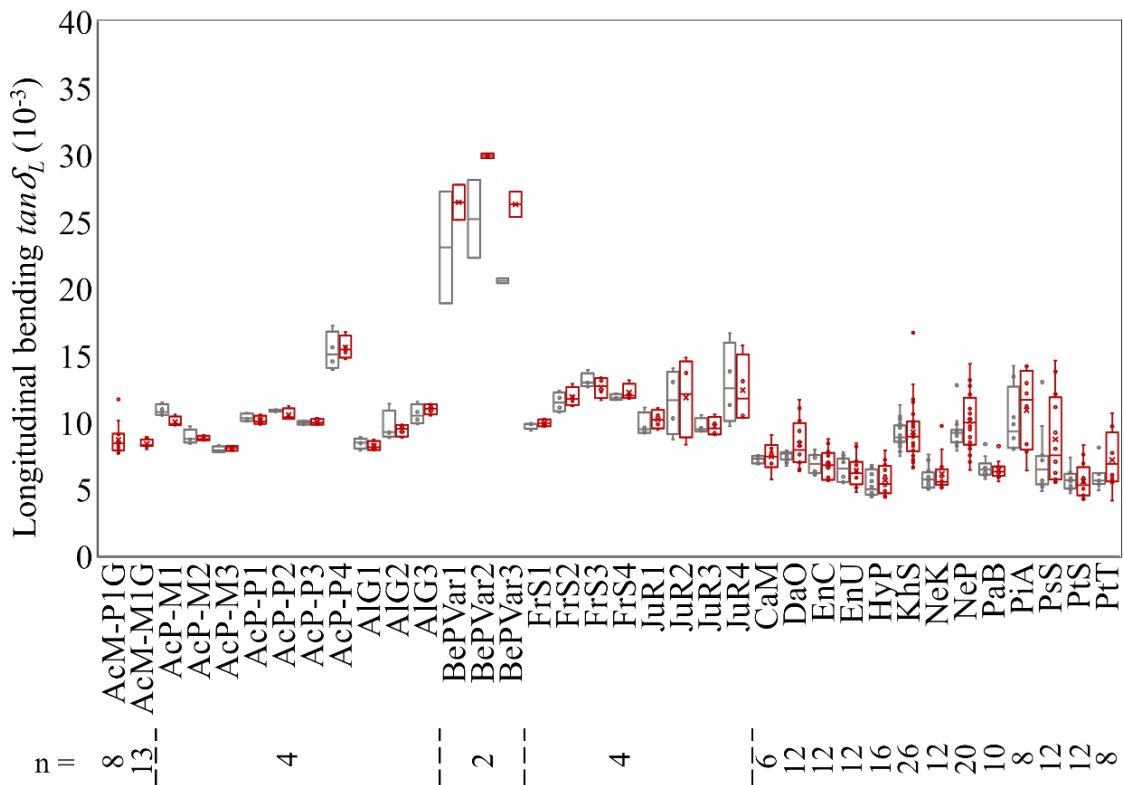


Fig. 79 Variability of the longitudinal damping coefficient, categorised by species and by initial plank. Data from the Vybris' quarter-sawn (in grey) and flat-sawn (in red) specimens; n: number of specimens from each plank.

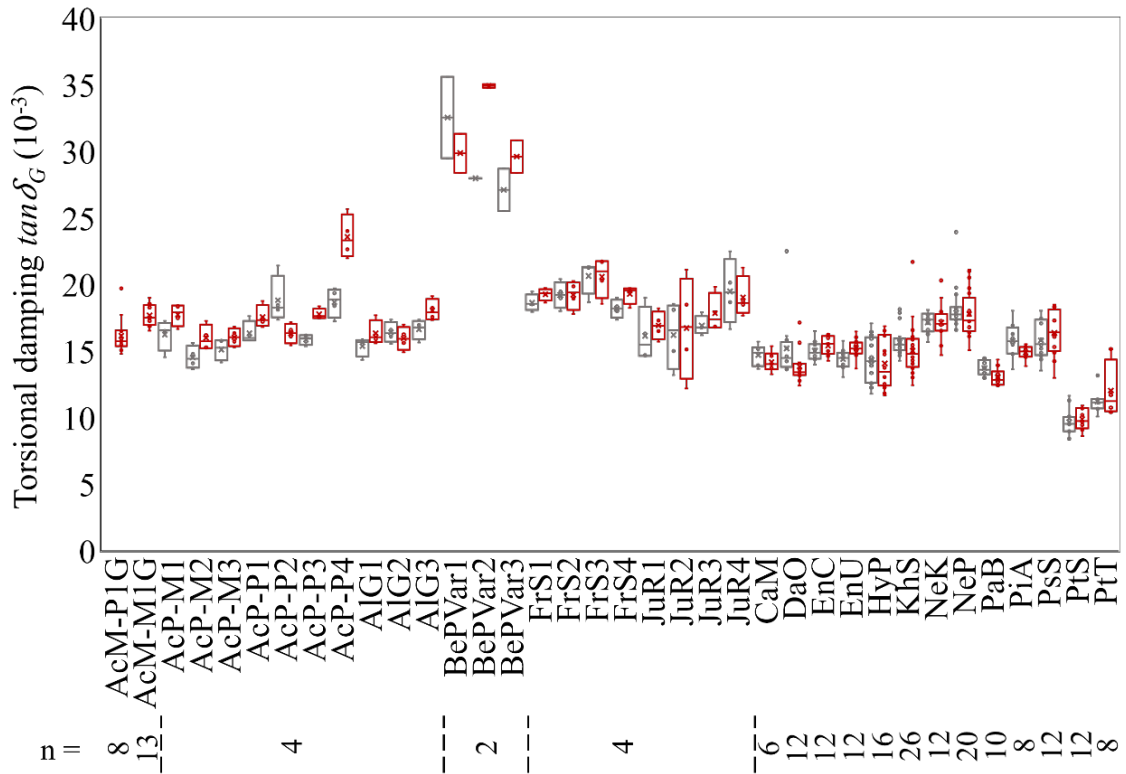


Fig. 80 Variability of the longitudinal damping coefficient, categorised by species and by initial plank. The grey colour is for the quarter-sawn specimens ($\tan \delta_{GRL}$), and the red colour is for the flat-sawn specimens ($\tan \delta_{GTL}$).

IV.B. Correlations between properties: Comparison of figured woods with standard relationships

The wood properties are variable, and the variation between- and within-species/individuals could be large or sometimes small. Still, based on wood's general structure and composition, wood is, when descending scales, a cellular material, a fibre-composite material, and a polymeric material. The different properties of wood are generally related to these different scales of organisation. These fundamental structure-properties relationships result in general correlations between the different physical-mechanical properties. Such correlations can give useful trends or predictions on the basis of a limited number of explanatory variables. Even when not knowing the structural (or chemical) characteristics of the studied wood quantitatively, these “standard” (on a statistical meaning) correlations can give indications. Here, specifically, the question is to compare the variety of studied figured woods with such “standard” relationships or trends.

Several studies have shown that several properties of wood (in a general and wide perspective) follow certain trends, depending on the density (also expressed as specific gravity). For example, Guitard and El Amri (1987) proposed statistically robust relationships for “standard” softwoods and hardwoods. The result is based on regression models from several literature data, and the main explanatory variable used in the model is the wood density at standard air-dry conditions (considered 12% MC). It provides good reference values for the orthotropic elastic moduli E_L , E_R , E_T , G_{RL} , G_{TL} , G_{RT} , as well as realistic estimations of the way in which these moduli will vary as a function of density. There are also general trends between shrinkage parameters and density, e.g. those presented in Skaar (1988) or relationships observed in CIRAD's Tropix software/database (Gérard et al. 2017).

Furthermore, wood's unit substance is the cell-wall material, a fibre-matrix composite, where the orientation of microfibrils dictates the specific modulus (i.e., the part of modulus not explained by the density) and the viscoelastic damping (which is further affected by chemical composition). Depending on the MFA and GA orientation, both the elastic (storage modulus) and the viscoelastic (damping coefficient, $\tan\delta$) evolve. The relationship between $\tan\delta$ and specific modulus (E_L/γ) has been statistically demonstrated on a large number of specimens from different species (Ono and Norimoto 1983, 1984; Brémaud et al. 2009, 2012) and in different grain angles (Ono 1983, Ono and Norimoto 1983) also in different directions (Ono and Norimoto 1985). This statistically strong relationship between $\tan\delta$ and E_L/γ can also be reconstructed

theoretically by considering the MFA (Obataya et al. 2000) or the GA (Brémaud et al. 2011b). Another standard trend is similar to the previous idea of connecting wood viscoelastic vibrational behaviour with its orientation and composition. This last trend relates to the axial-to-shear anisotropy in the damping and moduli due to the cell wall's microstructure and composition (Obataya et al. 2000).

The presented results do not include the microscopic (MFA) or macroscopic (GA) orientations yet. This section compares the present study's experimental results on woods with grain deviations, with the described trends from the literature, to show if and how the studied figured woods may either follow the standard trends or, on the contrary, behave differently, which may express the effects of their structural characteristics.

IV.B.1. Correlations describing anisotropic elastic moduli: comparison to the “Standard Hardwoods”

This section compares the three moduli of elasticity and the three shear moduli of studied figured woods with the “standard hardwood” values from Guitard’s regression result (Guitard 1987).

The Guitard’s standard hardwood statistical model consists of the power equation (48), where the six elastic moduli are predicted by the density (D , in $\text{g}\cdot\text{cm}^{-3}$, compared to a “standard” density of $0.65 \text{ g}\cdot\text{cm}^{-3}$) as the only explanatory variable, with two coefficients, a and b (Tab. 21). It can be expressed as in the following equation (56):

$$\text{Standard Hardwood Moduli} = a \left(\frac{D}{0.65} \right)^b \quad (56)$$

Tab. 21 The coefficients of Guitard’s standard hardwoods’ relations for six elastic moduli’.

Elastic moduli (GPa)	Coefficients		Shear moduli (GPa)	Coefficients	
	a	b		a	b
E_R	1.811	1.30	G_{RL}	1.260	1.14
E_L	14.40	1.03	G_{RT}	0.366	1.74
E_T	1.030	1.74	G_{TL}	0.971	1.26

IV.B.1.a) Correlations between density and anisotropic moduli

The first comparison between studied figured woods and Guitard’s model uses the experimental data from the ultrasonic test (US) to compare all three moduli of elasticity and three shear moduli (Fig. 81).

It can be seen that Guitard’s regression model is a relatively good reference, even for atypical woods such as those studied here. The coefficients of correlation between density and the different elastic moduli are usually highly significant ($r \geq 0.69$). However, the strength of the correlations is variable depending on the different moduli: as described by the coefficient of determination (R^2), the density can explain as little as 48% of some moduli (E_L , G_{TL}), or as high as 80% (E_R) or 88% (G_{RT}). The most dispersed result is on the E_L (Fig. 81c). It would have been expected that figured wood’s longitudinal elastic modulus would be small. However, the results show that four IG (interlocked grain) species have higher E_L values than Guitard’s estimation, i.e., CaM, EnC, NeK, PtT. However, on average, the relation with density follows nearly exactly the same trend as in Guitard’s model, with very similar coefficients a and b (Fig. 81 and Tab. 21) for E_R , E_L and G_{RL} .

On the contrary, E_T and G_{TL} values generally show higher values than the standard hardwood's trend (Fig. 81e). This seems consistent when considering the grain deviations mostly tend towards the T direction in the studied figured woods. However, the most deviated and higher values from the standard trend are for HyP, a nearly straight grain species. Though HyP has the crenulation grain pattern on the bark, it has no grain pattern shown from the splitting result. Still, it shows a clear trend judged from the elliptical distribution in E_T ; equally, the same behaviour in the G_{RT} (Fig. 81d).

As previously mentioned, the GA are mostly towards the T direction. It is also seeable that the E_T values are less correlated with density (vertical elliptical distribution). On the contrary, most species' E_R values correlate well with density and the standard trend. Instead, the AIG grain pattern varies mainly in the R direction, and its E_R (Fig. 81a) shows non-correlation with density and its values in the G_{TL} (Fig. 81f).

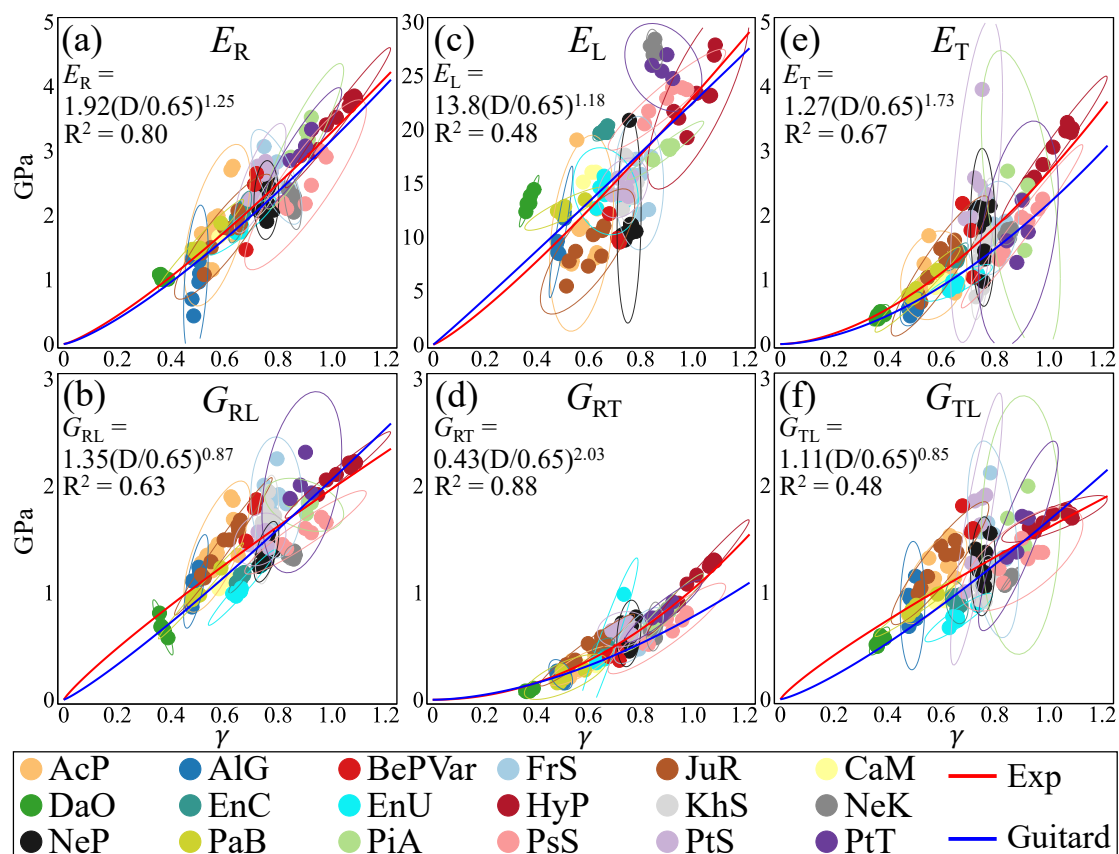


Fig. 81 The comparisons of the relations of 6 elastic moduli to density, between experimental results from US test on figured woods and Guitard's standard hardwood's model. The blue curves represent Guitard's standard trends, and the red curves are the regressions of experimental results.

However, it should be reminded that the results obtained by ultrasonic tests are from specimens with a relatively large section ($20 \times 20\text{mm}$, $R \times T$), i.e., the measurements may somehow average some more local effects from grain deviations. Therefore, in the next figure (Fig. 82), the correlations to density are observed for the results of three elastic moduli (E_L in Fig. 82a, G_{RL} in Fig. 82b, and G_{TL} in Fig. 82c) as measured on the smaller section ($2 \times 12\text{mm}$, $T \times R$ or $R \times T$) specimens measured by the Vybris tests. The result shows that the G_{RL} and G_{TL} are closer to Guitard's results. On the contrary, the E_L is generally (the whole trend) lower than Guitard's result. Yet, according to the elliptical distributions, some unusual results are observed, e.g., NeK, PiA, PsS, that the trends are differentiated from the general behaviour and Guitard's result.

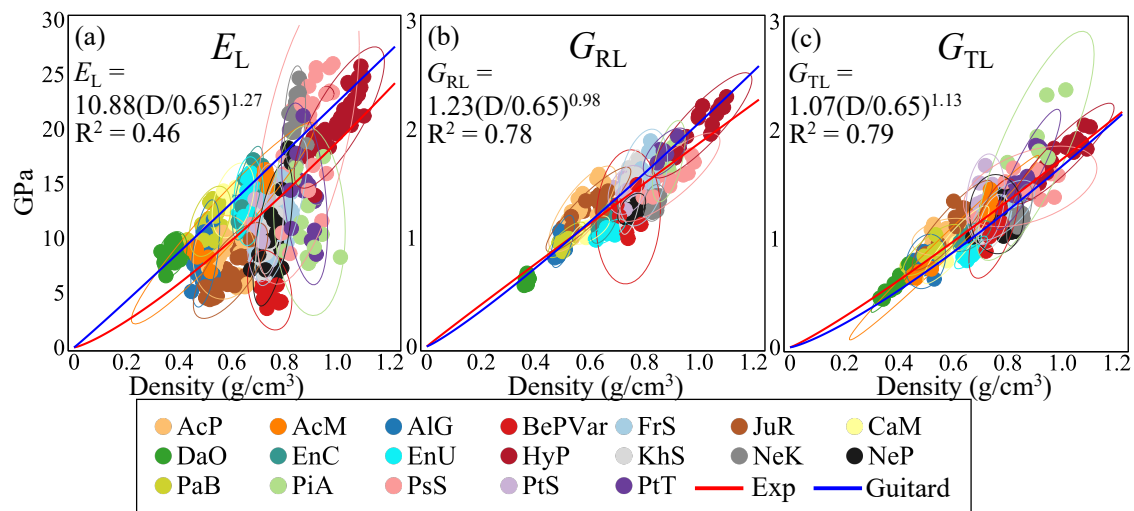


Fig. 82 The comparisons of the relations of 3 elastic moduli to density, between experimental results from Vybris test on figured woods and Guitard's standard hardwood's model. The blue curves represent Guitard's standard trends, and the red curves are the regressions of experimental results.

IV.B.1.b) *Correlations between the different ratios of elastic anisotropy*

The comparisons above concerned the correlations between the density and the values of the different anisotropic moduli of elasticity. Now, the focus is on the ratios of anisotropy (Fig. 83), and two explanatory variables are considered: the density as above, but also the longitudinal specific modulus of elasticity, i.e., the part of the variability in E_L that is not explained by density, and is therefore expected to express the effects of orientation (MFA and/or GA).

Generally, an increase in density goes along with a decrease in anisotropy. However, the strength of these tendencies is relatively weak: it is significant only for axial-to-transverse and for R-T anisotropy while explaining a maximum of 25~33 % of the variability, and there is no

correlation between the density and the axial to in-plane-shear anisotropy. The longitudinal specific modulus is a much stronger indicator of the ratios of anisotropy, except for the R-T anisotropy.

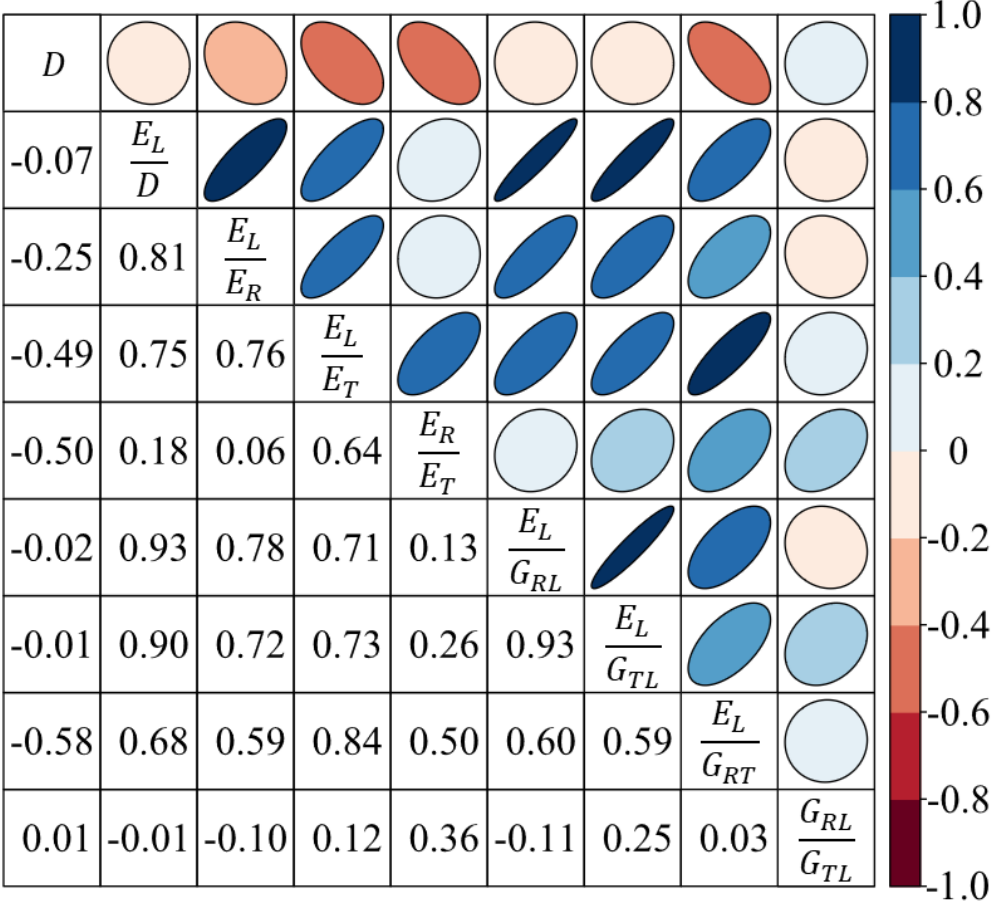


Fig. 83 Pearson' correlation matrix between the anisotropy ratios for the different elastic moduli and the density and L specific modulus as explanatory variables. Results from ultrasonic tests.

IV.B.2. Correlations between shrinkage property and specific gravity: comparison with statistical trends on temperate and tropical hardwoods

For shrinkage also, density is an “explanatory” factor often considered, as density represents is the quantity of the solid matter (cell wall, mainly) in wood because it absorbs water and changes the material dimension due to the MC state (below the FSP). According to the literature (Skaar1988, p127-131), a common trend is made between the specific gravity at FSP with the volumetric shrinkage, categorising wood species based on their climatic zone, i.e., temperate (Temp) and tropical (Trop).

Based on the experiment design in the present study, the shrinkage measurements are without the longitudinal shrinkage; however, it is usually far less than the R and T direction. Thus, the comparison between the present study with the literature result is made between the area shrinkage (R×T) and the volumetric shrinkage, respectively (58) (Fig. 84).

$$s_{vf} = G_f \times MC_{FSP} \tag{57}$$

$$s_{vf} = A + B(G_f) \tag{58}$$

s_{vf} is the predicted maximum percent volumetric shrinkage; G_f is the swollen volume specific gravity. In the reference (Skaar1988, p127-131), the coefficients A and B are: Temperate $A = 3.94$, $B = 18.51$, and $R^2 = 0.468$; tropical $A = 4.41$, $B = 12.22$, and $R^2 = 0.294$.

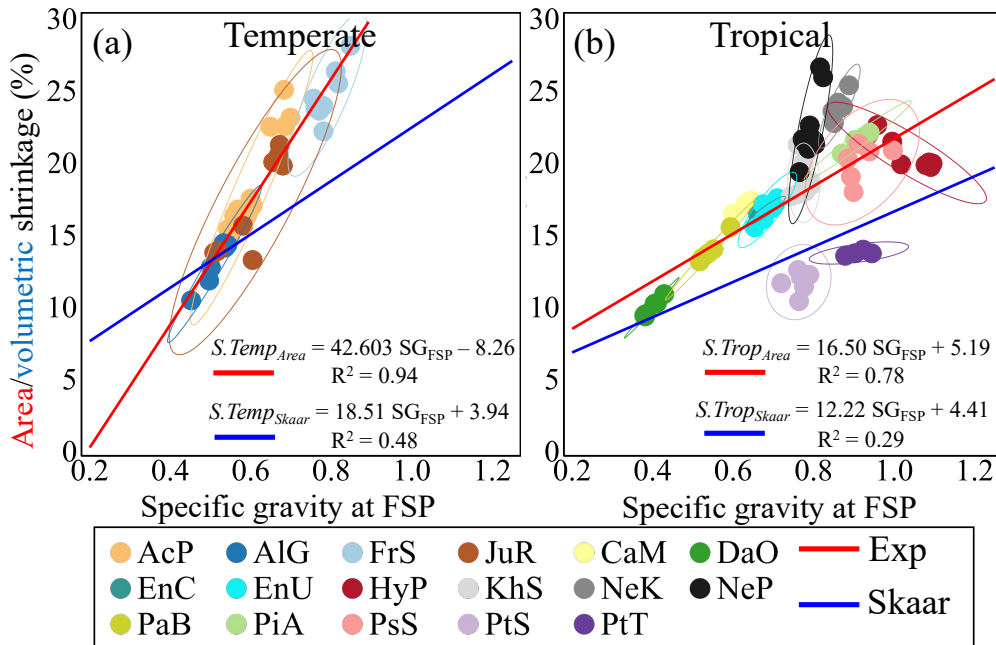


Fig. 84 The correlation between the specific gravity at FSP and the area/volumetric shrinkage, categorised with (a) temperate species ($S.Temp_{Area}$) and (b) tropical species ($S.Tropical_{Area}$). The present data uses the area shrinkage (red), and the literature data uses the volumetric (blue).

According to the present data, the relationships are more highly correlated than the literature. Whether the reason is on the longitudinal shrinkage is necessary to be verified since the longitudinal shrinkage is difficult to be correctly measured. Yet, some unusual trends could be seen from HyP, PtS, and PtT. HyP has an opposite trend, and the reason is unknown. While PtS and PtT are generally lower and without a clear trend, their FSPs are also atypically low, which is most likely due to their extractives.

IV.B.3. *Correlations describing the vibrational properties: comparison with standard trends between damping and dynamic moduli*

IV.B.3.a) *The relation between longitudinal damping and specific modulus*

The orientation of wood elements (grain angle GA and/or microfibril angle MFA) are known to affect both the longitudinal specific modulus (E'_L/γ , L being considered along the axis of a piece of wood), and the damping coefficient ($\tan\delta_L$). Increases in GA, or in MFA, decrease the specific modulus (E'_L/γ), and increase the damping coefficient ($\tan\delta_L$).

These respective effects of orientation (GA and/or MFA) on both E'/γ and $\tan\delta$ result in a very strong, standard relationship between these two properties. The standard correlation between $\tan\delta$ and E'/γ has been evidenced from Ono and Norimoto's research (1983, 1984, 1985). The first article was on the softwood species (Ono and Norimoto 1983), a second on hardwood species (Ono and Norimoto 1984), and another article focused on the different directions (three principal axes, L, R, T) for both hardwoods and softwoods (Ono and Norimoto 1985). All these studies showed a very strong correlation between $\tan\delta$ and E'/γ that can be expressed by a logarithm equation which has two coefficients:

$$\tan\delta \times 10^3 = 10^A \times (E'/\gamma)^{-B} \quad (59)$$

The values of coefficients A and B are rather stable between different studies and samplings (Tab. 22). Notably, it was later found that the first relation, based on softwoods (Ono and Norimoto 1983), was exactly the same for hardwoods with low extractives content (Brémaud et al. 2012), while the trend is generally shifted to lower $\tan\delta$ values for wood with high extractives content (Brémaud et al. 2011a, 2012). However, some particular extractives can also shift the trend to higher $\tan\delta$ values. The nature of the polymers of the cell-wall matrix can also induce vertical shifts from the standard relation (Brémaud et al. 2013). In short, the x -axis position of a specimen's data indicates effects of orientation, with "standard" chemical composition as long

as the data remains close to the standard relationship; while vertical shifts from the standard indicate effects of chemical variations.

The figured woods main characteristic is GA variations. As seen in Chapter II, the studied materials also exhibit variations in MFA, although this is more related to different species than to the GA variations. Furthermore, as indicated in the material description in Chapter II, the studied species have different extractives contents.

The comparison of the materials from the present study is thus made accordingly with those “standard” relationships (Tab. 22), and the result generally fits the literature curves (Fig. 85). Some out-of-trend species are seen with the help of the species elliptical distributions. For PtT, PtS, and HyP values locate relatively low, while they fit more with the hardwood species with high extractive contents (Fig. 8 in Brémaud et al. 2012). PtT is known to have exceptionally low values of $\tan\delta$ due to its particular values of extractives (Brémaud et al. 2011a). On the contrary, the BePVar species stands much above the literature data, for which all the other $\tan\delta$ values are below 0.02 (in the figure, 20×10^{-3}). It shows that the swirl grain structure for the Karelian Birch do induce a very low specific modulus of elasticity and high damping. Yet the exceptionally high damping value of BePVar stands much above the standard trend, thus indicating additional effects (either in chemical composition, or maybe effects of the voids in this particular type of wood).

Tab. 22 Parameters of the relationships indicated between the specific elastic modulus and damping. The comparative table is re-drawn from Brémaud et al. (2012). The Coefficient A is that usually expressed between values of E/γ in GPa and natural values of $\tan\delta$. The alternative coefficient A' is when expressing $\tan\delta$ in ‰ (values multiplied by 1000, in order to keep the same presentation as in the rest of the present study).

Ref.	Materials	Qty	A	(A')	B
Ono and Norimoto (1983)	25 softwoods (L)	1227	1.23	(1.77)	0.68
Ono and Norimoto (1983)	Spruce with GA in L-R plane	24	1.56	(1.44)	0.41
Ono and Norimoto (1984)	30 hardwoods (L)	118	1.34	(1.66)	0.62
	98 hardwoods and softwoods (L)	1792	1.32	(1.68)	0.69
Brémaud et al. (2012)	Hardwoods with low extractives content (L)	221	1.23	(1.77)	0.68
Present study	19 figured hardwood species	509	1.01	(1.99)	0.87

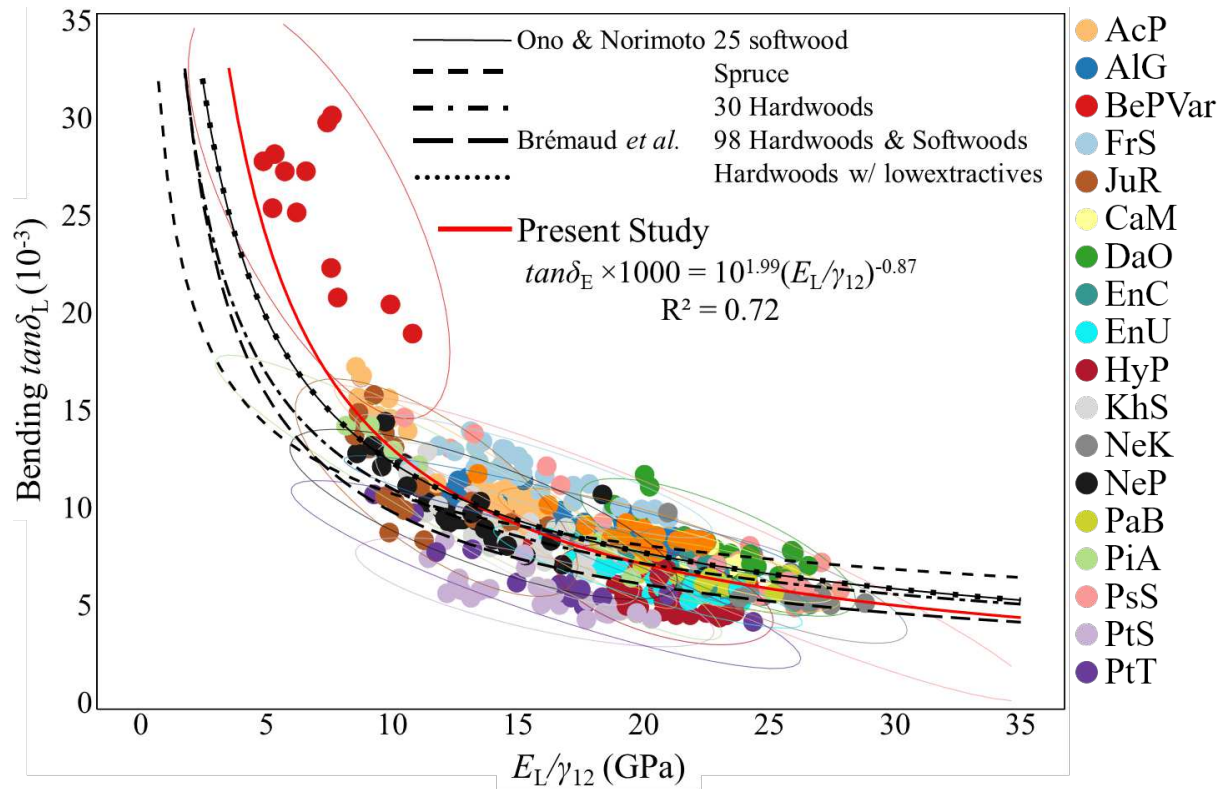


Fig. 85 Comparison of the regression results from the literature with the present study. The five regression curves are from the references listed in Tab. 22, and the red curve is the present study's result. The "standard" relation is the curve with plain line and dots (Ono and Norimoto 1983; Brémaud *et al.* 2012).

IV.B.3.b) *The relation between axial-to-shear anisotropy in damping and moduli*

The other comparison between a standard trend and the present study is the axial-to-shear anisotropy of dynamic elastic moduli and damping (still by internal friction). The study compared the ratio of longitudinal elasticity to the shear elasticity, E/G . Then, the corresponding shear (torsional) and longitudinal/axial (bending) dampings are compared, $\tan\delta_G/\tan\delta_L$ (Obataya et al. 2000). From an “acoustic” point of view, these two ratios are considered to give indications on the “tone quality” or more exactly the vibrational response at higher frequency (Obataya et al. 2000).

From the study, it stated the regression equation from 101 wood species as the standard trend (Obataya et al. 2000):

$$\frac{\tan \delta_G}{\tan \delta_L} = a \exp\left(b \frac{E'_L}{G'_L}\right) \quad (60)$$

a is 1; b is equal to 0.061. E' and G' are the storage moduli.

Due to the values acquired from the various tests, only the Vybris specimens have all the values for the comparison. So, the two types of values from Vybris quarter-sawn (L-R) and flat-sawn (L-T) specimens are used in the comparison (Fig. 86 for L-R and Fig. 87 for L-T).

Generally, the L-R's regression result is shifted parallelly ($a = 1.09$ and $b = 0.06$), and L-T's result shows a different increasing trend ($a = 1.05$ and $b = 0.05$). For L-R, the general behaviour is closer to the standard trend, even set $a = 1$ (b is then changed to 0.062). The L-R's result agrees with the standard trend. On the contrary, the L-T's result is lower than the standard trend. Its E/G ratio is higher than for the L-R specimens (on average, L-T: 10.34 and L-R: 9.16), and the $\tan\delta_G/\tan\delta_L$ is lower than L-R's result (on average, L-T: 1.77 and L-R: 1.83). For the ratio of E/G and $\tan\delta_G/\tan\delta_L$, L-R is 0.20, and L-T is 0.17.

In average, the results for L-R and L-T show not much difference compared with the standard trend. Still, two species have entirely different behaviour, both in L-R's (Fig. 86) and L-T's result (Fig. 87), compared to the other species (also to the standard trend), i.e., HyP and Dao. Coincidentally, they are the highest density (1.01 g/cm³) and lowest density (0.37 g/cm³) species, respectively, in the present study's material. While HyP is a straight grain species, DaO is the interlocked grain species. Therefore, for the moment density seems the only factor to explain this phenomenon for the deviation (beyond or beneath) compared with the standard anisotropy curve in the literature (Obataya et al. 2000).

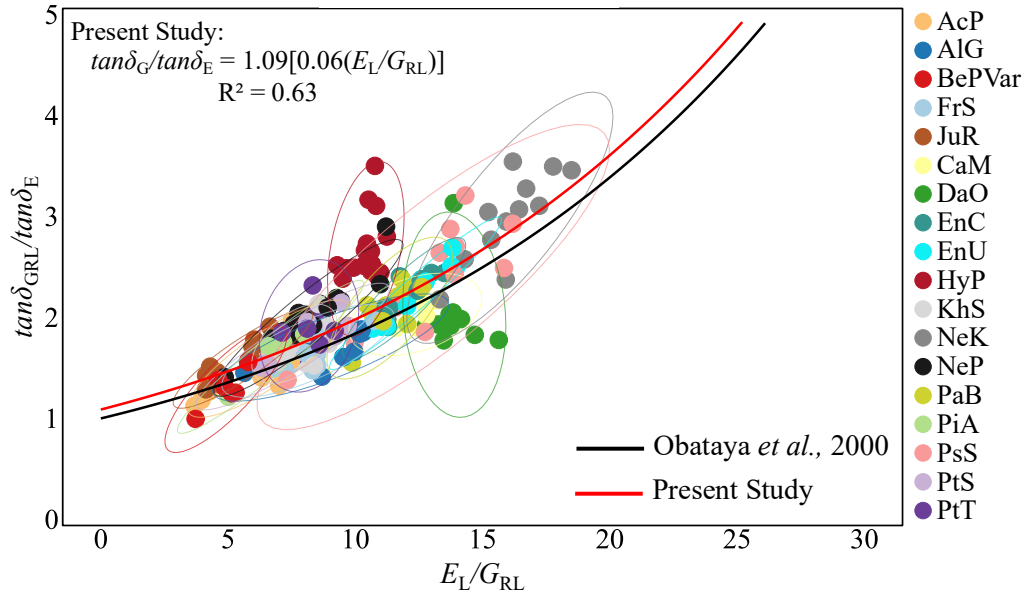


Fig. 86 Correlation between ratios of longitudinal moduli (E_L/G_{RL}) and of longitudinal damping factors ($\tan\delta_{GRL}/\tan\delta_{L-R}$) with Vybris quarter-sawn specimens. The black regression curve is from the literature, and the red is from the present study's result.

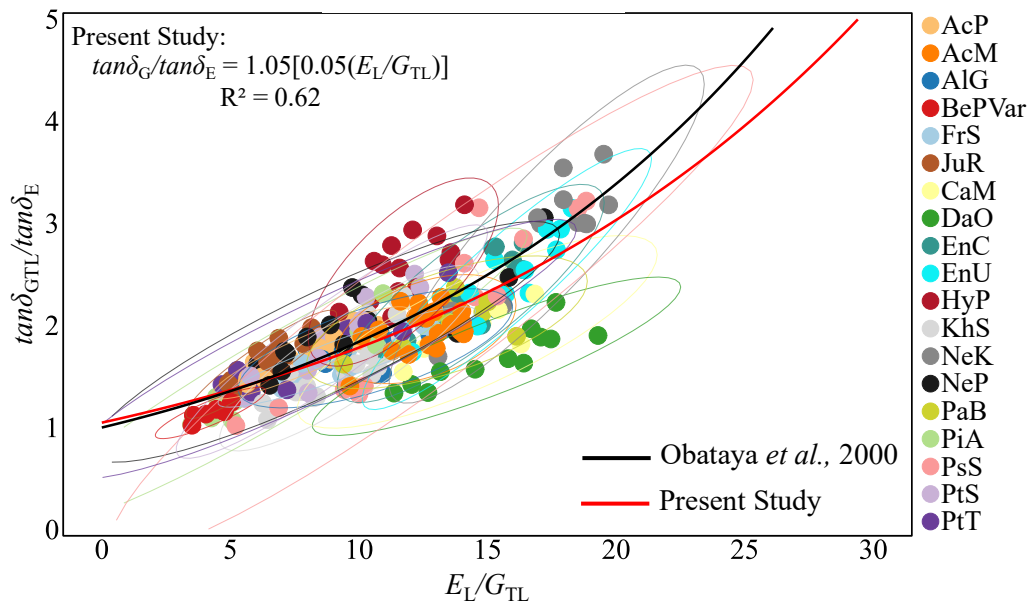


Fig. 87 Correlation between ratios of longitudinal moduli (E_L/G_{TL}) and of longitudinal damping factors ($\tan\delta_{GTL}/\tan\delta_{L-T}$) with Vybris flat-sawn specimens. The black regression curve is from the literature, and the red is from the present study's result.

IV.C. *Effects of Local Orientation on Physical-Mechanical Properties and their Anisotropy*

As a fibrous material, wood's global properties are dominated by the local orientations, including grain/fibre angle (GA) and the microfibril angle (MFA). GA and MFA influence mechanical and hygro-mechanical behaviours. Furthermore, the anisotropy of those behaviours. Thus, in this part, the correlations matrices are made mainly between the GA, MFA, and the measured properties, e.g., moduli, damping, shrinkage, and their anisotropy.

IV.C.1. *Global analysis of the factors affecting the measured properties*

Firstly, the properties are generally compared (Fig. 88). The properties are from several testing methods. The density (D_B) and longitudinal modulus of elasticity (MOE) are from the BING test (BING3). GA and MFA values are the average values (after turning into absolute values for the GA) from the Vybris flat-sawn (L-T) specimens (V_{L-T} in the following) by the XRD measurements. The shrinkage properties, including the total shrinkage and shrinkage coefficient, are from the FSP and shrinkage specimens. The other moduli are from the US measurement; the damping properties ($\tan\delta_L$ and $\tan\delta_G$) are from the Vybris test since they are more reliable than the B test.

Based on this brief correlation analysis, it could be found that the most influential factor (to all the other properties) is density, which relates to the mechanical and hygro-mechanical properties primarily. The MFA is the second one but mostly to the MOE (negatively), while GA (here an average of two local values) is less related to all the other properties.

Furthermore, the longitudinal modulus is interestingly less correlated than E_R and E_T to the density. While all the other moduli, especially E_R , E_T and G_{RT} , are highly significantly related to the density, and they are also highly correlated to each other.

On the contrary, the damping and shrinkage properties are generally not very significantly related to the other properties (structural, mechanical and physical). The only one that relates to the other properties more is α_{Area} , to the density, MFA, MOE, and G_{RT} .

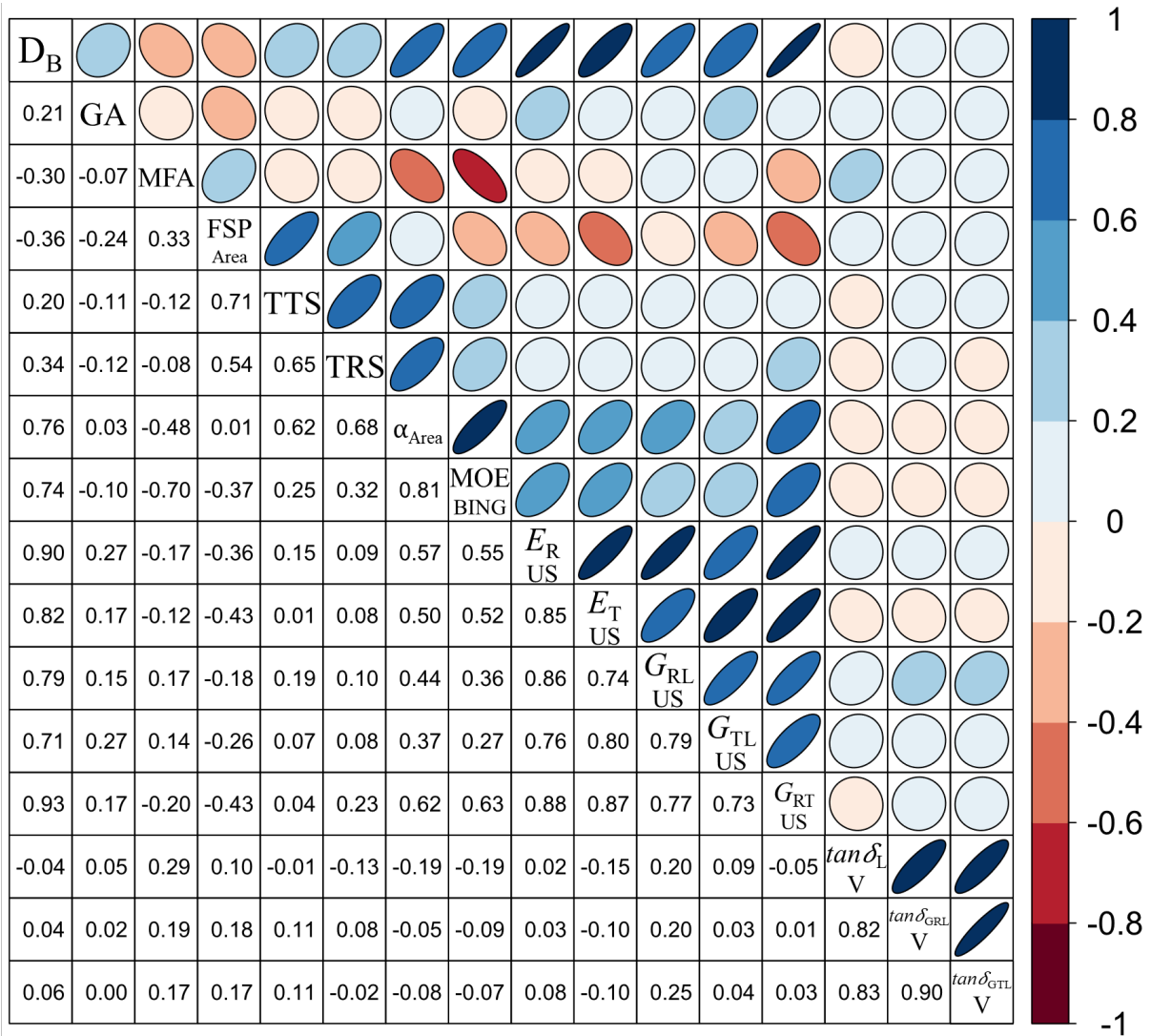


Fig. 88 The correlation matrix for exploring the relations between properties from the BING, US, V, and shrinkage and FSP_{Area} measurements. The r values are analysed by the Pearson correlation method.

IV.C.1.a) *All properties, at the scale of standard bar specimens (20×20 mm² transversal section)*

The further correlations are based on the local orientation and shrinkage properties with the moduli and specific modulus from the BING test.

The correlation result in the current section is the same as in the previous one (§IV.C.1). However, it is noticed that the MOE/ γ (specific modulus) is more related to the local orientation (GA and MFA) than the MOE value. Obviously, the specific modulus does not depend on density. It shows that the local orientations influence the efficiency of longitudinal modulus.

According to the idea from the above paragraph, the MOE/γ fundamentally reflects the unit property of longitudinal elasticity. Furthermore, the shear moduli have positive correlations to the density and the MOE. However, the MOE and MOE/γ have opposite correlation coefficients, positive and negative, respectively, on the shear moduli. This opposite correlation phenomenon shows that the efficiency of the longitudinal mechanical property, e.g., the extreme case is zero GA and MFA, has a negative effect on the shear modulus.

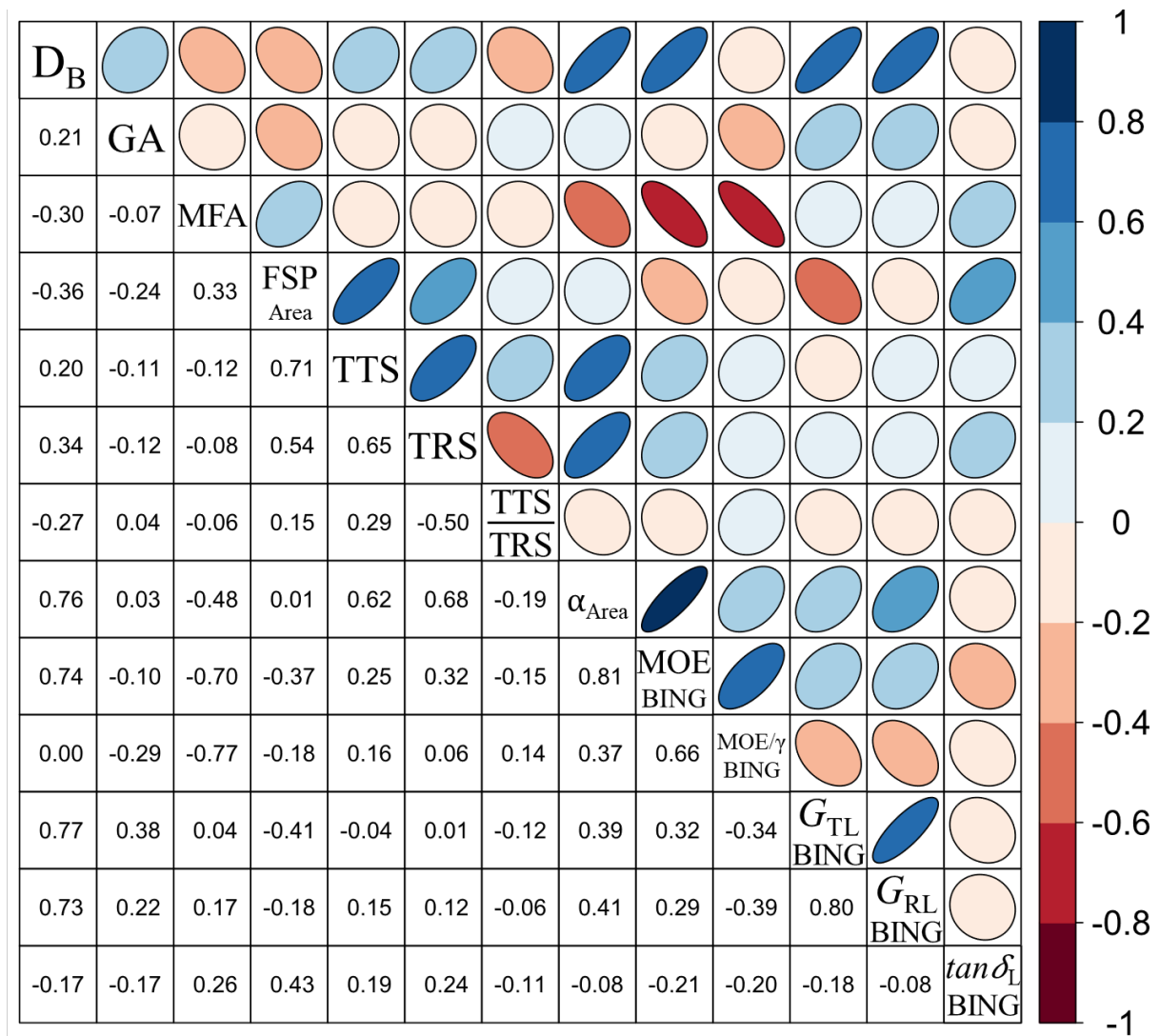


Fig. 89 The correlation matrix for the properties measured from BING, shrinkage & FSP, all obtained on specimens of section $20 \times 20 \text{ mm}^2$, and the local orientation (GA and MFA, from the thinner sections). The r values are analysed by the Pearson correlation method.

IV.C.1.b) Vibrational properties, at the scale of thin Vybris specimens ($2 \times 12 \text{ mm}^2$ transversal section)

Another correlation matrix is made from the properties measured from the Vybris test (flat-sawn specimens, V_{L-T}).

Compared to the previous topic (IV.C.1.a), the general scheme of correlations have no difference when observed on the Vybris result. However, the correlation between GA to E/γ and GA to G_{TL}/γ are higher. The GA in BING specimens is complex, and the values were processed as the average of two local measurements, while the GA values for the Vybris flat-sawn specimens are more representative as the GA was obtained on the same specimens, at a local scale. Anyhow, the correlation coefficients are still relatively low.

Furthermore, the relation between E/γ and G_{TL}/γ is examined again. The result shows as in the previous section (IV.C.1.a), the opposite correlation.

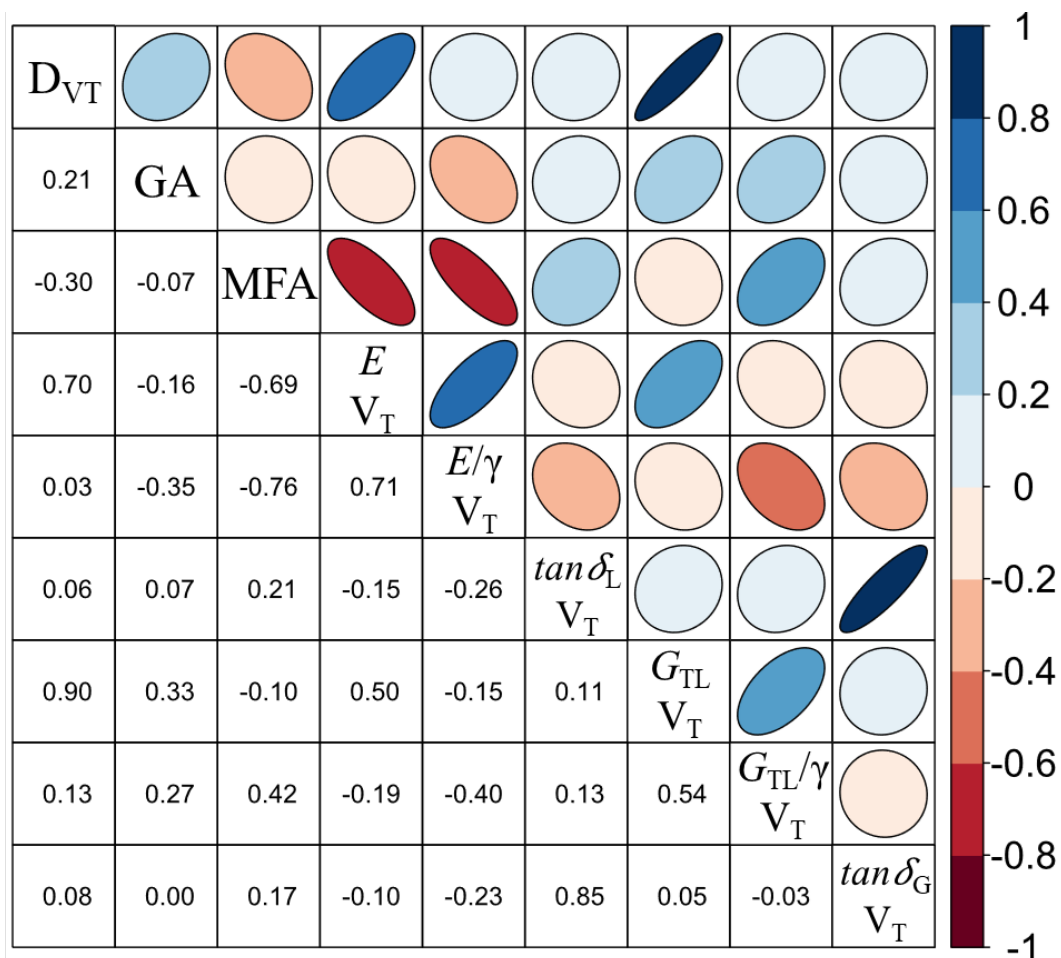


Fig. 90 The correlation matrix for the vibrational properties from the Vybris test. The data is from the Vybris flat-sawn L-T specimens (shortened to V_T for readability of the matrix). All measurements, structural and mechanical, are obtained on the same scale and specimens. The r values are analysed by the Pearson correlation method.

Accordingly, a further examination of the effects brought by GA and MFA is studied. A principal component analysis (PCA) is also made from the Vybris flat-sawn specimen result (Fig. 91).

It shows that the GA influences E/γ when its values exceed a certain angle. The negative influences to E/γ from GA and MFA are seeable, but the MFA is slightly more negatively influential. Furthermore, the E/γ has a totally opposite correlation to the $\tan\delta_L$ and less negative correlation to the $\tan\delta_{GTL}$. Instead, the $\tan\delta_{GTL}$ is positively correlated to the MFA. It shows that, on the total sampling (i.e., between-species and within-species) the microstructure property (MFA) dominates more among the two local orientation properties (for the relatively simple grain angle specimens). However, as seen in II.C.4.d), the distributions of GA and of MFA are not the same depending on the species: in some studied species, the GA varies widely while MFA remains relatively stable, while in some species the MFA varies widely and the GA remains in a relatively narrow range.

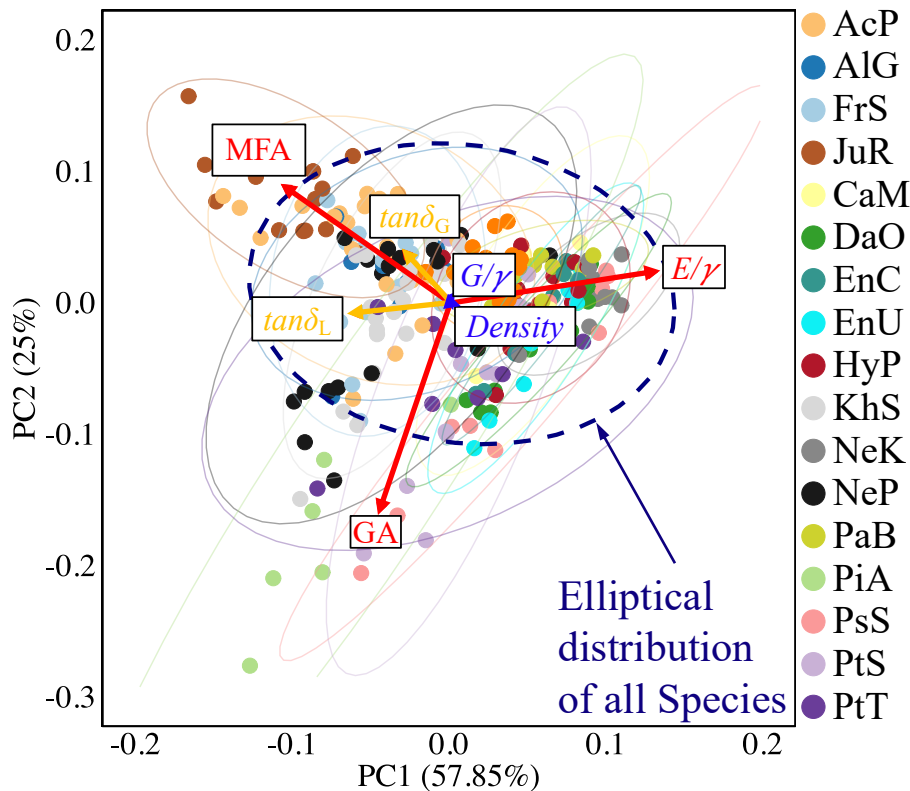


Fig. 91 A principal component analysis of the properties measured from the Vybris L-T (V_{L-LT} , flat-sawn) specimens, categorised by species.

IV.C.2. *Effects of local orientation on anisotropic moduli measured by ultrasound*

Another analysis is made for evaluating the influence of GA and MFA on the anisotropic elastic moduli. The moduli are from the US test, and their correlations between each modulus are shown (Fig. 92). All the transverse, and shear, moduli are quite strongly correlated between them, and to the density. Whereas, on the contrary, the longitudinal modulus is equally affected by MFA and by density.

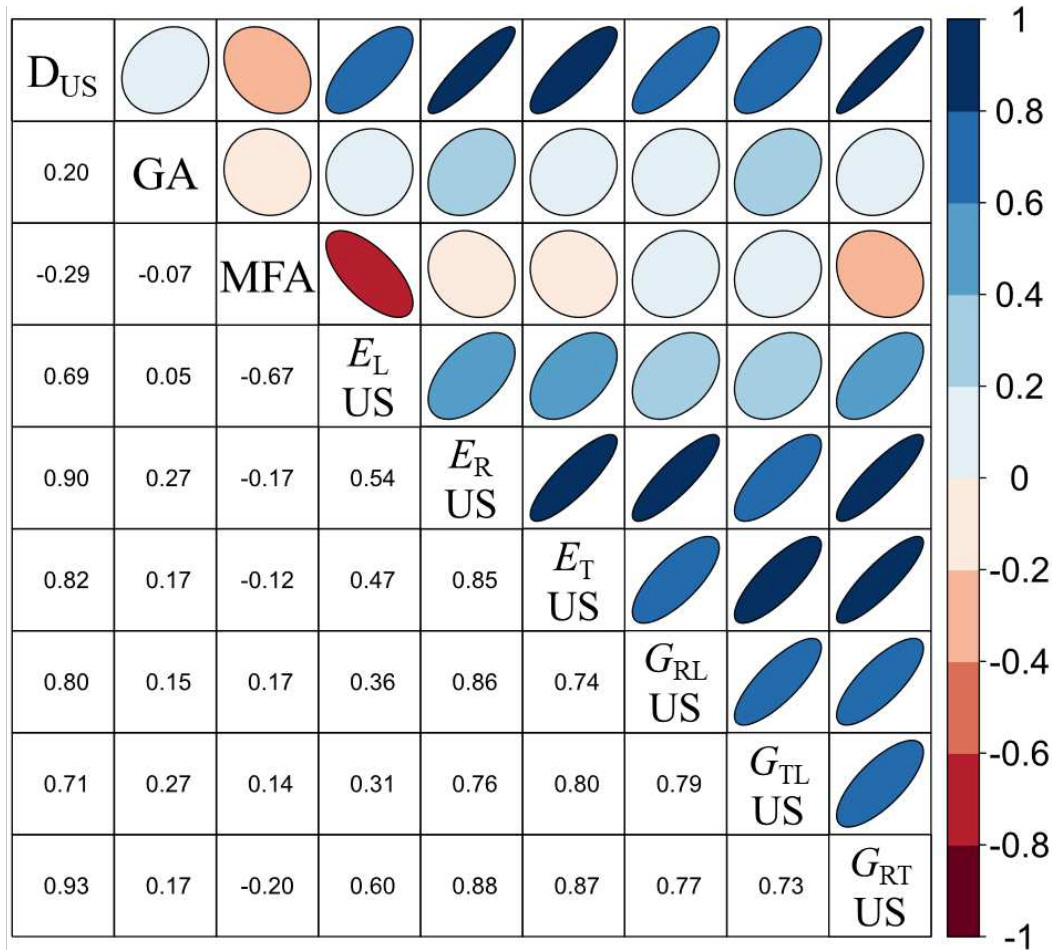


Fig. 92 The correlation matrix for the moduli measured by the US method. D_{US} is the density of the US cubes. The r values are calculated by the Pearson correlation method.

After that, the correlation matrix is made for the ratios of anisotropy between those moduli (Fig. 93). GA still shows a weak influence (with the same remark as previously that GA are complex in the US specimens). The relations to density are generally much weaker when observing the anisotropic ratios, than directly the individual moduli as above. On the contrary, the microstructure, MFA, affects the axial-to-shear anisotropy, e.g., E_L/G_{TL} and E_L/G_{RL} . Interestingly, E_R/G_{RL} is also strong negatively significant to the MFA, showing the contribution of MFA on the R direction force stabilisation (the higher MFA, the lower ratio of E_R and G_{RL}).

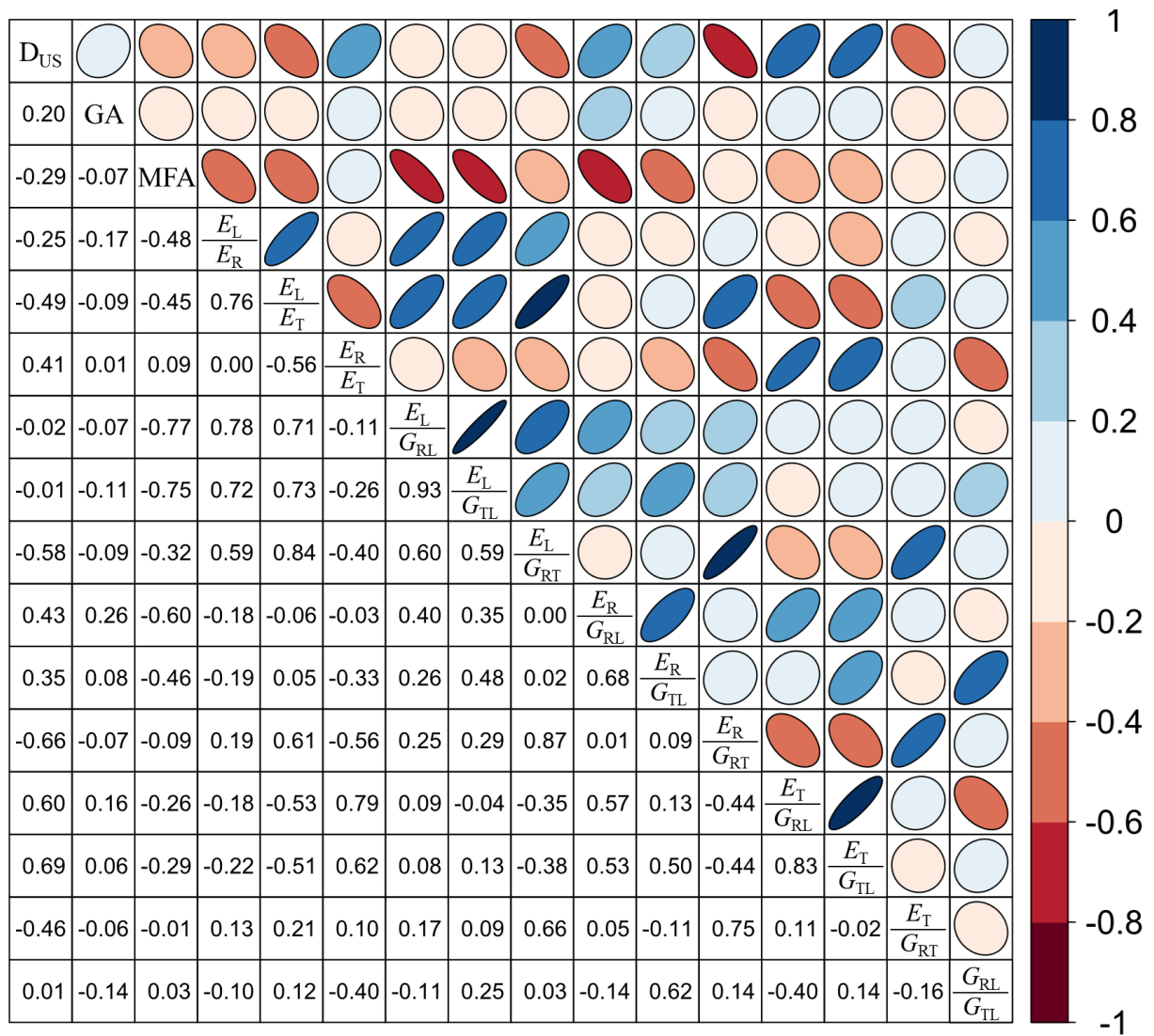


Fig. 93 The correlation matrix for the properties between the local orientation (MFA and GA) and the ratios of anisotropy between moduli from the US test.

IV.C.2.a) Grain angle and anisotropy (on ultrasound specimens)

Based on the previous result, the GA (averaged over a specimen from two local measurements) appeared to have weak or no correlation to the ratios of anisotropy properties. However, a more detailed study on the GA and the ratios of anisotropy is made because GA is known to strongly influence the mechanical properties (while not considering the microstructure or the density factors). So, in the current section, three selected comparisons are made (Fig. 94).

It shows that the no correlation result could be only at the level for all species because the E_L/G_{RL} and E_L/G_{TL} have a large range. It means that the correlation could be species-dependent. Therefore, each linear regression is examined, but their r values are mostly less than 0.1 in absolute value.

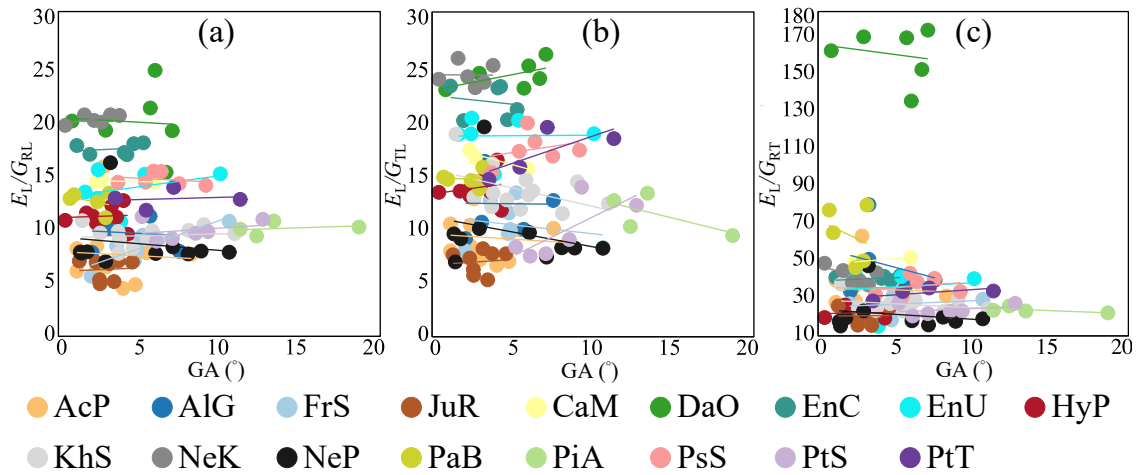


Fig. 94 The correlations of GA to three anisotropic ratios with shear moduli (a) E_L/G_{RL} , (b) E_L/G_{TL} , and (c) E_L/G_{RT} . Data from ultrasound tests, with the GA taken as an average value of two local measurements.

IV.C.2.b) MFA and anisotropy (from ultrasound tests)

The next topic is on the correlations between MFA and the ratios of anisotropy. According to the prior section (§IV.C.2), the MFA correlates negatively to E_L ($r = -0.67$) (Fig. 92), while E_L also has positive correlations with E_T and E_R . The first correlation is thus made between the MFA and the ratios of E_L/E_R (Fig. 95a) and E_L/E_T (Fig. 95b).

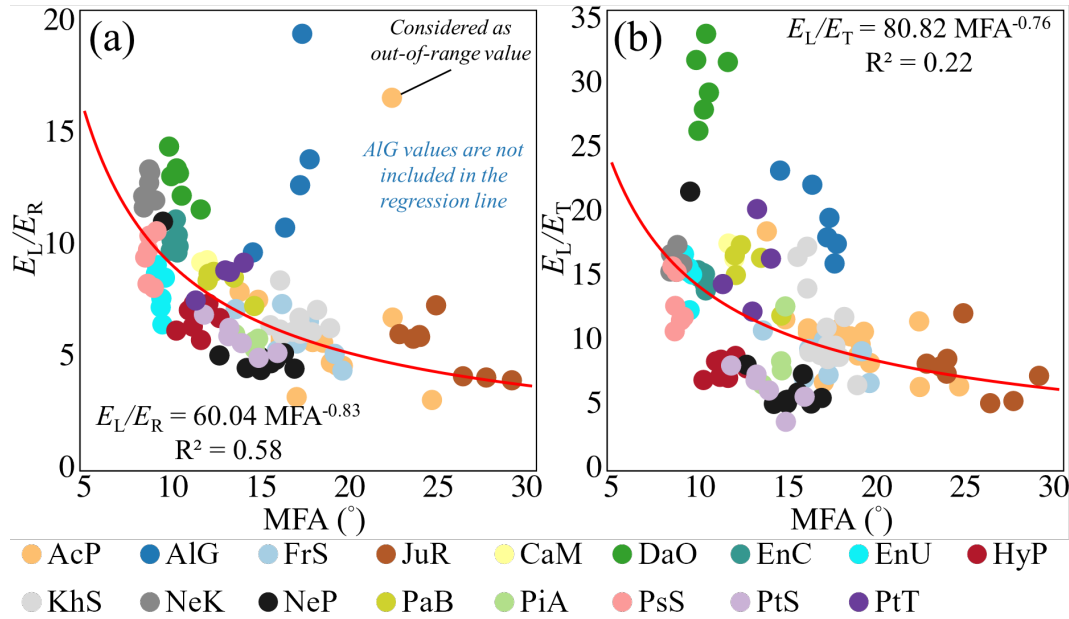


Fig. 95 The correlations between MFA and the ratios of E_L/E_R (a) and E_L/E_T (b). The regression in (a) doesn't consider the out-of-range value and AlG values. Data from ultrasound tests, with the MFA taken as an average value of two local measurements.

In the result of E_L/E_R (Fig. 95a), over all species there is a reasonably strong correlation between this ratio and MFA. This is much less the cases with the ratio E_L/E_T (Fig. 95b).

The AlG shows a high variation of E_L/E_R ratio within a small MFA difference (between 15 to 20°). The author assumes two possibilities: one is that the large ring angle exists and cause the measurement is on the mixture of shear moduli (shear-shear coupling term), and the other reason is that the “wavy+curly” grain pattern is the variation in R direction (mostly) However, in the ratio of E_L/E_T (Fig. 95b), the AlG's behaviour doesn't show a large dissimilarity from the other species. On the contrary, the DaO species shows a trend in Fig. 95b, unlike the other species, a similar result for the AlG in Fig. 95a. The explanation for the AlG's result between E_L/E_R and MFA is explicable from an anatomical-structural aspect. Yet, a similar situation for the DaO in the relationship between E_L/E_T and MFA has no explanation. DaO shares the same grain pattern (interlocked grain, T direction) as many other studied species, and not much ring angle is involved in the specimens.

The further correlations are on the anisotropic ratios between longitudinal elastic modulus (E_L) and the shear moduli (G_{RL} , G_{TL} , and G_{RT}) (Fig. 96). Unlike the comparison of GA (GA values from two flat-sawn specimens, on average, are a local sampling that cannot represent the materials' whole complex GA pattern), the analysis of MFA within a short radius section are

expected to be more stable. Here the MFA proved to correlate well with the ratios between E_L and shear moduli, showing a general trend across all the species (Fig. 96).

The anisotropy between longitudinal modulus of elasticity and in-plane-shear moduli appears to be strongly negatively related to MFA (Fig. 96a,b). The relation is the strongest for E_L/G_{RL} (Fig. 96a) and more dispersed for E_L/G_{TL} (Fig. 96b).

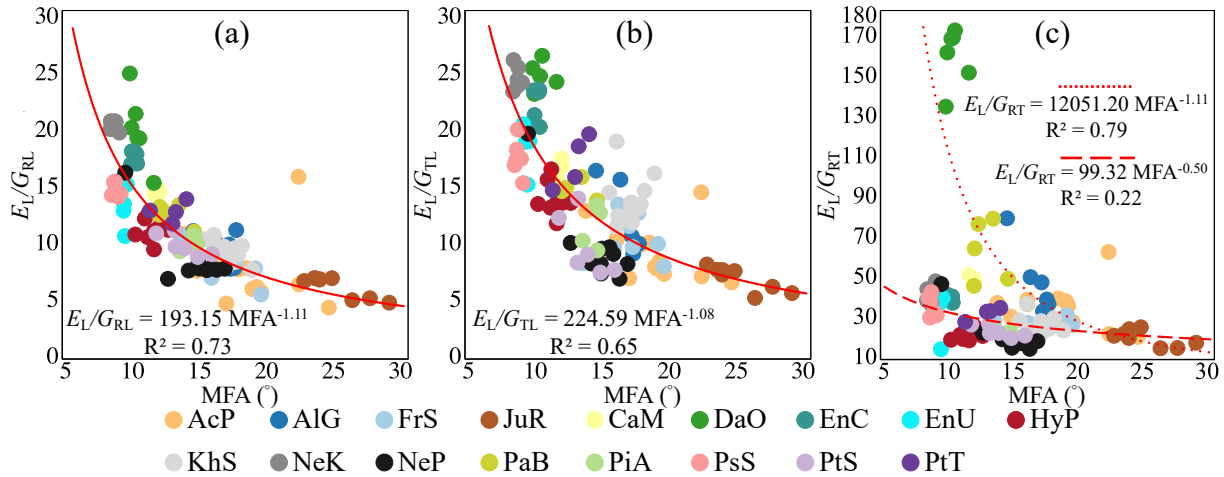


Fig. 96 The correlations of MFA and Anisotropy of longitudinal/shear moduli. (a): E_L/G_{RL} with MFA, (b): E_L/G_{TL} , and (c): E_L/G_{RT} .

In the result (Fig. 96c), between the E_L/G_{RT} and MFA, representing the function of the micro-structural property providing the anti-torsional rigidity corresponding with the longitudinal elasticity, shows two possible tendencies. The trial was made while removing the values considered as out-of-ranger, i.e., DaO, PaB, AlG, forming a regression line which is mostly tropical species (red dashed line). Also, another regression line was made preserving the DaO, PaB, AlG, AcP, FrS, and JuR species (red dotted line). There's no anatomically or structurally orientation pattern that could explain this result. The only found possibility is that the temperate species with DaO and PaB are more or less the lower density groups than the other species. Still, a further examination by including more species should be made to see whether there are two (or more) trends for the longitudinal elastic modulus in the unit of torsional resistance.

Furthermore, the MFA's contribution to wood's shear moduli is studied with the specific shear moduli (G_{RL}/γ , G_{TL}/γ , and G_{RT}/γ in Fig. 97).

The results confirm that the MFA is a main influential factor to the shear rigidity per unit-substance of wood, no matter which grain pattern exists. Still, this is mostly the case for G_{RL}/γ (Fig. 97a). For G_{TL}/γ (Fig. 97b) there is a much higher dispersion, and the behaviour for AlG,

FrS, KhS, and PtS are less concerned in the general trend, so the values are not included in the regression's calculation.

Furthermore, rather than the longitudinal shear rigidities have strong correlations to the MFA (Fig. 97a,b), similar as in the previous result (Fig. 96a and Fig. 96b), the correlation between G_{RT}/γ and MFA only shows on the AcP, AlG, FrS, JuR, DaO, and PaB (Fig. 97c). Using the same species selection as previously (Fig. 96), the tendency for the tropical wood (except DaO and PaB) shows no correlation behind ($R^2=0.00$). Thus, there are no two tendencies shown in the current result.

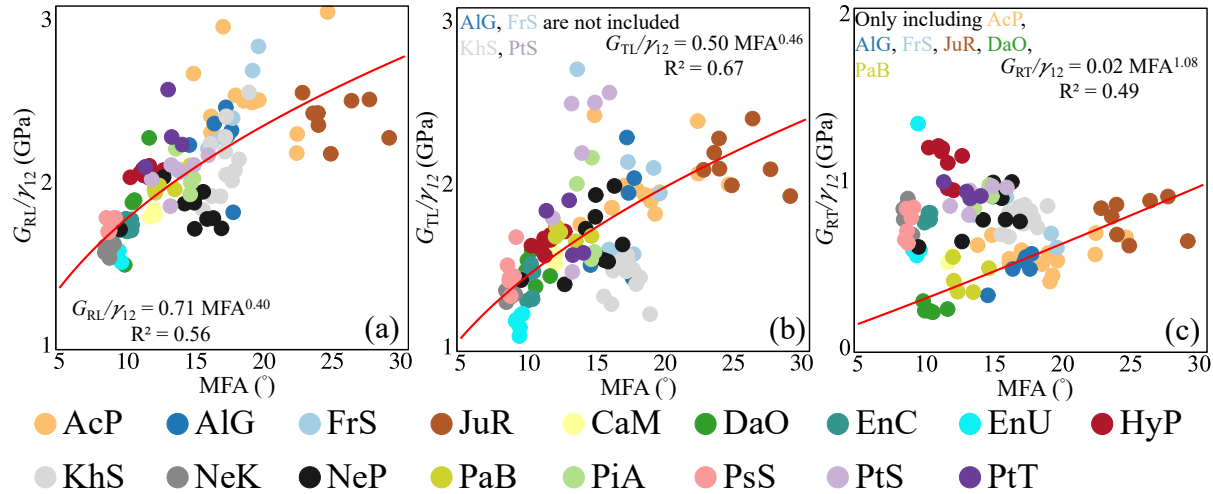


Fig. 97 The correlations between specific shear moduli (a) G_{RL}/γ , (b) G_{TL}/γ , and (c) G_{RT}/γ and MFA for all the species.

IV.C.3. *Effects of local orientation on shrinkage properties*

The local orientations effect is then observed for the shrinkage and hygro-mechanical properties. In the same process, a correlation matrix is made (Fig. 98) to demonstrate the basic information between each property.

In general, the density dominates the shrinkage coefficients (α_T , α_R , α_{Area}). Instead, it is less related to the total shrinkage properties (TTS, TRS), that are dominated by the differences in FSP (i.e., most likely to chemical variations). For the GA, no correlation appears with the studied (transverse) shrinkage properties. On the contrary, MFA is significantly negatively related with shrinkage coefficients (α_T , α_R , α_{Area}).

There is no particular relationship between the shrinkage transverse anisotropy (TTS/TRS) and the local orientation (GA and MFA). It would have been interesting to include tests on the axial shrinkage.

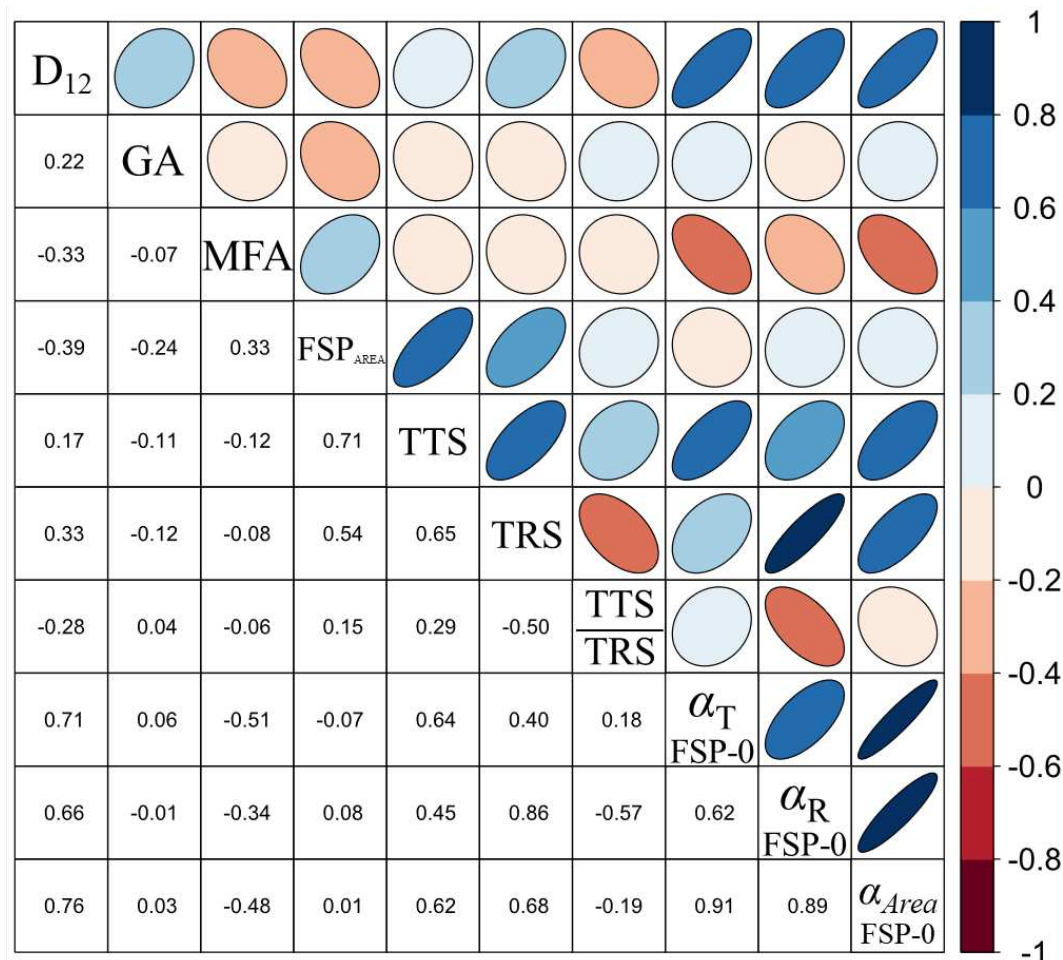


Fig. 98 The correlation matrix between density, local orientation (MFA and GA), FSP, total shrinkage, and shrinkage coefficient (α). The r values are analysed by the Pearson correlation method. D_{12} is the density measured at the MC_{12} state.

IV.C.4. *Effects of local orientation on vibrational properties*

The last analysis on the effects of local orientation is made on the vibrational properties further. The values are from the Vybris flat-sawn specimens as in the previous topic (IV.C.1.b), including the specific moduli (E_L/γ and G_{TL}/γ), ratios of anisotropy between moduli (E_L/G_{TL}), and damping anisotropy ($\tan\delta_{GTL}/\tan\delta_L$). Furthermore, the comparison will consider the previous topic (IV.B.3.b). The anisotropy of moduli and of damping will be verified with the local orientation influence, i.e., GA (IV.C.4.a) and MFA (IV.C.4.b).

The first observation from the matrix below is that density shows virtually no significant correlation to any of the properties considered here (in contrast to previous matrix on moduli or shrinkage). The second observation is that GA now shows several significant correlations, contrary to the previous matrix of correlations (in which a complex GA in a specimen section was simply approached by averaging two local values). The third global observation is that MFA shows the same patterns of relations to properties than GA, but with stronger significance for MFA. Finally, the specific longitudinal modulus of elasticity (E_L/γ), that could be considered as a macroscopic estimate of the superimposed effects of both GA and MFA (as will be studied in part IV.D), shows even stronger correlations to other studied properties, than MFA or GA considered separately.

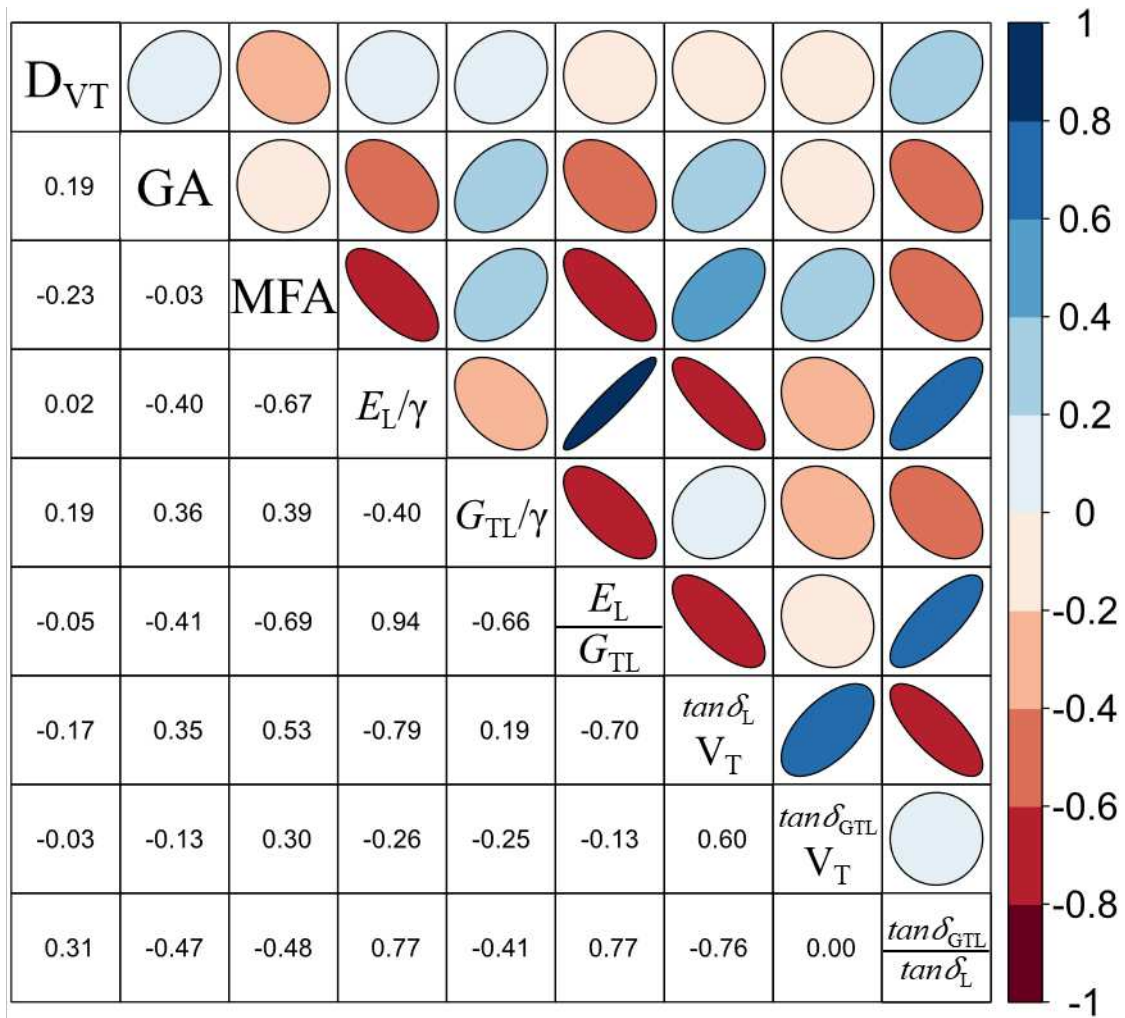


Fig. 99 The correlation matrix for local orientation and anisotropic vibrational properties. All the data (GA, MFA and vibrational properties) are measured at the same level, from the Vybris L-T (flat-sawn) specimens (shortened to V_T for readability in the matrix). The r values are analysed by the Pearson correlation method.

IV.C.4.a) *Effects of GA on the anisotropy of vibrational properties*

The first part is on the GA influence. The regressions used for the GA to E_L/G_{TL} (Fig. 100) and GA to $\tan\delta_{GTL}/\tan\delta_L$ (Fig. 101) are linear due to the higher R^2 than the power regression. Based on the results (Fig. 100 and Fig. 101), both ratios of anisotropy appear to have significant, but weak, GA correlations ($0.4 < r < 0.5$). However, the important dispersion observed here involves all the studied species considered together. When observing the properties over small GA, it is clear that the various species have their own distributions, i.e., that the specimens that happen to have nearly no GA inside show widely different anisotropy depending on species.

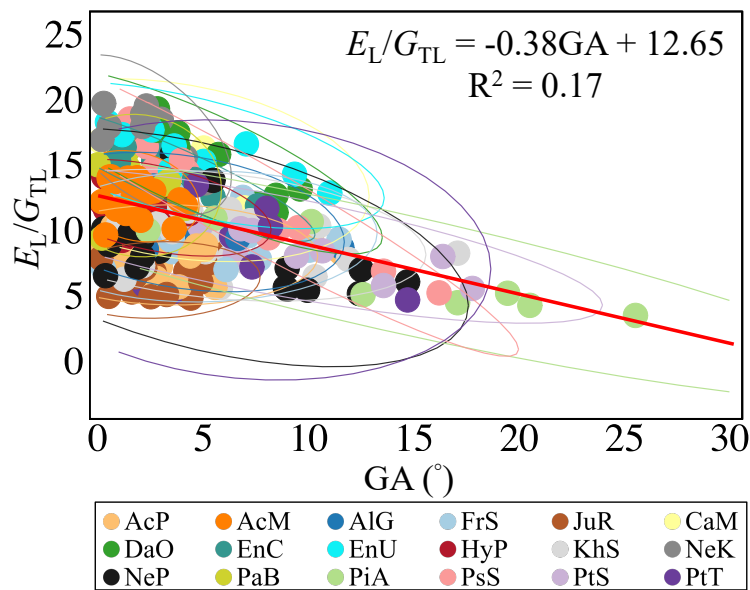


Fig. 100 Correlation between E_L/G_{TL} and GA, all species are considered together.

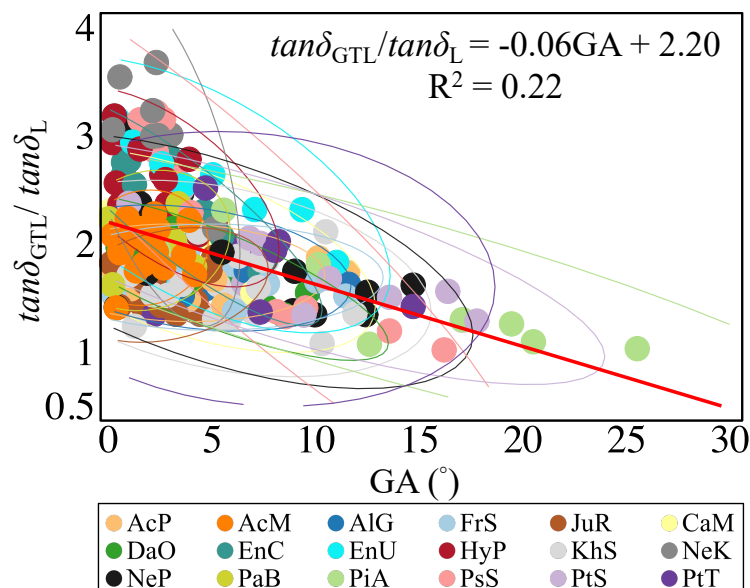


Fig. 101 Correlation between $\tan\delta_{GTL}/\tan\delta_L$ and GA, all species are considered together.

IV.C.4.b) *Effects of MFA on the anisotropy of vibrational properties*

Instead of the previous observation (Fig. 100 and Fig. 101 in topic IV.C.4.b), power regression is used for the MFA correlations because of higher R^2 values. MFA has strong correlations to the axial-to-shear anisotropy of moduli (E_L/G_{TL}), but its correlation to the anisotropy of damping ($\tan\delta_{G_{TL}}/\tan\delta_L$) is of the same order of magnitude as in the case of GA. Also, here again these correlations are observed on all species considered together. When observing the contribution of the different species to the global dispersion, it can be seen that in some species the anisotropy is indeed driven by the MFA (e.g., in JuR or AcP that have high values of MFA). While in some other species the distribution is nearly vertical, i.e., the anisotropy can vary widely within a very narrow range of MFA (e.g., PsS or EnU, that both have relatively wide ranges of GA).

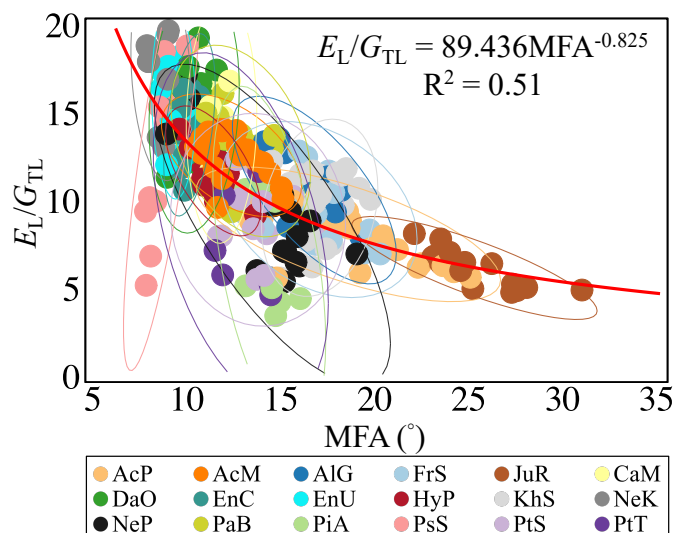


Fig. 102 Correlation between E_L/G_{TL} and MFA, all species are considered together.

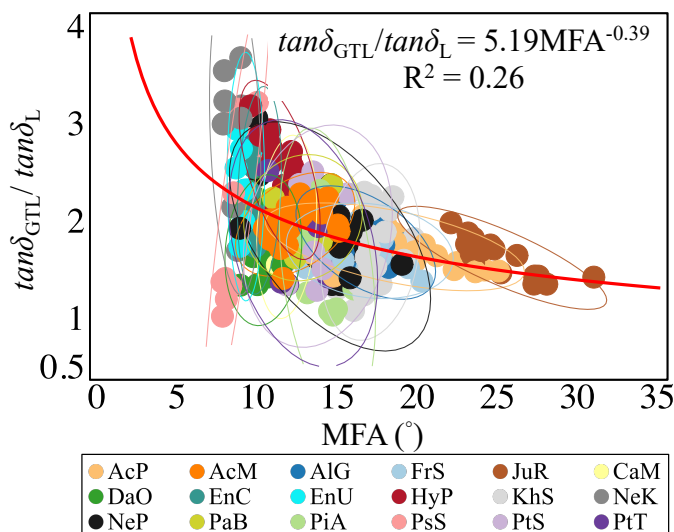


Fig. 103 Correlation between $\tan\delta_{G_{TL}}/\tan\delta_L$ and MFA, all species are considered together.

IV.C.5. Further Analysis for the selected Anisotropy Properties

Some anisotropic ratios are selected for further analysis according to the previously presented correlations (Fig. 93). Instead of focusing on the longitudinal anisotropy, three selected anisotropy ratios' comparisons are in the R and T directions, which are:

- the T-R anisotropy of moduli of elasticity and shear moduli (E_T/E_R to G_{RL}/G_{TL}) (IV.C.5.a),
- the axial rigidity to the tangential (figured) efficiency (E_L/G_{RT} to E_T/γ) (IV.C.5.b),
- radial rigidity to the hygro-mechanical anisotropy (E_R/G_{RT} to TTS/TRS) (IV.C.5.c).

IV.C.5.a) The T-R Anisotropy of moduli of Elasticity and in Shear

The first analysis examines the ratio of moduli of elasticity (E_T/E_R) and the ratio of shear moduli (G_{RL}/G_{TL}) (Fig. 104). The values from the experimental result are compared with Guitard's result (§IV.B.1). An elliptical distribution (the red oval shape, 95% confidence interval) is made first to examine the out-of-range values. Then the regression line (solid red) is made according to the rest of the data. Compared with the previous result (Fig. 81), the E_T values (Fig. 81e) are the only modulus larger than the standard trend. The current development shows that the figured wood's elastic anisotropy (E_T/E_R) to the shear anisotropy (G_{RL}/G_{TL}) has little difference.

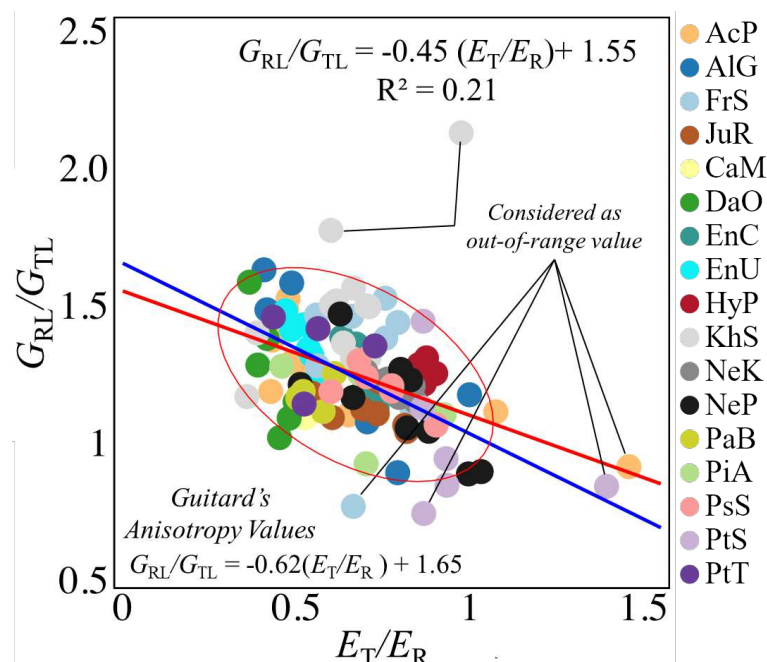


Fig. 104 The ratio of G_{RL}/G_{TL} to E_T/E_R . The red line is the regression result from the experimental measurement, and the blue line is the Guitard's "standard hardwood" (§IV.B.1).

IV.C.5.b) *The tangential specific elastic modulus and axial rigidity anisotropy*

The further correlation is then made with the longitudinal elastic per shear rigidity in the RT plane (E_L/G_{RT}) to the specific tangential elastic modulus (E_T/γ) (Fig. 105). The correlation is to verify whether the figured wood's adaptation (fibre towards to T direction, generally having larger E_T/γ) does contribute to the torsional resistance per longitudinal in the tree. The comparison is also made with Guitard's values.

As a result, it could be taken as two parts, and the boundary is the crossing point between the experimental result (red curve) and Guitard's regression result (blue curve). The left side shows that the species have a high specific tangential elastic modulus and relatively high torsional rigidity (low E_L/G_{RT}). The high GA values' interlocked grain species are mainly located on this side, i.e., PtS, PiA, and KhS. On the other hand, the species develop more on the E_L but less rigidity in the RT plane on the right side of the crossing point. Still, according to the regression result, the figured wood's E_T/γ are generally larger.

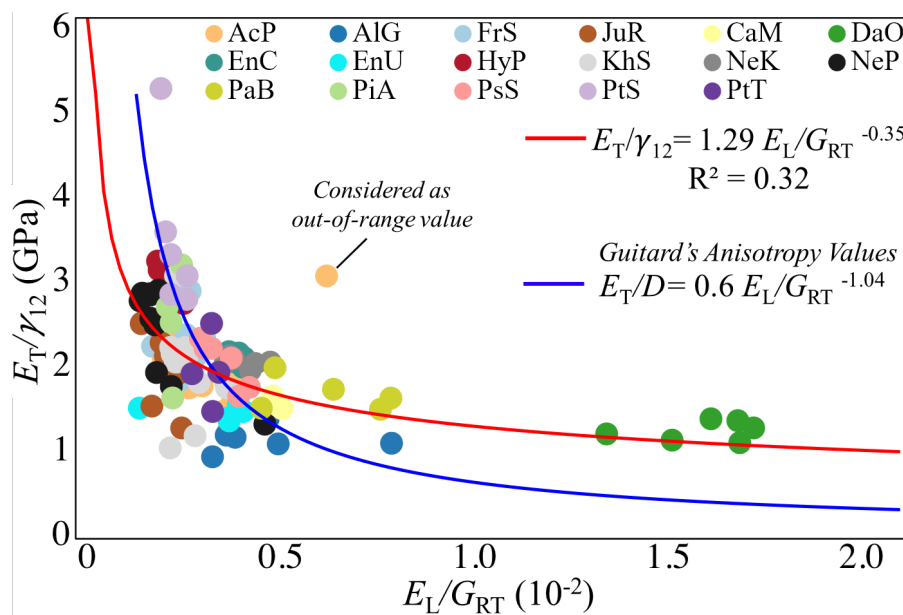


Fig. 105 The correlation of longitudinally torsional rigidity (E_L/G_{RT}) to the unit (specific) elastic modulus in T direction (E_T/γ). An out-of-range value (from AcP) is not considered in the regression's calculation (red line), and Guitard's model is the blue line.

IV.C.5.c) *The T-R elastic-shear anisotropy and hygro-mechanical anisotropy*

Another correlation posed on the anisotropic behaviour is the hygro-mechanical aspect. It is on whether the angle-shifting-layered structure or the radial varied grain structure in the radius direction reinforces wood's rigidity (R-T plane) while constraints wood's shrinkage proportional behaviour in the R and T directions (lower TTS/TRS) (Fig. 106). The lower shrinkage ratio TTS/TRS means a less unstable dimensional changes (from green to oven-dry) between two directions. Furthermore, the E_R/G_{RT} is also an elastic anisotropy factor to evaluate wood's acoustic property (Takeshi 1991).

As a result (Fig. 106), most species are in the same range for the E_R/G_{RT} . However, some species' E_R values are relatively high because their grain variations are radial, e.g., birdseye maple (AcP-M) and pommele maple (AcP-P). On the contrary, two interlocked grain species, i.e., PaB and DaO, seemingly have relatively lower G_{RT} than the others.

The author assumes that the adaptation for the interlocked grain species could have two different approaches. One has higher torsional resistance (preventing scissoring shear delamination, low E_R/G_{RT}). The other has a higher radial elastic modulus (preventing crack opening delamination, higher E_R/G_{RT}) but is less rigid. The previous one has less R and T difference in the hygroscopic deformation, and the latter could stand more from the hygroscopic change.

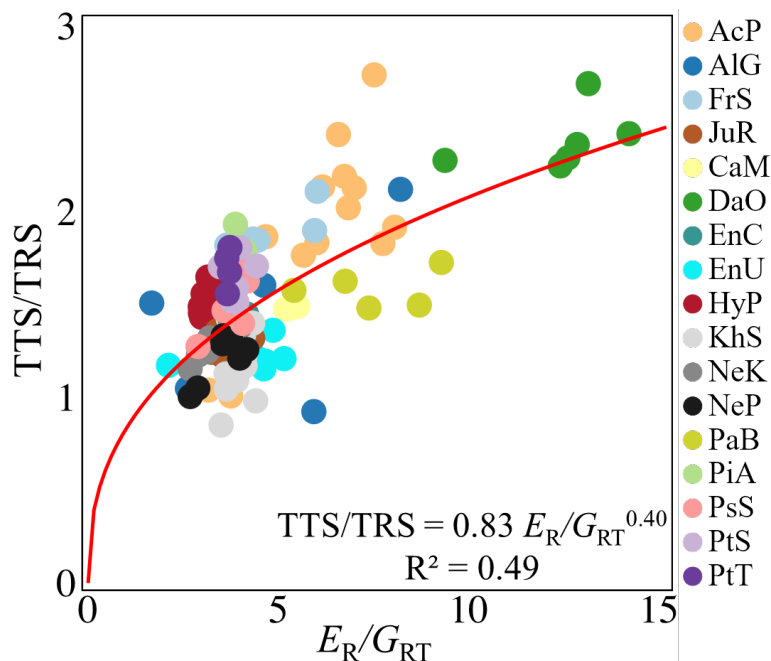


Fig. 106 The correlation between E_R/G_{RT} to TTS/TRS.

IV.D. Superimposed effects: Cumulated effects of GA and MFA on the longitudinal specific modulus of elasticity

The wood's longitudinal elastic modulus decreases when either the GA or the MFA have an included angle relative to the longitudinal axis. The specific modulus of elasticity E_L/γ is generally used for reflecting the influence of GA and MFA, as it excludes the other effect of density. While considering the two structural orientation characteristics for wood's longitudinal elastic modulus, the cumulation of two values (GA and MFA) is studied (Fig. 107)

The development is made to better understand the (relatively weak) individual correlations between GA and E_L/γ (Fig. 107a) and also between MFA and E_L/γ (Fig. 107b). Lastly, the correlation between GA+MFA and E_L/γ is done (Fig. 107c). The result shows a better correlation than each of the previous two. Therefore, a further model for the correlation is developed to consider the MFA's two in-plane angles.

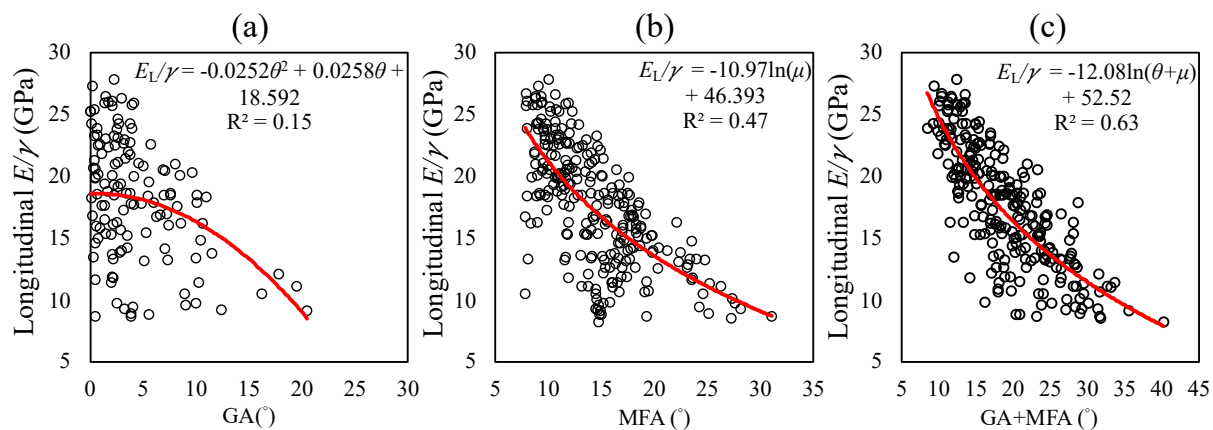


Fig. 107 The correlations between GA, MFA, and GA+MFA, and longitudinal specific modulus of elasticity.

The predicting model for the correlation between the specific modulus and GA+MFA ($\theta+\mu$) has two estimation approaches: the first is to adjust the apparent MFA, and the other uses Hankinson's equation (in 2D) to verify the estimated specific modulus.

For the MFA's correction, it is based on the assumption that the MFA's measurement by XRD can be biased due to the presence of GA. Thus, a linear relationship for adjusting the apparent MFA (μ^*) is listed below, of which a and b are constant, and $\mu > 0$:

$$\mu = a \times \mu^* + b \quad (61)$$

Assuming wood's specific modulus is dominated due to the macroscopic orientation, i.e., GA, and the microscopic orientation, i.e., MFA, the model considers two in-plane-angles of the MFA and the orientation of GA relative to the longitudinal direction (Fig. 108).

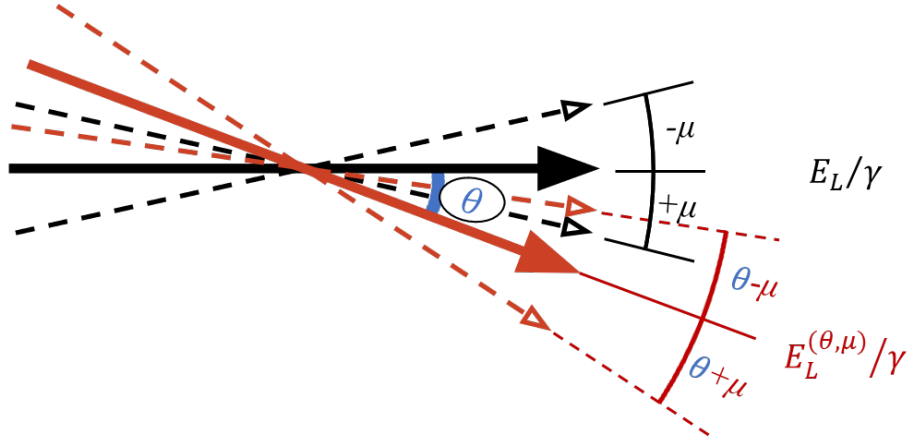


Fig. 108 The GA (θ) and MFA (μ) diagram (in black) and the situation when GA is not zero (in red).

Therefore, despite the other factors involved in the model, the predicting model for a piece of wood, in its longitudinal specific modulus's function is composed of two sub-functions, which are $E_L/\gamma(\theta+\mu)$ and $E_L/\gamma(\theta-\mu)$. The influential fractions of the two sub-functions are the same so that the composed function could be listed as:

$$\frac{E_L}{\gamma}(\theta, \mu) = \left[\frac{E_L}{\gamma}(\theta + \mu) + \frac{E_L}{\gamma}(\theta - \mu) \right] / 2 \quad (62)$$

The abbreviated marks for the GA+MFA(Θ) for the $\theta+\mu$ and $\theta-\mu$ express respectively:

$$\theta_1 = \theta + \mu = \& \theta_2 = \theta - \mu \quad (63)$$

Furthermore, the approaches between the specific modulus and the angle's orientation, i.e., MFA and GA, adopts Hankinson's equation that the empirical factor (n) of cosine and sine is set as 2. As a result, the two sub-functions of equation (62) are:

$$\frac{E_L}{\gamma}(\theta + \mu) = \frac{\frac{E_L}{\gamma} \times \frac{E_T}{\gamma}}{\frac{E_L}{\gamma} \sin^2 \theta_1 + \frac{E_T}{\gamma} \cos^2 \theta_1} \quad (64)$$

$$\frac{E_L}{\gamma}(\theta - \mu) = \frac{\frac{E_L}{\gamma} \times \frac{E_T}{\gamma}}{\frac{E_L}{\gamma} \sin^2 \theta_2 + \frac{E_T}{\gamma} \cos^2 \theta_2} \quad (65)$$

Then, E_L/γ , E_T/γ , Θ_1 and Θ_2 are calculated with Excel's solver (GRG Nonlinear, no assigned condition for the target value), to find the minimum of the root-mean-square error (RMSE) (66) between equation (62) and the measured value (E_L/γ):

$$RMSE = \sqrt{\frac{\sum \left(\frac{E_L(\theta, \mu)}{\gamma} - \frac{E_L^M}{\gamma} \right)^2}{n_{Qty}}} \quad (66)$$

E_L^M/γ is the measured result; $\frac{E_L(\theta, \mu)}{\gamma}$ is the predicted value; n_{Qty} is the sample's quantity

The a and b for adjusting the apparent MFA values are 0.80 and -4.21, respectively. The mean, maximum, and minimum values of the apparent MFA values are 14.38, 31.02, and 7.08, respectively. On the contrary, the adjusted MFA values are 7.27, 20.54, and 2.01, respectively. The adjusted values are still reasonable as there's no MFA value below 0° after being adjusted.

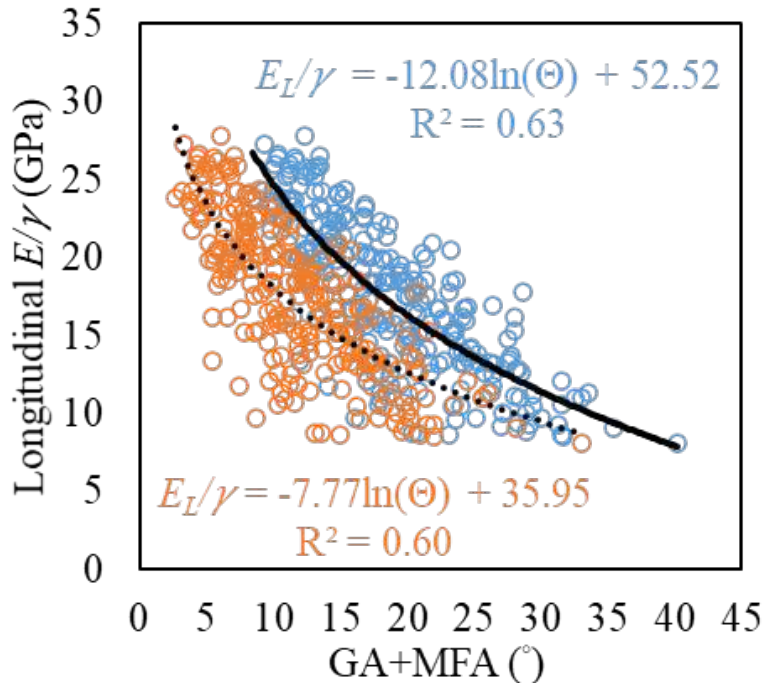


Fig. 109 The comparison of the original and adjusted GA+MFA (Θ) with the measured E_L/γ . The blue hollow points are the original Θ values, and the orange ones are the GA plus the adjusted MFA.

The estimated E_L/γ and E_T/γ values are 24.91 GPa and 1.13 GPa, respectively. On average, the E_T/γ result is lower than the adjusted E_T values from the US result (1.66 GPa) (adjusted US's E_T value = US's $E_T/1.237$). However, while considering the GA's measurement is also biased, from the experimental result, the maximum absolute GA value is 25.51° , and the maximum

GA+MFA value is 40.24° (33.05° after being adjusted). An inexact estimated result (E_T/γ) above two times the actually observed degree (40.24 to 90°) is fair enough.

The E_L/γ values' comparison between the predicted (from solver) and measured E_L/γ are close to each other : the correlation of coefficient is +0.8 and the ratio between them are 0.98 (Fig. 110).

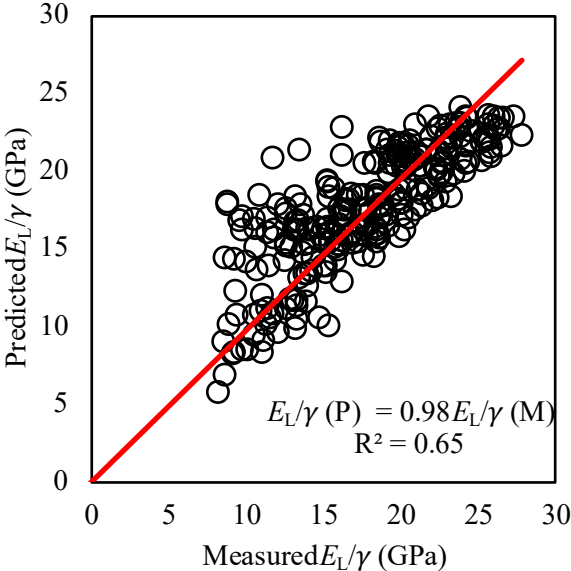


Fig. 110 The correlation of the predicted E_L/γ and measured E_L/γ . (P) indicates the predicted value of E_L/γ , and (M) is the measured value of E_L/γ .

The estimated E_L/γ values (by the solver in Excel) are then fitted with a logarithm curve (red curve in Fig. below) with finding the minimum RMSE (66). Also, the estimated Hankinson's equation curve is drawn (green curve) to show the correlation between the estimated wood's specific moduli (E_L/γ and E_T/γ) and the constitutive relationship of GA+MFA.

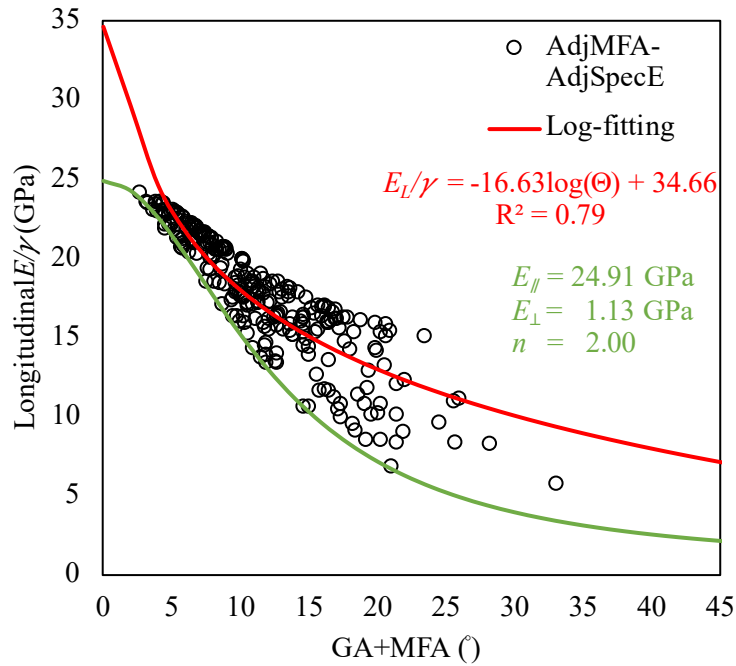


Fig. 111 The adjusted MFA (AdjMFA) and the model's E_L/γ values (AdjSpecE) from equation (62). The red curve is the logarithm fitting curve, the green curve is from Hankinson's equation, and the parameters of the equation are in green.

After that, another approach was made to re-examine/re-adjust the n parameter of Hankinson's equation (Fig. 112). Excel's solver approaches the n value according to RMSE between the measured E_L/γ and the GA plus the adjusted MFA, $n = 1.73$. The E_{\parallel} and E_{\perp} values are from the logarithm's maximum ($\Theta = 0^\circ$) and minimum ($\Theta = 90^\circ$) results, respectively.

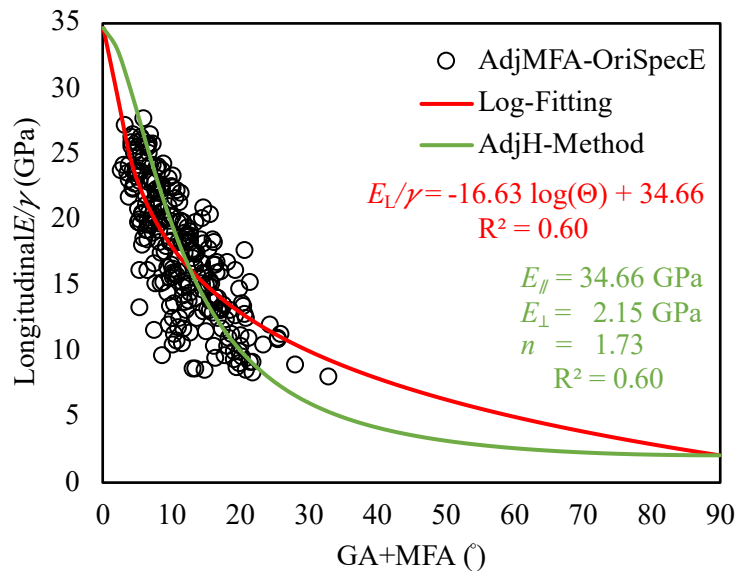


Fig. 112 Two models (Log-fitting & AdjH-Method) are compared in an extended range to $\Theta = 90^\circ$. The E_L/γ values (OriSpecE) are measured, and the MFA values are adjusted (AdjMFA).

The model is expanded to 90° to demonstrate the possible trend of E_L/γ corresponding to the angle (Θ) change. However, this trend is not applicable for the complex grain model because the maximum and minimum values could happen not at 0° nor 90° .

IV.E. Grain deviations in figured wood: “quality” or “defect”?

From an engineering viewpoint, a wood with a grain angle is a negative characteristic for the longitudinal mechanical properties. As a result, having a grain angle in a piece of wood would be a defect from a general perspective. The argument does not hold for a piece of wood with a single grain angle. Understandably, the included angle between the applying utilisation and the wood’s structural orientation is a fundamental error for wood’s application.

Additionally, mechanical property’s decreasing caused by the GA is certainly no matter the grain is complex or single (part IV.D). It is also clear that the wood’s longitudinal elastic modulus decreases largely only after a certain GA. In the literature, it is shown to decrease steeply even after 5° for very anisotropic woods such as softwoods and especially spruce “tonewoods”, but slower so for hardwoods (Brémaud et al. 2011b). In the present results, considering the diversity and the other causes of variability, the specific modulus decreases mostly above 10° (Fig. 107a). Therefore, the grain deviation within a small amount / with a small amplitude would not be much significant compared to other sources of variability.

A piece of figured wood with unidirectional waviness or quasi-unidirectional (or both-above-mentioned) grain structure, its measured GA from a thin plate (taken as simple GA) does not correspond to the complete grain structural pattern into a larger piece, also not to another plane. In this circumstance, a local measurement of GA is not very indicative and the material’s behaviour, in general, is more obviously influenced by the microstructure (MFA) (part IV.C).

The GA’s contribution evaluation is not applicable from the present study because the GA’s measurement is more on the two flat-sawn planes (topic II.C.2.c). Also, using the maximum angle values to evaluate the hygro-mechanical aspect in a whole piece of wood is also proved not applicable in another study (Coelho et al. 2020). Due to local variations of the GA, the corresponding relations to mechanical and hygro-mechanical property is less reliable than that of the MFA for the figured wood (§II.C.2).

Still, the advantage of having GA deviation could be seen as an adaptation of weakening the longitudinal characteristics but increasing the other properties, e.g., unit/specific moduli in the T and R direction (depending on the grain pattern and structure) and the torsional rigidity. Although the GA’s evaluation does not relate well with the mechanical property, there is no particular large difference compared with the standard trends in R and T directions (Fig. 81).

The diminished anisotropic behaviour due to the GA could still be seen (Fig. 105). The result also follows the same conclusion with another research that the grain deviation decreases the anisotropy (Buksnowitz et al. 2012). The originality of the present study is to observe this in the hygro-mechanical, elastic, and viscoelastic (dynamic) mechanical aspects (topic IV.C.5.c). Yet, if the strong anisotropy on “standard” wood is one of its main mechanical characteristics, there may be utilisations where a reduced anisotropy, while keeping the other qualities of wood, could be beneficial.

IV.F. *Comparison of physical-mechanical properties with recorded appearance (Chapter II) and with appreciations (Chapter I)*

The grain deviation’s effects are not a straight-forward-relationship to the GA’s measured values (neither the largest value nor the local variations value), but the GA eventually affects the properties. While the larger grain deviation generally shows a stronger figure (degree of figure, doF; or optical contrast), the relation between the appearance and the mechanical property could be built according to the figure appearance. However, the comparison among different species could be still limited due to the species properties.

In Chapter II, according to the recorded surfaces of the materials (Tab. 6), the largest band/ribbon figure (one type of figure for the interlocked grain) species, i.e., KhS, PsS, PiA, and PtS, have higher E_T/γ (Fig. 105) and higher torsional rigidity per longitudinal elastic modulus (E_L/G_{RT}). On the other hand, the more intense birdseye (Fig. 24) and shorter wavy frequency’s figures (FrS and JuR, Fig. 22 and Tab. 7) have a lower specific modulus of longitudinal elasticity (Fig. 77). At the same time, the bending $\tan\delta_L$ are also higher (Fig. 79).

There is no quantitative method to evaluate the curly and pommele grain pattern’s GA or grain pattern. From the appearance judgement, the mechanical and viscoelastic properties can still be graded, the same as the conclusion of birdseye and wavy figures, the more doF, the lower the specific modulus of longitudinal elasticity and higher $\tan\delta_L$ (Fig. 77 and Fig. 79).

For the interlocked grain, the appearance of its band figure could connect to the mechanical properties and their anisotropy. However, it is hard to grade the interlocked grain’s mechanical property since density plays a strong role for the mechanical property, and density is more associated to species’ characteristics than to figured woods. For the other grain pattern, within some species the doF and the grain deviation were coincidentally connected to the density, in some other cases there were just no relations to density (part IV.A).

To finish, the appearance of the material's surface does connect to the mechanical properties in several aspects. However, the connection is not only species-dependent but also figure-dependent. Thus, the physical-mechanical evaluation from the appearance is not an absolute indicating way. However, it could be workable if either the density is a fixed variable, e.g., two different band figure species in a similar density range; or if the figure pattern is a fixed variable, e.g., same figure pattern for two species having different density values.

Summary of Chapter IV

The objective of Chapter IV was to explore the detailed effects of the figured grain on the measured physical-mechanical properties and their anisotropy. It started by comparing their variability at the within-species and the between-species levels. To continue, obtained results on figured woods were compared to literature-based correlations between properties, established on “standard” woods. Then, the effects of local orientation (grain angle GA and microfibril angle MFA) on the different properties were analysed, with a special focus on their anisotropy.

The results were presented while keeping in mind some methodological limitations. These include mainly that:

- The sampling is focused on representing a wide array of grain patterns, but the drawback is that there are a limited number of individuals for a given grain pattern inside a species.

- The strength of the present study is to include a wide array of properties (structural, physical and mechanical), but the drawback is that there are some scale-effects due to the different dimensions of specimens required for the different tests. This mostly affects the GA estimations, because local measurements of GA can be related to local mechanical measurements, but cannot represent the complex variations of GA within the specimens of relatively wide sections (used for ultrasound or shrinkage for example).

Notwithstanding these methodological aspects, the obtained results allow to draw several tendencies and/or conclusions, as summarised below:

- The density is widely variable between species, but within species it is the most stable of the studied properties. There are some exceptions however: for the temperate species represented by several individuals, there were three cases where a higher degree of figure (doF) was accompanied by a higher density: birdseye and pommele maple, wavy walnut. For the tropical species with interlocked grain, there were also three cases where amplitude of figure (GA) was associated to density, although the relation was not strong, and this rather revealed effects of the radial position. In all other cases, the density was not associated to the strength of the figured grain.

- The axial specific modulus of elasticity (E_L/γ) was highly variable within-species. For the temperate species with several individuals, the higher doF were usually associated to smaller values of E_L/γ . For the tropical species with interlocked grain, there was a very high variability

within a single individual, as measured on small-scale specimens, and this was particularly pronounced for flat-sawn specimens, i.e., the specimens cut in the L-T plane of the GA variations.

-The within-species (or within-individual) variability was also pronounced for the other vibro-mechanical properties, but proportionally less for the in-plane shear modulus (G_{LR} and G_{LT}), the axial damping ($\tan\delta_L$) and the shear dampings ($\tan\delta_{GRL}$ and $\tan\delta_{GTL}$), than observed above for E_L/γ .

-The correlation between density and 6 elastic moduli (E_L , E_R , E_T , G_{RL} , G_{TL} , G_{RL}) were globally very similar to the “standard hardwoods” (Guitard’s statistical models). However, the dispersion was very important for E_L , and the moduli E_T and G_{TL} for figured woods tend to be above the “standard hardwoods”. For the “local”, small-section specimens, the axial modulus E_L is not only very dispersed, but also tends to be lower than the “standard” relation to density.

-The standard relation between axial damping and specific modulus is also well conserved compared to the literature, but here again with a high dispersion, both in E_L/γ (expressing effects of orientation – GA and/or MFA) and in shifts of $\tan\delta_L$ from the relation (expressing effects of variations in chemistry).

-The relation between axial-to-shear anisotropies in dampings ($\tan\delta_G/\tan\delta_L$), and in moduli (E/G), is also similar, but more dispersed, than in the literature, with, in average, higher $\tan\delta_{GRL}$, and lower $\tan\delta_{GTL}$, over the figured woods studied here.

-The anisotropy for the axial moduli (E_L/G_{RL} and E_L/G_{TL}) is low for figured woods because of the higher shear moduli and lower elastic modulus. The lower E_L (higher GA and doF) could sum up more shear rigidity for wood.

Regarding the different factors that can affect the studied properties and their anisotropy, the main results were as follow:

-The density, grain angle GA and microfibril MFA, three know affecting factors of properties, were very little, or not at all, correlated between them, whatever the level and scale of observation.

-The density was the principal affecting factor for shrinkage coefficients and elastic moduli. But density was not relevant for vibrational properties (E_L/γ , G/γ , $\tan\delta_L$, $\tan\delta_G$). Density was an important affecting factor for the ratios of anisotropy involving transverse (T-R) plane, but not

much so for axial-to-shear or axial-to-transverse ratios of anisotropy, where MFA plays a stronger role.

-On relatively “bulk” specimens (used for shrinkage and ultrasound tests), the effects of MFA were significant on shrinkage coefficients, on axial modulus and specific modulus, on axial-to-shear and axial-to-transverse ratios of anisotropy. On the other hand, the potential effects of GA could not be observed because GA was measured locally and not inside the whole section of these specimens. Even on small-section specimens, however, GA effects had smaller correlations to local vibro-mechanical properties and their anisotropy, than MFA did.

-Over all species considered together, MFA was a strong predictor of E_L/G_{RL} , also (but weaker) of E_L/G_{TL} , and (weaker) of E_L/E_R . But it was only very weakly correlated to E_L/E_T .

-When looking more closely at the respective effects of GA and MFA, however, it appears that for some species the axial properties (and their axial-to-shear anisotropy) are mostly driven by GA (for interlocked grain species with the widest variations in GA), while in some species there are mostly driven by MFA (temperate species with moderate and/or complex grain variations and high and variable values of MFA).

-Accordingly, a detailed analysis focused on E_L/γ proved that it is much better explained by the superimposed effects of GA and MFA (mesoscopic and microscopic orientations), than by each factor separately. This would be interesting to be further analysed on the other properties.

-The more figured wood (higher doF) shows a higher appreciated/complexity on the visual appearance. While the higher doF also implies lower axial elastic modulus, higher shear and transverse moduli, lower anisotropy and higher damping. Thus, the comparatively visual grading (between the same species and different individuals) is generally applicable for the figured wood.

Some perspective could help in the future to deepen the understanding of above results:

- Multiscale modelling (not only of axial modulus, but also of shear and of damping).
- More synthetic indicators of grain deviations and complex grains within specimens.
- Multiple correlations to evaluate respective effects of density, GA and MFA on various properties.
- Studying not only elastic and (viscoelastic) dynamic properties, but also strength properties.

General Conclusion and Perspective

The present study works on the figured wood for its diversity and terminology (Chapter I), grain structure (Chapter II), local orientation angle measurement (Chapter II), visual inspection evaluation (Chapter II), mechanical and hygro-mechanical properties (Chapter III). Furthermore, the results are compared with the related literature data (Chapter IV), including the local orientation effect and anisotropy properties. In the end, the relation between the visual appearance and the mechanical property evaluation (Chapter IV) are studied subjectively (according to the author).

The most featured characteristic of the figured wood is its appearance, the figure of the wood. Many basic grain patterns have been indicated, and the basic elements have been defined for their form and directions. However, according to the collected literature and the wood figures from the professional vendors' websites, a wide diversity of figures exist, beyond the indicated basic patterns. A further study is needed to determine whether some complex figures can also be categorised as one of the basic elements of grain patterns or just as a singularity (combination of different patterns) to the figured wood.

In the present study, the author used the indications and figures from the professional website to distinguish and expand the knowledge on the figured wood in the real world. Yet, the name for the wood figure could be complicated because the exact figure name could have different grain patterns, e.g., pommele/blister in different species and due to the degree of figure. According to this, the terms are geographical-, linguistic-, cultural-, and species-dependent, which would be an advantage to exploring the existence of the figured wood worldwide. On the contrary, it would be difficult to explore in this way due to the language ability.

From the mechanical and more general way, a non-destructive method for detecting the grain angle should be developed for verifying the figure and the grain pattern. In the present study, a trial for the optical light is roughly built. The workability could be seen while comparing with the image, but not yet be proved with the real internal structure. The combination with the digital image correlation method is necessary to be further built. Also, the comparison with the splitting result is essential to verify the optical detection result since the grain patterns could be highly complex for the general cases, e.g., interlocked with curly grain.

The figure wood's appearance shows the grain pattern type and the result of fibres angle, implying the behaviour of the mechanical properties. However, the comparison of the

mechanical behaviour is not absolute but comparatively. Thus, the inter-species or inter-pattern-type are not applicable. This means that it is possible to reach the same species, same grain pattern, but different figure degrees. Also, the grading by the mean of visual appearance is workable for the figured wood.

A wide set of results on the physical-mechanical properties of figured woods has been obtained. These results include a rather complete view of anisotropy – in hygromechanical, elastic, en vibrational-viscoelastic properties. The reduced anisotropy of figured woods was confirmed. The decrease in longitudinal mechanical properties, i.e., E_L and E_L/γ , caused by the grain pattern/deviation, is evident, resulting in less axial-to-shear anisotropy values on E_L/G_{RL} and E_L/G_{TL} . However, between very different species, the effects of orientation include the superposition of grain angle and of microfibril angle. Over moderate grain angles, the between-species variability of microfibril angle can be predominantly seen.

Accordingly, several further studies are suggested in the perspectives:

- A study including a higher number of different degrees of figure within a given species and its effect on the anisotropy in different applying directions. The purpose is to complete the shear-extension and shear-shear coupling terms in the stiffness matrix to see the impact of different axial sawing orientations of the plank on the final application.
- The finite element analysis should be made for the figured wood, based on the relative volume element analysis, to understand the full information on the stiffness matrix elements.
- According to the above mentioned, the experimental values could be compared with the simulation result, proving the workability.
- The hygro-mechanical properties should be studied with the digital image coupling method to understand the heterogenous shrinkage properties occurring in those complex grain pattern wood, not just a simple macroscopic measurement.
- Then, the mechanical simulation could couple with the hygro-mechanical simulation. So, the real application case could be studied, expanding the knowledge on the more real situation.

Furthermore, some other suggestion is made:

- For the splitting part, the author suggests that the splitting specimens should be no less than $5 \times 5 \times 5 \text{ cm}^3$. Also, according to the literature and author experience, the splitting should be done in different positions (still, along radial).
- Some further methods could help better describe the complex organisation of grain, maybe by microtomography, for example.
- The X-ray diffraction allows measuring both the GA and MFA in the case when the grain angle is along the plane of the specimen (for example, interlocked grain studied on thin flat-sawn specimens); however such type of measurements would not be a proper study for other orientations of grain, due to the undulating grain structure against the surface plane.

The optical grain measurements have two ways, one is the reflection from the fibre wall, and the other is the light absorption (due to the diving angle). The author would suggest the latter one because the wood fibre is semi-transparent, and some other non-structural (e.x., extractives) would affect the reflection quality.

Résumé étendu en français

Le bois est utilisé depuis des milliers d'années et fait l'objet de nombreuses applications. Toutes les fibres s'alignent théoriquement selon trois directions principales, à savoir longitudinale, radiale et tangentielle. En conséquence, un système de structure mésoscopique, le "fil", a été proposé pour décrire l'alignement continu des fibres longitudinales, en fonction d'aspects de fonction biologique (Ogata et al. 2003 ; Kramer 2006). D'un point de vue d'ingénierie, le fil est préféré droit en raison de son efficacité mécanique. Les déviations du fil réduisent les propriétés mécaniques longitudinales. En revanche, certains bois ont des schémas, ou des organisations spécifiques de déviations de fil, qui sont préférés dans plusieurs domaines artisanaux, utilisés pour l'ébénisterie, le placage, le tournage et la fabrication d'instruments. Ces bois présentant des schémas spécifiques de déviations de fil sont appelés les bois figurés.

L'objectif de ce travail de thèse est d'explorer la diversité des bois figurés, en commençant par leur nomenclature et leur description structurale, puis en caractérisant leurs propriétés physiques et mécaniques, pour analyser l'effet de ces déviations de fil spécifiques sur la variabilité et l'anisotropie des bois figurés. La thèse est organisée en quatre chapitres.

Chapitre I : Définition, occurrence et nomenclature des bois figurés

Le bois dit figuré est un bois qui présente une déviation de fil suivant un motif ou un schéma relativement constant. Plusieurs types d'organisation, ou de schémas, de bois figurés ont été indiqués (Beals et David 1977 ; Richter 2015). Ici, une analyse statistique a été faite à partir de sources de la littérature, pour connaître la proportion de bois figurés suivant différents schémas, pour des bois tropicaux (Figure 1).

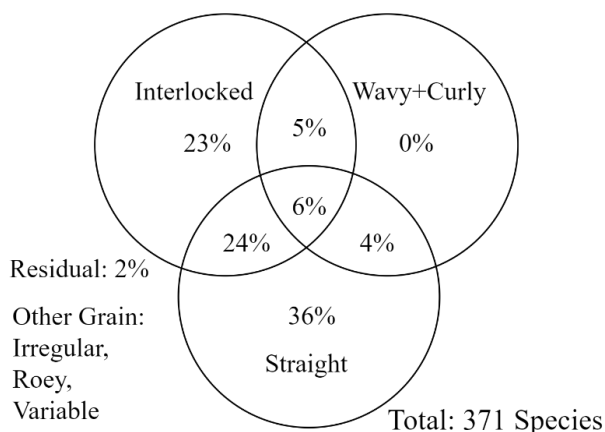


Figure 1 Analyse de la proportion de trois schémas de fil (fil droit, contrefil, et ondé/frisé) à partir des données de la littérature de Chudnoff (1984).

Ce résultat statistique reflète la proportion d'espèces susceptibles de présenter certains schémas de fil. Cependant, les schémas de fil dans la référence bibliographique analysée sont relativement moins nombreux que la diversité des motifs connus et utilisés par les travailleurs du bois. Ce n'est qu'à partir de leur apparence et de leur description textuelle que l'on peut évaluer la diversité et la nomenclature des bois figurés.

C'est pourquoi, dans cette thèse, une revue a été faite sur les photos et les descriptions détaillées des ressources (sites web) de vendeurs professionnels de bois dans différentes langues. Ce travail permet d'explorer le bois figuré dans son ensemble en comparant la terminologie, les schémas et le niveau de déviations de fil. De plus, les combinaisons de différents schémas de fil du bois figuré peuvent être étudiées.

Chapitre II : Description structurelle et visuelle de bois figurés

Au début de cette thèse, deux tentatives ont été faites pour comprendre le fil et sa structure dans le bois figuré. La première a utilisé une équation analytique qui suppose que la structure du fil est une courbe sinusoïdale. Une équation sinusoïdale incluse dans une équation sinusoïdale a été utilisée pour décrire toutes les combinaisons possibles de motifs de fil (Figure 2).

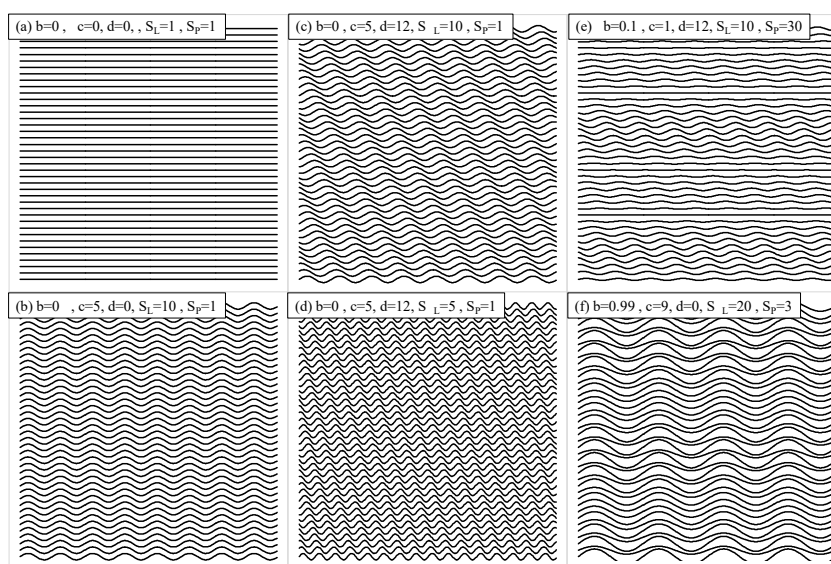


Figure 2 Une démonstration des résultats de l'équation analytiques en faisant varier les paramètres.

L'autre tentative a utilisé la lumière visible pour détecter l'angle plongeant du fil par rapport à la surface, selon l'idée indiquée dans la littérature (Shen et al. 2000 ; Liu et Lin 2016). L'essai d'utilisation de la lumière incidente sous différents angles est basé sur l'idée de l'approche multidirectionnelle (Carman et al. 2008 ; Huang et al. 2008 ; Sole et al. 2017). Le présent essai

de méthodes optiques comportait deux approches : l'une utilisait l'angle plongeant du fil (Figure 3), et l'autre détectait l'angle plongeant en faisant tourner l'échantillon sur un scanner optique (Figure 4).

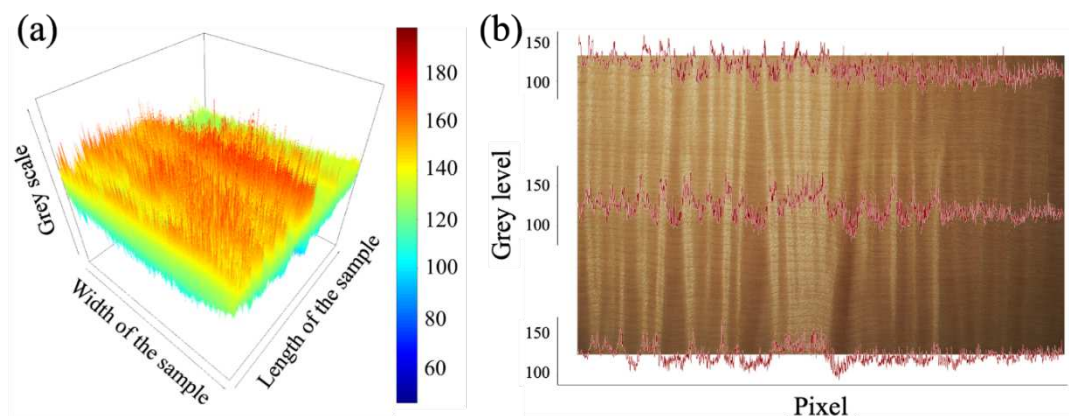


Figure 3 La réponse optique sur un échantillon d'érable sycomore ondé (figure « fiddelback »). (a) l'angle inclus entre la lumière incidente et le capteur optique. (b) la rotation de l'échantillon. La planche a été marquée avec le degré d'azimut de rotation.

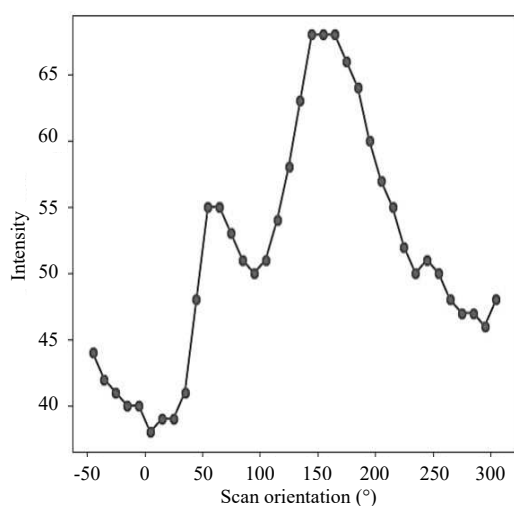


Figure 4 Résultat en intensité d'échelle de gris pour un pixel sélectionné, durant la rotation d'une surface de bois sur un scanner optique.

Ensuite, la part principale de ce chapitre présente la sélection de l'échantillonnage pour la suite de l'étude, et les mesures d'orientations locales qui ont été réalisées. Dans la présente étude, 18 espèces ont été sélectionnées. Six sont des espèces tempérées (avec des fils ondé, frisé, pommelé, moucheté, madré) et douze sont des espèces tropicales (avec contrefil principalement). La principale caractéristique du bois figuré étant la déviation du fil, des mesures d'orientations locales sont effectuées. L'étude se concentre aussi sur les éléments d'orientation du bois car ils influencent les comportements mécaniques et hygromécaniques du bois. L'orientation est mesurée à une échelle mésoscopique avec l'angle de fil (GA), et à l'échelle microscopique avec

l'angle de microfibrilles (MFA). L'angle de fil GA a été indiqué comme l'un des facteurs influençant les propriétés mécaniques (Hernández 2007b ; Brémaud et al. 2011b) et hygroscopiques-dimensionnelles du bois (Ormarsson et Cown 2005 ; Hernández 2007c, d ; Straže et al. 2011). Le MFA a une corrélation positive avec le retrait tangentiel et une corrélation négative avec le retrait longitudinal (Harris et Meylan 1965 ; Meylan 1972 ; Barnett et Bonham 2004 ; Donaldson 2008). Le MFA et le GA contribuent tous deux négativement au module d'élasticité (MOE).

Les mesures de GA dans ce chapitre sont effectuées de deux manières. L'une est la méthode de fendage, et l'autre est basée sur des échantillons minces sur dosse = sciés dans le plan longitudinal-tangentiel (présentés au Chapitre III, Figure 7) mesurés par la méthode de diffraction des rayons X (XRD). L'autre est la méthode de fendage, ici l'oscillation du contrefil suivant le rayon est simulée sur la base de la mesure de l'angle de pic maximum (Hernández et Almeida 2003) (Figure 5). D'autre part, la méthode XRD mesure/estime les valeurs de GA d'une part, et de MFA d'autre part, à partir du plan (200). D'après les résultats obtenus, il n'y a pas de corrélation entre GA et MFA au sein d'une même espèce ni entre les espèces (Figure 6).

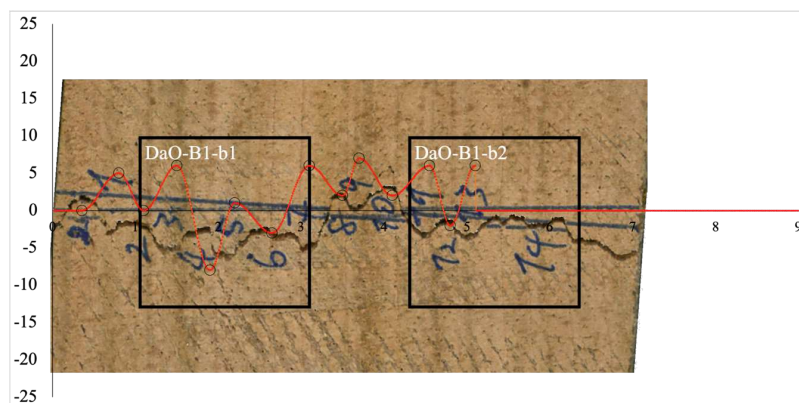


Figure 5 Un exemple de résultat de test de fendage compare avec l'équation cosinusoidale développée (courbe rouge). (Axe des x : position sur le rayon en cm ; axe des y : angle en degrés).

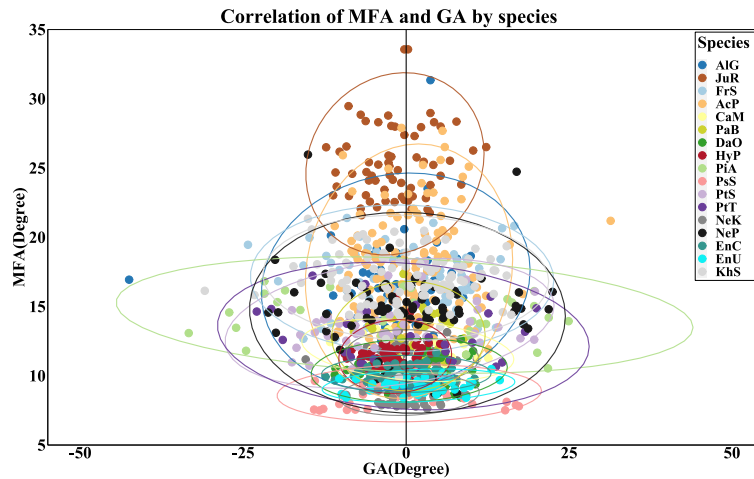


Figure 6 Nuage de points des angles de microfibrilles (MFA) et angles de fil (GA) mesurés par XRD sur les mêmes spécimens. Les ellipses représentent les distributions au seuil de confiance $\alpha = 0.95$.

Chapitre III : Caractérisation des propriétés physiques et mécaniques

Ce chapitre détaille l'échantillonnage testé, les méthodes de caractérisation, et décrit les résultats génériques en termes de comparaison entre méthodes, et en termes de propriétés par espèces. Certaines méthodes sont couramment employées dans les laboratoires où la thèse a été réalisée, tandis qu'un nouveau dispositif de mesure vibratoire en torsion a été validé durant ce travail.

Les échantillons dans cette étude étaient d'abord prélevés sous la forme de barreaux « standards », (section : $20 \times 20 \text{ mm}^2$) (B), puis ont ensuite été ré-usinés en plusieurs sous-dimensions d'échantillons adaptés aux différents objectifs expérimentaux (Figure 7). Les spécimens sous forme de barreaux ont servi à acquérir le module d'élasticité longitudinal E_L (ou MOE) et les modules de cisaillement G_{TL} et G_{RL} par l'essai BING (théorie de Timoshenko). Des fines lamelles de 2mm d'épaisseur ont été débitées sur quartier (V_{L-R}) et sur dosse (V_{L-T}) pour les mesures de module d'élasticité longitudinal (E_L) et, respectivement, des modules de cisaillement G_{TL} et G_{RL} par la méthode Vybris. Cette méthode a également fourni les coefficients d'amortissement ($\tan\delta$) en direction longitudinale ($\tan\delta_L$) ainsi qu'en cisaillement ($\tan\delta_{G_{TL}}$ et $\tan\delta_{G_{RL}}$). Le cube (US) était pour les mesures de 3 modules d'élasticité (E_L , E_R , E_T) et de 3 modules de cisaillement (G_{RL} , G_{TL} , G_{RT}), par une méthode ultrasonore et une approche par initialisation à partir des modèles de « feuillus standards » de Guitard (Guitard 1987). Tous les spécimens ci-dessus ont été testés dans des conditions de 20°C et 65% RH, et le temps de stabilisation était selon la littérature (Brémaud and Gril 2021a). Par ailleurs, les spécimens de sous-dimension TR1 et TR2 (Figure 7) étaient pour les mesures de propriétés hygro-mécaniques

(suivant le protocole usuel au CIRAD). Ils ont été mesurés à partir de l'état saturé jusqu'à l'état anhydre, suivant différentes étapes de conditionnement en humidité relative (RH) et de teneur en eau (MC), pour obtenir les retraits totaux en directions tangentielle et radiale (TTS et TRS), les coefficients de retrait (α_T et α_R) et le point de saturation des fibres (FSP).

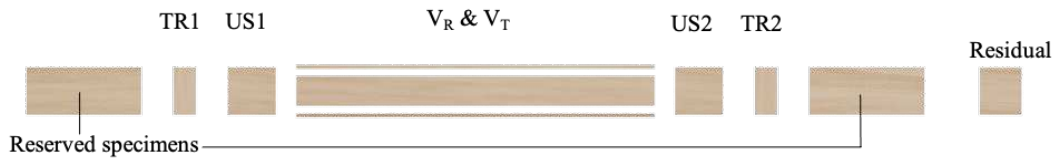


Figure 7 Vue explosée des différentes sous-dimensions d'échantillons ré-usinés à partir de chaque barreau standard ($360 \times 20 \times 20 \text{ mm}^3$).

Les premières comparaisons sont effectuées entre différentes méthodes, pour le module d'élasticité longitudinal (Figure 8) et pour les modules de cisaillement dans le plan (Figure 9). Pour le module d'élasticité longitudinal les résultats correspondent aux différences connues entre méthodes (Brémaud et al. 2012 ; Rakotovololonanana et al 2015), tandis que pour les modules de cisaillement il n'existe que peu de références permettant la comparaison.

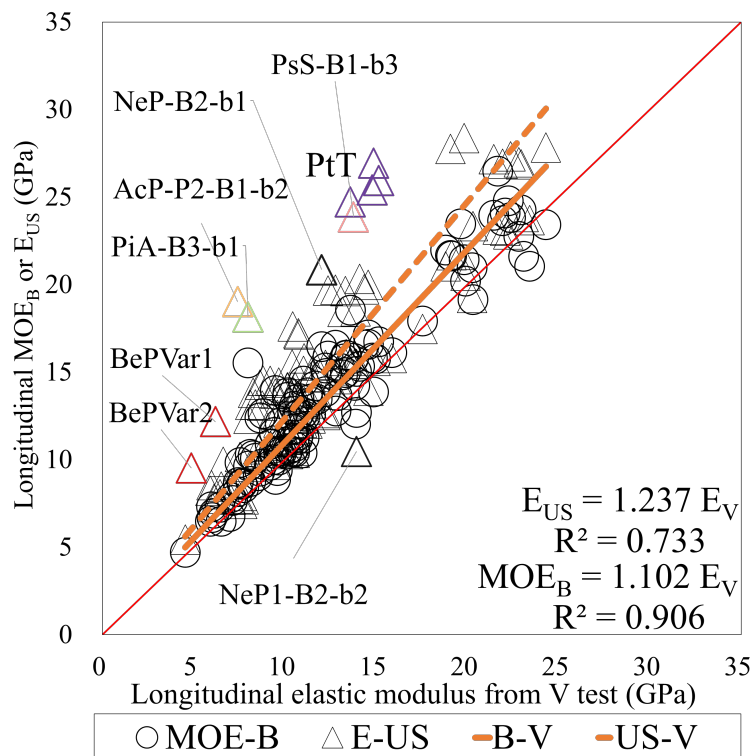


Figure 8 Comparaison des valeurs de module d'élasticité longitudinal (E_L) mesurées par les méthodes BING, Vybris, et ultrasonore.

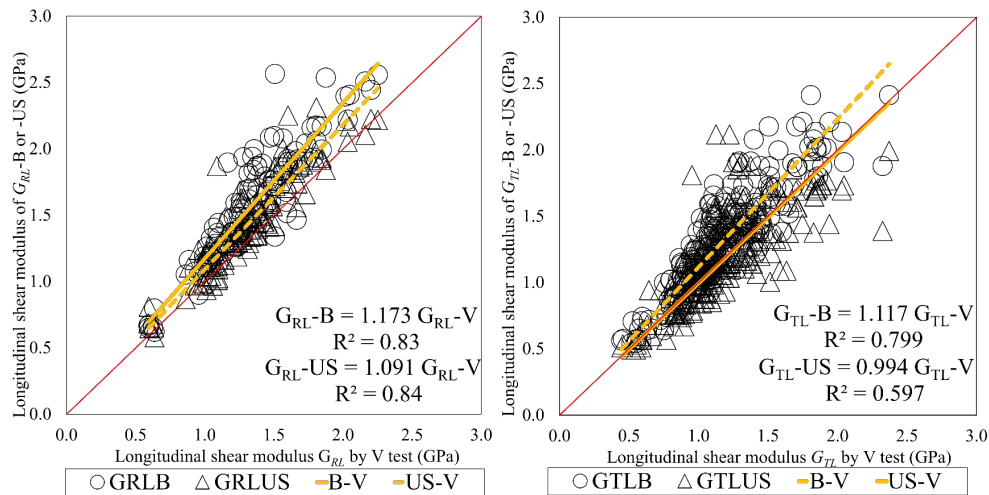


Figure 9 Comparaison des valeurs de modules de cisaillement G_{RL} (à gauche) et G_{TL} (à droite) mesurées par les méthodes BING, Vybris, et ultrasonore.

Pour les retraits, les valeurs en direction T sont plus importantes qu'en direction R ($TTS > TRS$ et $\alpha_T > \alpha_R$). Pour le FSP, les espèces tempérées ont des valeurs plus élevées (20 à 40%) tandis que les espèces tropicales sont entre 15% et 30% (Figure 10). Les valeurs extrêmes de FSP sont relevées pour deux espèces de *Pterocarpus* (de l'ordre de 15%), ce qui correspond néanmoins aux informations de la littérature (Jankowska and Kozakiewicz 2016).

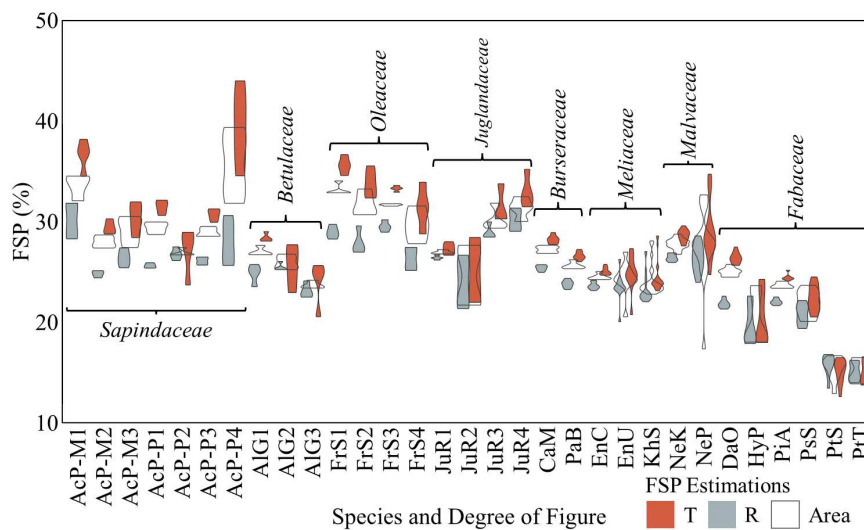


Figure 10 Les valeurs de point de saturation des fibres (FSP) obtenues par les mesures selon la direction R (en gris), T (en rouge), et selon l'aire (cadre gris clair).

De façon synthétique, les résultats obtenus dans ce chapitre constituent un ensemble particulièrement complet sur l'anisotropie (des modules élastiques, des propriétés vibratoires viscoélastiques avec l'amortissement par frottement interne, et des propriétés hygromécaniques avec les retraits). Globalement, les résultats obtenus indiquent de plus faibles rapports

d'anisotropie que dans des synthèses de données de la littérature, confirmant ainsi qu'une anisotropie réduite est une signature des bois figurés.

Chapitre IV : Variabilité et anisotropie mécanique en relation avec les angles de fil et de microfibrilles

Ce chapitre commence par l'observation de la variabilité des propriétés mesurées, entre différentes espèces, et à l'intérieur d'une espèce – soit par différents spécimens venant d'un même arbre pour les bois tropicaux contrefilés, soit par des individus ayant différents degrés de figure pour les bois tempérés (avec fils ondé, moiré, pommelé, moucheté, madré).

Ensuite, des comparaisons sont effectuées entre les résultats obtenus sur bois figurés, et des corrélations « standard » entre propriétés, issues de la littérature. L'objectif étant d'observer les différences potentiellement causées par les déviations de fil. La première analyse est sur les corrélations entre densité et modules d'élasticité et de cisaillement dans les différents plans et directions, en prenant comme base de comparaison les modèles statistiques de Guitard (1987) sur les « feuillus standard » (Figure 11). En moyenne, les relations entre densité et modules sont assez bien conservées entre les présents résultats et la littérature. En revanche, le module d'élasticité longitudinal (E_L) montre une très grande dispersion par rapport à la tendance, ainsi que le module de cisaillement G_{TL} et, dans une moindre mesure, le module d'élasticité tangentiel E_T . Les modules incluant la direction tangentielle (E_T , G_{TL} , G_{RT}) tendent à avoir des valeurs un peu supérieures à la tendance générale.

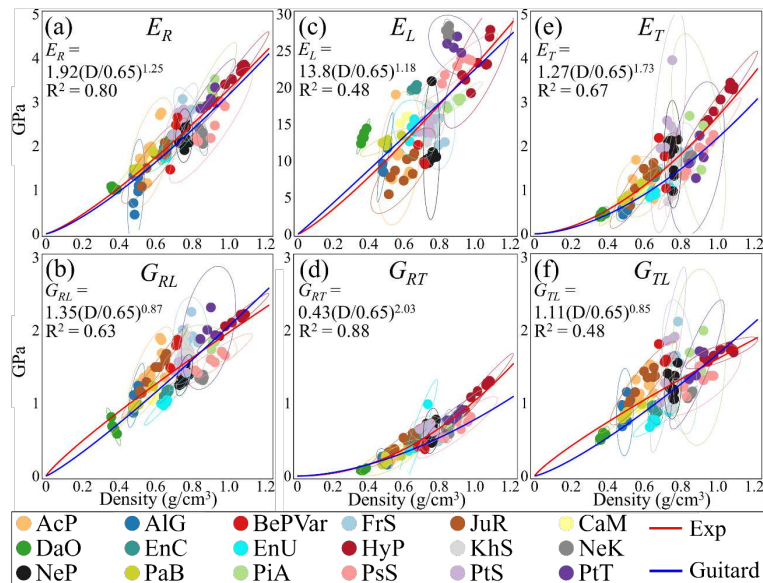


Figure 11 Comparaison des relations entre 6 modules élastiques et la densité, entre la présente étude (courbes rouges et points de données) et le modèle « feuillus standards » de

Guitard (courbes bleues).

Une autre relation basée sur la densité concerne les propriétés hygro-mécaniques (Skaar 1988, p127-131). Les résultats montrent que les espèces tempérées ont une corrélation très forte entre retraits et densité, tandis que les espèces tropicales ont plusieurs relations dépendantes des espèces, et ces dernières expriment probablement des effets supplémentaires dus aux extractibles.

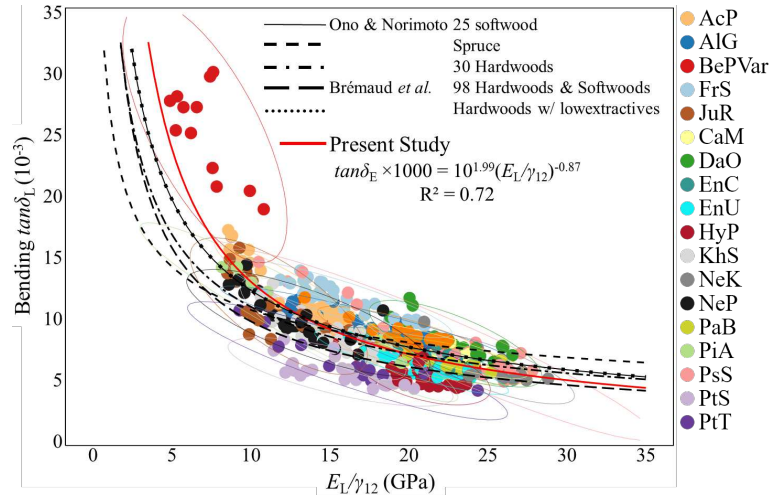


Figure 12 Relation entre coefficient d'amortissement et module d'élasticité spécifique : comparaison entre relations de la littérature (courbes noires) et la présente étude (courbe rouge).

La comparaison suivante (Figure 12) est entre le coefficient d'amortissement $\tan\delta_L$ et le module d'élasticité spécifique E'_L/γ . Les résultats expérimentaux suivent globalement la relation standard de la littérature, qui exprime les effets d'orientation (GA et/ou MFA) (Obataya et al. 2000 ; Brémaud et al. 2011, 2013). Les valeurs sont cependant dispersées entre espèces, avec notamment des décalages de l'amortissement vers de faibles valeurs pour deux espèces de *Pterocarpus* (attribuables à leurs extractibles, Brémaud et al. 2011), et vers des valeurs exceptionnellement élevées pour le bouleau madré (ou « Karelian birch »).

Ensuite, les contributions respectives des orientations locales – angle de fil GA et angle de microfibrilles MFA – sont explorées par des analyses de corrélations avec toutes les propriétés mesurées. Du fait des dimensions différentes entre mesures structurales et physiques - mécaniques, les analyses les plus directes sont sur les lamelles employées à la fois pour les mesures par DRX, et de propriétés vibratoires. En conséquence, la contribution des GA et des MFA aux propriétés est examinée à l'aide d'une analyse en composantes principales (ACP) (Figure 13). Le résultat montre que, sur l'ensemble des espèces, le MFA est l'élément d'orientation local le plus influent sur E_L . Cependant, le GA peut également jouer un rôle

important dans celles des espèces où les valeurs de GA sont suffisamment grandes. En revanche, en comparant toutes les valeurs des espèces et spécimens, la densité est très peu représentée dans les 2 premières composantes principales, indiquant un effet décorrélié des effets d'orientation.

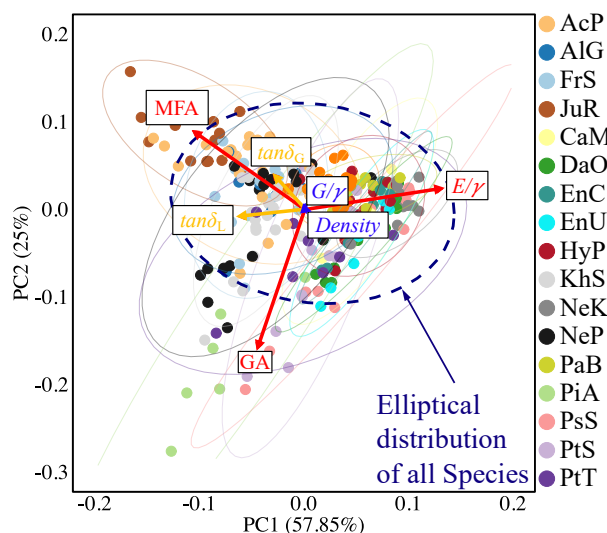


Figure 13 Une analyse en composantes principales sur toutes les propriétés mesurées sur les mêmes spécimens de petites dimensions (lamelles coupées sur dosse pour méthodes Vybris et DRX).

Ensuite, un examen plus approfondi de l'effet des MFA sur l'anisotropie des propriétés est étudié. Le résultat montre que les ratios d'anisotropie entre propriétés (module et amortissement) axiales, et de cisaillement dans le plan, i.e., E_L/G_{TL} et $\tan\delta_{GTL}/\tan\delta_L$, respectivement, sont clairement diminués avec l'augmentation des MFA (Figure 14). La dispersion est cependant élevée, surtout pour les valeurs faibles à modérées de MFA, et sur ces plages de valeurs la dispersion observée relève en grande partie des effets de GA.

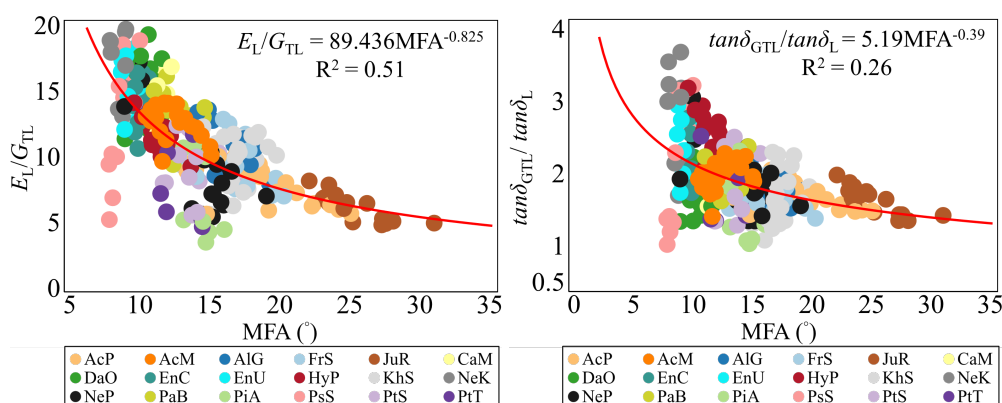


Figure 14 Corrélations entre les MFA et les ratios d'anisotropie E_L/G_{TL} et $\tan\delta_{GTL}/\tan\delta_L$.

Enfin, pour prendre en compte de manière complète les effets respectifs des GA et MFA, une relation cumulée avec GA et MFA est proposée pour étudier l'effet de l'orientation locale

(mésoscopique et microscopique) sur le module d'élasticité spécifique longitudinal. Les valeurs proviennent des lamelles coupées sur dosse (V_{L-T} , dans la Figure 7) et testées par Vybris et DRX. Le modèle se compose de deux sous-modèles, prenant en compte les deux effets d'orientation : l'un est le GA+MFA, et l'autre le GA-MFA. Ensuite, les fractions influentes des deux sous-fonctions sont insérées dans l'équation d'Hankinson pour simuler la distribution possible selon GA+MFA (Figure 15). Ici, les valeurs de MFA sont également réajustées (en utilisant le solveur Microsoft Excel, AdjMFA dans la Figure 16). En résultat, les valeurs estimées de E_L/γ et E_T/γ sont respectivement 24.91 (GPa) et 1.13 (GPa) (courbe verte dans la Figure 15). Une autre comparaison est faite entre les valeurs prédites et les valeurs d'angle cumulé unique (GA+MFA) par une courbe logarithmique (la courbe rouge dans la Figure 15).

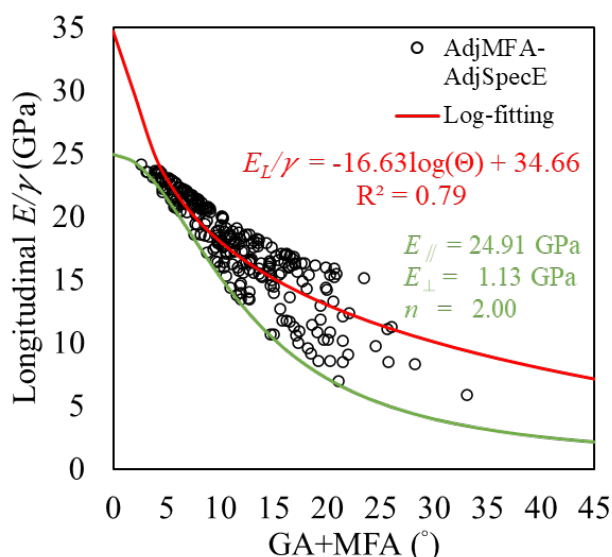


Figure 15 Le MFA ajusté et valeurs de E_L/γ du modèle. En rouge : courbe de tendance logarithmique ajustée, en vert : courbe issue de l'équation de Hankinson, et paramètres de l'équation.

Conclusion

Les bois figurés sont caractérisés par leurs schémas (ou motifs) de fil. Les motifs de fil causent une apparence visuelle unique sur les surfaces de pièces de bois. Dans cette thèse, les différents motifs de fil élémentaires ont été présentés, et la relation entre les "bois figurés" et les "figures du bois" a été discutée, y compris avec une nomenclature multilingue illustrée. Plusieurs pistes pour la description structurelle ont été testées (analytique, optique, fendage, diffraction des rayons X). L'angle de fil (GA) et l'angle de microfibrilles (MFA), ainsi que les propriétés physico-mécaniques et leur anisotropie ont été caractérisés sur un échantillon de 18 essences présentant différents motifs de fil (ondé, frisé, pommelé, madré, contrefilé). Un large jeu de

données sur l'anisotropie (hygromécanique, élastique et viscoélastique-vibratoire) a été produit, qui confirme l'anisotropie réduite comme une caractéristique des bois figurés. Alors que les éléments d'orientation locale (MFA et GA) dominent les propriétés mécaniques et hygromécaniques, les résultats montrent que la variabilité de MFA domine lorsqu'on considère des espèces très différentes, à moins que les valeurs GA ne soient particulièrement élevées. L'anisotropie des bois figurés est réduite en raison de la diminution du module d'élasticité longitudinal et des modules transverses et de cisaillement presque identiques - ou légèrement supérieurs - par rapport au bois droit. Cependant, la contribution de GA n'est pas aussi claire qu'attendu pour les bois figurés en raison de ses importantes variations locales et de la méthode de mesure simplifiée de GA utilisée dans les analyses. Par conséquent, une méthode non-destructive doit être développée pour vérifier la figure et le motif du fil. Dans la présente étude, un essai basé sur des mesures optiques a commencé à être grossièrement construit. La combinaison avec la méthode de corrélation d'images numériques pourrait être approfondie. De plus, la comparaison avec le résultat d'essais de fendage serait essentielle pour vérifier le résultat de futurs essais optiques, car les organisations et motifs de fil peuvent être très complexes.

LIST OF FIGURES

- Fig. 1 The multi-layered microstructure of wood fibre cell wall (Edited from Huang et al. 2003). The blue arrow is the direction of the axial cell (fibre or tracheid), and the red arrow is the orientation of the cellulose microfibrils in the S2 layer. Thus, the included angle of two arrows is the microfibril angle (MFA, μ). 4
- Fig. 2 Three principal directions (L_{Tree} , R_{Tree} , T_{Tree}) of tree, and the “grain” concept (green dashed arrow). 5
- Fig. 3 The internal grain development of Beech tree, detected from the bark. (Reprinted and translated from German to English from figure 12 in Knigge and Schulz 1959)) 8
- Fig. 4 (a) Wavy Beech and (b) interlocked Cypress. Reprinted record from “Timber: an elementary discussion of the characteristics and properties of wood” (Fig. 12 and 13 in p. 22, Roth 1895). (Figure edited for clarity, notation of direction added). 8
- Fig. 5 The six types of grain patterns indicated by the literature (Beals and Davis 1977). (a) straight, (b) wavy/curly, (c) spiral, (d) ring depression, (e) interlocked, and (f) blister formation. 10
- Fig. 6 The definition of (a) curly grain and (b) wavy grain by Richter (2015). (a) is from Fig. 5.112 and (b) is from Fig. 5.113 in the reference. 10
- Fig. 7 The analysis of three selected grain patterns (straight, interlocked, and wavy+curly) from the literature data of Chudnoff (1984). 11
- Fig. 8 The various figures could be indicated under a same figure name, here under “pommele”. 14
- Fig. 9 Explaining the relationship between name and figure with three examples in Japanese for the grains and figures shown on the Keyaki (*Zelkova sp.*) flat-sawn board . (a): 板目杓 (flat-sawn board grain); (b): 上杓目 (premium/fine figured grain); (c): ババラ玉杓 (rose (flower) figured grain). 15
- Fig. 10 A demonstration of the figures and the preferred sawn planes. The codes correspond to specimens listed in §II.C. 36
- Fig. 11 A demonstration for the manipulation of parameters in equation (1). (a) is the straight grain; (b) is the wavy pattern; (c) and (d) is the phase-shifting in different amplitude, respectively; (e) is the phase-shifting including the amplitude shifting; (f) is the amplitude shifting without the phase shifting. In the program, L is set as 1 to 500 in step 1, and P is set as 5 to 395 in step 5. A smoothing aids for the visualisation. The parameters of L and P are for the intensity of the points on longitudinal coordinate and demonstrated density of curves. 39

- Fig. 12 The result of the OCT scan for the wavy Sycamore maple. (a) The fibres' directions are clear to be identified. (b) The schematic diagram of the known wavy grain pattern is drawn. 40
- Fig. 13 The result drawn in 3D for the Sycamore maple from one diagonal angle of the incident light. (a) its original result (transformed into B/W) and (b) the result from the blank test. The result of the blank test was transformed to compensate for the degradation in the sample's result according to equation (5). 41
- Fig. 14 The light response of the fiddleback figure on the Sycamore maple. (a) is the result after compensation made from the previous calculation, and (b) is the acquired response along the longitudinal direction. 42
- Fig. 15 The diagram of the experimental setup in the DIC analysis. (a) The included angle of scanner between the incident light and the optical sensor. (b) the rotation of the sample. The board was marked the rotated azimuth degree. 43
- Fig. 16 The result of the DIC analysis in two kinds of demonstrations. (a) and (c) is the max and min values for each pixel. (b) and (d) is the max and min values of each pixel from the rotation. 44
- Fig. 17 A result of intensity and correlated rotation angle of a randomly selected pixel. 44
- Fig. 18 The comparison between 20 families of the percentage of species recorded as "highly figured" under the author's criteria, and of the global percentage of representation of species in the CIRAD's xylarium. 47
- Fig. 19 The general cutting plan for the macroscopic sampling. The geometries include the plank in original dimension, sub-dimension of the plank (B), and the final bar, BING bar (b1, b2...) within the sub-plank. The numbering detail is in the following section (§III.A.2). Also, the corresponding blocks for the splitting method are noted (F). All numbers are in series along with the radius/radial direction, from the smallest (bark) to the largest (pith). The subfigures of (a) and (b) represent the different types of the sawn pattern. 54
- Fig. 20 The diagrams for the determination of GA for interlocked grain (a) and wavy grain (b) in literature. The MAD in (a) was calculated with the Z_i and S_i , the maximum angle in the split blocks. 56
- Fig. 21 The measurement of the GA for the interlocked grain pattern. In (a), the projected radial line (in yellow) was indicated by clamping a straight wood, also as the baseline for measuring the magnitude. The split peaks were therefore marked with a number. Later, in (b), another piece of wood was used to help the measurement of the GA (value of the included angle between the green line and the red line). 57
- Fig. 22 The grain angle's measurement for the wavy grain pattern. 58

- Fig. 23 Three figure types show the difficulty of evaluating their grain variations by the GA measurement due to the (a) non-parametricalized pattern, e.g., birdseye figure (AcP-M1), (b) pommele structure in the present study's material, and (c) the non-detectable (from the surface) (JuR1). (L length: 20 mm) 59
- Fig. 24 The evaluation of the birdseye figure by the quantity of the figure per area. Three local captures of the birdseye maple (*Acer pseudoplatanus* L.). The doF (as graded by the wood vendor) is $a > b > c$. The scales of the three images are the same. 59
- Fig. 25 The 4 measured positions by XRD on the Vybris specimen in the present study. The red and green colours represent the X-ray beam's direction due to the flip of the specimen. 63
- Fig. 26 The setup of the GA and MFA measurement. The general view of the instrument (a) and the detailed setup for the measurement (b). The holding base was rotated 45° vertically. 64
- Fig. 27 The estimation for the MFA in the present study, exemplified with the measuring position 4, of HyP-B1-b2_2-T2 specimen (material preparation in topic III.C.2.b). 65
- Fig. 28 The GA distributions of the interlocked grain species, from the interpolated profiles calculated from splitting blocks. 70
- Fig. 29 The comparison of grain angle measurement by the splitting method (II.C.2.a) and XRD method (II.C.2.c). 71
- Fig. 30 The MFA values categorised by species. From AlG to AcM, left to right, are the temperate species. 73
- Fig. 31 The comparison of MFA values between different species and planks. The temperate species marked with a number means the doF categorized by the provider (the larger means the figure degree is higher, except the AcP-M. The order of AcP-M is reversed). In contrast, the marked number for the tropical ones means the different planks. 73
- Fig. 32 The comparison of GA and MFA from the XRD measurement. The comparison shows that the GA and MFA have no relationship from the current study. The elliptical distribution (confidence level $\alpha = 0.95$) demonstrates that each species has its distribution. 75
- Fig. 33 The demonstration of the separation of HeartW from SapW by using CAD software (Fusion 360). For example, (a) a flat-sawn specimen, NeP2, was separated according to its SapW and HeartW; (b) a flat-sawn specimen, PtT, was noted as having characteristics of SapW, HeartW, and possibly a part of JW. 83
- Fig. 34 Exploded view of a 360 mm length beam cut into several specimens for conducting the multi-disciplinary experiments. US2 was also reserved. 85

- Fig. 35 The calculation of FSP by the intersection on the y-axis (solid red circle), taking the JuR-B1-b2_TR2 specimen's result (FSP = 27%) as an example. 89
- Fig. 36 The diagram of BING experiments under different dimensions and conditions, with the date of the tests. 93
- Fig. 37 The schematic of the BING experiment in bending mode. The hit is on one end, and the receiver (microphone) is on the other end. The supports made of elastic wires were chosen depending on the specimen's dimension and weight. For (a), the test for the original specimen dimension, two sawhorses were used to support two wooden bars to hang the specimen on with elastic wires; for (b), the standard test for the smaller dimension bars. 93
- Fig. 38 The cross-section of the "standard beams/bars" showing the subsequent cutting for four Vybris specimens, two in each of the two planes L-R (quarter-sawn) and L-T (flat-sawn). 97
- Fig. 39 Diagram of Vybris device for the resonant bending frequency measurement. Figure adapted from Fig 1 in Brémaud (2012). 98
- Fig. 40 A circular steel wire in place of the wood sample was placed on the threads to verify the vertical adjustment of the system and the detecting position of the laser and its focus. 99
- Fig. 41 The diagram of the dynamic torsional rotation in the present study for measuring, for example, G_{RL} . The two ends are clamped. 101
- Fig. 42 The diagram for the span S between the bottom and upper clamp and s the length of the sample in the bottom clamp. 102
- Fig. 43 The comparison between considering anisotropic shear moduli involved in the calculation and without considering it with $G_a = G_{tL} / G_{wL}$. The red dashed lines are the $\pm 5\%$ indicator lines. The x -axis is u ratio from 1.001, 2, 3, ...8, 9, 10 (from left to right). The black regression lines are for $G_a < 1$ ($R^2 = 1.00$), and the grey regression lines are for $G_a > 1$ (R^2 is on the plot). 104
- Fig. 44 The detection of the maximum amplitude (green line). The diagram is the half of the cross-section for the bottom clamp (grey) and the specimen (brown). 106
- Fig. 45 The drafting for the bottom clamp geometry and size for forced torsion device. It was made by the Autodesk Fusion 360 and Autodesk Inventor. 107
- Fig. 46 The comparison between experimental results and simulation by FEM for different span settings. Two types of section are tested, $w/t = 15/1.27$ and $w/t = 12/1.96$. The filled red symbols are the experimental result, and the black filled symbols are the FEM results for the same w/t ratio, and the hollow symbols are for another w/t ratio. 109

- Fig. 47 The demonstration of the influence of span for different simulated wood in different densities (Guitard's hardwood) to the torsion test result (f_t^2 , y-axis). Different densities are in different colours. 109
- Fig. 48 Diagram of the devices used in the US measurement. Two sub-types of measurements were involved, i.e., longitudinal and transverse measurements. The previous one measures C_{ii} by CMP 123, and the latter measures transversal elastic properties (G_{ij}) by CMP 124. 115
- Fig. 49 (a) without the sample for the reference signal, the self-aligning and self-centring equipment. A loading block with a certain weight allows a slight and repeatable pressure to be applied between the sample and the US probes. (b) a zoom showing the positioning of the sample during the test with the two transverse probes whose polarization direction is marked by the black line, e.g., G_{LR} is measured in this case. 116
- Fig. 50 An example of a detected longitudinal wave. (a), signals on the oscilloscope: the yellow waves are the received signal measured on an AcP sample, while the square wave (blue) is the generator synchronisation signal of the input wave. (b) the calibration of the reference signal and sample signal and their result. 117
- Fig. 51 The total tangential shrinkage categorised by species. The shapes in the dashed line are the result without the correction of the ring angle rotation, and the solid line filled with colours are the rotated result. The order follows the temperate-tropical species and the species' families. 122
- Fig. 52 The total radial shrinkage categorised by species. The shapes in the dashed line are the result without the correction of the ring angle rotation, and the solid line filled with colours are the rotated result. The order follows the temperate-tropical species and the species' families. 122
- Fig. 53 The anisotropic ratio of total shrinkage (TTS/TRS) categorized by species. The shapes in the dashed line are the result without the correction of the ring angle rotation, and the solid line filled with colours are the rotated result. The order follows the temperate-tropical species and the species' families. 123
- Fig. 54 The tangential shrinkage coefficient compared by species. The shapes in the dashed line are the result without the correction of the angle rotation, and the solid line filled with colours are the rotated result. The order follows the temperate-tropical species and the species' families. 124
- Fig. 55 The radial shrinkage coefficient compared by species. The shapes in the dashed line are the result without the correction of the angle rotation, and the solid line filled with colours are the rotated result. The order follows the temperate-tropical species and the species' families. 124

- Fig. 56 The criteria for the saturation state. The outlier groups are the specimens of EnU, KhS, PaB, PsS, PtS, and PtT. 125
- Fig. 57 The oven-dry density and MC_{sa} comparison. The solid regression line represents the result with removing the outliers: EnU, KhS, PaB, PtS, PtT. In contrast, the dashed line is the regression line for all the species. 127
- Fig. 58 The comparison between FSP's estimations (re-calculated values) in R-direction (grey colour), T-direction (red colour), and by area (light grey colour frame). 127
- Fig. 59 The comparison of FSP calculated by area (R×T), categorised by species and family. The shapes in the dashed line are the result without the correction of the angle rotation, and the solid line filled with colours are the rotated result. 128
- Fig. 60 The comparison of MOEL values of standard bars tested at different times (see Fig. 36). The standardized MOEL values show a general decreasing trend. The cyan line indicates the 0 difference (standardized value = 1), and the two red lines indicate the ± 5%. 130
- Fig. 61 The comparison of shear modulus G_{RL} estimated by Timoshenko theory. The values are standardized, and the comparisons are made from different testing times (Fig. 36). The cyan line indicates the 0 difference (standardized value = 1), and two red lines indicate the ± 5%. 131
- Fig. 62 The comparison of shear modulus G_{TL} estimated by Timoshenko theory. The values are standardized, and the comparisons are made from different testing times (Fig. 36). The cyan line indicates the 0 difference (standardized value = 1), and two red lines indicate the ± 5%. 131
- Fig. 63 The comparison of longitudinal elastic modulus (E_L) as measured by three methods BING, Vybris and ultrasounds. 133
- Fig. 64 The comparison of longitudinal shear modulus, G_{RL} between BING, Vybris and ultrasounds test. 135
- Fig. 65 The comparison of longitudinal shear modulus, G_{TL} between BING, Vybris and US test. 136
- Fig. 66 The comparisons of the anisotropic ratio between shear moduli G_{RL}/G_{TL} were measured using three methods and on three specimens' dimensions: BING, Vybris and ultrasounds. 137
- Fig. 67 The standardized $\tan\delta_L$ values of BING1, BING2, and BING3 tests (in the order of the testing time, 42 days, 52 days, and 60-72 days after starting the conditioning in a climatic room set at 20°C and 65% RH). The cyan line indicates the non-changed values, and the red lines indicate ± 5% differences from the values in uncontrolled ambient conditions. 139

- Fig. 68 The longitudinal bending $\tan\delta_L$ values grouped by the species from the last BING test (BING3). The values are from the BING test made by hitting on the L-R plane. 139
- Fig. 69 The longitudinal bending damping $\tan\delta_L$ values are grouped by the species. The red colour is for the quarter-sawn specimens (wider side on the L-R plane), and the grey colour is for the flat-sawn specimens (wider side on the L-T plane). 140
- Fig. 70 The comparison of $\tan\delta_L$ values acquired from the BING (BING3) and Vybris test (average of two quarter-sawn specimens). 141
- Fig. 71 The in-plane shear damping values are grouped by the species. The red colour is for the quarter-sawn (L-R) specimens ($\tan\delta_{GRL}$), and the grey colour is for the flat-sawn (L-T) specimens ($\tan\delta_{GTL}$). 142
- Fig. 72 The correlation of anisotropic damping of the Vybris R and T specimens. The solid lines in (a) and in (b) are the regression lines of all the data points. The dashed lines represent the anisotropic ratio of longitudinal shear and bending damping from 1.0 to 3.2. 143
- Fig. 73 The comparison of different properties' COV among the species and methods. The line between the species doesn't mean the data are continuous. 146
- Fig. 74 Comparison of the coefficients of variations (COV) for the different measured properties, (a) ranked by order of higher variability between species; (b) ranked by order of higher variability within-species. 150
- Fig. 75 Variability of the density, categorised by species and initial plank. Data from the Vybris' quarter-sawn and flat-sawn specimens, n: specimen number from each plank. 158
- Fig. 76 Variability of the longitudinal elastic modulus, categorised by species and by initial plank. Data from the Vybris' quarter-sawn (in grey) and flat-sawn (in red) specimens, n: number of specimens from each plank. 160
- Fig. 77 Variability of the longitudinal specific modulus, categorised by species and initial plank. Data from the Vybris' quarter-sawn (in grey) and flat-sawn (in red) specimens, n: number of specimens from each plank. 161
- Fig. 78 Variability of the in-plane shear moduli (G_{RL} in grey, G_{TL} in red), categorised by species and by initial plank. Data from the Vybris' quarter-sawn (in grey) and flat-sawn (in red) specimens, n: number of specimens from each plank. 162
- Fig. 79 Variability of the longitudinal damping coefficient, categorised by species and by initial plank. Data from the Vybris' quarter-sawn (in grey) and flat-sawn (in red) specimens; n: number of specimens from each plank. 163

- Fig. 80 Variability of the longitudinal damping coefficient, categorised by species and by initial plank. The grey colour is for the quarter-sawn specimens ($\tan\delta_{GRL}$), and the red colour is for the flat-sawn specimens ($\tan\delta_{GTL}$). 164
- Fig. 81 The comparisons of the relations of 6 elastic moduli to density, between experimental results from US test on figured woods and Guitard's standard hardwood's model. The blue curves represent Guitard's standard trends, and the red curves are the regressions of experimental results. 168
- Fig. 82 The comparisons of the relations of 3 elastic moduli to density, between experimental results from Vybris test on figured woods and Guitard's standard hardwood's model. The blue curves represent Guitard's standard trends, and the red curves are the regressions of experimental results. 169
- Fig. 83 Pearson' correlation matrix between the anisotropy ratios for the different elastic moduli and the density and L specific modulus as explanatory variables. Results from ultrasonic tests. 170
- Fig. 84 The correlation between the specific gravity at FSP and the area/volumetric shrinkage, categorised with (a) temperate species ($S.Temp_{Area}$) and (b) tropical species ($S.Tropical_{Area}$). The present data uses the area shrinkage (red), and the literature data uses the volumetric (blue). 171
- Fig. 85 Comparison of the regression results from the literature with the present study. The five regression curves are from the references listed in Tab. 22, and the red curve is the present study's result. The "standard" relation is the curve with plain line and dots (Ono and Norimoto 1983; Brémaud et al. 2012). 174
- Fig. 86 Correlation between ratios of longitudinal moduli (E_L/G_{RL}) and of longitudinal damping factors ($\tan\delta_{GRL}/\tan\delta_{L-R}$) with Vybris quarter-sawn specimens. The black regression curve is from the literature, and the red is from the present study's result. 176
- Fig. 87 Correlation between ratios of longitudinal moduli (E_L/G_{TL}) and of longitudinal damping factors ($\tan\delta_{GTL}/\tan\delta_{L-T}$) with Vybris flat-sawn specimens. The black regression curve is from the literature, and the red is from the present study's result. 176
- Fig. 88 The correlation matrix for exploring the relations between properties from the BING, US, V, and shrinkage and FSP_{Area} measurements. The r values are analysed by the Pearson correlation method. 178
- Fig. 89 The correlation matrix for the properties measured from BING, shrinkage & FSP, all obtained on specimens of section 20×20 mm², and the local orientation (GA and MFA, from the thinner sections). The r values are analysed by the Pearson correlation method. 179

- Fig. 90 The correlation matrix for the vibrational properties from the Vybris test. The data is from the Vybris flat-sawn L-T specimens (shortened to V_T for readability of the matrix). All measurements, structural and mechanical, are obtained on the same scale and specimens. The r values are analysed by the Pearson correlation method. 180
- Fig. 91 A principal component analysis of the properties measured from the Vybris L-T (V_{L-LT} , flat-sawn) specimens, categorised by species. 181
- Fig. 92 The correlation matrix for the moduli measured by the US method. D_{US} is the density of the US cubes. The r values are calculated by the Pearson correlation method. 182
- Fig. 93 The correlation matrix for the properties between the local orientation (MFA and GA) and the ratios of anisotropy between moduli from the US test. 183
- Fig. 94 The correlations of GA to three anisotropic ratios with shear moduli (a) E_L/G_{RL} , (b) E_L/G_{TL} , and (c) E_L/G_{RT} . Data from ultrasound tests, with the GA taken as an average value of two local measurements. 184
- Fig. 95 The correlations between MFA and the ratios of E_L/E_R (a) and E_L/E_T (b). The regression in (a) doesn't consider the out-of-range value and AIG values. Data from ultrasound tests, with the MFA taken as an average value of two local measurements. 185
- Fig. 96 The correlations of MFA and Anisotropy of longitudinal/shear moduli. (a): E_L/G_{RL} with MFA, (b): E_L/G_{TL} , and (c): E_L/G_{RT} . 186
- Fig. 97 The correlations between specific shear moduli (a) G_{RL}/γ , (b) G_{TL}/γ , and (c) G_{RT}/γ and MFA for all the species. 187
- Fig. 98 The correlation matrix between density, local orientation (MFA and GA), FSP, total shrinkage, and shrinkage coefficient (α). The r values are analysed by the Pearson correlation method. D_{12} is the density measured at the MC_{12} state. 188
- Fig. 99 The correlation matrix for local orientation and anisotropic vibrational properties. All the data (GA, MFA and vibrational properties) are measured at the same level, from the Vybris L-T (flat-sawn) specimens (shortened to V_T for readability in the matrix). The r values are analysed by the Pearson correlation method. 190
- Fig. 100 Correlation between E_L/G_{TL} and GA, all species are considered together. 191
- Fig. 101 Correlation between $\tan\delta_{GTL}/\tan\delta_L$ and GA, all species are considered together. 191
- Fig. 102 Correlation between E_L/G_{TL} and MFA, all species are considered together. 192
- Fig. 103 Correlation between $\tan\delta_{GTL}/\tan\delta_L$ and MFA, all species are considered together. 192
- Fig. 104 The ratio of G_{RL}/G_{TL} to E_T/E_R . The red line is the regression result from the experimental measurement, and the blue line is the Guitard's "standard hardwood" (§IV.B.1). 193

- Fig. 105 The correlation of longitudinally torsional rigidity (E_L/G_{RT}) to the unit (specific) elastic modulus in T direction (E_T/γ). An out-of-range value (from AcP) is not considered in the regression's calculation (red line), and Guitard's model is the blue line. 194
- Fig. 106 The correlation between E_R/G_{RT} to TTS/TRS. 195
- Fig. 107 The correlations between GA, MFA, and GA+MFA, and longitudinal specific modulus of elasticity. 196
- Fig. 108 The GA (θ) and MFA (μ) diagram (in black) and the situation when GA is not zero (in red). 197
- Fig. 109 The comparison of the original and adjusted GA+MFA (Θ) with the measured E_L/γ . The blue hollow points are the original Θ values, and the orange ones are the GA plus the adjusted MFA. 198
- Fig. 110 The correlation of the predicted E_L/γ and measured E_L/γ . (P) indicates the predicted value of E_L/γ , and (M) is the measured value of E_L/γ . 199
- Fig. 111 The adjusted MFA (AdjMFA) and the model's E_L/γ values (AdjSpecE) from equation (62). The red curve is the logarithm fitting curve, the green curve is from Hankinson's equation, and the parameters of the equation are in green. 200
- Fig. 112 Two models (Log-fitting & AdjH-Method) are compared in an extended range to $\Theta = 90^\circ$. The E_L/γ values (OriSpecE) are measured, and the MFA values are adjusted (AdjMFA). 200

LIST OF TABLES

Tab. 1 The figure names in four languages and the meaning and reference photos.	17
Tab. 2 A part of the photo record during screening CIRAD's Xylarium and the selecting reason for the figured wood.	46
Tab. 3 The involved grain patterns and the selected species.	50
Tab. 4 The indicated anatomical features in the present study and their marks used in IAWA.	51
Tab. 5 The relatively quantitative mark for the characteristics of the selected materials and the basic properties in the databases	52
Tab. 6 The maximum IG angles' values are measured by the angle method (ANG) and the MAD method. All the values below, mean value and standard deviation are in degree.	61
Tab. 7 The record of the figures of materials used in the present study.	66
Tab. 8 The GA diversity of all the figures in studied materials.	69
Tab. 9 Species and dimensions in the initial condition of the specimens	82
Tab. 10 The record of the composition and the type of sawn pattern for specimens with heartwood (HeartW) and the sapwood (SapW), calculated with the CAD software	83
Tab. 11 The comparison of different approximated C values with C_{\tanh} of equation (34) for different u ratios and the error (%).	103
Tab. 12 The transverse shear wave response of three samples: CaM-B3-b2, DaO-B3-b1, and PtS-B1-b1. The correlated peaks are in different forms for the LR, LT, RT, and TR measurements. On the contrary, the RL and TL direction's signals are single peaks.	118
Tab. 13 The comparison of total shrinkage in T and R directions (TTS and TRS) and T/R shrinkage anisotropic ratio (TTS/TRS). Mean values and (standard deviation in brackets). Raw experimental values (Exp) and the rotated values (ExpD) were obtained by calculation according to R-T Ring angle (RA, °). Ref. = Literature values (-.- means no standard deviation in the literature reference).	121
Tab. 14 The MCsa and related FSP (in %) of the outlier species	126
Tab. 15 Specimen quantity of each testing method	146
Tab. 16 The mean values and the coefficient of variation (COV, %) of species' density, longitudinal elastic modulus and in-plane shear moduli for the different species and from different methods. Specimen quantity: Tab. 15	147

Tab. 17 The mean values and the coefficient of variation (COV, %) of species' longitudinal specific modulus of elasticity (E_L/γ), longitudinal bending damping ($\tan\delta_L$) and shear (torsional) damping ($\tan\delta_G$) from different methods.	148
Tab. 18 The mean values and the coefficient of variation (COV, %) of the ultrasonic test results. Specimen quantity: Tab. 15	149
Tab. 19 Comparing data from the present study with data from three wide-scale references. The data is hardwood only, and the average is made between the mean values of each species.	151
Tab. 20 Anisotropic ratios for all studied properties. Data from wide-scale literature references are compared to average anisotropic ratios obtained in the present study.	152
Tab. 21 The coefficients of Guitard's standard hardwoods' relations for six elastic moduli'.	167
Tab. 22 Parameters of the relationships indicated between the specific elastic modulus and damping. The comparative table is re-drawn from Brémaud et al. (2012). The Coefficient A is that usually expressed between values of E/γ in GPa and natural values of $\tan\delta$. The alternative coefficient A' is when expressing $\tan\delta$ in ‰ (values multiplied by 1000, in order to keep the same presentation as in the rest of the present study).	173

V. References

- Alfonso VA, Baas P, Carlquist S, Chimelo JP, Coradin VTR, Détienne P, Gasson PE, Grosser D, Ilic J, Kuroda K, Miller RB, Ogata K, Richter HG, ter Welle BJH, Wheeler EA (2007) IAWA list of microscopic features for hardwood identification: with an Appendix on non-anatomical information (4th ed.). IAWA Bull. 10(3): 219-332.
- Alkadri A, Carlier C, Wahyudi I, Gril J, Langbour P, Brémaud I (2018) Relationships between anatomical and vibrational properties of wavy sycamore maple. IAWA J. 39(1): 63-86.
- Almeida G and Hernández RE (2006) Changes in physical properties of tropical and temperate hardwoods below and above the fiber saturation point. Wood Sci Technol. 40: 599-613.
- Anderhub BM, O'Brien Jr WD (1987) Excerpt from ultrasonic physics and instrumentation for sonographers: density, elasticity, and speed. J Diagn Med Sonog. 3(6): 281-284.
- Ashman RB, Cowin SC, Van Buskirk WC, Rice JC (1984) A continuous wave technique for the measurement of the elastic properties of cortical bone. J Biomech. 17(5): 349-361.
- ASTM (2014) D4933-99: Standard guide for moisture conditioning of wood and wood-based Materials. Reapproved 2010. ASTM. 8 pp.
- Baas P, Blokhina N, Fujii T, Gasson P, Grosser D, Heinz I, Ilic J, Jiang X, Miller R, Newsom LA, Noshiro S, Richter HG, Suzuki M, Terrazas T, Wheeler E, Wiedenhoeft A (2004) IAWA list of microscopic features for softwood identification. IAWA J. 25(1): 1-70.
- Ban M, Inagaki T, Ma T, Tsuchikawa S (2018) Effect of cellular structure on the optical properties of wood. J Near Infrared Spec. 26(1): 53-60.
- Barnett JR and Bonham VA (2004) Cellulose microfibril angle in the cell wall of wood fibres. Biol Rev. 79(2): 461-472.
- Baumer M (1952) A propos des figures du bois. Bois et Forêts des Tropiques. 24: 233–255.
- Beals HO and Davis TC (1977) Figure in wood: An illustrated review. Bulletin 486, Alabama Agricultural experiment station, Auburn, Alabama, USA. 84pp.
- Beech E, Rivers M, Oldfield S, Smith PP (2017) GlobalTreeSearch: The first complete global database of tree species and country distribution. J Sustain Forest. 36(5): 454-489.
- Bossu J, Lehnebach R, Corn S, Arnaud R, Beauchêne J, Clair B (2018) Interlocked grain and density patterns in *Bagassa guianensis*: changes with ontogeny and mechanical consequences for trees. Trees. 32(6): 1643-1655.
- Bragg DC, Mroz GD, Reed DD, Shetron SG, Stokke DD (1997) Relationship between “birdseye” sugar maple (*Acer saccharum*) occurrence and its environment. Can J Forest Res. 27: 1182-1191.
- Brancheriau L and Bailleres H (2002) Natural vibratio analysis of clear wooden beams: A theoretical review. Wood Sci Technol. 36: 347-365.
- Brancheriau L, Kouchade C, Brémaud I (2010) Internal friction measurement of tropical species by various acoustic methods. J Wood Sci. 56(5): 371-379.
- Brémaud I (2006) Diversité des bois utilisés ou utilisables en facture d'instruments de musique – Etude expérimentale des propriétés vibratoires en direction axiale de types de bois contrastés en majorité tropicaux. – Relations à des déterminants de microstructure et de composition chimique secondaire. Doctoral thesis, University of Montpellier II. 302 pp.

- Brémaud I (2012) Acoustical properties of wood in string instruments soundboards and tuned idiophones: Biological and cultural diversity. *J Acoust Soc Am.* 131(1): 807-818.
- Brémaud I (2016) Vers une vision « ethno-bio-mécanique » des bois - La rhéologie du matériau-bois à l'interface entre diversité botanique et usages en lutherie et artisanats. Habilitation thesis, University of Montpellier. 151 pp.
- Brémaud I, Amusant N, Minato K, Gril J, Thibaut B (2011a) Effect of extractives on vibrational properties of African Padauk (*Pterocarpus soyauxii* Taub.). *Wood Sci Technol.* 45(3): 461-472.
- Brémaud I, Cabrolier P, Gril J, Clair B, Gérard J, Minato K, Thibaut B (2010) Identification of anisotropic vibrational properties of Padauk wood with interlocked grain. *Wood Sci Technol.* 44: 355-367.
- Brémaud I, el Kaïm Y, Guibal D, Minato K, Thibaut B, Gril J (2012) Characterisation and categorisation of the diversity in viscoelastic vibrational properties between 98 wood types. *Ann For Sci.* 69(3): 373-386.
- Brémaud I and Gril J (2021a) Moisture content dependence of anisotropic vibrational properties of wood at quasi equilibrium: analytical review and multi-trajectories experiments. *Holzforschung.* 75(4): 313-327.
- Brémaud I and Gril J (2021b) Transient destabilisation in anisotropic vibrational properties of wood when changing humidity. *Holzforschung.* 75(4): 328-344.
- Brémaud I, Gril J, Thibaut B (2011b) Anisotropy of wood vibrational properties: Dependence on grain angle and review of literature data. *Wood Sci Technol.* 45(4): 735-754.
- Brémaud I, Minato K, Thibaut B (2009) Mechanical damping of wood as related to species classification: a preliminary survey. In: *Thibaut B (ed) 6th Plant Biomechanics Conference, Cayenne, French Guiana. 16-21 Nov 2009.* pp 536-542.
- Brémaud I, Ruelle J, Thibaut A, Thibaut B (2013) Changes in viscoelastic vibrational properties between compression and normal wood: roles of microfibril angle and of lignin. *Holzforschung.* 67(1): 75-85.
- Brillouin L (2013) Wave propagation and group velocity (vol 8). Academic Press, New York. 154 pp.
- Buksnowitz C, Evans R, Müller U, Teischinger A (2012) Indented rings (hazel growth) of Norway spruce reduce anisotropy of mechanical properties. *Wood Sci Technol* 46(6): 1239–1246.
- Buksnowitz C, Müller U, Evans R, Teischinger A, Grabner M (2008) The potential of SilviScan's X-ray diffractometry method for the rapid assessment of spiral grain in softwood, evaluated by goniometric measurements. *Wood Sci Technol* 42: 95–102.
- Butterfield RP, Crook RP, Adams R, Morris R (1993) Radial variation in wood specific gravity, fibre length and vessel area for two central American hardwoods: *Hyeronima alchorneoides* and *Vochysia guatemalensis*. *IAWA J.* 14(2): 153–161
- Cabrolier P, Beauchêne J, Thibaut B (2009) Is interlocked grain an adaptive trait for tropical tree species in rainforest? In: *Thibaut B (ed) 6th Plant Biomechanics Conference, Cayenne, French Guiana. 16-21 Nov 2009.* pp 279–284.
- Camara VC, Laux D, Arnould O (2010) Enhanced multiple ultrasonic shear reflection method for the determination of high frequency viscoelastic properties. *Ultrasonics* 50(7): 710–715.

- Caracciolo R and Giovagnoni M (1996) Frequency dependence of Poisson's ratio using the method of reduced variables. *Mech Mater* 24(1): 75–85.
- Carman GM, Briskey WJ, Ayers DD, Christopher DK, Freeman PS, Gibson CD, Paul AR, Shirkey P, Weintraub JH (2008) Grain angle sensor (U.S. Patent No. 20080074670A1). U.S. Patent and trademark office. <https://rb.gy/okclgq>
- Cave ID (1972) A theory of the shrinkage of wood. *Wood Sci Technol* 6: 284–292.
- Cave ID (1966) Theory of X-ray measurement of microfibril angle in wood. *For Prod J*. 16: 37-42.
- Cegla FB, Cawley P, Allin J, Davies J (2011) High-temperature (>500°C) wall thickness monitoring using dry-coupled ultrasonic waveguide transducers. *IEEE T Ultrason Ferr*. 58(1): 156–167.
- Chandra R, Singh SP, Gupta K (2002) Micromechanical damping models for fiber-reinforced composites: A comparative study. *Compos Part A-Appl S*. 33(6): 787–796.
- Channel Veneers (2021) <http://www.channelveneers.com>
- Chauhan S and Sethy A (2016) Differences in dynamic modulus of elasticity determined by three vibration methods and their relationship with static modulus of elasticity. *Maderas Cienc y Technol*. 18(2): 373-382.
- Chudnoff M (1984) *Tropical Timbers of the World* (No. 607). Agriculture handbook, Forest service, United States Department of Agriculture. 464 pp.
- Chui YH, Smith I (1990) Influence of rotatory inertia, shear deformation and support condition on natural frequencies of wooden beams. *Wood Sci Technol*. 24:233–245.
- Coelho JCF, Vidaurre GB, da Silva JGM, de Almeida MNF, Ramon Oliveira RF, Segundinho PGA, Alves RC, Hein PRG (2020) Wood grain angles variations in *Eucalyptus* and their relationships to physical-mechanical properties. *Holzforschung*. 74(12): 1089–1097.
- Collings DA, Thomas J, Dijkstra SM, Harrington JJ (2021) The formation of interlocked grain in African mahogany (*Khaya spp.*) analysed by X-ray computed microtomography . *Tree Physiol*. 1–16.
- Cook Woods (2021) <https://www.cookwoods.com>
- Corbineau P and Flandin J-M (2009) *Identification des bois : esthétique et singularités*. VIAL edition. 336 pp.
- Cown DJ, Ball RD, Riddell MJC (2004) Wood density and microfibril angle in 10 *Pinus radiata* Clones: Distribution and influence on product performance. *New Zeal J For Sci*. 34(3): 293–315.
- Cown DJ, Harrington J, Bourreau D, Haug J, Lee J (2010) Spatial variation in spiral grain: A single stem of *Pinus radiata* D.Don. *New Zeal J For Sci*. 40: 211–224.
- de Borst K and Bader TK (2014) Structure-function relationships in hardwood - Insight from micromechanical modelling. *J Theor Biol*. 345:78–91.
- Desch HE and Dinwoodie JM (1996) *Timber structure, properties, conversion and use* (7th edition). Palgrave, London. 320 pp. <https://doi.org/10.1007/978-1-349-13427-4>
- Détienne P (1979) Contrefil à rythme annuel dans les Faro, *Daniellia sp.* pl. *Rev Bois Forêts des Trop*. 183: 67–71.

- Donaldson L (2008) Microfibril angle: Measurement, variation and relationships - A review. *IAWA J.* 29(4): 345–386.
- Donaldson LA (1992) Within- and between-tree variation in microfibril angle in *Pinus radiata*. *New Zeal J For Sci.* 22(1): 77–86.
- Dooge Veneers (2020) <https://doogeveneers.com>
- Dudek TJ (1970) Young's and shear moduli of unidirectional composites by a resonant beam method. *J Compos Mater.* 4(2): 232–241.
- Evans R, Stringer S, Kibblewhite RP (2000) Variation of microfibril angle, density and fibre orientation in twenty-nine *Eucalyptus nitens* trees. *Appita J.* 53(5): 450–457.
- Eurogroup Belcaire S.L. (2021) <https://eurogrouobelcaire.com>
- Fan Y, Rupert K, Wiedenhoef AC, Woeste K, Lexer C, Meilan R (2013) Figured grain in aspen is heritable and not affected by graft-transmissible signals. *Trees.* 27(4): 973–983.
- França FJN, França TSFA, Vidaurre GB (2020) Effect of growth stress and interlocked grain on splitting of seven different hybrid clones of *Eucalyptus grandis* × *Eucalyptus urophylla* wood. *Holzforschung.* 74(10): 917–926.
- Fukuda E (1950) The vibrational properties of wood I. *J Phys Soc Jpn.* 5(5): 321–327.
- Gérard J, Guibal D, Cerre J-C, Paradis S, et al (2016) Atlas des bois tropicaux: caractéristiques technologiques et utilisations (*In English: Atlas of tropical woods: Technological characteristics and uses*)(Quæ Ed.) (1st edition). 1000 pp.
- Gérard J, Guibal D, Paradis S, et al (2017) Tropix 7. Version (7.5.1). <https://doi.org/10.18167/74726F706978>
- Gérard J, Paradis S, Thibaut B (2019) Survey on the chemical composition of several tropical wood species. *Bois et Forêts des Tropiques.* 342(4): 79–91.
- Gindl W, Teischinger A, Schwanninger M, Hinterstoisser B (2001) The relationship between near infrared spectra of radial wood surfaces and wood mechanical properties. *J Near Infrared Spec.* 9: 255–261.
- Gjerdrum P, Bernabei M (2009) Three-dimensional spiral grain pattern in five large Norway spruce stems. *Silva Fenn.* 43(3): 457–464.
- Gjerdrum P, Säll H, Storø HM (2002) Spiral grain in Norway spruce: Constant change rate in grain angle in Scandinavian sawlogs. *Forestry.* 75(2): 163–170.
- Gril J, Jullien D, Bardet S, Yamamoto H (2017) Tree growth stress and related problems. *J Wood Sci.* 63: 411–432.
- Guitard D and Hubert P (1987) Mécanique du matériau bois et composites (*In English: Mechanics of wood and composite materials*) (Cépadues-Editions). Toulouse, France.
- Guitard D, ElAmriF (1987) Modèles prévisionnels de comportement élastique tridimensionnel pour les bois feuillus et les bois résineux (*In English: Predictive models of three-dimensional elastic behaviour for hardwoods and softwoods*). *Ann Sci Forest.* 44(3): 335–358.
- Haines DW, Leban JM, Herbé C (1996) Determination of Young's modulus for spruce, fir and isotropic materials by the resonance flexure method with comparisons to static flexure and other dynamic methods. *Wood Sci. Technol.* 30: 253–263

- Harris JM (1989) Spiral grain and wave Phenomena in wood Formation (1st edition). Springer Berlin, Heidelberg. 215 pp. <https://doi.org/10.1007/978-3-642-73779-4>
- Harris JM and Meylan BA (1965) The Influence of microfibril angle on longitudinal and tangential shrinkage in *Pinus radiata*. *Holzforschung* 19(5): 144–153.
- Hearmon RFS and Barkas WW (1941) The effect of grain direction on the Young's moduli and rigidity moduli of beech and sitka spruce. *P Phys Soc.* 53(6): 674–680.
- Hein PRG and Brancheriau L (2011) Radial variation of microfibril angle and wood density and their relationships in 14-year-old *Eucalyptus urophylla* S.T. Blake wood. *Bioresources.* 6(3): 3352–3362.
- Hejnowicz Z and Romberger JA (1979) The common basis of wood grain figures is the systematically changing orientation of cambial fusiform cells. *Wood Sci Technol.* 13:89–96.
- Hernández RE (2007a) Effects of extraneous substances, wood density and interlocked grain on fiber saturation point of hardwoods. *Wood Mater Sci Eng.* 2(1): 45–53.
- Hernández RE (2007b) Influence of accessory substances, wood density and interlocked grain on the compressive properties of hardwoods. *Wood Sci Technol.* 41(3): 249–265.
- Hernández RE (2007c) Swelling properties of hardwoods as affected by their extraneous substances, wood density, and interlocked grain. *Wood Fiber Sci* 39(1): 146–158.
- Hernández RE (2007d) Moisture sorption properties of hardwoods as affected by their extraneous substances, wood density, and interlocked grain. *Wood Fiber Sci.* 39(1): 132–145.
- Hernández RE and Almeida G (2003) Effects of wood density and interlocked grain on the shear strength of three Amazonian tropical hardwoods. *Wood Fiber Sci.* 35(2): 154–166.
- Huang C-L, Floyd SL, Stanish MA, Bogue DN (2008) Methods for using light reflection patterns to determine diving angle of grain (U.S. Patent No. US007499171B2). U.S. Patent and trademark office. <https://rb.gy/swxwlv>
- Huang C-L, Lindström H, Nakada R, Ralston J (2003) Cell wall structure and wood properties determined by acoustics - A selective review. *Holz Roh Werkst.* 61: 321–335.
- Huang TC (1961) The effect of rotatory inertia and of shear deformation on the frequency and normal mode equations of uniform beams with simple end conditions. *J Appl Mech-T ASME.* 28(4): 579–584.
- ISO 6721-2 (2019) Plastics - determination of dynamic mechanical properties - Part 2: Torsion-pendulum method.
- Jankowska A, Kozakiewicz P (2016) Determination of fibre saturation point of selected tropical wood species using different methods. *Drewno.* 59(197): 89–97.
- Janowiak J and Pellerin R (1992) Shear moduli determination using torsional stiffness measurements. *Wood fiber Sci.* 24(4): 392–400.
- Kamala FD, Sakagami H, Matsumura J (2014) Mechanical properties of small clear wood specimens of *Pinus patula* planted in Malawi. *Open J For.* 04(01): 8–13.
- Keunecke D, Sonderegger W, Pereteanu K, Pereteanu K, Lüthi T, Niemz P (2007) Determination of Young's and shear moduli of common yew and Norway spruce by means of ultrasonic waves. *Wood Sci Technol.* 41:309–327.

Khashaba UA (2015) Toughness, flexural, damping and interfacial properties of hybridized GFRE composites with MWCNTs. *Compos Part A-Appl S.* 68:164–176.

Kimberley MO, Cown DJ, McKinley RB, Moore JR, Dowling LJ (2015) Modelling variation in wood density within and among trees in stands of New Zealand-grown radiata pine. *New Zeal J For Sci.* 45:22, pp 1–13.

Knigge W and Schulz H (1959) Methodische Untersuchungen über die Möglichkeit der Drehwuchsfeststellung in verschiedenen Alterszonen von Laubhölzern (*In English: Methodological studies on the possibility of detecting spiral growth in different age zones of hardwoods*). *Eur J Wood Wood Prod (Holz als Roh- und Werkst).* 17(9): 341–351.

Kohlhauser C, Hellmich C, Vitale-Brovarone C, Boccaccini AR, Eberhardsteiner RJ (2009) Ultrasonic Characterisation of Porous Biomaterials Across Different Frequencies. *Strain.* 45(1): 34–44.

Kohlrausch F (1996) *Praktische Physik: zum Gebrauch für Unterricht, Forschung und Technik Band 1 (24th edition) (In English: Practical physics: for use in teaching, research, and technology Volume 1)*. B.G. Teubner, Stuttgart, Germany. 894 pp.

Krajnc L, Čufar K, Brus R (2015) Characteristics and geographical distribution of fiddleback figure in wood of *Acer pseudoplatanus* L. in Slovenia. *Drvna Ind.* 66(3): 213–220.

Krajnc L, Farrelly N, Harte AM (2019) Relationships between wood properties of small clear specimens and structural-sized boards in three softwood species. *Holzforschung.* 73(11): 987–996.

Kramer EM (2006) Wood grain pattern formation: A brief review. *J Plant Growth Regul.* 25:290–301.

Krauss A and Kúdela J (2011) Ultrasonic wave propagation and Young's modulus of elasticity along the grain of Scots pine wood (*Pinus sylvestris* L.) varying with distance from the pith. *Wood Res-Slovakia.* 56(4): 479–488.

Langbour P, Paradis S, Thibaut B (2019) Description of the Cirad wood collection in Montpellier, France, representing eight thousand identified species. *Bois et Forêts des Tropiques.* 339(1): 7–16.

Larson PR (1969) Wood formation and the concept of wood quality. Bulletin No. 74, School of Forestry, Yale University, Northern research station, U.S. department of agriculture, Wisconsin, U.S.A. 75 pp.

Lev-Yadun S and Aloni R (1990) Vascular differentiation in branch junctions of trees: circular patterns and functional significance. *Trees.* 4(1): 49–54.

Liu AJ, Dong Z, Hašan M, Marschner S (2016) Simulating the structure and texture of solid wood. *ACM T Graphic* 35: 1–11.

Liu C-Y and Lin S-H (2016) Characterizing surface of wood laminates by out-of-plane polarimetric light-scattering measurement. *Optik.* 127(4): 2346–2353.

Lukacevic M, Lederer W, Füssl J (2017) A microstructure-based multisurface failure criterion for the description of brittle and ductile failure mechanisms of clear-wood. *Eng Fract Mech.* 176: 83–99.

Martley JF (1920) Double cross-grain. *Ann Appl Biol.* 7: 224–268.

- Mattheck C, Kubler H (1997) *Wood- the internal optimization of Trees* (1st edition). Springer Berlin Heidelberg, Berlin, Heidelberg. 131 pp.
- McLean JP, Zhang T, Bardet S, Beauchêne J, Thibaut A, Clair B, Thibaut B (2011) The decreasing radial wood stiffness pattern of some tropical trees growing in the primary forest is reversed and increases when they are grown in a plantation. *Ann For Sci.* 68(4): 681-688.
- McPherson Guitars (2022) <https://mcpersonguitars.com>
- Mertz M (2016) *Wood and traditional woodworking in Japan* (2nd Edition). Kaiseisha Press. 259 pp.
- Meylan BA (1972) The influence of microfibril angle on the longitudinal shrinkage-moisture content relationship. *Wood Sci Technol.* 6: 293-301.
- Missanjo E and Matsumura J (2016) Wood density and mechanical properties of *Pinus kesiya* Royle ex Gordon in Malawi. *Forests.* 7(135): pp 1-10.
- Miyaki M, Hatakeyama S, Goshu K (1983) 割裂法における繊維傾斜度と樹心軸 との関係 (*In English: Relationship between grain inclination and axis of pith when using the splitting method*). *J The Jpn For Soc.* 65: 183–186.
- Moore JR, Cown DJ, McKinley RB (2015) Modelling spiral grain angle variation in New Zealand-grown radiata pine. *New Zeal J For Sci.* 45(15): pp 1–9.
- Morihiro Y and Mori E (1973) The torsional vibration in a prismatic bar. *J Acoust Soc Japan.* 29(3): 139–143.
- Mott PH, Dorgan JR, Roland CM (2008) The bulk modulus and Poisson's ratio of "incompressible" materials. *J Sound Vib.* 312(4-5): 572–575.
- Nakai T (1985) Mechanical properties of tropical woods. *JARQ-Jpn Agr Res Q.* 18(4): 315–323.
- Nederveen CJ and Tilstra JF (1971) Clamping corrections for torsional stiffness of prismatic bars. *J Phys D Appl Phys.* 4(11): 1661–1667.
- Nederveen CJ and van der Wal CW (1967) A torsion pendulum for the determination of shear modulus and damping around 1 Hz. *Rheol Acta.* 6(4): 316–323.
- Normand D, Mariaux A, Détienne P, Langbour P (2017) CIRAD's xylotheque. CIRAD. <https://doi.org/10.18167/xylotheque>
- Northcott PL (1957) Is spiral grain the normal growth pattern? *Forest Chron.* 33(4): 335–352.
- Novitskaya LL, Tarelkina TV., Galibina NA, Moshchenskaya YL, Nikolaeva NN, Nikerova KM, Podgornaya MN, Sofronova IN, Semenova LI (2020) The Formation of Structural Abnormalities in Karelian Birch Wood is Associated with Auxin Inactivation and Disrupted Basipetal Auxin Transport. *J Plant Growth Regul.* 39: 378–394.
- Nozaki K, Hayashida H, Yamada T (1988) ピアノ音質のエンジニアリング：材料と音とのかわりについて (*In English: Engineering approach for piano timber - relation between material and timber*). *Japan Soc Mech Eng.* 91(836): 653–659.
- Obataya E, Ono T, Norimoto M (2000) Vibrational properties of wood along the grain. *J Mater Sci.* 35: 2993–3001.
- Ogata Y and Fujita M (2005a) New anatomical method of grain angles measurement using confocal microscopy and image cross-correlation. *Trees.* 19: 73–80.

- Ogata Y and Fujita M (2005b) Z-Axis calibration in optical sectioning from Xylem cross sections for grain angle measurement. *IAWA J* 26(4): 427–441.
- Ogata Y, Fujita M, Nobuchi T, Sahri MH (2003) Macroscopic and anatomical investigation of interlocked grain in *Acacia mangium*. *IAWA J.* 24(1): 13–26.
- Olorunnisola AO (2018) Design of structural elements with tropical hardwoods (1st edition). Springer, Cham. 284 pp.
- Ono T (1980) 振り振動による木材の動的剛性率及び内部摩擦 (*In English: The dynamic rigidity modulus and internal friction of several woods in torsional vibration*). *Mokuzai Gakkaishi.* 26(3): 139–145.
- Ono T (1983) 木材の動力学的性質に及ぼす繊維傾斜角の影響 (*In English: Effect of grain angle on dynamic mechanical properties of wood*). *J Soc Mater Sci.* 32(352): 108–113.
- Ono T and Kataoka A (1979) 楽器響板用材の動的ヤング率及び内部摩擦の周波数依存性 (1) 撓み振動における回転慣性及び剪断力の影響 (*In English: The frequency dependence of the dynamic Young's modulus and internal friction of wood used for the soundboards of musical instruments. I. Effect of rotatory inertia and shear on the flexural vibration of free-free beams*). *Mokuzai Gakkaishi.* 25: 461–468
- Ono T and Norimoto M (1984) On physical criteria for the selection of wood for soundboards of musical instruments. *Rheol Acta.* 23: 652–656.
- Ono T and Norimoto M (1983) Study on young's modulus and internal friction of wood in relation to the evaluation of wood for musical instruments. *Jpn J Appl Phys.* 22(4): 611–614.
- Ono T and Norimoto M (1985) Anisotropy of dynamic Young's modulus and internal friction in wood. *Jpn J Appl Phys* 1. 24(8): 960–964.
- Orfanidis SJ (2016) Electromagnetic Waves and Antennas. Electronic version: <https://www.ece.rutgers.edu/~orfanidi/ewa/>
- Ormarsson S and Cown D (2005) Moisture-related distortion of timber boards of Radiata Pine : Comparison with Norway Spruce. *Wood Fiber Sci.* 37(3): 424–436.
- Ouis D (2002) On the frequency dependence of the modulus of elasticity of wood. *Wood Sci Technol.* 36(4): 335–346.
- Özden S, Slater D, Ennos R (2017) Fracture properties of green wood formed within the forks of hazel (*Corylus avellana* L.). *Trees.* 31: 903–917.
- Passarini L, Hernández RE (2016) Effect of the desorption rate on the dimensional changes of *Eucalyptus saligna* wood. *Wood Sci Technol.* 50(5): 941–951.
- Peck EC (1960) News and views of this kiln drying business (Report No. 1769-27). Forest products laboratory, Forest service, United States Department of Agriculture. 9 pp.
- POWO (2019) Plants of the World Online. Facilitated by the Royal Botanic Gardens, Kew. Published on the Internet; <http://www.plantsoftheworldonline.org/> (Retrieved 03 04 2019)
- Polymer Database (2020) <https://www.polymerdatabase.com/>
- Priestley JH (1945) Observations on spiral grain in timber. *Am J Bot.* 32(5): 277–284.

- Rakotovololonalimanana H, Chaix G, Brancheriau L, Ramamonjisoa L, Ramananantoandro T, Thévenon MF (2015) A novel method to correct for wood MOE ultrasonics and NIRS measurements on increment cores in *Liquidambar styraciflua* L. *Ann For Sci.* 72(6): 753–761.
- Reiterer A, Lichtenegger H, Tschegg S, Fratzl P (1999) Experimental evidence for a mechanical function of the cellulose microfibril angle in wood cell walls. *Philos Mag A.* 79(9): 2173–2184.
- Richter C (2015) *Wood characteristics - Description, causes, prevention, impact on use and technological adaptation* (1st edition). Springer International Publishing, Switzerland. 222 pp.
- Ross RJ (2010) *Wood handbook: Wood as an engineering material (FPL-GTR-190)*. Forest products laboratory, Forest service, United States Department of Agriculture. 509 pp.
- Roth F (1895) *Timber: An elementary discussion of the characteristics and properties of wood*. Washinton Government Printing Office. 90 pp.
- Saarinen K and Muinonen K (2001) Light scattering by wood fibers. *Appl Optics.* 40(28): 5064-5077.
- Sakagami H, Matsumura J, Oda K (2009) In situ visualization of hardwood microcracks occurring during drying. *J Wood Sci.* 55: 323–328.
- Sarén MP and Serimaa R (2006) Determination of microfibril angle distribution by X-ray diffraction. *Wood Sci Technol.* 40(6): 445–460.
- Schulgasser K and Witztum A (2007) The mechanism of spiral grain formation in trees. *Wood Sci Technol.* 41(2): 133-156.
- Schulgasser K and Witztum A (2015) How the relationship between density and shrinkage of wood depends on its microstructure. *Wood Sci Technol.* 49(2): 389–401.
- Sekhar AC and Rajput SS (1967) Some studies on the shrinkage behaviour of wood. *Wood Sci Technol.* 1: 99–108.
- Semenov PI (1966) Determination of shear moduli of orthotropic materials from torsion tests. *Polym Mech.* 2(1): 27–33.
- Shen J, Zhou J, Vazquez O (2000) Experimental study of optical scattering and fiber orientation determination of softwood and hardwood with different surface finishes. *Appl Spectrosc* 54(12): 1793–1804.
- Siau JF (1984) *Transport processes in wood* (1st edition). Springer-Verlag Berlin Heidelberg. 248 pp. <https://doi.org/10.1007/978-3-642-69213-0>
- Simonaho SP and Silvenoinen R (2004) Light diffraction from wood tissue. *Opt Rev.* 11(5): 308–311.
- Skaar C (1988) *Wood-Water Relations* (1st edition). Springer-Verlag Berlin Heidelberg. 283 pp. <https://doi.org/10.1007/978-3-642-73683-4>
- Slater D, Bradley RS, Withers PJ, Roland Ennos A (2014) The anatomy and grain pattern in forks of hazel (*Corylus avellana* L.) and other tree species. *Trees.* 28: 1437–1448.
- Sole A, Farup I, Nussbaum P (2017) Evaluating an image based multi-angle measurement setup using different reflection models. *IS&T Int Symp Electron Imaging Sci Technol* 101–107.
- Soma T, Shida S, Arima T (2002) 超音波を用いた繊維傾斜角の推定と球形試験体による検証 (*In English: Calculation of grain angle and verification with spherical wood specimens using ultrasonic waves*). *Mokuzai Gakkaishi.* 48:407–412

- Straže A, Kliger R, Johansson M, Gorišek Ž (2011) The influence of material properties on the amount of twist of spruce wood during kiln drying. *Eur J Wood Wood Prod.* 69(2): 239–246.
- Suarez SA, Gibson RF, Sun CT, Chaturvedi SK (1986) The influence of fiber length and fiber orientation on damping and stiffness of polymer composite materials. *Exp Mech.* 26:175–184.
- Sugimoto H, Kawabuchi S, Sugimori M, Gril J (2018) Reflection and transmission of visible light by sugi wood: effects of cellular structure and densification. *J Wood Sci.* 64: 738–744.
- Sun C-T, Gibson RF, Chaturvedi SK (1985) Internal material damping of polymer matrix composites under off-axis loading. *J Mater Sci.* 20: 2575–2585.
- Takeshi O (1991) 木材の音響的性質 (*In English: Acoustic properties of wood*). *Mokuzai Gakkaishi* 37(11): 991–998.
- Taleb NN (2012) *Antifragile: things that gain from disorder*. New York: Random House.
- Teissier du Cros E, Kleinschmit J, Azoeuf P, Hoslin R (1980) Spiral grain in Beech, variability and heredity. *Silvae Genet.* 29(1): 5–13.
- Thomas J and Collings DA (2017) Imaging spiral grain in *Pinus radiata* with X-ray microtomography. In Pandey K, Ramakantha V, Chauhan S, Kumar A (eds) *Wood is Good*. Springer Nature Singapore Pte Ltd, Singapore. pp 29–36.
- Tu LY, Brennan JN, Sauer JA (1955) Dispersion of Ultrasonic pulse velocity in cylindrical rods. *J Acoust Soc Am.* 27: 550–555.
- Viala R, Placet V, Cogan S (2018) Identification of the anisotropic elastic and damping properties of complex shape composite parts using an inverse method based on finite element model updating and 3D velocity fields measurements (FEMU-3DVF): Application to bio-based composite violin soundboards. *Compos Part A-Appl S.* 106: 91–103.
- Vincent P (2006) Comportement viscoélastique thermoactive en torsion du bois de peuplier à l'état vert (*In English: Thermoactive viscoelastic behaviour in torsion of poplar wood in the green state*). [Doctoral dissertation, University of Montpellier] LMGC. 153 pp.
- Wheeler EA (2011) InsideWood - A web resource for hardwood anatomy. *IAWA J.* 32(2): 199–211.
- Woodcock D and Shier A (2002) Wood specific gravity and its radial variations: The many ways to make a tree. *Trees.* 16: 437–443.
- Working the grain LCC (2021) <https://www.wtghardwoods.com>
- Stumpon AH (2021, June 22) Wood Identification Group in Facebook. <https://www.facebook.com/photo?fbid=10217642625169514&set=pcb.2902338140094005>
- Xavier J, Oliveira M, Morais J, Pinto T (2009) Measurement of the shear properties of clear wood by the Arcan test. *Holzforschung.* 63: 217–225.
- Yamamoto H and Kojima Y (2002) Properties of cell wall constituents in relation to longitudinal elasticity of wood: Part 1. Formulation of the longitudinal elasticity of an isolated wood fiber. *Wood Sci. Technol.* 36(1): 55–74.
- Yamamoto H, Okuyama T, Yoshida M (1993) Method of determining the mean microfibril angle of wood over a wide range by the improved Cave's method. *Mokuzai Gakkaishi.* 39(4): 375–381.

Yamamoto H, Sassus F, Ninomiya M, Gril J (2001) A model of anisotropic swelling and shrinking process of wood: Part 2. A simulation of shrinking wood. *Wood Sci Technol.* 35:167–181.

Yang Z, Clouston PL, Schreyer AC (2013) Torsional shear tests on laminated veneer lumber using a universal-type test machine. *J Mater Civ Eng.* 25: 1979–1983.

Yoshihara H and Maruta M (2018) Shear moduli in the longitudinal-radial and radial-tangential planes of Sitka spruce measured by torsional vibration tests. *Holzforschung.* 72(6): 507–512.

Yoshizawa N (1986) Cambial responses to the stimulus of inclination and structural variations of compression wood tracheids in Gymnosperms. [Doctoral thesis, Kyoto University] Wood products, department of forestry, Utsunomiya University, Utsunomiya. pp 23–141.

Young WC and Budynas RG (2002) Roark's formulas for stress and strain (7th edition). McGraw-Hill Book Companies, Inc., USA. 855 pp.

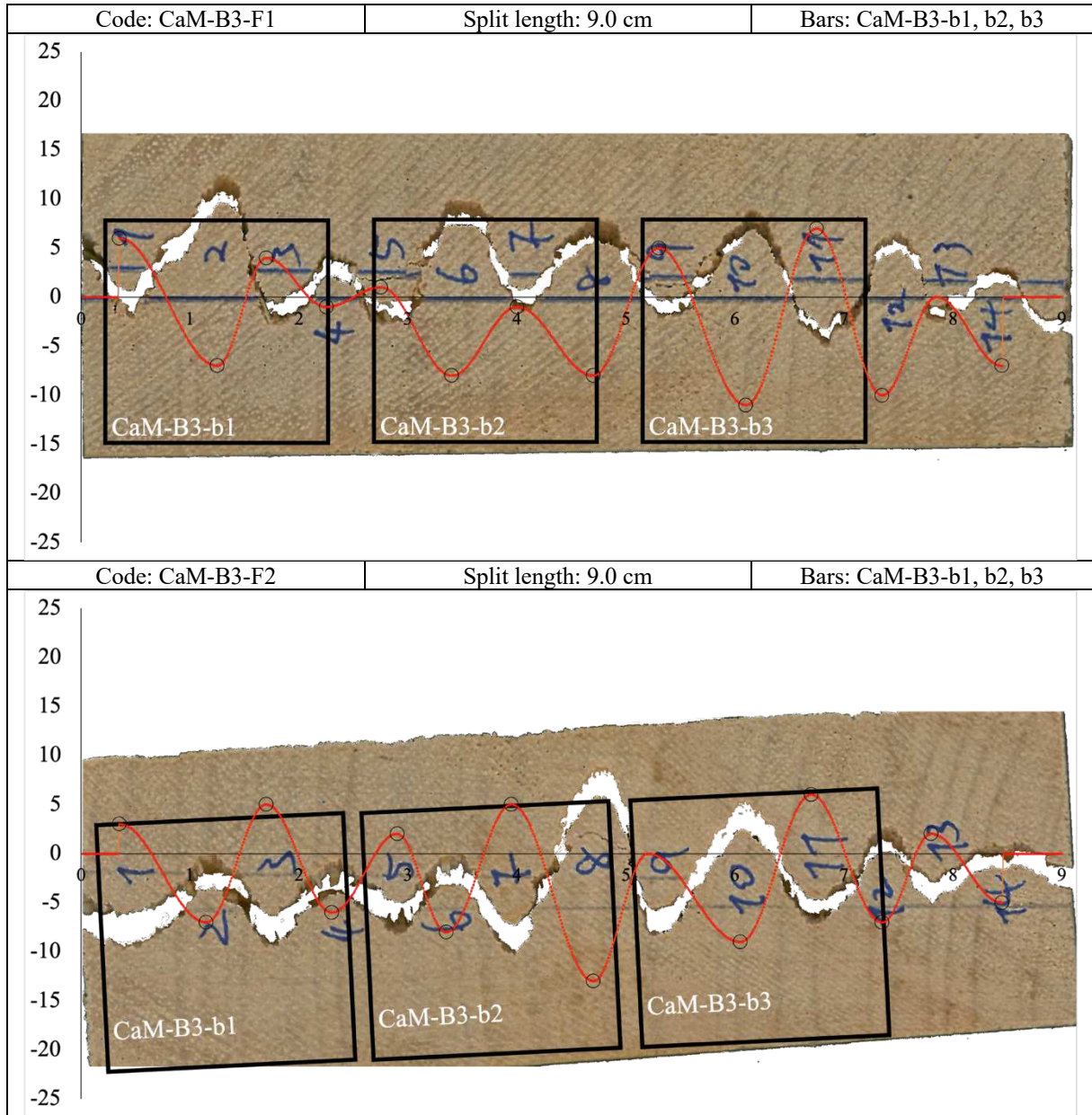
Zhang T, Bai S-L, Bardet S, Alméras T, Thibaut B, Beauchêne J (2011) Radial variations of vibrational properties of three tropical woods. *J Wood Sci.* 57: 377-386.

一枚板比較 (2019) <https://solidwood.jp/solidwood/slab/type/woodgrain>

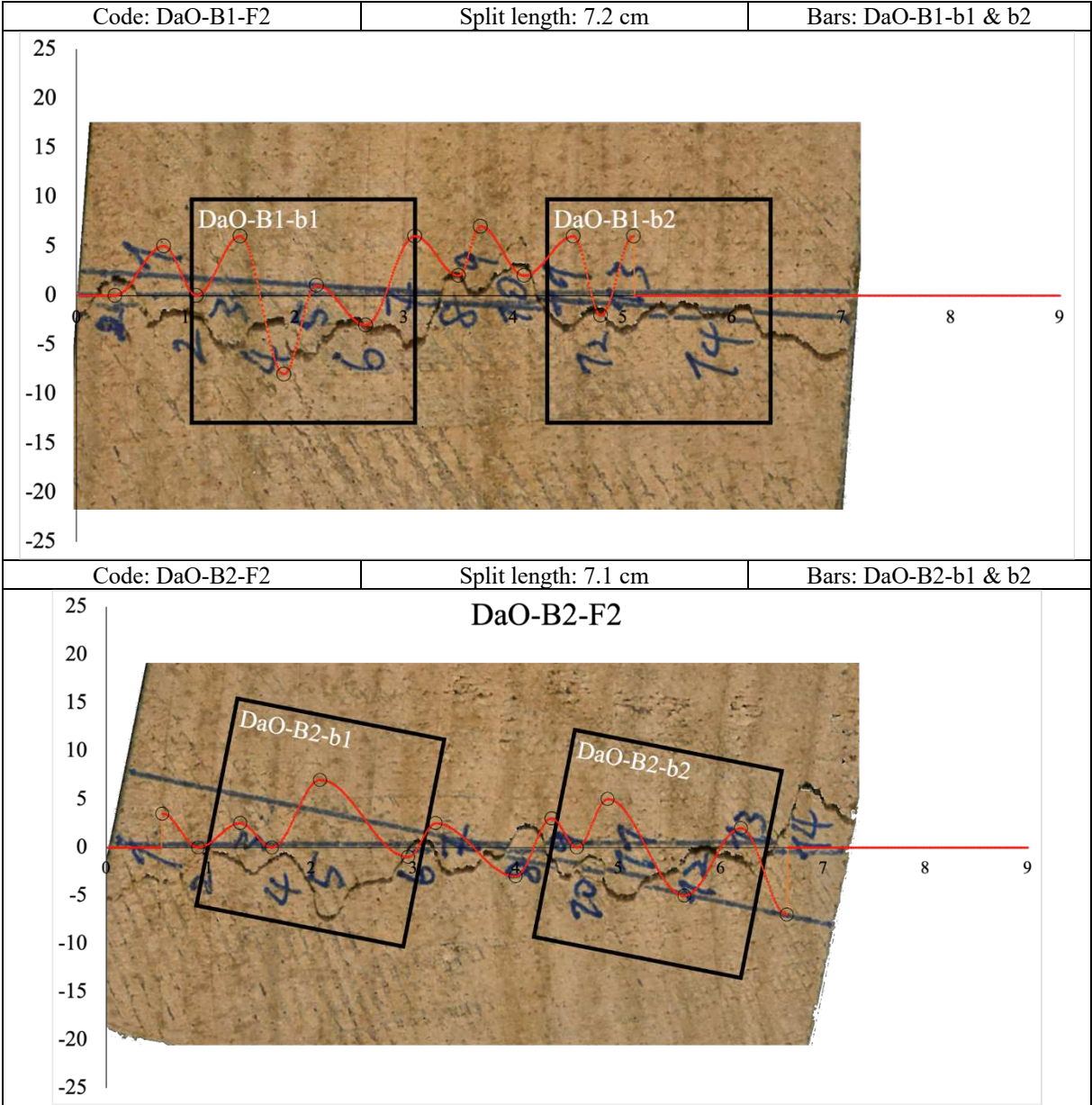
府中家具工業協同組合 (2019) <https://wp1.fuchu.jp/~kagu/siryō/moku.htm>

VI. Annexes

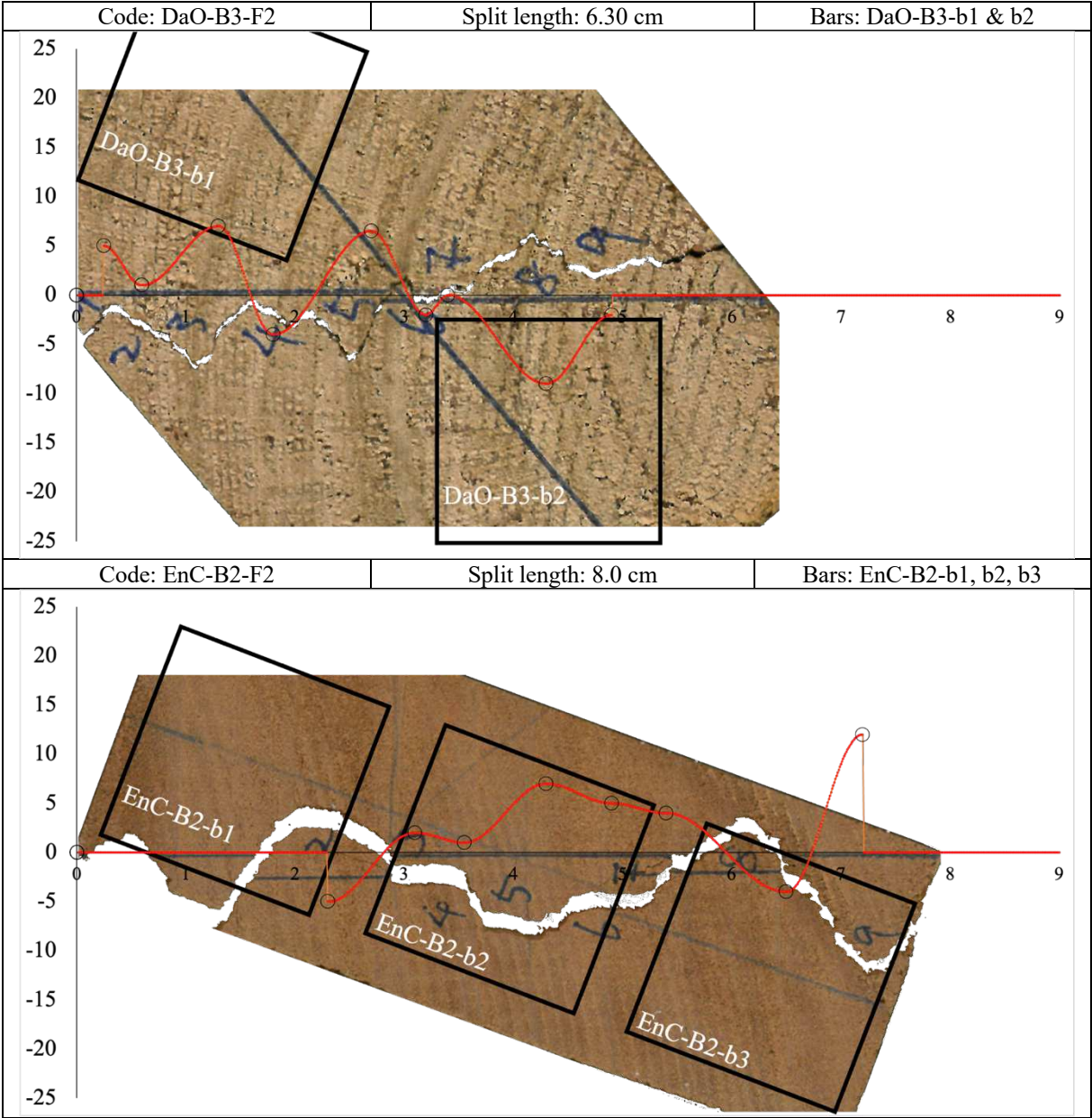
Annex Tab. 1 The record of splitting method and estimated data points by the function. The horizontal axis represents the record of peaks' positions, and vertical axis represents the angles measured at the peaks. The hollow circular points are the measured values and the solid points (connecting line) are the estimated values. Some of the split length values don't correspond to the photo because of the trimming by image processing



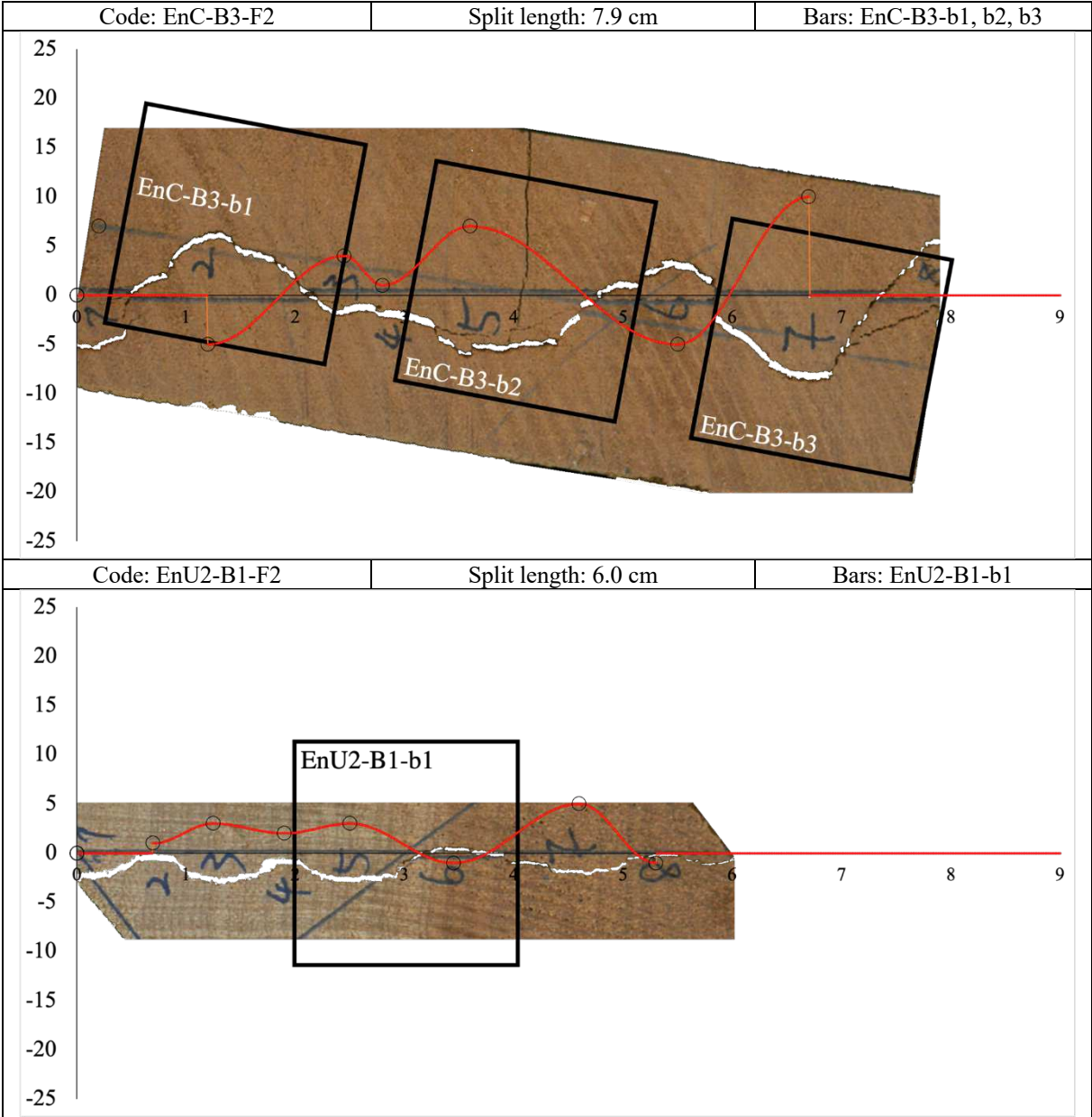
Annex Tab. 1 (continued)



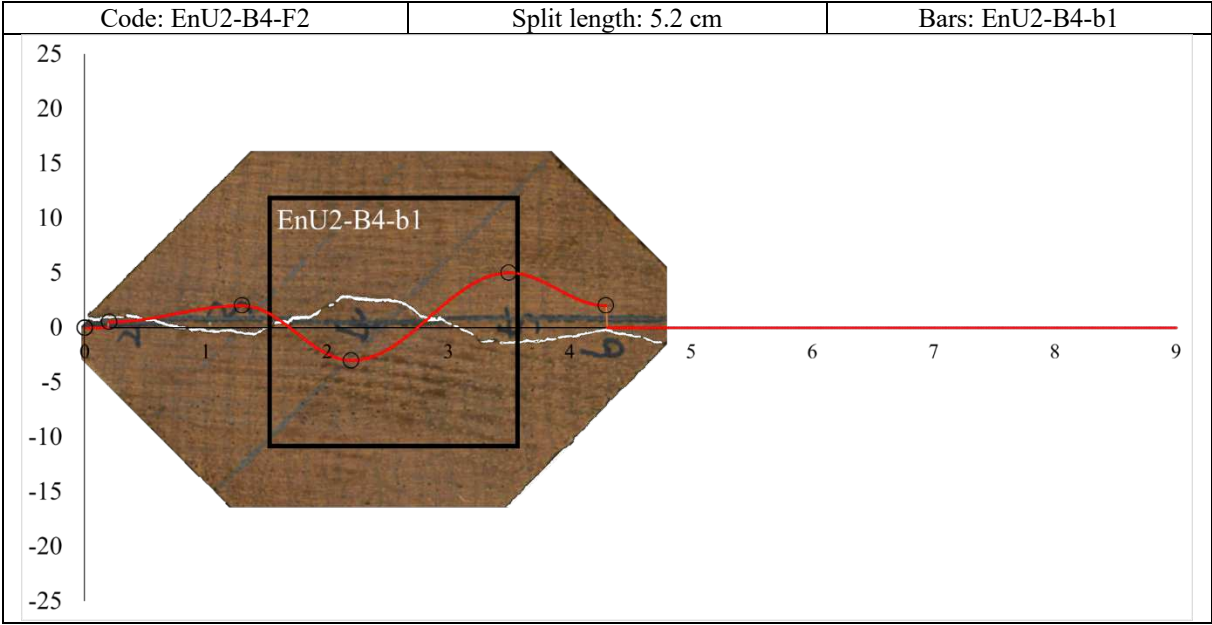
Annex Tab. 1 (continued)



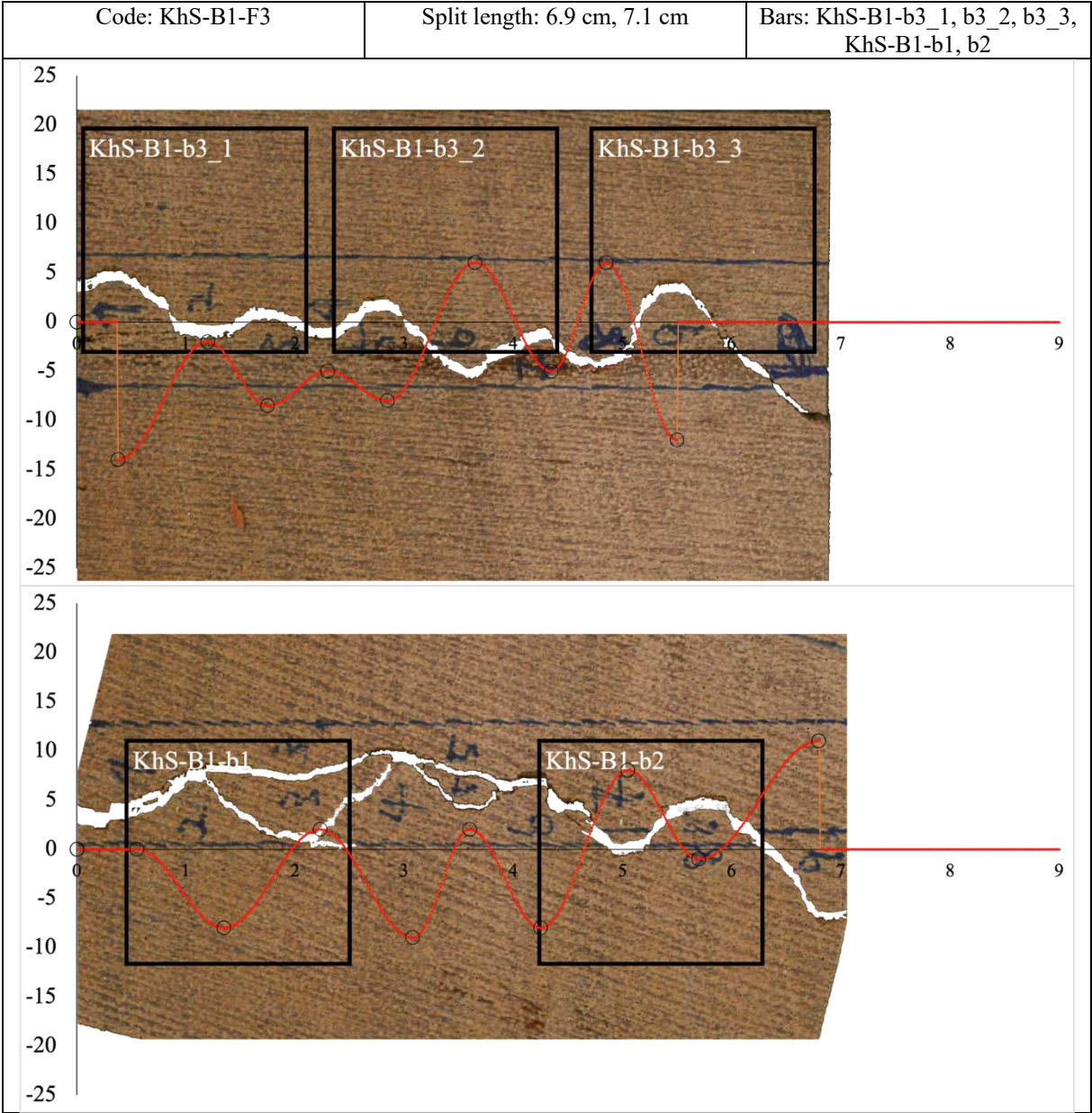
Annex Tab. 1 (continued)



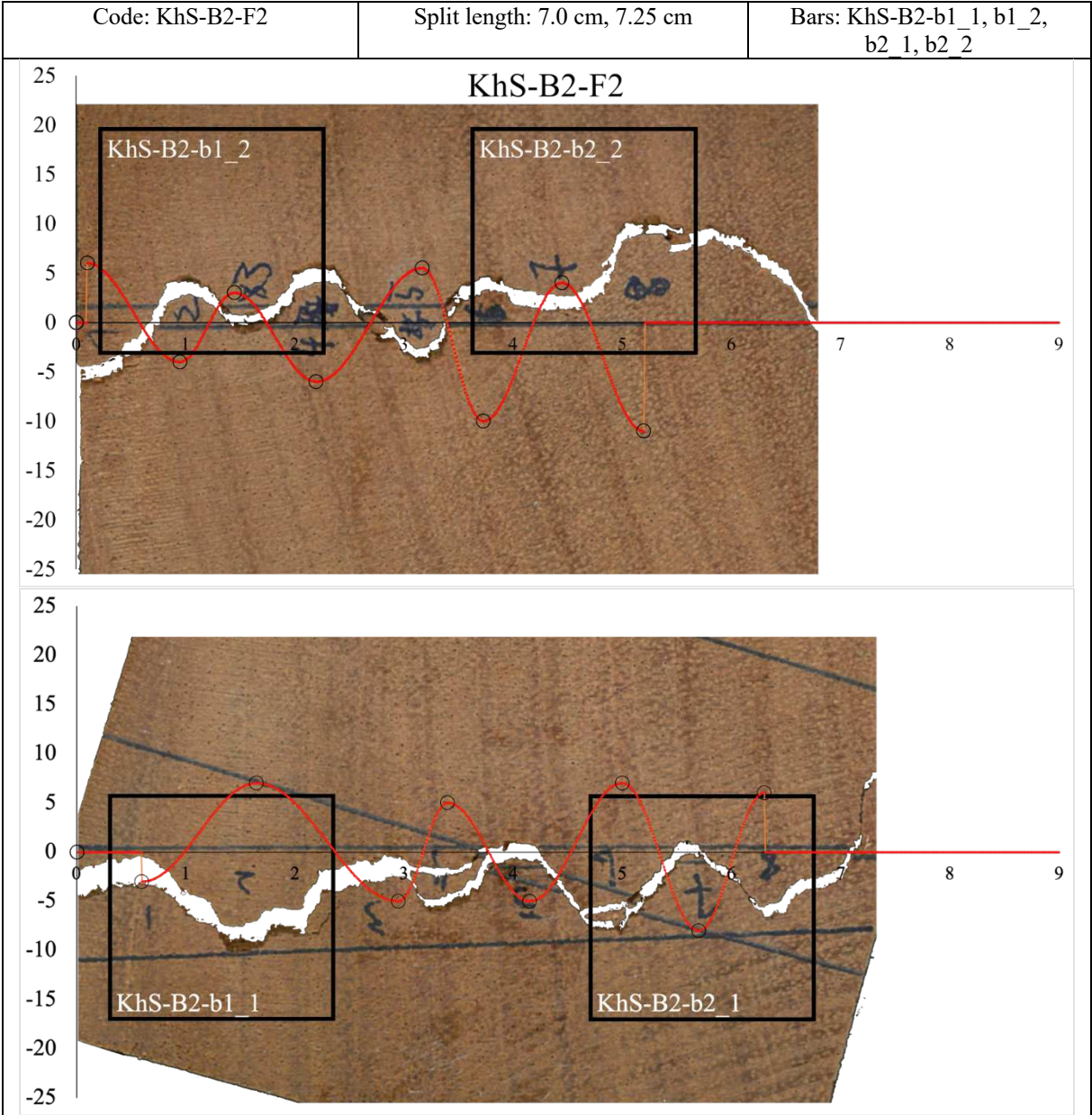
Annex Tab. 1 (continued)



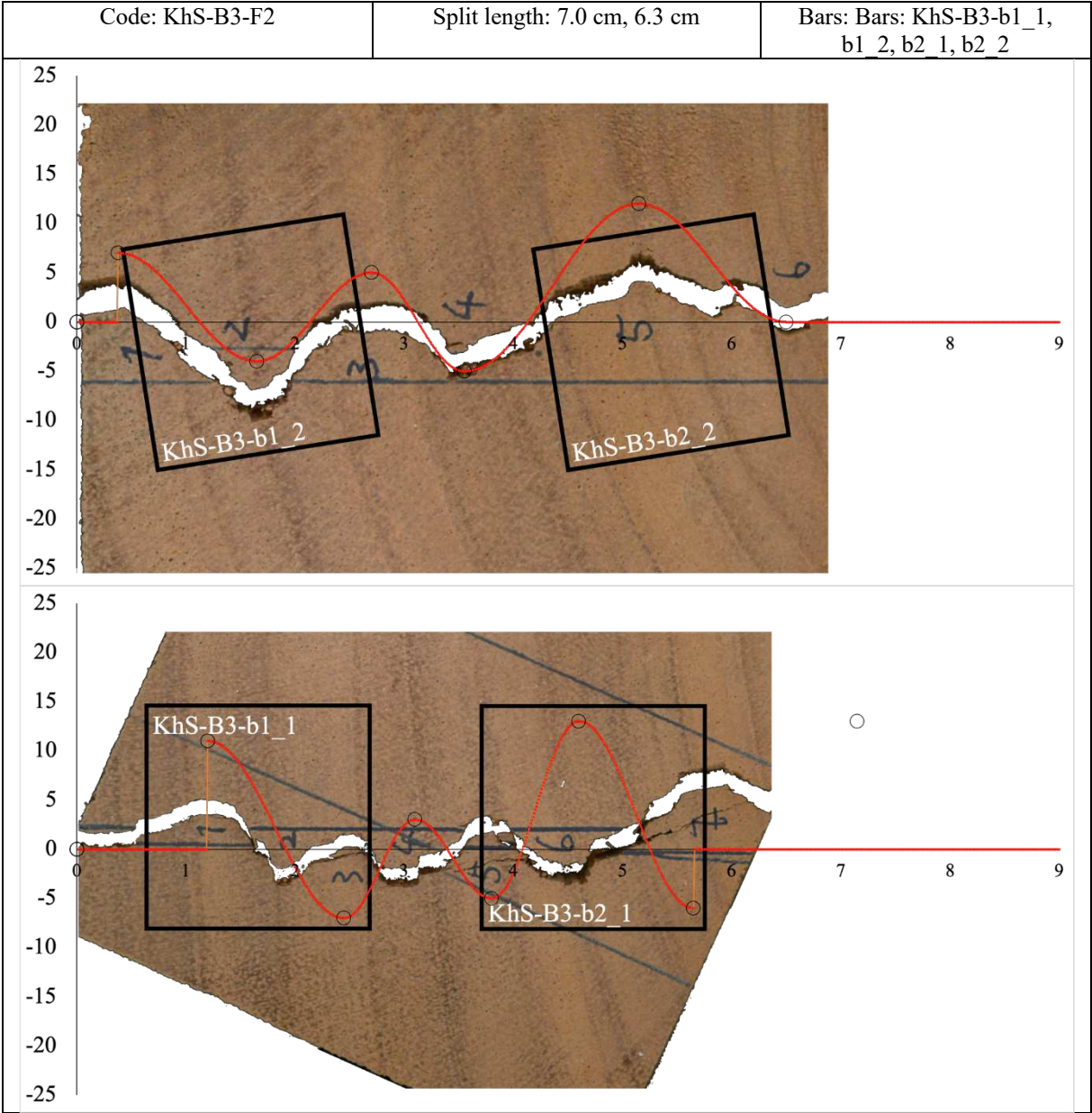
Annex Tab. 1 (continued)



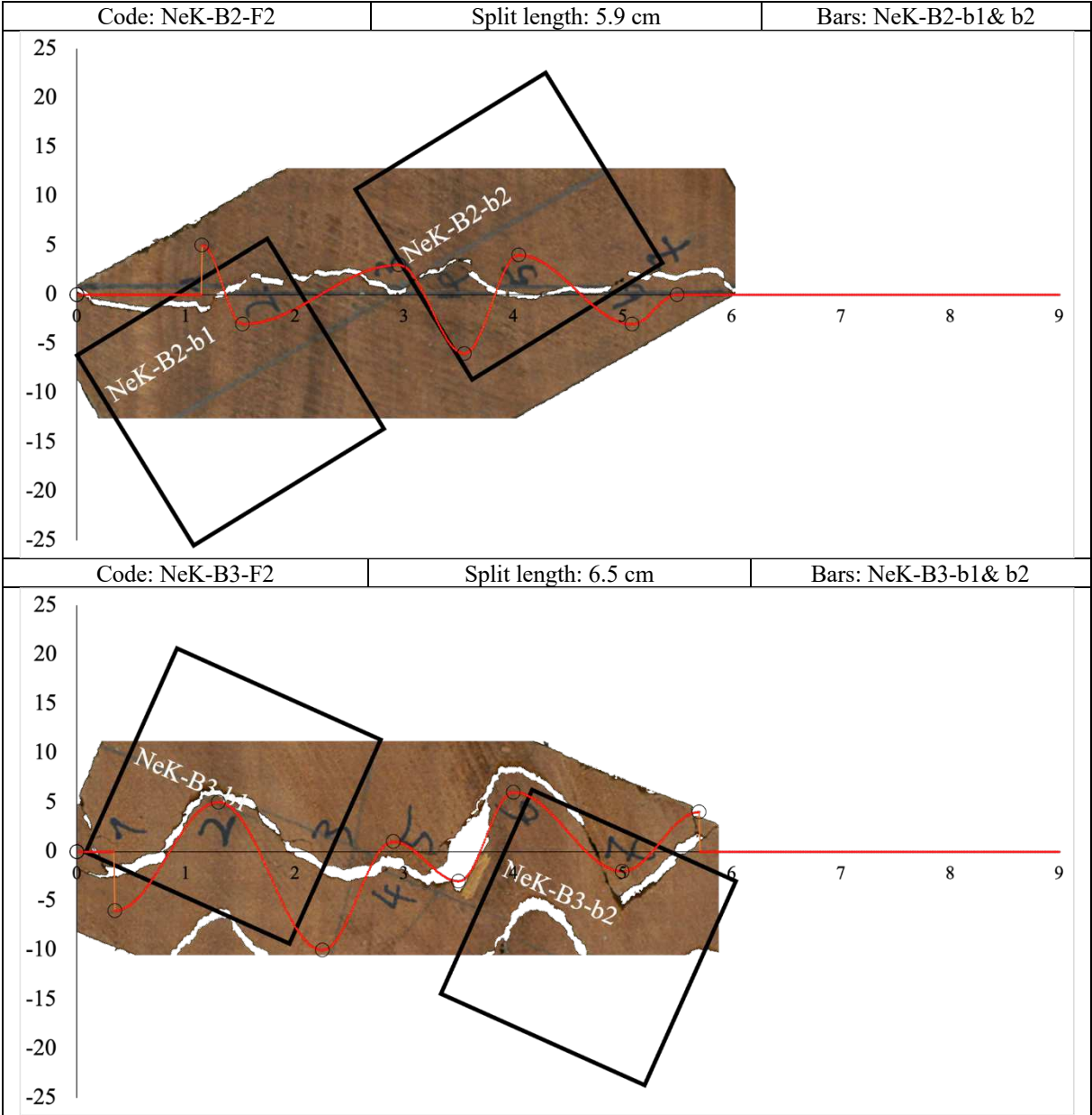
Annex Tab. 1 (continued)



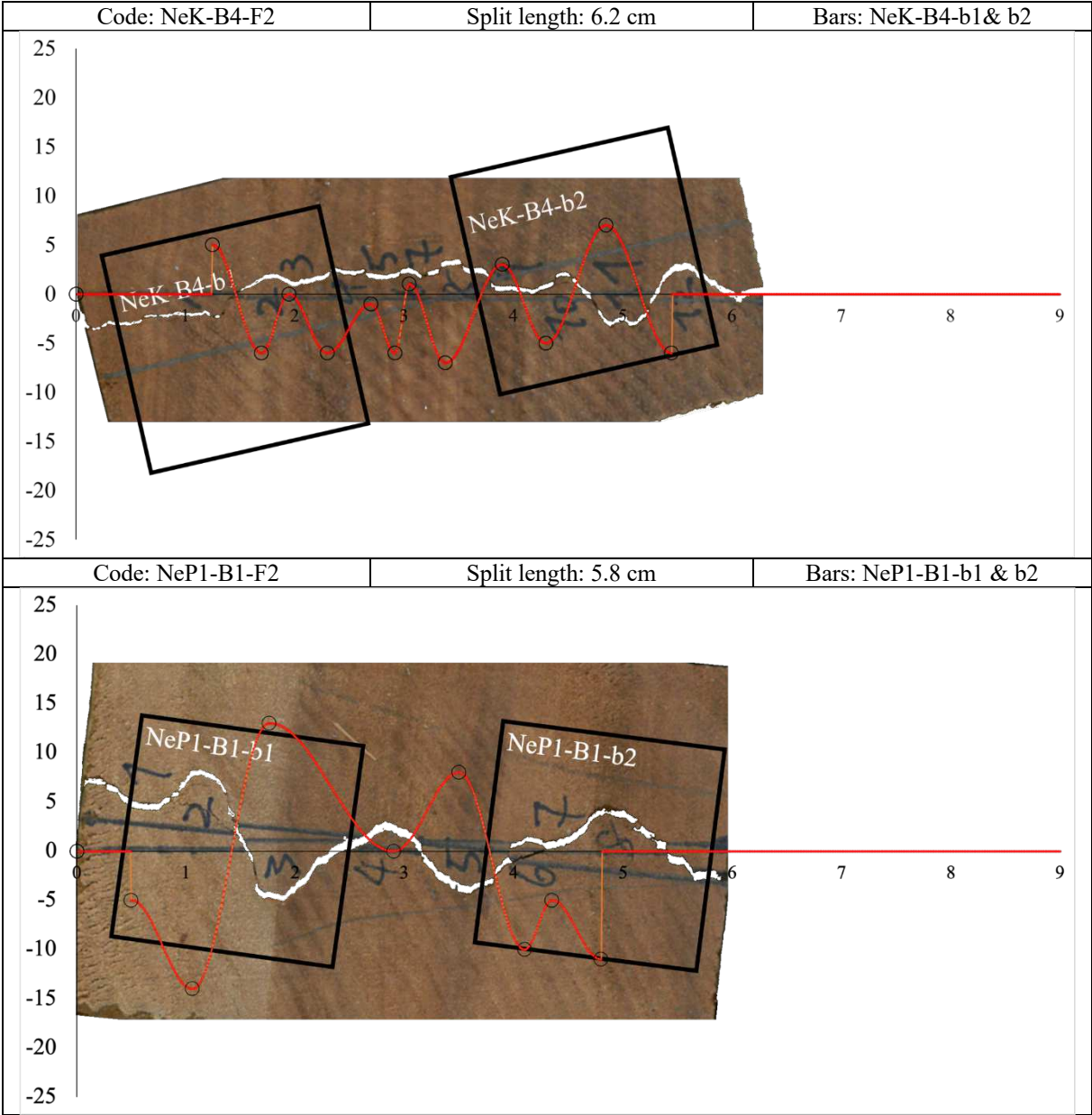
Annex Tab. 1 (continued)



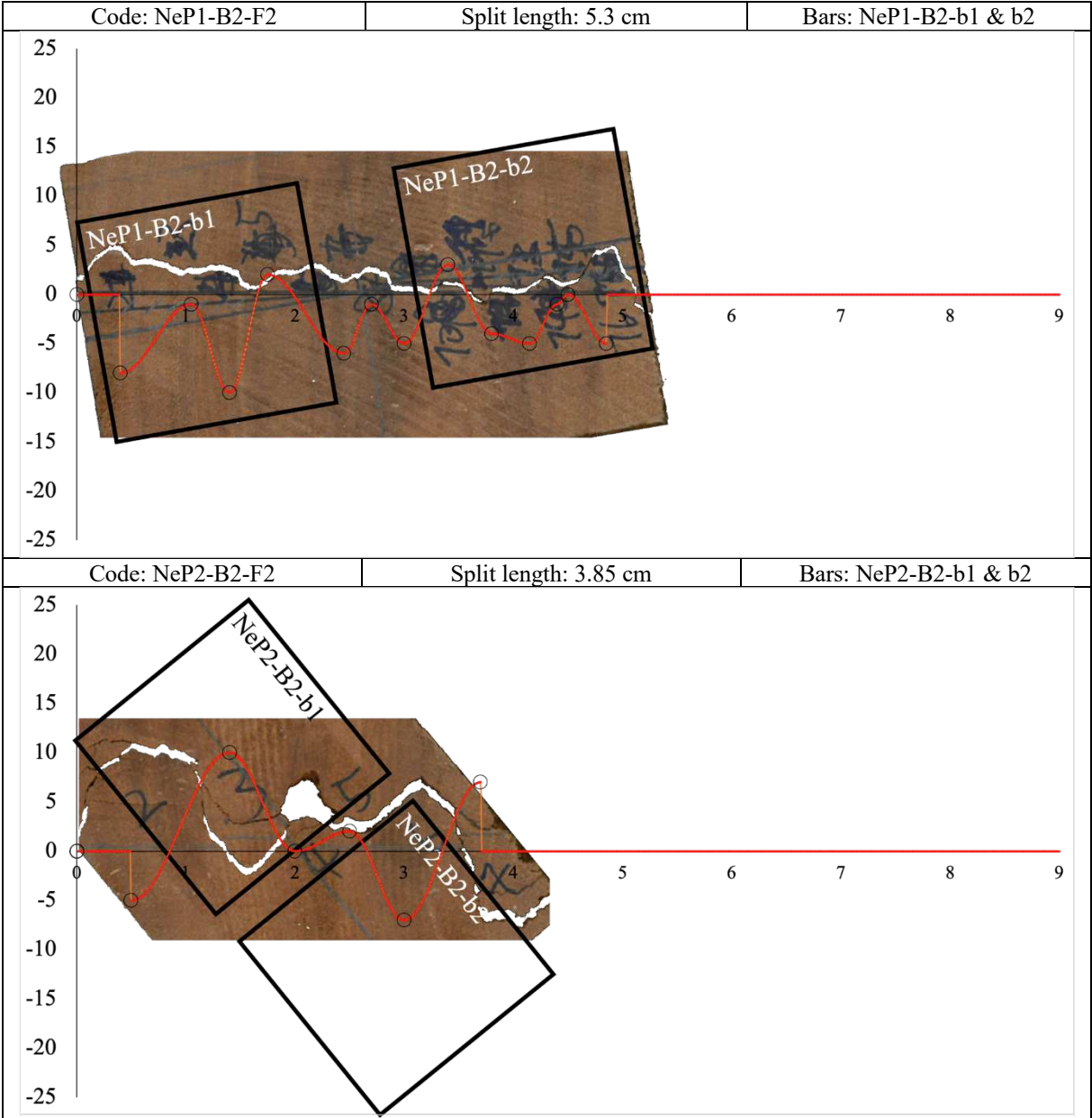
Annex Tab. 1 (continued)



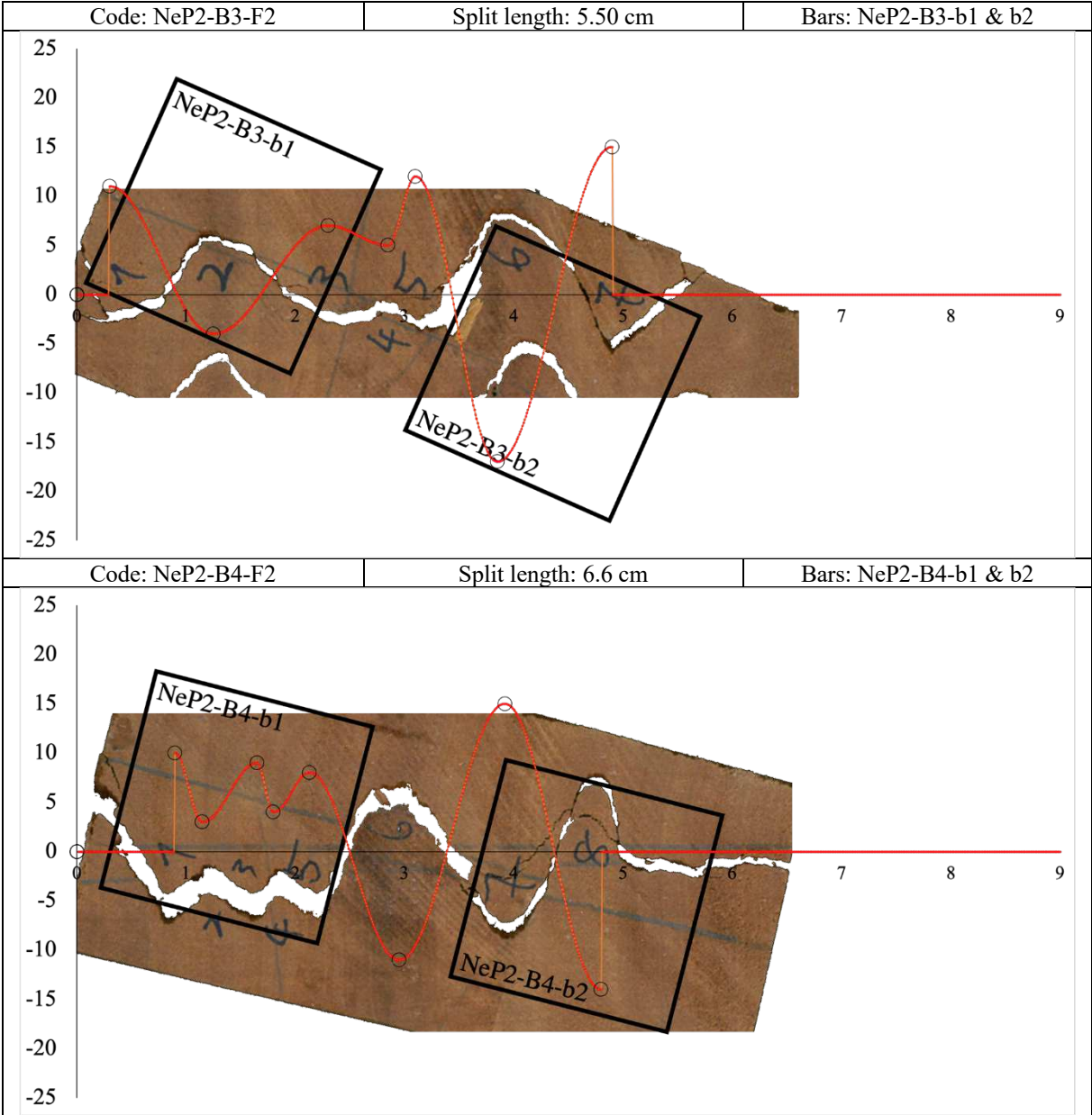
Annex Tab. 1 (continued)



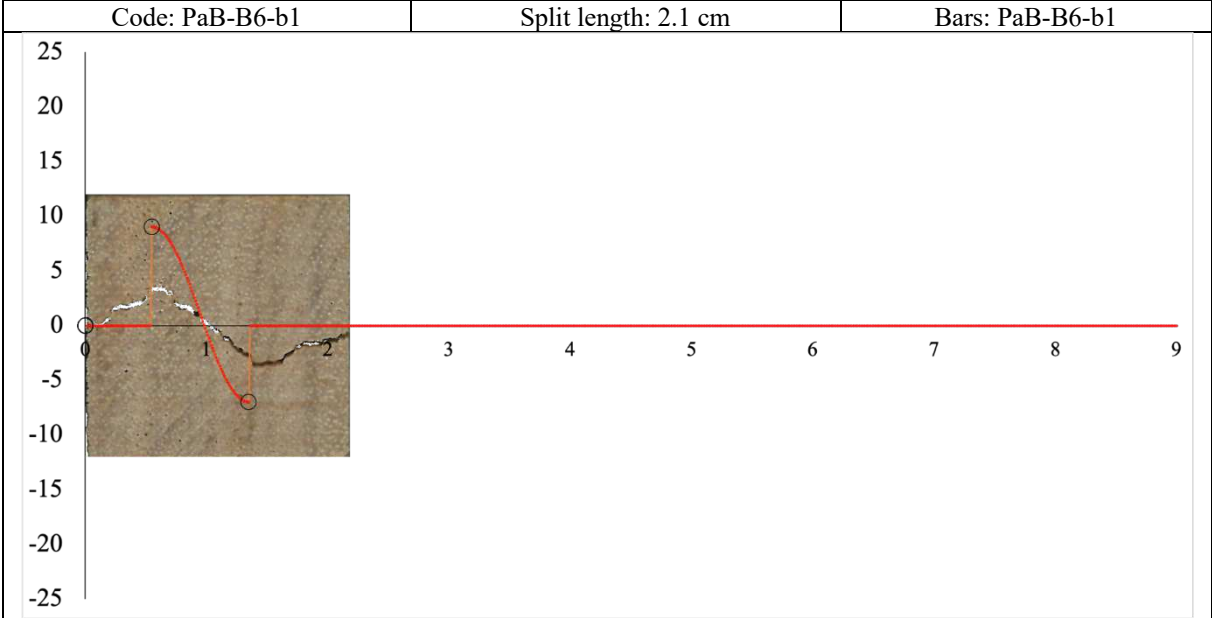
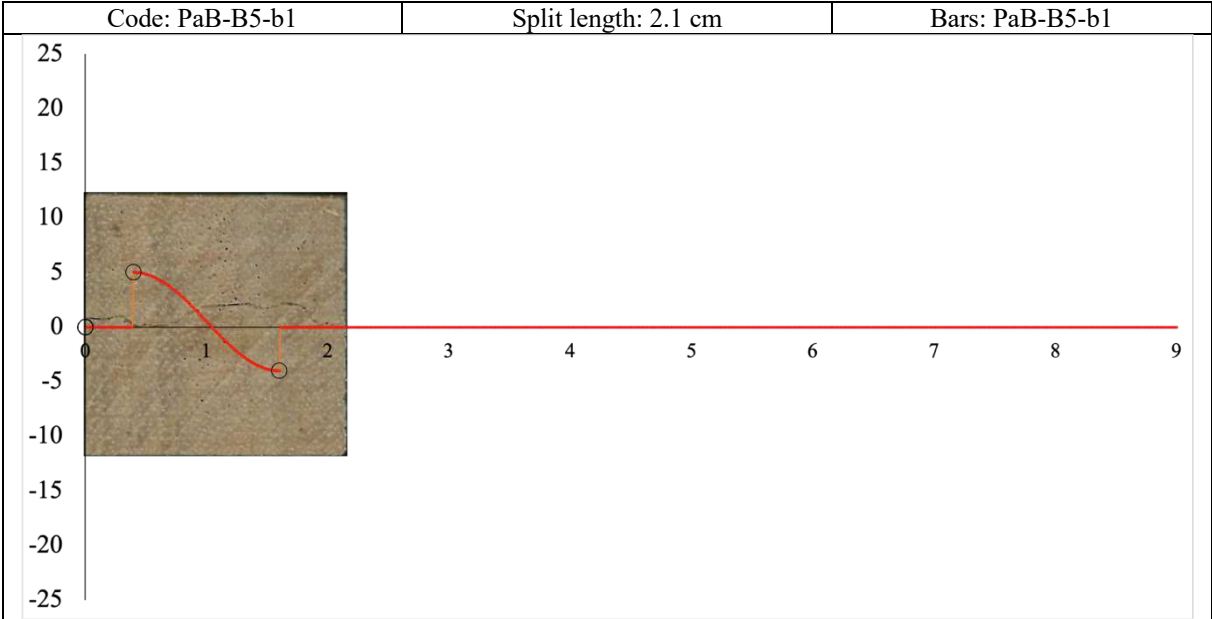
Annex Tab. 1 (continued)



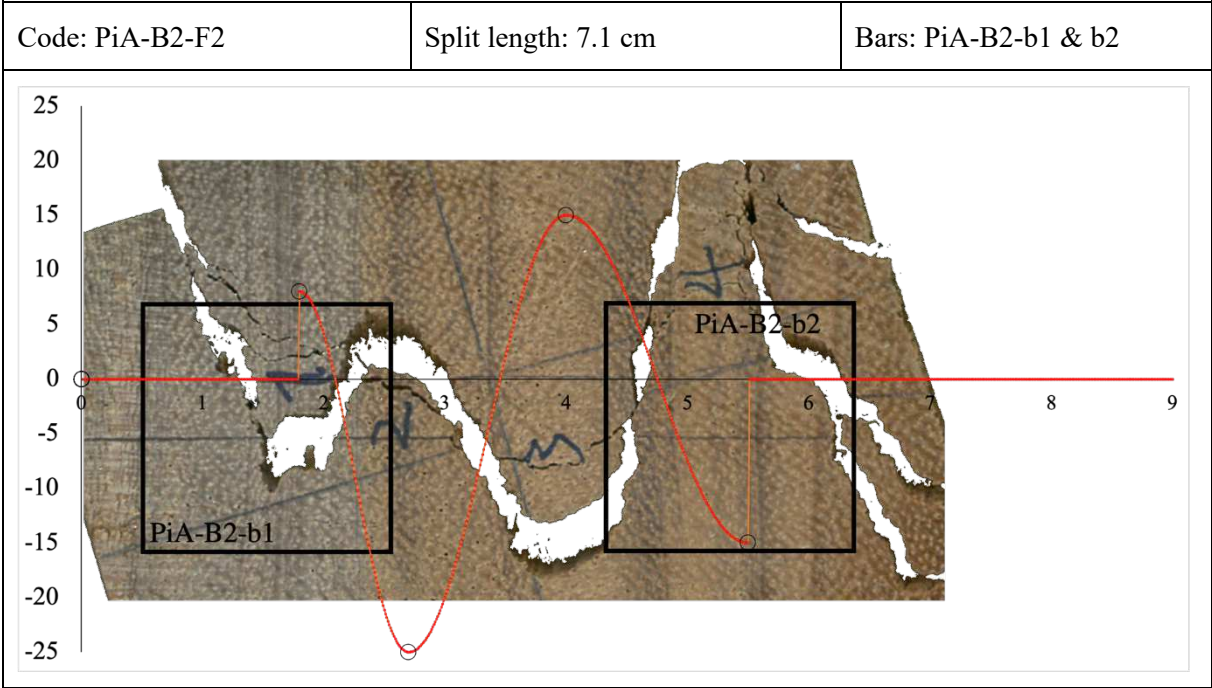
Annex Tab. 1 (continued)



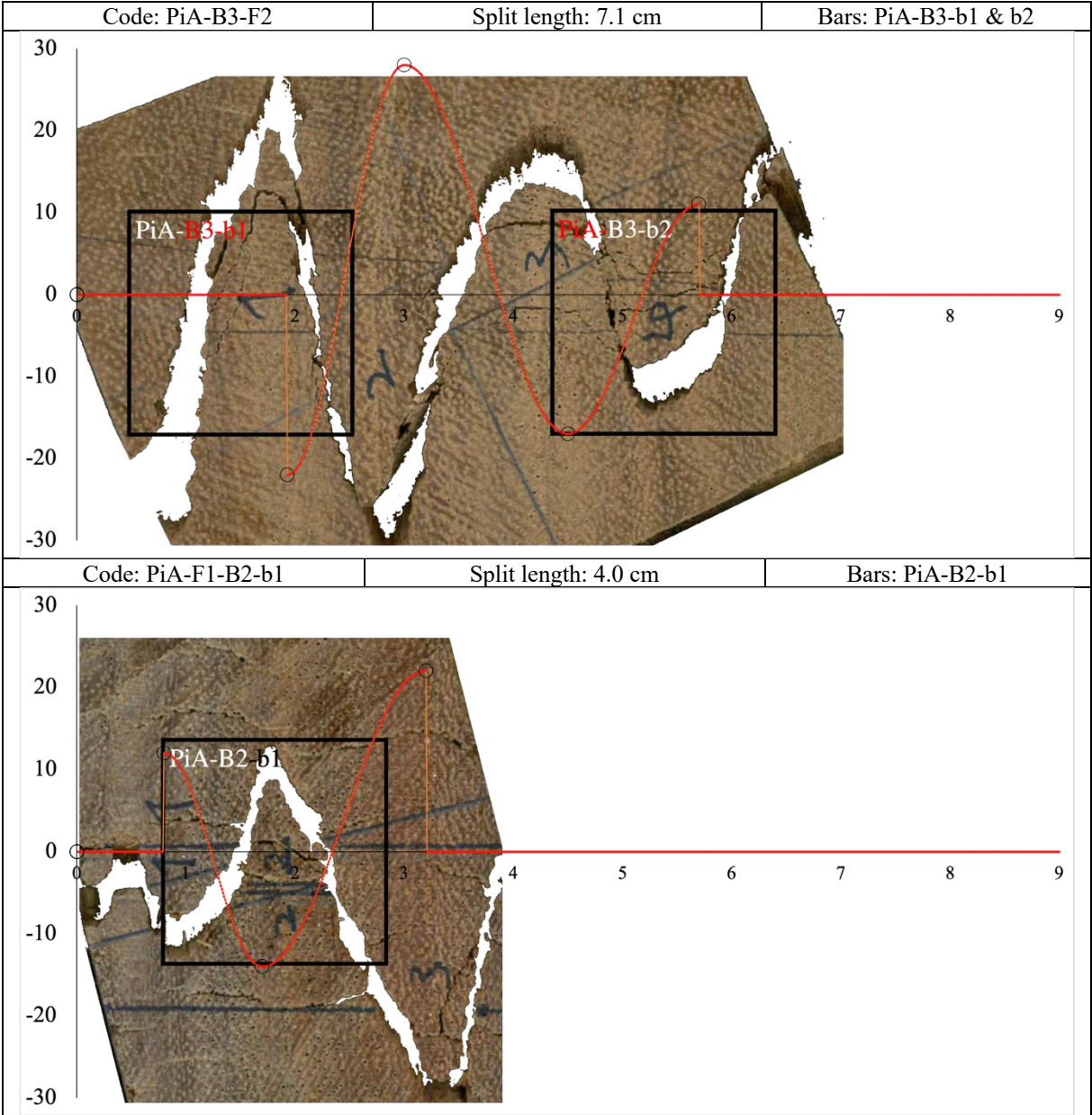
Annex Tab. 1 (continued)



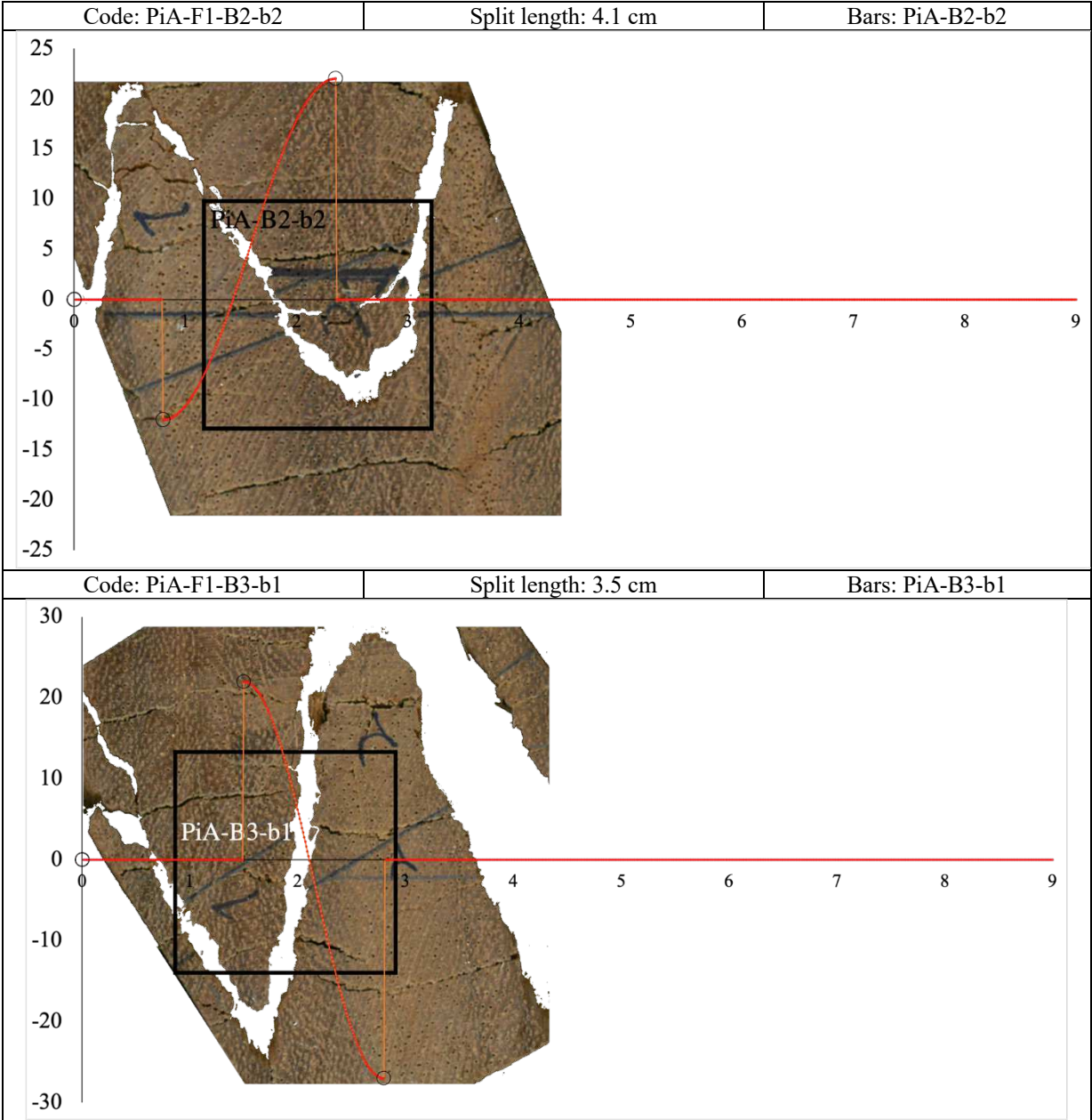
Annex Tab. 1 (continued)



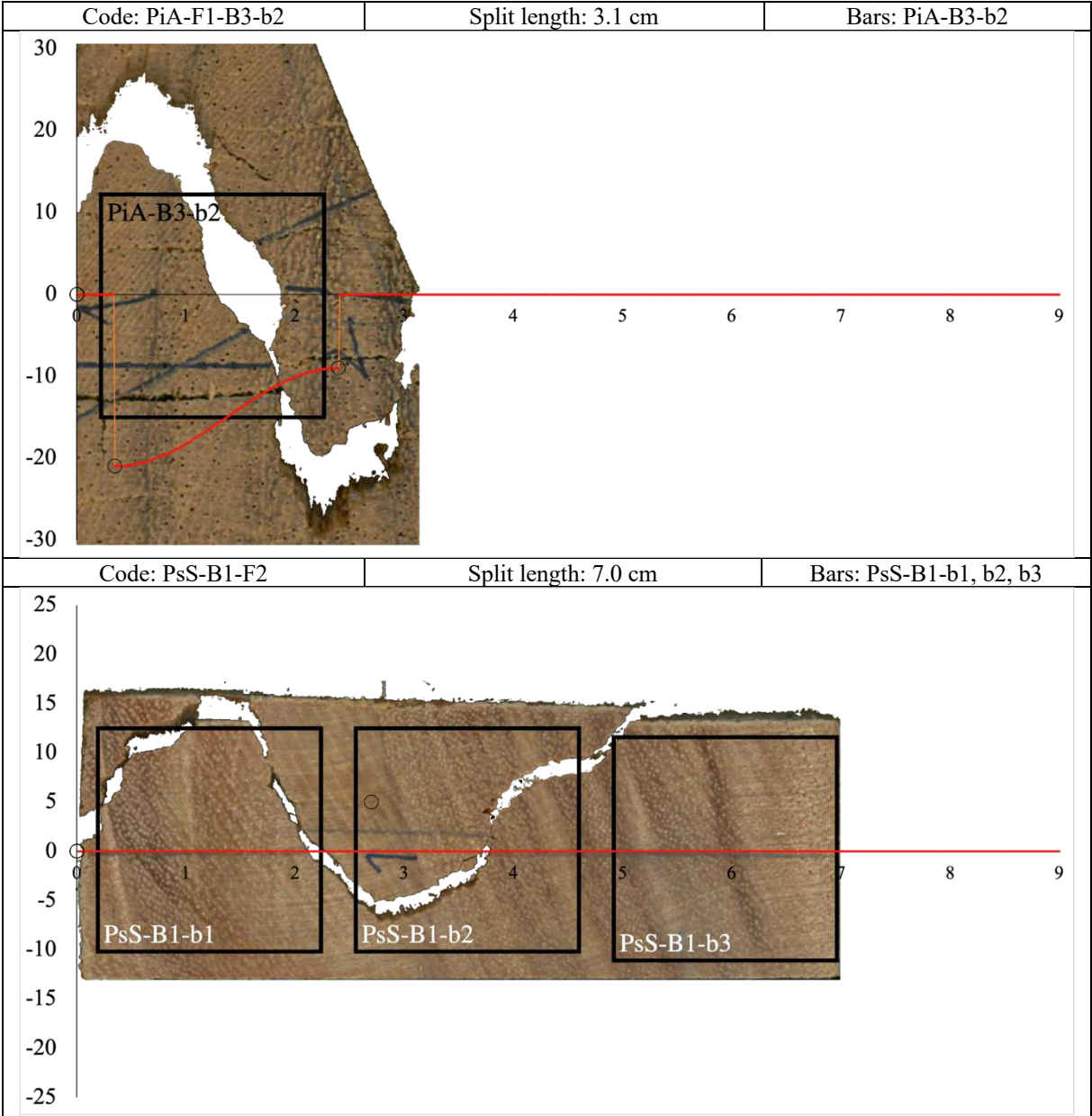
Annex Tab. 1 (continued)



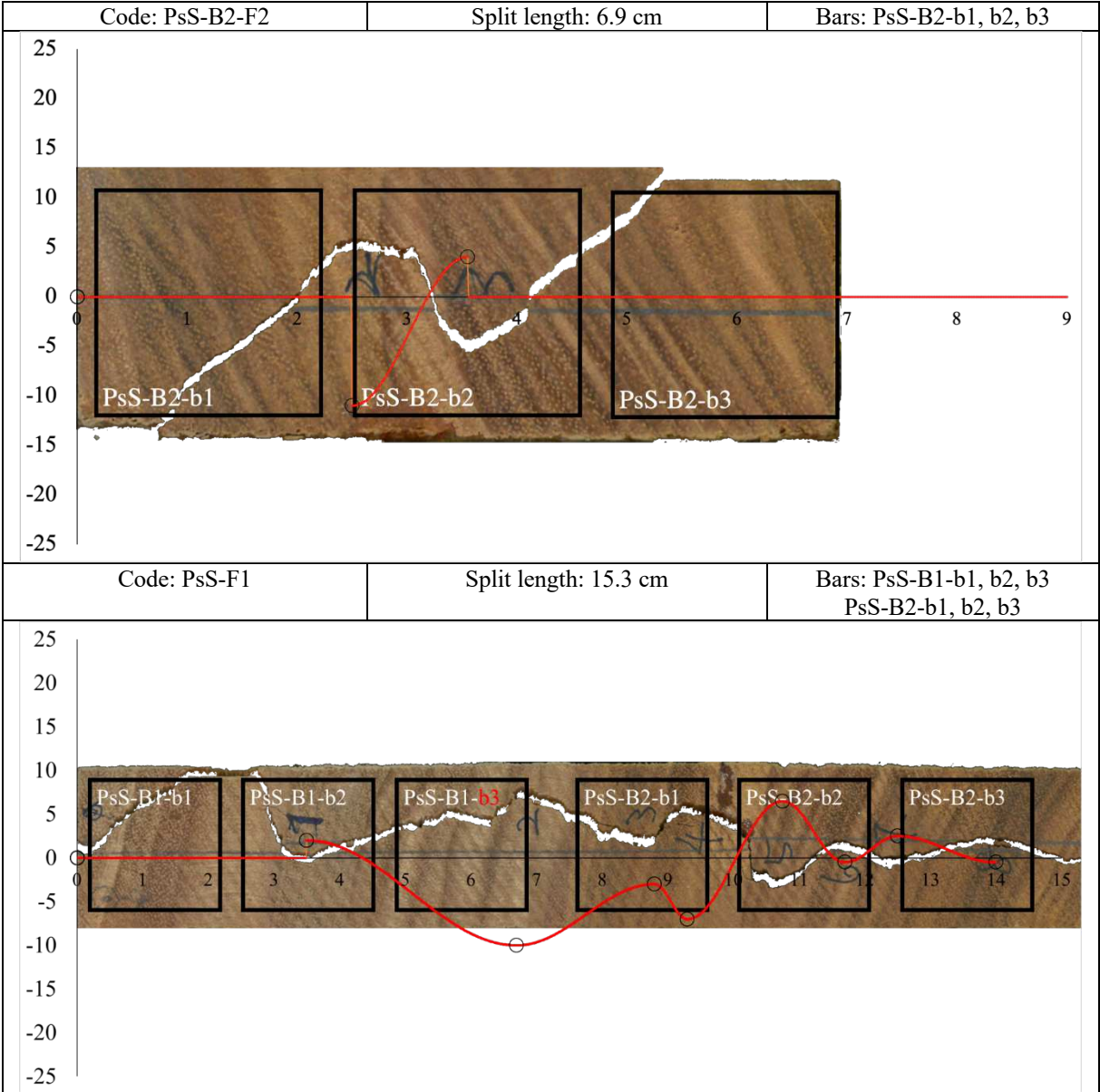
Annex Tab. 1 (continued)



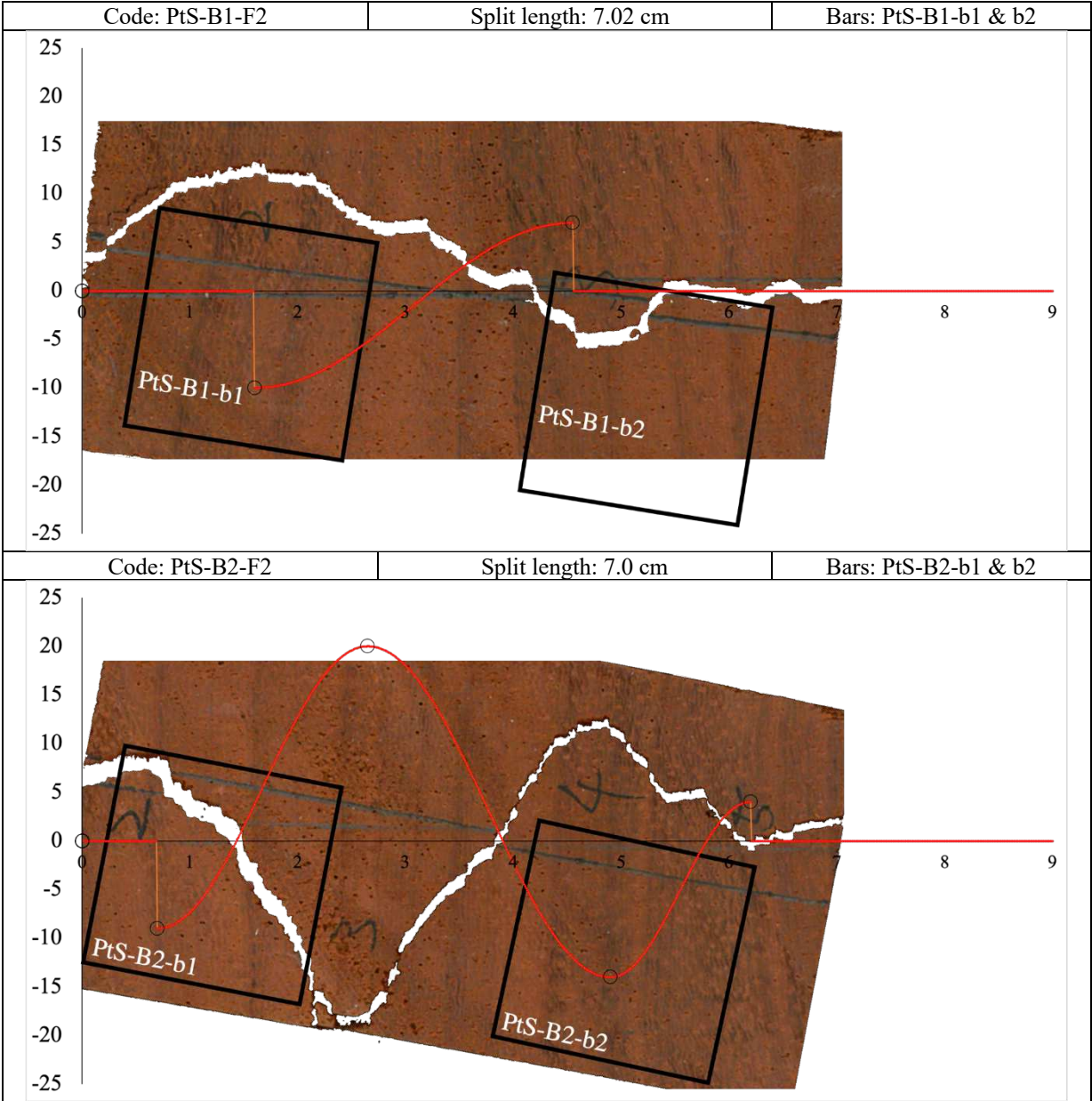
Annex Tab. 1 (continued)



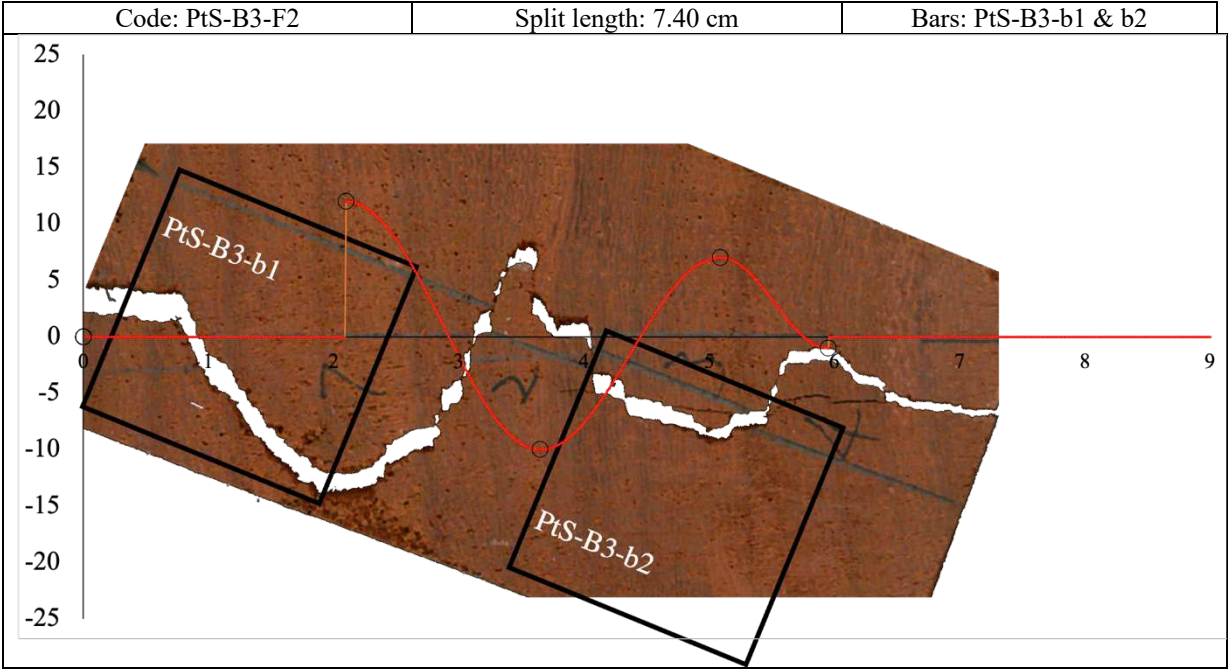
Annex Tab. 1 (continued)



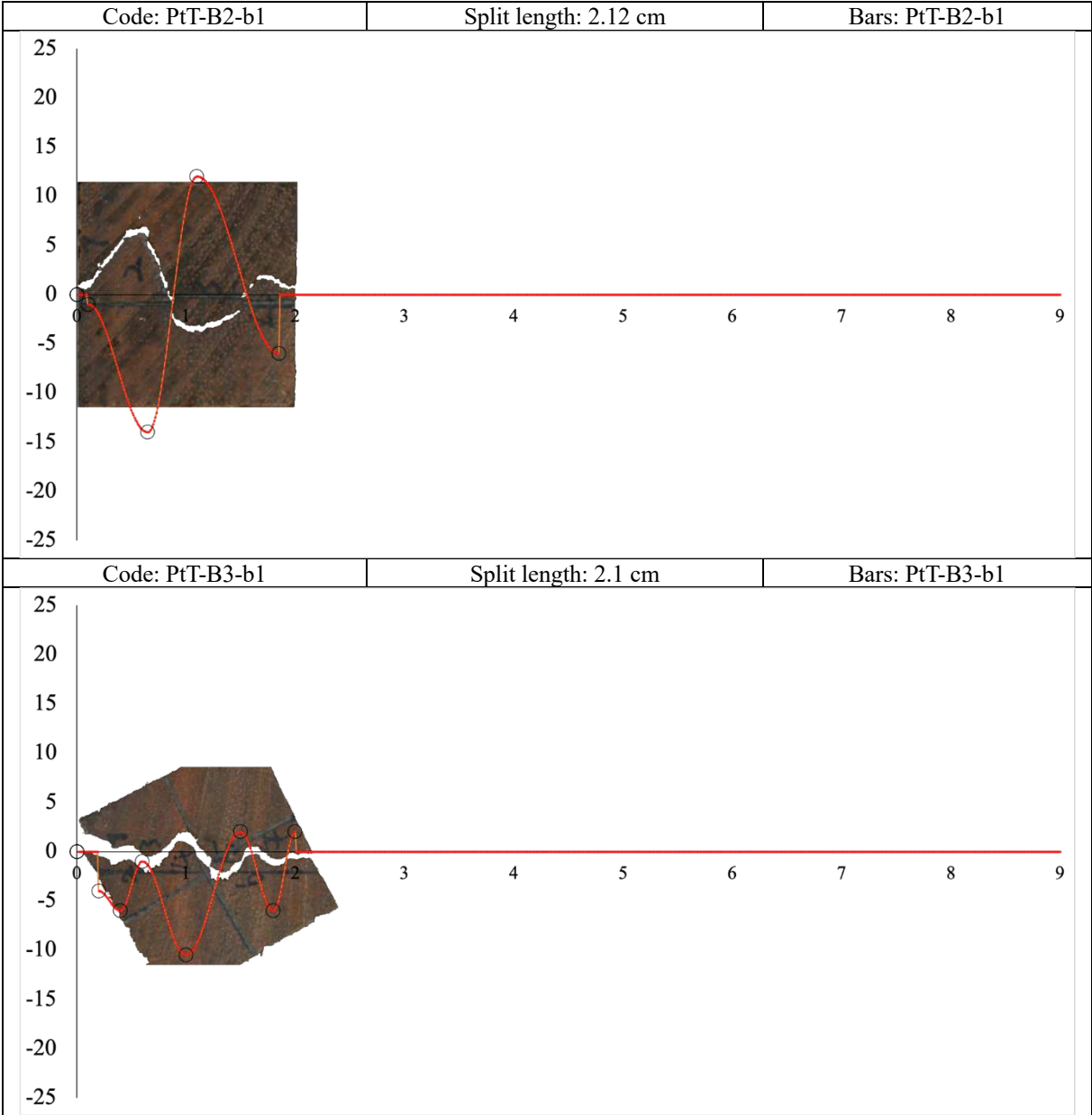
Annex Tab. 1 (continued)



Annex Tab. 1 (continued)



Annex Tab. 1 (continued)



Annex Tab. 1 (continued)

